Equations of state for the thermodynamic properties of cryogenic mixtures

Jakub Tkaczuk

THÈSE

Pour obtenir le grade de

DOCTEUR DE L'UNIVERSITÉ GRENOBLE ALPES

Spécialité : PHYSIQUE APPLIQUEE

Arrêté ministériel : 25 mai 2016

Présentée par

Jakub TKACZUK

Thèse dirigée par **Nicolas LUCHIER**

préparée au sein du **Laboratoire Service des Basses Températures**
dans **l'École Doctorale Physique**

Equations d'état pour les propriétés thermodynamiques des mélanges de fluides cryogéniques

Equations of state for the thermodynamic properties of cryogenic mixtures

Thèse soutenue publiquement le **13 décembre 2021**,
devant le jury composé de :

Monsieur ROLAND SPAN
PROFESSEUR, Ruhr-Universität Bochum, Rapporteur
Monsieur JEAN-NOËL JAUBERT
PROFESSEUR DES UNIVERSITES, UNIVERSITE DE LORRAINE, Rapporteur
Monsieur FREDERIC AYELA
PROFESSEUR DES UNIVERSITES, UNIVERSITE GRENOBLE ALPES, Président
Monsieur BERTRAND BAUDOUY
INGENIEUR HDR, CEA CENTRE DE PARIS-SACLAY, Examinateur
Madame PASCALE DAUGUET
INGENIEUR HDR, AIR LIQUIDE, Examinatrice

EQUATIONS OF STATE FOR THE THERMODYNAMIC PROPERTIES OF CRYOGENIC MIXTURES

Jakub Tkaczuk

13 December 2021

PhD Supervisor	:	Nicolas Luchier	CEA Grenoble
EASITrain supervisor	:	François Millet	CEA Grenoble

PhD Graduation Committee:

Chairman	:	Frederic Ayela	Université Grenoble Alpes
Reviewers	:	Roland Span	Ruhr-Universität Bochum
		Jean-Noël Jaubert	Université de Lorraine
Members	:	Bertrand Baudouy	CEA Saclay
		Pascale Dauguet	Air Liquide Advanced Technologies

The research described in this thesis was carried out at:
The French Alternative Energies and Atomic Energy Commission, Grenoble, France
Commissariat à l'énergie atomique et aux énergies alternatives (CEA),
Direction de la Recherche Fondamentale (DRF),
Institut de Recherche Interdisciplinaire de Grenoble (IRIG),
Département des Systèmes Basses Températures (DSBT),
Laboratoire Cryogénie Fusion (LCF).

Equations of state for the thermodynamic properties of cryogenic mixtures
Equations d'état pour les propriétés thermodynamiques des mélanges de fluides cryogéniques
Jakub Tkaczuk, PhD thesis
Université Grenoble Alpes
École doctorale de Physique
Physique appliquée

EQUATIONS OF STATE FOR THE THERMODYNAMIC PROPERTIES OF CRYOGENIC MIXTURES

DISSERTATION

to obtain
the degree of doctor at the Université Grenoble Alpes,
on account of the decision of the graduation committee,
to be publicly defended on 13 December 2021

by

Jakub Tkaczuk

born on 17 January 1989
in Warsaw, Poland

EASITrain – European Advanced Superconductivity Innovation and Training.
This Marie Skłodowska-Curie Action (MSCA) Innovative Training Network (ITN)
has received funding from the European Union's H2020 Framework Programme
under Grant Agreement no. 764879.

Acknowledgements

I would not have made it without the help of many people.

I want to thank François and Nicolas for providing me with the opportunity of becoming a part of the Cryogenic Engineering Department at CEA Grenoble, as well as a part of the EASITrain network. Thank you for the supervision, where it was necessary. The guidance and freedom you gave me were well balanced so that I could have developed and grown. Thank you for pushing me forward, for your in-depth questions, and the support I received throughout my stay in the lab.

I cannot be more grateful for having a chance to work with Ian and Eric. You sparked a passion for computer science in me. I will remember the care you demonstrated, and I will do my best to pay it forward. Thank you for all the professional and personal opportunities you offered during my stay in Boulder, both inside and outside the NIST buildings. I hope our paths will cross once again in the future.

I thank Eric for making his cryostat available for the duration of my experiment. There is a large chance I would not have been able to complete the measurements without your willingness to share the work and resources. I also want to thank Pierre, Thomas, Patrick, and Bertrand for your time spent on the test setup preparations. My experiment was successful, thanks to your technical support.

To the EASITrain fellows, thank you for the endless laughter and a great time we shared. These three years would not be the same without you: Aisha, Alice, Andrea, Dmitry, Dorothea, Jean-Francois, Johannes, Linn, both Mattias, Maxime, Paola, Sofiya, Stewart, and Vanessa. To the EASITrain crew at CERN, your work put us all together and allowed us to grow.

To all my labmates, especially to Jeya for the everyday abstract discussions, Morgane for the Polish accents at work, and Christian for being so motivated to work when retired.

To my Mum and Dad, thank you for your long-term support.

Last but not least – Ewa and Jan, thank you for being there when I needed you most.

CONTENTS

List of Tables xiii

List of Figures xix

Nomenclature xxi

Physical constants and fluid-specific data xxvii

Abstract xxix

Résumé xxxi

1 Introduction 1

2 Different forms of the equations of state 3

2.1 Phase diagrams of cryogenic fluids . . . 3

2.1.1 Pure fluids . . . 3

2.1.2 Binary mixtures . . . 4

2.2 Equations of state . . . 6

2.2.1 Ideal gas equations of state . . . 7

2.2.2 Van der Waals equation of state . . . 7

2.2.3 Other cubic equations of state . . . 8

2.2.4 Non-cubic equations of state . . . 9

2.2.5 Virial equation of state . . . 10

2.2.6 Molecular-based equations . . . 11

2.2.7 Pressure-explicit equations of state . . . 12

2.2.8 Empirical, multi-parameter equation of state explicit in Helmholtz energy . . . 13

3 Developing the multi-parameter equations of state for mixtures 15

3.1 Modern form of the Helmholtz energy equation of state . . . 15

3.2 Optimization algorithm . . . 20
3.2.1 Methodology . . . 20
3.2.2 Fitter . . . 22
3.2.3 Constraining the fitter behavior . . . 22
3.2.4 Weighting the data . . . 23
3.3 Experimental data available for the equations development . . . 24
3.4 Results of the equations of state development . . . 26
3.4.1 Helium-neon . . . 27
3.4.2 Helium-argon . . . 29
3.4.3 Neon-argon . . . 31
3.4.4 Helium-nitrogen . . . 33
3.5 Uncertainty discussion at phase boundary . . . 35
3.6 EOS performance comparison . . . 39
3.7 Validation data . . . 40
3.8 Conclusions from the EOS development . . . 41

4 Isenthalpic Joule-Thomson coefficient measurements 43
4.1 Thermodynamic determination of the Joule-Thomson coefficient . . . 43
4.2 Literature review for the JT coefficient . . . 47
4.3 Measurement methods . . . 49
4.4 Experimental setup design . . . 51
4.4.1 Equipment design and choice according to flow and thermal considerations . . . 52
4.4.2 Test bench design . . . 59
4.5 Experimental procedure . . . 66
4.5.1 Step-by-step measurement description . . . 66
4.5.2 Measured isenthalpic curves for pure fluids . . . 69

5 Measurements analysis and results comparison against EOS 71
5.1 Determining the Joule-Thomson coefficient . . . 71
5.1.1 Fitting a polynomial and choosing its degree . . . 72
5.1.2 Fit behavior at extremities . . . 73
5.1.3 Removing inlet measurements from the analysis . . . 74
5.2 Results analysis for pure fluids . . . 75
5.2.1 Conventional uncertainty analysis . . . 76
5.2.2 Monte Carlo simulation for uncertainty propagation . . . 79
5.2.3 Polynomial selection to fit the data . . . 82
5.3 Results analysis for mixtures . . . 83

5.3.1 Influence of the composition uncertainty 86
5.3.2 Corrections for heat losses and kinetic energy 87
5.4 Conclusions from the measurements 89

6 Conclusions **91**

Bibliography **95**

Appendix A - Experimental data for the EOS development **109**

Appendix B - Thermodynamic properties calculated with the EOS **115**

Appendix C - Python script for validating EOS implementation **125**

Appendix D - Experimental setup for the Joule-Thomson coefficient measurements **129**

Appendix E - Results from the Joule-Thomson coefficient measurements **135**

List of Tables

3.1 Reducing temperature and density parameters 16
3.2 Summary of the experimental data available for the equations development 24
3.3 Binary specific parameters 26
3.4 Departure function coefficients for the helium-neon mixture 27
3.5 Departure function coefficients for the helium-argon mixture 29
3.6 Departure function coefficients for the neon-argon mixture 31
3.7 Departure function coefficients for the helium-nitrogen mixture 33
3.8 Data points at equimolar (0.5/0.5) composition for EOS validation 40

4.1 Deviations of existing experimental data for μ_{JT} from Helmholtz energy EOS 49

5.1 Uncertainties of the key components 77
5.2 Mean absolute and relative corrections to $\left.\frac{\Delta T}{\Delta p}\right|_{path}$ from Eq. (4.9) 88

A.1 Experimental data for ^4He-Ne 109
A.2 Experimental data for ^4He-Ar 110
A.3 Experimental data for $Ne-Ar$ 111
A.4 Experimental data for $^4He-N_2$ 112

B.1 Single-phase properties as a function of Helmholtz energy. 115

D.1 List of equipment used for measurements 129

E.1 $p-T$ measurements for the Joule-Thomson coefficient in pure fluids . . . 135
E.2 $p-T-x$ measurements for the Joule-Thomson coefficient in mixtures . . 137
E.3 Calculated Joule-Thomson coefficient values for pure fluids 140
E.4 Calculated Joule-Thomson coefficient values for mixtures 141

List of Figures

2.1 Phase diagrams of fluids used in this work, with isopycnic (ρ = const.) lines plotted in blue and critical points marked with black stars. 4

2.2 Class III phase envelope with the vapor-liquid equilibrium (VLE) – gray area in (b), and existing gas-gas equilibrium (GGE) – yellow area in (b). x is the mole fraction of a lighter component. The star represents the critical point and the dashed line, the critical line. 5

3.1 $p-T$ coverage of available ρpT data with composition dependent color scale. x_1 is the molar concentration of a lighter component 25

3.2 Vapor-liquid equilibrium (VLE) of helium-neon 28

3.3 Relative deviations of the ^{4}He − Ne equation from the single-phase data . 28

3.4 Temperature-entropy diagram of the ^{4}He − Ne mixture at equimolar composition with isobars, saturation line, and the critical point marked with a star. More plots are available in Fig. B.1. 29

3.5 Vapor-liquid (VLE) and gas-gas equilibria (GGE) of helium-argon 30

3.6 Relative deviations of the ^{4}He − Ar equation from the single-phase data . 30

3.7 Vapor-liquid equilibrium (VLE) of neon-argon 32

3.8 Relative deviations of the Ne − Ar equation from the single-phase data . . 32

3.9 Vapor-liquid (VLE) and gas-gas equilibria (GGE) of helium-nitrogen 33

3.10 Relative deviations of the ^{4}He − N_2 equation from the single-phase data . 34

3.11 Schematic representation of the orthogonal error calculations for the phase envelopes. 36

3.12 Absolute orthogonal error for the vapor-liquid and gas-gas equilibria . . . 37

3.13 Distribution of the orthogonal error values plotted with marginal histograms 37

3.14 Orthogonal error and resulting absolute errors plotted for four mixtures. Colors in subfigures (b) and (c) follow the colors imposed in subfigure (a). 38

3.15 VLE isotherms of ^{4}He − Ne calculated with empirical equation of state from this work, quantum-corrected cubic equation, and quantum-corrected SAFT equations. Circles mark the experimental data. 40

4.1 Joule-Thomson coefficient and compressibility factor for pure helium–4 and pure neon, calculated with CoolProp. 45
4.2 Inversion curves for the only fluids with negative Joule-Thomson coefficients at ambient conditions. μ_{JT} is positive in colored regions. 46
4.3 One of the versions of the radial flow apparatus used by Roebuck *et al.* . . 47
4.4 Relative deviation of existing experimental data from EOS. Grey rectangle is the ±5% band. Colors vary for authors. 48
4.5 Schematic representation of two methodologies for the JT coefficient measurement with $\Delta p_{(a)} << \Delta p_{(b)}$, black dots representing the measurement points, and red dot representing the point at which the coefficient is to be defined. 50
4.6 Schematically represented cycles for the Joule-Thomson coefficient measurements with flow restriction, two pressure sensors, and two temperature sensors. 52
4.7 Schematic fluid flow in the proximity of an orifice restriction. 53
4.8 Inversion curves for the ^{4}He − Ne mixture with helium mole fraction, x_{He} as a parameter. The green rectangle marks the target pressure and temperature ranges for the μ_{JT} measurements. Thick inversion curves mark the helium concentration range, $x_{He} = \langle 0.2, 0.5 \rangle$, for which the Joule-Thomson coefficient is measured in this work. 56
4.9 Capillary length calculated for $p_{in} = 10$ MPa, $p_{out} = 1.1$ MPa, equimolar composition of ^{4}He − Ne, and internal diameter in mm as a parameter. . . 57
4.10 Downstream pressure, p_{out} for 0.4 × 1 mm, 6 m long capillary calculated as a function of the mass flow rate, parametrized with inlet pressures ranging from 4 MPa to 10 MPa, plotted for four mixture compositions x_{He} (columns) and two inlet temperatures T_{in} (rows). 58
4.11 Temperature change as a function of pressure, calculated for two inlet temperature values and four molar compositions with inlet pressure as a parameter. 59
4.12 Process Flow Diagram (PFD) of the Joule-Thomson measurement setup. . 60
4.13 Joule-Thomson expansion capillary and the surrounding hardware. 61
4.14 Diameter verification flow meter scheme and measurement results for 2 m long capillary. 63

4.15 Minimal achievable temperature of AL300 cold head for mass flow rate at 10 MPa cooled from 300 K to 65 K (black) and 80 K (blue). 64
4.16 Flow coefficient calculations for downstream valves HV013 and HV015. The horizontal red lines represent the minimal and maximal C_v values for two chosen valves. 65
4.17 Pressure and temperature evolution during a single isenthalpic line measurements of $He-N_2$. 67
4.18 Composition stability during a single isenthalpic line measurements of $He-N_2$. 68
4.19 Measurements for 'hysteresis' verification. The isenthalpic line in plotted in the left figure. The upper-right figure shows deviations of measured μ_{JT} with increasing (blue) and decreasing (red) pressure drop in the course of measurements. The lower-right figure shows a relative difference between the two values. 69
4.20 Results of the $p-T$ pairs measurements for pure fluids. Solid lines are the constant enthalpy lines calculated with EOS. Black lines are the saturation lines, and black stars are the critical points. The color-coded measurement data used to plot the figures are available in Table E.1 and are represented with circles. 70

5.1 AAD calculated for the Joule-Thomson coefficient of pure fluids as a function of the fit order. The filled points are the minima of the measurements deviations from the EOS. 73
5.2 Deviations of a fit (dashed line) from the polynomial (solid line). 74
5.3 Measured $p-T$ pairs (top figures), resulting Joule-Thomson coefficients (middle figures), and measurement deviation relative to EOS (bottom figures) plotted with uncertainty bars from conventional analysis in black and the Monte Carlo analysis in grey. The color-coded numerical values of $p-T$ measurements at $h = \text{const.}$ are available in Table E.1, the calculated Joule-Thomson coefficients – in Table E.3. 75
5.4 Relative expanded uncertainties for measured isenthalpic lines, calculated with Eq. (5.10). Circles mark values of measured $p-T$ pairs from Fig. 5.3 and Table E.1. 78
5.5 Visual representation of an isenthalpic line measurement error. Black points are the perfect measurements, ellipses are their statistically calculated uncertainties, and rings are the randomly selected measurements within the uncertainty bounds. 80

5.6 Mean relative expanded uncertainty for the measurements of the integrated Joule-Thomson coefficient in pure fluids, calculated with Monte Carlo uncertainty propagation. 81
5.7 Influence of the type of polynomial used for fitting the measurements on the Joule-Thomson coefficient results. 83
5.8 Measured $p-T$ pairs for ^4He-Ne mixture with variable molar composition (top row). Resulting Joule-Thomson coefficients (middle row) and the relative deviation from the EOS (bottom row) presented with black uncertainty bars from Eq. (5.10) and gray bars from the Monte Carlo analysis. The color-coded numerical values of $p-T$ measurements are available in Table E.2. The calculated Joule-Thomson coefficients are given in Table E.4. 84
5.9 Measured $p-T$ pairs and μ_{JT} values for $^4He-N_2$ mixture and two molar composition values. The color-coded numerical values of $p-T$ measurements are available in Table E.2. The calculated Joule-Thomson coefficients are given in Table E.4. 85
5.10 Measurement error of differentiated isenthalpic Joule-Thomson coefficient for ^4He-Ne, plotted for a variable number of points on a single $h = \text{const.}$ line, excluding the extremities, averaged over a number of points on the isenthalpic line. Figures show results of the Monte-Carlo analysis for mixture measurement uncertainty. The yellow lines are the moving average for plotted points – including all uncertainty components. The red lines are the moving average estimating the composition uncertainty influence on μ_{JT} measurements. 86
5.11 Estimated heat loss impact on deviations of measurements and EOS. Colors in the figures match the colors given in Tables E.3 and E.4. 88
5.12 Relative deviation of existing experimental data from Fig. 4.4, extended with data from this work, compared to the EOS. Grey rectangle is the ±5% band. Colors vary for authors. 90

B.1 Characteristic plots for ^4He-Ne. 116
B.2 Characteristic plots for ^4He-Ar. 118
B.3 Characteristic plots for $Ne-Ar$. 120
B.4 Characteristic plots for $^4He-N_2$. 122

D.1 Piping and instrumentation diagram (P&ID) of the Joule-Thomson measurements setup. 131

D.2 Print screen from Panorama E2 SCADA - software for data acquisition and hardware control. Image taken during test setup validation with pure argon. 132
D.3 Gas manifold. 133
D.4 Complete experimental setup. 133
D.5 Multi-layer insulation on the thermal shield around the capillary. 133

NOMENCLATURE

Symbol	Unit	Description
a	J mol^{-1}	Specific Helmholtz energy
a	Pa m^6 mol^{-2}	Measure of average attraction between particles
A	J	Helmholtz energy
A	-	First virial coefficient
Ar	-	Argon
b	m^3 mol^{-1}	Volume excluded by a mole of particles
B	m^3 mol^{-1}	Second virial coefficient
C	m^6 mol^{-2}	Third virial coefficient
C_k	-	k-th coefficient of Chebyshev polynomial
c_p	J (kg K)$^{-1}$	Specific heat at constant pressure
c_p^o	J (kg K)$^{-1}$	Reference state specific heat at constant pressure
c_v	J (kg K)$^{-1}$	Specific heat at constant volume
C_v	-	Valve flow coefficient
$d_{ij,k}$	-	Fitted parameter of a mixture departure function
$d_{oi,k}$	-	Fitted parameter for residual Helmholtz energy of pure fluid i
D	m	Diameter
D_ext	m	External diameter
D_h	m	Hydraulic diameter
D_int	m	Internal diameter
err	-	Calculated relative error
e_k	J kg^{-1}	Specific kinetic energy
f	-	Darcy friction factor
F_{ij}	-	Scaling parameter applied to departure function
F_y	-	Function minimizing relative deviations of property y
g	J kg^{-1}	Molar-specific Gibbs energy
h	J kg^{-1}	Molar-specific enthalpy
h	J s	Planck constant

h_o^o	J mol^{-1}	Reference state specific enthalpy
h_{in}	J mol^{-1}	Inlet specific enthalpy
h_{out}	J mol^{-1}	Outlet specific enthalpy
H	J	Enthalpy
H_2	-	Hydrogen
He	-	Helium–4
He-I	-	Normal component of helium–4
He-II	-	Superfluid component of helium–4
i	-	Iteration variable
J_i	-	Gradient in point i
k	-	Coverage factor for expanding uncertainty
k	W (m K)$^{-1}$	Thermal conductivity
k_{B}	J K^{-1}	Boltzmann constant
k_{ij}	-	Coupling parameter
K_{c}	-	Number of critical terms of pure fluid residual Helmholtz energy
K_{e}	-	Number of exponential terms of pure fluid residual Helmholtz energy
K_{p}	-	Number of polynomial terms of pure fluid residual Helmholtz energy
l	m	Unitary length
$l_{oi,k}$	-	Fitted parameter for residual Helmholtz energy of pure fluid i
L	m	Length
m	kg	Mass
$\dot{m}$	kg s^{-1}	Mass flow rate
M	kg mol^{-1}	Molar mass
n	mol	Number of moles
n	-	Number of points
$n_{oi,k}$	-	Fitted parameter for residual Helmholtz energy of pure fluid i
N	-	Number of particles
N	-	Number of points
N_{A}	mol^{-1}	Avogadro constant
$N_{ij,k}$	-	Fitted parameter of a mixture departure function
Ne	-	Neon
N_2	-	Nitrogen
p	Pa	Pressure
p_{atm}	Pa	Atmospheric pressure
p_i	Pa	Pressure at point i
p_{c}	Pa	Critical point pressure of fluid
p_{calc}	Pa	Calculated pressure

p_r	Pa	Reducing pressure
p_in	Pa	Inlet pressure
p_max	Pa	Maximal pressure in the system
p_out	Pa	Outlet pressure
$\hat{p}$	-	Reduced pressure
q_L	W m^{-2}	Heat transferred through conductivity
Q_k	-	derivative of k-th coefficient of Chebyshev polynomial
$\dot{Q}$	W	Heat transfer rate
r	m	Distance between two interacting particles
R	J (mol K)$^{-1}$	Molar gas constant
Re	-	Reynolds number
s	J (mol K)$^{-1}$	Molar specific entropy
s_o^o	J (mol K)$^{-1}$	Reference state specific entropy
S	J K^{-1}	Entropy
t	s	Time
$t_{ij,k}$	-	Fitted parameter of a mixture departure function
$t_{oi,k}$	-	Fitted parameter for residual Helmholtz energy of pure fluid i
T	K	Temperature
$T_{\mathrm{c},i}$	K	Critical point temperature of fluid i
T_in	K	Inlet temperature
T_out	K	Outlet temperature
$T_\mathrm{out}^\mathrm{h}$	K	Outlet temperature at isenthalpic conditions
T_r	K	Reducing temperature
T_λ	K	Lambda point temperature of Helium–4
$U(q)$	-	Standard measurement uncertainty of property q
U_c	-	Combined expanded uncertainty
U_r	-	Relative standard expanded uncertainty
u	J kg^{-1}	Internal energy
$\bar{u}$	m s^{-1}	Mean flow velocity
u_in	m s^{-1}	Inlet velocity
u_out	m s^{-1}	Outlet velocity
v	m^3 kg^{-1}	Specific volume
V	m^3	Volume
$\dot{V}$	m^3 s^{-1}	Volumetric flow rate
w	m s^{-1}	Speed of sound
W_y	-	Weight assigned to data points of property y
x_i	-	Mole fraction in liquid phase of component i

$x_{\text{calc}}^{\min}$	-	Calculated mole fraction
x_{data}	-	Mole fraction of a data point
x	-	Vector of mole fractions
y_i	-	Mole fraction in vapor phase of component i
$y_{\text{data},i}$	-	Value of experimental data point i
$y_{\text{EOS},i}$	-	Value calculated with equation of state in point i
Z	-	Compressibility factor
α	-	Total reduced Helmholtz energy
α^{o}	-	Ideal gas part of total reduced Helmholtz energy
α_{τ}^{o}	-	First derivative of ideal gas Helmholtz energy with respect to reduced temperature
$\alpha_{\tau\tau}^{\text{o}}$	-	Second derivative of ideal gas Helmholtz energy with respect to reduced temperature
α_{oi}^{o}	-	Pure fluid ideal Helmholtz energy
α^{r}	-	Residual part of total reduced Helmholtz energy
α_{oi}^{r}	-	Pure fluid residual Helmholtz energy
α_{ij}^{r}	-	Pairwise departure function
$\alpha_{\delta}^{\text{r}}$	-	First derivative of residual Helmholtz energy with respect to reduced density
$\alpha_{\delta\delta}^{\text{r}}$	-	Second derivative of residual Helmholtz energy with respect to reduced density
α_{τ}^{r}	-	First derivative of residual Helmholtz energy with respect to reduced temperature
$\alpha_{\tau\tau}^{\text{r}}$	-	Second derivative of residual Helmholtz energy with respect to reduced temperature
$\alpha_{\delta\tau}^{\text{r}}$	-	Second derivative of residual Helmholtz energy with respect to reduced density and temperature
β	K^{-1}	Isobaric expansion coefficient
$\overline{\beta}$	-	Vector of fitted parameters
$\beta_{ij,k}$	-	Fitted parameter of a mixture departure function
$\beta_{oi,k}$	-	Fitted parameter for residual Helmholtz energy of pure fluid i
$\beta_{T,ij}$	-	Fitted parameter for reducing property calculations
$\beta_{v,ij}$	-	Fitted parameter for reducing property calculations
$\gamma_{ij,k}$	-	Fitted parameter of a mixture departure function
$\gamma_{oi,k}$	-	Fitted parameter for residual Helmholtz energy of pure fluid i
$\gamma_{T,ij}$	-	Fitted parameter for reducing property calculations

$\gamma_{v,ij}$	-	Fitted parameter for reducing property calculations
δ	-	Reduced density
Δy		Change of property y
ϵ	m	Absolute pipe roughness
$\epsilon_{oi,k}$	-	Fitted parameter for residual Helmholtz energy of pure fluid i
$\epsilon_{ij,k}$	-	Fitted parameter of a mixture departure function
ζ_i	-	Relative residual of experimental point i
η	-	Packing fraction
$\eta_{ij,k}$	-	Fitted parameter of a mixture departure function
κ	-	Ratio of gas heat capacities
λ_a	-	Attractive exponent of the Lennard-Jones potential
λ_r	-	Repulsive exponent of the Lennard-Jones potential
λ_th	m	Thermal de Broglie wavelength
ρ	mol dm^{-3}	Molar density
ρ_c	kg m^{-3}	Critical density of fluid
ρ_m	kg m^{-3}	Mass density
μ	Pa s	Dynamic viscosity
μ_i	J mol^{-1}	Chemical potential
μ_JT	K Pa^{-1}	Joule-Thomson coefficient
τ	-	Reduced temperature
τ_o	-	Reduced temperature at reference state

Acronym	Description
AAD	Average absolute deviation
ALAT	Air Liquide Advanced Technology
CABTR	Centrale d'Acquisition Basses Températures Rapide
CEA	Commissariat à l'énergie atomique et aux énergies alternatives
CERN	European Organization for Nuclear Research
DSBT	Département des Systèmes Basses Températures
EASITrain	European Advanced Superconductivity Innovation and Training
EOS	Equation of state
FCC	Future Circular Collider
FS	Full scale
GGE	Gas-gas equilibrium
HTS	High temperature superconductor
ITER	International Thermonuclear Experimental Reactor
JET	Joint European Torus
JT	Joule-Thomson *effect*, *coefficient*
JT-60SA	Superconducting Japan Torus-60 *research tokamak*
ITN	Innovative Training Network
LHC	Large Hadron Collider
LLE	Liquid-liquid equilibrium
LNG	Liquid natural gas
LMA	Lavenberg-Marquardt algorithm
MSCA	Marie Skłodowska-Curie Action
MLI	Multi-layer insulation
NIST	National Institute of Standards and Technology
SSQ	Sum of squares
VLE	Vapor-liquid equilibrium
w.r.t.	*Derivative* with respect to *a variable*

PHYSICAL CONSTANTS AND FLUID-SPECIFIC DATA

Symbol	Value	Unit	Description
h	$6.626\,070\,15 \times 10^{-34}$	J s	Planck constant[a]
k_B	$1.380\,649 \times 10^{-23}$	$J\,K^{-1}$	Boltzmann constant
N_A	$6.022\,140\,76 \times 10^{23}$	mol^{-1}	Avogadro constant
R	8.314 462 618	$J\,(mol\,K)^{-1}$	Molar gas constant[a]

[a] Source: CODATA – database of the National Institute of Standards and Technology[1]

Parameter	Value	Unit
	argon	
Molar mass	0.039 948	kg mol^{-1}
Triple point temperature	83.806	K
Triple point pressure	68 892.477	Pa
Critical point temperature	150.687	K
Critical point pressure	4 863 000.0	Pa
Critical point density	13 407.4	mol m^{-3}
	helium–4	
Molar mass	0.004 002 602	kg mol^{-1}
Lower λ-point temperature	2.176 8	K
Lower λ-point pressure	5 033.548	Pa
Upper λ-point temperature	1.763 3	K
Upper λ-point pressure	3 013 000.0	Pa
Critical point temperature	5.195 3	K
Critical point pressure	227 600.0	Pa
Critical point density	18 130.0	mol m^{-3}
	nitrogen	
Molar mass	0.028 013 48	kg mol^{-1}
Triple point temperature	63.151	K
Critical point temperature	126.192	K
Critical point pressure	3 395 800.0	Pa
Critical point density	11 183.9	mol m^{-3}
	neon	
Molar mass	0.020 179	kg mol^{-1}
Triple point temperature	24.56	K
Critical point temperature	44.4	K
Critical point pressure	2 661 630.808	Pa
Critical point density	24 100.0	mol m^{-3}

Source: CoolProp[2]

ABSTRACT

This work is motivated by the needs of large cryogenic facilities and aims to improve their thermal efficiency in the range of 40—80 K. It allows describing the thermodynamic properties of cryogenic mixtures accurately.

The empirical multiparameter equations of state explicit in the Helmholtz energy are developed for the binary mixtures of helium, neon, argon, and nitrogen. The development process is presented and consists of the experimental data review, data points weighting, and minimizing the objective function using the supervised non-linear regression.

The equations are valid in the single-phase and at the phase envelopes for the entire composition span and pressures as high as 1000 MPa. The single-phase uncertainties at low pressure ($0-10$ MPa) reach $0.5-2.5\%$ for 95% of data points used for the EOS development. At higher pressures, some of the equations deviate up to 5% in density from the experimental data. The deviations in the speed of sound vary from 4 to 10%.

In addition to the single-phase uncertainty discussion, a new metric is proposed to evaluate the uncertainties in phase equilibria calculations. Its advantages and shortcomings over the classical pressure-based metric are presented.

The equations of state are validated at cryogenic temperatures in the single-phase region with measurements of the Joule-Thomson coefficient. Indirect measurements are first acquired for pure fluids, allowing for the experiment validation and then for mixtures, providing new results to the study. The expanded relative standard uncertainty is presented and discussed along with the Monte Carlo analysis for the combined uncertainty. The impact of the composition uncertainty on the Joule-Thomson coefficient is quantified for mixtures using the Monte Carlo simulations.

The presented equations of state are in good agreement with the obtained Joule-Thomson coefficient values. A short discussion on perspectives and further steps concludes this work and aims at a more accurate mixture property description thanks to new, more accurate measurements and modern minimization algorithms used to develop the equations.

RÉSUMÉ

Ce travail est motivé par le développement de nouvelles installations cryogéniques de grande capacité et vise à améliorer leur efficacité thermique en tirant parti des propriétés des mélanges de gaz. Pour répondre à ces besoins, une connaissance précise des propriétés thermodynamiques de ces mélanges est nécessaire. Contrairement aux fluides purs, cette connaissance reste lacunaire aujourd'hui.

Les résultats de la présente thèse permettent de déterminer avec précision l'équation d'état de mélanges binaires à base de gaz nobles: hélium–4, néon, argon et azote. Cette équation d'état permet de calculer les propriétés thermodynamiques de ces mélanges de façon fiable et précise.

La première partie de ce travail est dédiée à la mise au point d'équations d'état (EOS) empiriques et précises. Une revue soigneuse de l'état de l'art montre que la formulation explicite des EOS en énergie de Helmholtz est la plus prometteuse pour atteindre les niveaux de précision recherchés, à la fois dans les régions monophasiques et aux enveloppes de phase où les changements d'état surviennent. La méthode de détermination de cette formulation est décrite de façon extensive dans les Chapitres 2 et 3. Le modèle résultant de cette étude est ajusté aux données expérimentales afin de déterminer un jeu de coefficients pour chacun des mélanges binaires étudiés dans cette thèse: ^{4}He — Ne, ^{4}He — Ar, Ne — Ar ainsi que ^{4}He — N_2. Les résultats pour ces quatres premiers mélanges ont fait l'objet d'une publication dans le *Journal of Physical and Chemical Reference Data* et on été intégré dans la base de données REFPROP, CoolProp et TREND.

La deuxième partie de ce document (Chapitres 4 et 5) décrit le travail expérimental de validation des EOS dans le domaine cryogénique (50—120 K) où les mesures manquent dans la littérature. Le banc expérimental de mesure du coefficient de Joule-Thomson aux températures cryogéniques est présenté, la méthodologie est discutée et les résultats obtenus sont analysés. Un effort important est consacré à l'amélioration de la précision des mesures et à la discussion des erreurs rencontrées.

État de l'art des équations d'état pour les mélanges

Les équations d'état peuvent être utilisées pour calculer les propriétés des fluides dans les régions monophasiques et aux envelopes de phases. Elles se traduisent graphiquement dans les diagrammes de phase où sont décrites les régions gazeuses, liquides, supercritiques et solides. Pour les quatre mélanges binaires discutés dans ce travail, les diagrammes de phases sont tracés dans la Fig. 2.1. Les enveloppes de phase pour les mélanges fluides diffèrent considérablement selon les constituants. D'intérêt particulier dans ce travail, l'hélium–4 forme les équilibres de phases de classe III comportant un équilibre vapeur-liquide (VLE) et un équilibre gaz-gaz ouvert (GGE). L'équilibre gaz-gaz implique une séparation de phase au-dessus de la température critique du composant le plus lourd. Les isothermes dans l'équilibre gaz-gaz gardent une pente positive et ne sont fermées par aucune ligne critique. Un exemple d'enveloppe de phase avec un équilibre vapeur-liquide supercritique et l'équilibre gaz-gaz est présenté Fig. 2.2. Dans notre étude, les équilibres vapeur-liquide dans les mélanges sont toujours supercritiques, où l'hélium est au-dessus de sa température critique, et la région diphasique commence au point d'ébullition du deuxième composant.

Diverses équations d'état sont discutées à partir des modèles du gaz parfait et de Van der Waals, en terminant par la forme explicite en énergie de Helmholtz moderne des équations d'état empiriques multi-paramètres. Chaque équation est discutée à l'aune de nos besoins: une grande précision à la fois dans les domaines monophasiques mais également capable de décrire proprement les enveloppes de phase. À ce titre, l'équation d'état explicite en énergie de Helmholtz semble la plus prometteuse et est appliquée à nos mélanges dans les chapitres suivants.

Détermination des équations d'état des mélanges

L'énergie de Helmholtz pour les mélanges, $\alpha(\delta, \tau, \overline{x})$, est définie dans l'Eq. (3.1). Elle est présentée sous sa forme réduite fonction des quantités adimensionnelles – densité δ et température réduites τ. Les contributions parfaites $\alpha^{o}(\rho, T, \overline{x})$ et résiduelle $\alpha^{r}(\delta, \tau, \overline{x})$ dans l'équation constituent l'énergie de Helmholtz pour les mélanges. Ces deux quantités s'exprime comme une combinaison des énergies de Helmholtz pour les fluides purs composant le mélange $\alpha^{o}_{oi}(\delta, \tau)$ et $\alpha^{r}_{oi}(\delta, \tau)$. Outre ces contributions, l'équation d'état pour les mélanges comprend également une fonction de départ $\alpha^{r}_{ij}(\delta, \tau)$ – décrivant la différence entre le gaz parfait et les propriétés réelles du gaz. Cette fonction permet de décrire précisément des propriétés du fluide dans tout l'espace $p - T - x$. L'ensemble des relations entre ces différentes fonctions est décrit avec les équations (3.1) à (3.8).

Les propriétés thermodynamiques du mélange sont alors déterminées en fonction de l'énergie de Helmholtz et de ses dérivées. Par exemple, le coefficient de Joule Thomson étudié dans ce travail est calculé *via* l'Eq. (3.14). D'autres propriétés souvent utilisées sont présentées dans le Chapitre 3 et plus généralement dans le Tableau B.1.

La méthode d'optimisation utilisée tire avantage d'une régression non linéaire de Lavenberg-Marquardt (LMA). L'optimisation non linéaire est actuellement la méthode la plus efficace utilisée pour développer les équations d'état. Par rapport à la régression linéaire des moindres carrés parfois utilisée, elle ne nécessite pas de linéarisation des données à l'aide d'équations d'état préliminaires. Comme de nombreux algorithmes d'ajustement, le LMA ne trouve que le minimum local de la somme des moindres carrés (SSQ). Afin de trouver le minimum global ou de l'approcher suffisamment pour que l'EOS reproduise les données expérimentales avec une erreur satisfaisante, cette somme est modifiée par des constantes supplémentaires, des coefficients aléatoires et des pondérations pendant la procédure d'optimisation.

L'algorithme utilisé pour minimiser le SSQ est un programme écrit en Fortran, spécifiquement développé au NIST pour l'application aux équations d'état. Il utilise la forme fonctionnelle de l'énergie de Helmholtz défini dans l'Eq. (3.1). C'est un projet en constante évolution, initié depuis plus de 20 ans et dirigé par Eric W. Lemmon (NIST). Sa partie centrale a été écrite pour la première fois par Robert D. McCarty et Vincent D. Arp pour développer l'équation d'état de l'hélium–4. L'algorithme a énormément évolué depuis et aujourd'hui, il permet d'ajuster les équations d'états aux données expérimentales pour des mélanges complexes.

Le point de départ important pour la description des propriétés d'un mélange fluide est constitué par les équations d'état pour les fluides purs. Les propriétés de l'hélium–4, du néon, de l'argon et de l'azote sont bien établies et disponibles sous la forme des équations explicites d'énergie de Helmholtz. Les paramètres variables de l'équation sont les paramètres réducteurs, décrits dans l'Eq. (3.3) et Table 3.1, et les paramètres de la fonction de départ, décrits dans l'Eq. (3.8). Selon le nombre de termes gaussiens utilisés dans les équations, le nombre total de paramètres varie de 42 à 49 dans ce travail.

Les résultats sont discutés pour chaque mélange séparément et les paramètres spécifiques pour tous les fluides présentés dans le Tableau 3.3. Les coefficients de la fonction de départ sont présentés dans les Tableaux 3.4 à 3.7. L'incertitude des équations en régime monophasique est discutée séparément pour chaque équation dans les Sec. 3.4.1 à 3.4.4. L'incertitude à la limite de phase est discutée pour les quatre mélanges dans Sec. 3.5, où l'erreur orthogonale est introduite. L'erreur orthogonale est une nouvelle métrique déterminée par la plus courte distance entre le point de données expérimen-

tales et l'isotherme respective évaluée avec l'EOS. Elle permet de pallier une limitation de la métrique standard qui diverge lorsque la pente de l'enveloppe de phase est verticale. Sa définition mathématique est donnée dans l'Eq. (3.28). L'erreur orthogonale absolue pour les équilibres vapeur-liquide et gaz-gaz est présentée Fig. 3.12. Les erreurs absolues calculées en convertissant l'erreur orthogonale sont illustrées Fig. 3.14.

Toutes les équations d'état présentées montrent des performances satisfaisantes en monophasique et à l'enveloppe de phase pour des pressions allant jusqu'à $10-20$ MPa, ce qui couvre la plupart des applications d'ingénierie. Pour des pressions plus élevées, si les données expérimentales sont disponibles, les performances des équations diminuent. Cependant, l'erreur reste dans la marge de 5% pour les données ρpT et dans la marge de 10% pour la vitesse des données du son.

Validation expérimentale des équations d'état dans le domaine cryogénique

Un nombre limité de données expérimentales peut être trouvé dans la littérature pour les mélanges d'hélium-4 à des températures cryogéniques (aucune donnée dans la région monophasique pour $50-230$ K), cette partie expérimentale de mon travail vise à compléter ces données entre 50 et 100 K et des pressions jusque 10 MPa par des mesures du coefficient de Joule Thomson (JT) défini par l'Eq. (4.1). L'effet Joule-Thomson est une variation de température créée lors d'une détente isenthalpique. L'équation d'état moderne, explicite en énergie de Helmholtz développée au cours de cette thèse est capable de décrire avec précision les coefficients JT comme discuté dans le Chapitre 4.2. Par conséquent, s'il est mesuré avec précision, le coefficient JT doit permettre de démontrer la validité de notre équation d'état. La dériviation de ce coefficient à partie de l'équation d'état (Eq. (3.14)) comprend presque toutes les dérivées de l'énergie résiduelle de Helmholtz, à l'exception de $\alpha^{\mathrm{r}}_{\tau}(\delta,\tau,\overline{x}) = (\partial\alpha^{\mathrm{r}}/\partial\tau)_{\delta,\overline{x}}$ ce qui en fait, avec la vitesse du son, une excellente propriété pour vérifier le comportement de l'équation.

Cette seconde partie de la thèse a en conséquence concerné la conception, la fabrication et l'exploitation d'un banc de mesure du coefficient JT des mélanges étudiés *via*. La chute de pression est assurée par un capillaire de petit diamètre. Les valeurs de pression et de température sont mesurées à l'entrée et à la sortie du capillaire. La Sec. 4.4.1 présente les calculs guidant le choix du diamètre du capillaire: perte de charge, transformation isenthalpique et effets non isenthalpiques provoqués par le changement d'énergie cinétique. Le banc expérimental ainsi conçu et fabriqué est décrit *in extenso* au Chapitre 4.

Les paires $p-T$ mesurées sont les valeurs intégrales du coefficient de Joule-Thomson. La plupart des mesures de la littérature optent pour une approximation directe du coefficient en n'imposant que de petites variations de pression. Nous avons choisi une voie différente, le coefficient Joule-Thomson est mesuré indirectement par la dérivée des courbes T(P) obtenues par ajustement polynomial des mesures. Une représentation schématique de cette approche est présentée dans la Fig. 4.5b.

Le schéma de principe du banc est présenté sur la Fig. 4.12, le diagramme complet de tuyauterie et d'instrumentation (P&ID) est illustré sur la Fig. D.1. Le cheminement du fluide débute par un volume de 50 litres, où un mélange est stocké à haute pression, connecté à la vanne de réduction de pression puis au volume tampon de 1 gallon, qui lisse les corrections de pression manuelles. À l'intérieur du cryostat, un échangeur de chaleur en cuivre est brasé sur la tête froide du cryoréfrigérateur Cryomech AL300 capable de refroidir le débit fluide de 300 K à environ 40 K à l'entrée du capillaire. Deux capteurs de température calibrés Lake Shore Cernox sont placés en amont et en aval du capillaire. Le câblage des sondes de température est thermalisé au niveau de la tête froide. Les mesures de pression en amont et en aval sont effectuées à l'aide des transducteurs de pression Mensor CPT 6100. Deux vannes à réglage fin sont installées en parallèle afin d'offrir une plage plus large de régulation de la pression en aval. Enfin, un analyseur de gaz est placé à la sortie du système permet de mesurer la composition du mélange à pression ambiante au cours du temps. Une liste complète des équipements utilisés dans l'expérience, divisée en catégories fonctionnelles, est présentée dans le Tableau D.1.

Le banc expérimental et la méthode de mesure sont validés par des mesures de fluides purs, azote, argon et Hélium-4. Dans la Fig. 4.20, les points expérimentaux sont tracés dans l'espace $p-T$ avec des lignes isenthalpiques respectives calculées à partir des équations d'état des fluides purs. Les résultats des mesures effectuées sont les couples pression-température pour les fluides purs et les couples pression-température à composition molaire constante pour les mélanges. Les paires $p-T$ mesurées sur une seule ligne isenthalpique pour la constante (p_{in}, T_{in}) forment un ensemble de mesures. Le coefficient de Joule-Thomson peut être représenté géométriquement comme la pente d'une ligne isenthalpique dans l'espace bidimensionnel de pression et de température. Un polynôme de Chebyshev est ajusté aux paires $p-T$ mesurées, et la première dérivée est calculée à chaque pression mesurée et est rapportée comme le coefficient de Joule-Thomson isenthalpique, μ_{JT}.

Résultats et incertitudes des mesures du coefficient de Joule-Thomson

La détermination indirecte des coefficients JT par la dérivée de la courbe ajustée $T(p)$ exige quelques précautions. La nécessité d'ajuster un polynôme aux données pose un problème de résultats divergents aux extrémités de l'ensemble de données, ce qui est illustré sur la Fig. 5.2. Même les mesures idéales avec zéro erreur dans p et T peuvent entraîner une déviation des résultats uniquement parce que l'ajustement à la ligne ne représente pas avec précision la ligne insenthalpique. Ce problème est résolu en ajustant les extrémités des lignes isenthalpiques mesurées mais en les excluant des calculs de μ_{JT}.

La Fig. 5.3 montre les paires $p-T$ mesurées pour les fluides purs, les coefficients Joule-Thomson résultants et les écarts de mesure par rapport à EOS avec leurs barres d'incertitude. Deux descriptions de l'incertitude sont présentées: l'analyse conventionnelle et l'analyse Monte Carlo. Le coefficient de Joule-Thomson dérivé $\mu_{\mathrm{JT}} = \mu_{\mathrm{JT}}(p,\ T)$ dépend de l'ensemble complet de mesures, du nombre de points mesuré sur une seule ligne isenthalpique, et du polynôme ajusté aux données. Une tentative de quantification de ces facteurs est présentée dans la discussion sur l'incertitude de Monte Carlo dans la Sec. 5.2.2. La Fig. 5.6b montre qu'une seule ligne isenthalpique mesurée pour le néon, l'azote ou l'argon avec au moins cinq points (y compris les extrémités) devrait donner des erreurs inférieures à 2% pour la plupart des cas, à l'exception de quelques lignes isenthalpiques de néon fortement courbées. Un nombre plus important de points mesurés sur une seule ligne isenthalpique pour l'hélium-4 ne devrait pas réduire les erreurs. Si les extrémités sont conservées dans l'analyse, au moins sept points doivent être mesurés sur une seule ligne pour réduire l'erreur moyenne au niveau de cinq points sur la même ligne sans les extrémités. Une étude complète des incertitudes permet de valider les mesures et le banc expérimental.

Fort de cette validation, la seconde partie du travail expérimental a été dédié à la mesure du coefficient Joule-Thomson isenthalpique des mélanges binaires. Par rapport aux mesures de fluides purs, la préparation du mélange gazeux a été nécessaire avant les mesures. La composition du mélange est contrôlée par l'analyseur de gaz et aucune dérive de composition n'a été observée durant les mesures.

Par un procédé identique à celui mis en place pour les fluides purs, le polynôme de Chebyshev de l'Eq. (5.1) est ajusté à chaque ligne isenthalpique séparément, et les coefficients de Joule-Thomson sont calculés à partir de l'Eq. (5.3). La Fig. 5.8 montre les paires $p-T$ mesurées pour le mélange ^{4}He — Ne avec une composition molaire variable, les coefficients de Joule-Thomson résultants et l'écart relatif par rapport à l'EOS. Encore

une fois, l'analyse d'incertitude conventionnelle est comparée aux simulations de Monte Carlo. La Fig. 5.9 montre des résultats similaires obtenus pour le mélange $^4He-N_2$ à deux compositions molaires différentes.

Dans la Fig. 5.10, l'erreur de mesure du coefficient de Joule-Thomson isenthalpique pour ^4He-Ne est tracée pour un nombre variable de points sur une seule ligne de l'entalpie constante, moyennée sur le nombre de points sur la ligne. Une erreur de mesure élevée est visible pour l'hélium pur, où peu de changement de température est observé, et pour le néon pur avec peu de points expérimentaux pris, et où la courbure de la ligne isenthalpique est la plus prononcée. L'impact de l'incertitude de mesure de la composition sur le coefficient JT est illustré par les lignes rouges et est indépendant du nombre de points. Cette influence sur l'erreur totale est marginale, sauf pour les valeurs de concentration d'hélium très faibles, où un changement mineur de la pente d'une ligne isenthalpique plate entraîne une augmentation significative de l'erreur relative.

Les mesures du coefficient Joule-Thomson isenthalpique dans les fluides purs (azote et argon) sont dans l'incertitude attendue des équations d'état précises. Cette précision obtenue permet de valider le banc expérimental. Les mesures caractérisées par un faible changement de température (hélium pur) sont chargées d'incertitudes élevées, comme le montrent les simulations de Monte Carlo. Pour l'hélium, les écarts rencontrés par rapport à l'EOS sont encore plus élevés que prévu car les pertes thermiques présentes dans le cryostat peuvent fortement influencer le processus isenthalpique caractérisé par un changement de température très faible.

Les mesures μ_{JT} pour les mélanges se caractérisent par des écarts plus importants par rapport aux fluides purs, hors hélium–4. Les données expérimentales obtenues ont été utilisées pour réajuster l'équation d'état pour le mélange d'hélium–4 et de néon. L'algorithme de minimisation n'a pas été en mesure de diminuer les écarts entre l'EOS et les données μ_{JT}, en gardant l'équation contrainte par l'enveloppe de phase. Même après avoir libéré l'enveloppe de phase et ajusté uniquement les coefficients de Joule-Thomson mesurés, l'optimisation n'a pas entraîné d'écarts significativement inférieurs à ceux déjà présentés. Cette tentative de minimisation est considérée comme une réponse valable à la question de savoir si les mesures sont plus précises que l'EOS ou le contraire: l'erreur de mesure pour ^4He-Ne est plus élevée que prévu et atteint 9% au maximum. Par rapport aux coefficients de Joule-Thomson mesurés précédemment, les erreurs rencontrées dans ce travail sont plus faibles, notamment lors de l'étude d'autres mesures en conditions cryogéniques. La Fig. 5.12 présente les résultats obtenus dans ce travail, comparés aux mesures de la littérature. Même si toutes les mesures de ce travail ne correspondent pas à une erreur relative inférieure à 5%, les résultats sont satisfaisants.

Conclusions

Les travaux sur les équations d'état ont déjà trouvé une application industrielle et académique. Air Liquide a appliqué les équations d'état pour l'hélium-néon et l'hélium-azote aux calculs du cycle cryogénique de Brayton avec des mélanges de gaz. L'équation $^4\mathrm{He}-\mathrm{Ne}$ a également été utilisée par l'Université de Dresde pour les calculs du cycle cryogénique de l'étage de prérefroidissement du Futur Collisionneur Circulaire (FCC). Les équations développées montrent un potentiel d'application significatif avec le mélange hélium-néon candidat pour la liquéfaction de l'hydrogène. L'attractivité des équations publiées ($^4\mathrm{He}-\mathrm{Ne}$, $^4\mathrm{He}-\mathrm{Ar}$ et $\mathrm{Ne}-\mathrm{Ar}$) a été récemment soulignée en suivant les publications sur d'autres équations d'état pour les propriétés thermodynamiques des mélanges quantiques. Les travaux sur les équations et les travaux parallèles sur leur application se poursuivent à Linde, SINTEF, et à l'Université de Stuttgart. En conclusion, les équations d'état développées s'inscrivent dans la tendance industrielle à appliquer des mélanges de gaz et ouvrent des portes à la conception d'infrastructures scientifiques à grande échelle de nouvelle génération, telles que le Futur Collisionneur Circulaire (FCC) ou le démonstrateur de réacteur nucléaire par fusion (DEMO).

1 INTRODUCTION

Background

The work described in this manuscript was performed in its majority in the Cryogenic Engineering Department (DSBT) of the French Atomic Energy and Alternative Energies Commission (CEA) in Grenoble, France. The Cryogenic Engineering Department focuses on technological research in a wide range of temperatures, from millikelvin to 120 K. Its main interests fall within the space applications, the fundamental research facilities (CERN, Herschel, and others), and the fusion programs (JET, ITER, JT-60SA for magnetic confinement, and Laser MegaJoule for inertial confinement). Thanks to all the above, DSBT has been a favorable place to perform the presented work.

The modeling results achieved their quality thanks to the collaboration with the Material Measurement Laboratory of the National Institute of Standards and Technology (NIST) in Boulder, Colorado, USA. The industrial application of the work was possible thanks to a local collaboration with Air Liquide Advanced Technologies (ALAT) based in Sassenage, France.

This thesis exists thanks to the H2020/MSCA/ITN funding for the Innovative Training Network EASITrain - European Advanced Superconductivity Innovation and Training.

Motivation and objectives

The importance of fluid mixtures in the petrochemical industry cannot be overestimated. Their precise description is essential for extracting, refining, and separating oil and natural gas mixtures. Mixtures also gain interest within the industrial world, focused on refrigeration and cryogenic engineering. They allow to optimize the thermodynamic cycles and increase their overall thermal efficiency, e.g., by using the centrifugal compressors, so far impossible with pure helium–4 characterized by too low a molecular mass. The properties of fluid mixtures, sometimes very different from the behavior of pure fluids, brought interest of the scientific communities.

One motivation for the following work is the conceptual design study of the Future Circular Collider (FCC),[3] a new generation particle accelerator, where gas mixtures are considered as a working fluid in the cryogenic precooling stage.[4,5] Improvement in the cooling production efficiency motivated this work, as two parallel industrial engineering studies, performed by Linde[6] and Air Liquide[7] for the FCC, concluded that accurate property description for the cryogenic mixtures is fundamental for the study results to be credible. If the cryogenic properties are to be precisely predicted, accurate equations of state have to be developed and available for the communities of engineers and scientists.

Other foreseen applications of the cryogenic, mixture-based systems include:

- hydrogen refrigeration and liquefaction;
- High-Temperature Superconductors (HTS) cooling;[8,9]
- small space-ready cryogenic refrigerators[10]
- scientific samples refrigeration;
- zero-boil-off in the maritime LNG tanks;
- methane and biogas liquefaction.

Designing any of these systems requires precise fluid property description and, therefore, the equations of state capable of calculating the thermodynamic properties in a broad range of temperatures and pressures. Developing the equations of state for cryogenic mixtures is the objective of this work.

Document structure

The accurate, empirical Helmholtz equations of state (EOS) for the binary gas mixtures of helium, neon, argon, and nitrogen are developed and presented in the first part of this work (Chapters 2 and 3). The set of published equations (^{4}He — Ne, ^{4}He — Ar, and Ne — Ar) is extended with the equation of state for the thermodynamic properties of the helium-nitrogen mixture. These equations are meant to provide the state-of-the-art accuracy in both the single-phase regions and at the phase envelopes. They are fitted to experimental data collected from multiple sources in the literature.

In the second part (Chapters 4 and 5), the experimental setup for measuring the Joule-Thomson coefficient at cryogenic temperatures is presented, the methodology is discussed, and the results are analyzed. The experiment is conducted to confirm the performance of developed equations of state in the cryogenic regions with little or no experimental data. A significant effort is put into improving the measurement precision and discussing the encountered errors.

2 Different forms of the equations of state

This chapter reviews different forms of the equations of state. The discussion starts with an overview of the phase diagrams and continues towards the mathematical forms of the equations. It focuses on the equations of state for fluid mixtures, their limitations, and their advantages.

2.1 Phase diagrams of cryogenic fluids

The fluids discussed in this work are predominantly the binary mixtures of noble gases: helium–4, neon, argon, extended with nitrogen. Some thermodynamic properties of these fluids are known for a century,[11] others have been measured more recently.[12] Today, the properties of pure fluids are known in broad pressure-temperature regions, and the state-of-the-art models which allow calculating these properties from other state properties are relatively recent, with the last out of four models released in 2018.[13] These models are the *equations of state*, the thermodynamic equations relating the state variables, and describing the state of matter under given physical conditions.

2.1.1 Pure fluids

The equations of state can be used to calculate the properties of fluids in the single-phase regions and at phase boundaries. The properties at phase boundaries are shown in the phase diagrams, where gaseous, liquid, supercritical, and solid regions are visible. For four fluids discussed in this work, the phase diagrams are plotted in Fig. 2.1. A black star in each diagram marks the critical point. The liquid cannot be distinguished from the gas in the *supercritical region*, where pressure and temperature are above their critical values (p_c and T_c). The black line ending in the critical point is the *saturation line*, the line above the p_c is the *melting line*. These lines meet in the *triple point*, where

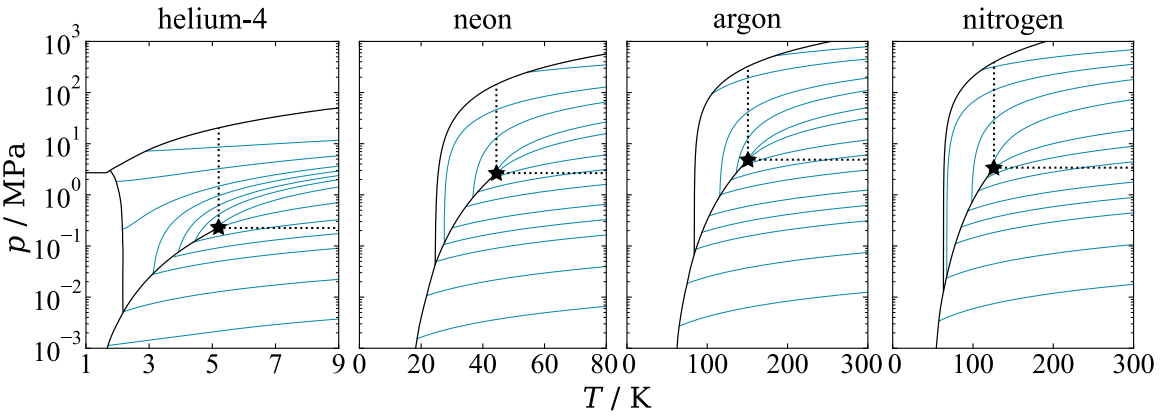

Fig. 2.1. Phase diagrams of fluids used in this work, with isopycnic (ρ = const.) lines plotted in blue and critical points marked with black stars.

all three phases - liquid, vapor, and solid coexist in equilibrium. The saturation line becomes the sublimation line for pressure and temperature below the triple point where the solid phase transforms directly into gas (sublimates). All the above is valid for the vast majority of fluids but not for helium. When analyzing the phase diagrams of neon, argon, and nitrogen, the similarities are apparent. For helium, the solid phase does not exist below 26 kPa, even at very low temperature. Liquid helium, when cooled down, transforms into a *superfluid*. This unusual state of matter can be described as a mixture of two pseudo-fluids: the first one is Newtonian and dissipative, the second one is non-dissipative – it is characterized by zero-viscosity, zero-entropy, and high thermal conductivity. The liquid phases of helium: He-I (normal fluid), and He-II (superfluid), are separated with a vertical lambda line, which meets the saturation line in the lambda point. Because of this phenomenon, helium–4 does not have the standard triple point of solid-liquid-vapor coexistence. Instead, at $T_\lambda \approx 2.17$ K and 5 kPa, the so-called lambda point is the triple point of vapor–He-I–He-II equilibrium.

2.1.2 Binary mixtures

The single-phase properties of mixtures are often not significantly different from those of pure fluids. However, the phase equilibria can be much more complex and, depending on the constituents, can show very different behavior.

The Gibbs phase rule[14] gives the number of thermodynamic degrees of freedom of any system, i.e., the number of independent variables that change the state of this system. According to the phase rule, a binary mixture in the single-phase state has three degrees of freedom – its thermodynamic state is characterized by three variables, e.g., pressure, temperature, and the mole fraction. In a pure fluid, the critical state has no degree of

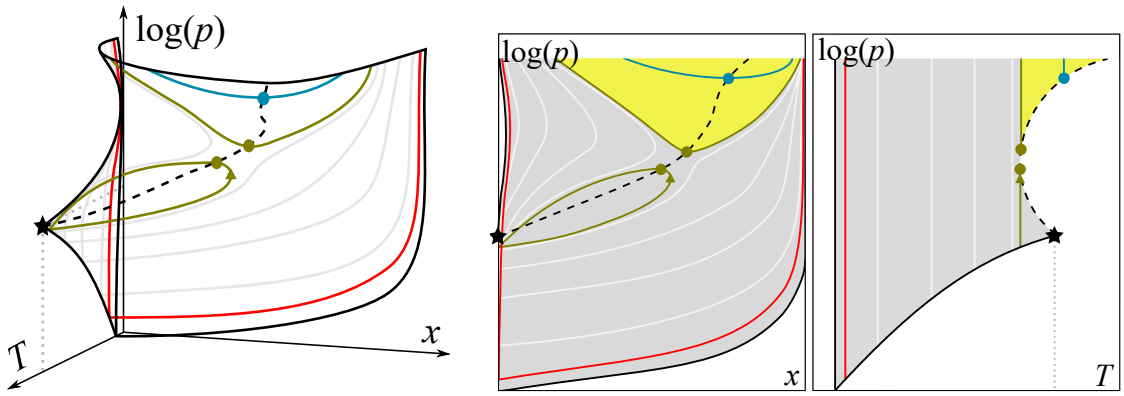

(a) Phase envelope in $\log(p) - T - x$ three dimensional space

(b) 2D projections of the envelope

Fig. 2.2. Class III phase envelope with the vapor-liquid equilibrium (VLE) – gray area in (b), and existing gas-gas equilibrium (GGE) – yellow area in (b). x is the mole fraction of a lighter component. The star represents the critical point and the dashed line, the critical line.

freedom and is the critical point, whereas in a binary mixture, the critical states have one degree of freedom and form the critical line.

Various classes of phase equilibria exist. This work does not attempt to describe the phase equilibria in binary mixtures fully but focuses on helium–4 and a few other cryogenic fluids. A complete discussion on the phenomenology of phase diagrams is available in the extensive work of Deiters and Kraska,[15] according to which, helium with practically all other substances forms the phase equilibria of class III, with *vapor-liquid equilibrium* (VLE) and open *gas-gas equilibrium* (GGE). The name gas-gas equilibrium implies that the phase separation occurs beyond the critical temperature of the heavier component. The isotherms in the gas-gas equilibrium maintain a positive slope and are not closed by a critical line.

An exemplary phase envelope with the supercritical vapor-liquid equilibrium and the gas-gas equilibrium is shown in Fig. 2.2. The left subfigure is the 3D phase envelope, whereas the right one shows its projections on $\log(p)-x$ and $\log(p)-T$ planes. The gray and yellow areas in Fig. 2.2b mark the VLE and the GGE, respectively. The black star in the figures is the critical point of the less volatile component (the second constituent of a helium mixture), and the dashed black line is the mixture critical line. The critical point of helium is not shown because it is too low in temperature. The light-grey lines are the isotherms. Red, green, and blue lines are selected isotherms where $T_{\text{red}} < T_{\text{green}} < T_{\text{blue}}$. The green and blue points are the critical points at T_{green} and T_{blue}. The green line is the isotherm of temperature close to the minimum temperature below which only

the VLE exists. Only the GGE exists above the critical temperature of the less volatile component (star), as illustrated by the T_{blue} isotherm. The mole fraction maximum of an isothermal dew point curve is called the maxcondentherm (marked with a triangle for T_{green}). The mixture at T_{green} and composition beyond the maxcondentherm of the vapor-liquid equilibrium can be expanded from high to low pressures without crossing the vapor-liquid phase boundary.

The vapor-liquid equilibria in mixtures discussed in this work are always supercritical, where helium is above its critical temperature, and the two-phase region starts at the boiling point of the second component. The dew lines of the phase envelope do not run to the boiling point of helium but bend around and reach the mixture critical line. The complex behavior at the phase boundaries described above can be one of the reasons why the reliable equations of state (EOS) were not established so far for the binary mixtures of helium–4.

No data is available for phase equilibria at high pressures for two out of four mixtures developed in this work. Therefore, no experimentally confirmed information is given on the existence of the gas-gas equilibrium. Although helium–4 is said to usually have the gas-gas equilibrium with other constituents, no attempt is made to model this behavior in the no-data regions.

Before discussing the equation development procedure, the EOS used today and throughout the history are presented, with a special focus put on the equation used in this work.

2.2 Equations of state

This section presents a general overview of the most important equations of state developed throughout history. Research on fluid behavior have existed for a few centuries. However, the modern equations had started getting their shape in the late 19th century, when Johannes Diderik van der Waals introduced a description of the attractive and repulsive forces between the fluid particles. Inspired by the work of van der Waals, other physicists started describing fluid behavior with cubic and non-cubic equations. This section discusses the important equations in brief detail, including the van der Waals-, statistical-based hard-sphere interactions-, the molecular-based- and the empirical Helmholtz energy equations of state.

2.2.1 Ideal gas equations of state

Ideal gas is a hypothetical fluid that can approximate the behavior of real substances under specific conditions of high temperature and low pressure. It neglects the molecular size (molecules are points) and the intermolecular forces (molecules do not interact), and results in the smallest error when used for monoatomic substances. The ideal gas low can be successfully applied to calculations of a dilute gas at high reduced temperature. It is often written as

$$pV = nRT, \tag{2.1}$$

where p is the pressure in Pa, V is the volume in m^3, T the is temperature in K, n is the number of moles enclosed in volume V, and R is the ideal gas constant in J $(K\ mol)^{-1}$.

Many gases, e.g., nitrogen, carbon dioxide, oxygen, and hydrogen, can be treated as ideal gas, but the approximation is only fairly accurate if used for fluids at standard conditions. The equation is useful for quick calculations in limited $p-T$ space but the simplifications introduced are too large for most engineering applications.

2.2.2 Van der Waals equation of state

The *van der Waals equation of state* generalizes the ideal gas equation and tries to answer why the real gases do not act ideally.[16] It is based on the assumptions that all particles are hard spheres of the same finite radius and that attractive forces exist between these particles. The equation can be written in its extensive form as

$$\left(p + \frac{n^2 a}{V^2}\right)(V - nb) = nRT, \tag{2.2}$$

where p is the pressure in Pa, T is the temperature in K, $n = N/N_A$ is the number of moles, R is the universal gas constant, a is a measure of the average attractions between particles in J mol^{-1}, b is the volume occupied by a mole of particles in $m^3\ mol^{-1}$. In other words, the term b is the excluded volume per mole or the co-volume. In literature, it is sometimes referred to as the repulsive term. The equation can be derived using statistical thermodynamics,[17] where the values of a and b are estimated with the intermolecular potential constants and the molecular diameters. The equation has a clear physical significance, and it is the result for which Johannes Diderik van der Waals received the Noble price in 1910.

Van der Waals proposed extending his equation to mixtures.[18] It can be done by substituting the pure fluid a and b terms with

$$a = \sum_{i=1}^{n} \sum_{j=1}^{n} x_i x_j (1 - k_{ij}) \sqrt{a_{ii} a_{jj}}, \tag{2.3}$$

$$b = \sum_{i=1}^{n} x_i b_{ii}, \tag{2.4}$$

where x_i is the mole fraction of constituent i, a_{ii} is the average attraction between particles in component i, b_{ii} is the volume occupied by one mole of particles of component i, and k_{ij} is the numerically fitted coupling parameter.

According to van der Waals, all fluids should have similar properties when compared at the same reduced temperature and pressure. In other words, they should have similar thermodynamic properties at their corresponding states. The reduced quantities are defined,

$$p_\mathrm{r} = \frac{p}{p_\mathrm{c}}, \quad T_\mathrm{r} = \frac{T}{T_\mathrm{c}}, \quad V_\mathrm{r} = \frac{V}{V_\mathrm{c}}, \tag{2.5}$$

where p_c, T_c, and V_c are the pressure, temperature, and volume at the critical point. These quantities, applied to Eq. (2.2), allow to rewrite the van der Waals equation in its reduced form:

$$\left(p_\mathrm{r} + \frac{3}{V_\mathrm{r}^2}\right)\left(V_\mathrm{r} - \frac{1}{3}\right) = \frac{8}{3} T_\mathrm{r}. \tag{2.6}$$

The equation above is remarkably universal; it states that one can obtain V_r for any fluid by imposing p_r and T_r, that is calculate V by knowing p, T, and the critical properties.

The Van der Waals equation can approximate the behavior of fluids above their critical temperatures and shows reasonable performance for low-pressure liquids and gases at low temperatures but fails to predict the phase transition. It also gives unrealistic results in the close vicinity of the critical point and cannot be used to accurately calculate the properties of compressed gasses and liquids.[19]

2.2.3 Other cubic equations of state

When expanding Eq. (2.6), the volume is raised to the power of 3. It makes the van der Waals equation the first out of many important *cubic equations of state*. The other cubic equations, such as the Peng-Robinson[20] or the Peng–Robinson-Stryjek-Vera[21] can be formulated as a pressure function of temperature T and molar volume v. The general form of the cubic equations of state is:

$$p(T,v) = \frac{RT}{v-b} - \frac{a(T)}{(v-r_1 b)(v-r_2 b)}. \tag{2.7}$$

Some formulations represent the attraction between particles as a function of temperature, $a = a(T)$. Depending on the actual equation, the additional terms r_1 and r_2 are used. The cubic equations can show substantial improvements over the van der Waals equation and can be successfully used for accurate vapor-liquid equilibria calculations. However, they often predict the critical behavior and the caloric properties with low accuracy. The deficiencies of the van der Waals, and cubic equations in general, initiated research on other, more complex, and more accurate equations of state. That includes a recent work of Aasen *et al.*,[22] which introduces quantum corrections to the cubic equation and allows for accurate equilibria calculations for the mixtures of quantum fluids, e.g., ^{4}He − Ne, H_2 − Ne, D_2 − Ne.

2.2.4 Non-cubic equations of state

The non-cubic EOS originate from the van der Waals equation and modify both its a and b terms. They represent the fluid properties more precisely at higher temperatures when repulsion between particles becomes more important. The general pressure-explicit formulation for the non-cubic equations is given as

$$p = \frac{RT}{v} Z - \frac{a}{v^2}, \tag{2.8}$$

where $Z = Z(\eta)$ is the hard-sphere compressibility factor, a function of the packing fraction η. The packing fraction is the fraction of space occupied by the molecules, and it is a function of the molecular co-volume b, defined in the van der Waals equation. Several researchers worked on these equations, trying to reformulate the hard-sphere compressibility factor. There are many examples of the compressibility factor definitions based on the non-attracting rigid spheres models, e.g., the Reiss-Frisch-Lebowitz equation:[23]

$$Z = \frac{1+\eta+\eta^2}{(1-\eta)^3}, \tag{2.9}$$

the Carnahan-Starling equation:[24]

$$Z = \frac{1+\eta+\eta^2-\eta^3}{(1-\eta)^3}, \tag{2.10}$$

or the Guggenheim equation:[25]

$$Z = \frac{1}{(1-\eta)^4}. \tag{2.11}$$

A comprehensive study on the hard-sphere models for the fluid properties is presented by Mulero *et al.*[26] Various equations find use in different domains, depending on their performance in specific calculations, such as the vapor-liquid or solid-liquid equilibria, properties of polar fluids or molecules with arbitrary geometry.

The hard-sphere models, which modify only the co-volume term from the van der Waals equation, tend to work well at high temperatures but do not predict the fluid behavior well enough in near-critical conditions. There exist attempts to combine both the hard-sphere models with the temperature-dependent attractive term, $a = a(T)$. One of them is the Carnahan-Starling EOS combined with the Redlich-Kwong temperature-dependent term,[27] proposed by Carnahan and Starling themselves

$$p = \frac{RT(1+\eta+\eta^2-\eta^3)}{v(1-\eta)^3} - \frac{a}{v(v+b)\sqrt{T}}. \tag{2.12}$$

This equation represents the phase equilibria of the hydrocarbons well and can accurately predict their high-temperature properties.

The presented discussion is by no means complete. There exist a large number of equations of state developed from the van der Waals equation. They vary in performance and find use in domains where no other, more accurate equation is available.

2.2.5 Virial equation of state

In 1901, Heike Kamerlingh Onnes proposed the *virial equation of state*. It contains an infinite series of the molar specific volume raised to the negative power. Often, its first three terms are sufficient to represent the vapor-liquid equilibrium of many substances accurately. The compressibility factor can be expressed as a power series in molar density

$$Z \equiv \frac{p}{RT\rho} = A(T) + B(T)\rho + C(T)\rho^2 + \dots, \tag{2.13}$$

where $A(T)$, $B(T)$, $C(T)$, ... are the virial coefficients. The first term, $A(T) = 1$, states that all fluids behave like ideal gas when density is small. The second virial coefficient, $B(T)$, describes the pair-wise interactions. The third, $C(T)$, depends on interactions between triplets of molecules. The j^{th} virial coefficient can be calculated in terms of the interaction of j molecules in a volume V. The virial coefficients are only temperature-

dependent for pure components. For mixtures, they are temperature and composition-dependent.

The virial equation is not the most convenient to use but has important advantages over the empirical equations – the coefficients of the equation, the virial coefficients can be estimated based on interactions between molecules described by statistical thermodynamics. They can also be calculated from low pressure ρpT data,

$$B = \lim_{\rho \to 0} \left(\frac{\partial Z}{\partial \rho} \right)_T \text{ and } C = \lim_{\rho \to 0} \frac{1}{2!} \left(\frac{\partial^2 Z}{\partial \rho^2} \right)_T . \tag{2.14}$$

The relations above show that the virial coefficients are the properties of a fluid at the limit of zero-density.

The virial equation can be used to predict properties at low and moderate densities and fails to do so accurately at high densities with no experimental and theoretical capabilities to estimate the higher-order virial coefficients.

2.2.6 Molecular-based equations

The cubic, non-cubic, and virial equations are valid for simple fluids, where the van der Waals forces are the only leading interactions between the fluid particles. For plenty of fluids used in industry, other forces must be considered, e.g., coulombic, polar activity, association, or chain flexibility. For these cases, standard cubic or non-cubic equations fail to predict fluid behavior accurately.

The molecular-based equations often adopt the concepts of chain molecules and the perturbation theory.[28] The molecular models are successfully applied to small, argon-size molecules and large polymeric fluid mixtures. Depending on the equation, the model can predict properties of non-associating, near-spherical fluids (methane); non-spherical fluids (polymers); and associating, non-spherical fluids (alkanols). Even though the consistency and the accuracy of results obtained with the molecular-based equations are sometimes questionable, they are often the only source of information on the properties of complex mixtures encountered in the petrochemical industry.[29]

A commonly used example of the molecular-based equation is the Statistical Associating Fluid Theory (SAFT),[30] which considers the fluid composed of chain molecules. The SAFT equation if often expressed in terms of the Helmholtz energy of ideal gas with applied perturbation terms

$$a(\rho, T) = a^{\text{IDEAL}} + a^{\text{MONO}} + a^{\text{CHAIN}} + a^{\text{ASSOC}}, \tag{2.15}$$

where a^{IDEAL} is the Helmholtz energy of ideal gas, a^{MONO} is the monomer contribution to the Helmholtz energy, a^{CHAIN} is the contribution to the formation of molecular chains, and a^{ASSOC} is the contribution to association and bonding.

In order to describe the particle interactions in the SAFT equation, a pair-potential model is applied to calculate the intermolecular potential energy. Very often, the Lennard-Jones (LJ) potential is used.[31] It is a simple but realistic model of soft interactions in the form of

$$u^{\mathrm{Mie}}(r) = C(\lambda_{\mathrm{r}}, \lambda_{\mathrm{a}})\, \epsilon \left(\left(\frac{\sigma}{r} \right)^{\lambda_{\mathrm{r}}} - \left(\frac{\sigma}{r} \right)^{\lambda_{\mathrm{a}}} \right), \tag{2.16}$$

where λ_{r} is the repulsive exponent, λ_{a} is the attractive exponent, r is the distance between two interacting particles, ϵ is the potential well depth, and σ is the distance at which $u^{\mathrm{Mie}}(r) = 0$. Eq. (2.16) describes a generalized potential developed from the Lennard-Jones potential (for the Lennard-Jones fluid: $\lambda_{\mathrm{r}} = 12$, $\lambda_{\mathrm{a}} = 6$, and $C(\lambda_{\mathrm{r}}, \lambda_{\mathrm{a}}) = 4$). Particles interacting with the LJ potential have no uniquely defined size, opposite to the hard sphere potential described in Sec. 2.2.4, yielding more realistic description of interactions. On the other hand, the phase equilibria for complex, quantum mixtures and the single-phase properties (including the caloric properties) are reproduced less accurately, compared to the empirical equations explicit in Helmholtz energy.

A corrected SAFT equation has recently been applied to quantum fluid mixtures and yields good phase equilibria predictions for some of the mixtures, i.e., $H_2 - Ne$, $He - H_2$, or $He - D_2$.[32]

2.2.7 Pressure-explicit equations of state

The pressure-explicit equations are still important for technical applications up to these days. The Benedict-Webb-Rubin equation[33] (BWR) showed a significant advancement in predicting the fluid properties accurately, even at high densities. It defines pressure as

$$\begin{aligned} p = {} & \rho RT + \left(B_0 RT - A_0 - \frac{C_0}{T^2} \right) \rho^2 + (bRT - a)\, \rho^3 \\ & + \alpha a \rho^6 + \frac{c\rho^3}{T^2} \left(1 + \gamma \rho^2 \right) \exp\left(-\gamma \rho^2 \right), \end{aligned} \tag{2.17}$$

where A_0, B_0, C_0, a, b, c, α, and γ are the parameters of the equation. According to the authors, the exponential term allows for improved calculations in the critical region, better data reproduction at high densities, and improved equilibrium calculations. The

BWR equation performs much better than the cubic equations of state and was further modified and improved. Jacobsen and Stewart proposed the most successful modification.[34] Their equation, often called the mBWR equation, is still used for a large number of applications, e.g., investigation of particle fragmentation, entropy-scaling in refrigerants, or cryogenic storage calculations. The mBWR equation for nitrogen has been the reference equation for almost 30 years. It defines pressure as

$$p = \sum_{i=1}^{9} a_n \rho^n + \exp\left(-\gamma\rho^2\right) \sum_{n=10}^{15} a_n \rho^{2n-17}, \tag{2.18}$$

where $\gamma = 1/\rho_c^2$ and a_n are 15 different polynomial coefficients defined with 32 constants. Thanks to the proven acceptance of the equation in representing the fluid properties of hydrocarbons, it is continuously used today for calculations of the thermodynamic properties of R123.[35] However, the BWR and mBWR formulations used for hydrocarbons and nitrogen were replaced by other equations of state providing more accurate predictions in wide pressure-temperature range. These equations are presented in the following section.

2.2.8 Empirical, multi-parameter equation of state explicit in Helmholtz energy

The equations explicit in Helmholtz energy are one of the most accurate equations developed over time. The *Helmholtz energy* itself, $a(T,\rho)$ has two important advantages. Unlike the internal energy $u(v,s)$ and the enthalpy $h(p,s)$, where v is the specific volume, s is the specific entropy, and p is the pressure, it is a function of measurable properties – temperature T and density ρ. Moreover, unlike the Gibbs energy $g(T,p)$, it is continuous through the phase boundary.

Schmidt and Wagner were the first to propose a modern, functional form of the Helmholtz energy equation.[36] Its application to oxygen almost fully represented the experimental data accurately, within the experimental uncertainties, giving a precise description of the whole thermodynamic surface. The authors defined their equation in terms of *reduced Helmholtz energy* divided into an ideal gas part α^o and a residual part α^r:

$$\alpha(\delta,\tau) = \frac{a(\rho,T)}{RT} = \alpha^o(\delta,\tau) + \alpha^r(\delta,\tau), \tag{2.19}$$

where $\delta = \rho/\rho_c$ and $\tau = T_c/T$ are the density and the reciprocal temperature reduced with the critical properties, ρ_c and T_c. They define the ideal gas part as

$$\alpha^{\mathrm{o}}(\delta,\tau)=\frac{h_{\mathrm{o}}^{\mathrm{o}}\tau}{RT_{\mathrm{c}}}-\frac{s_{\mathrm{o}}^{\mathrm{o}}}{R}-1+\ln\left(\frac{\delta\tau_{\mathrm{o}}}{\delta_{\mathrm{o}}\tau}\right)-\frac{\tau}{R}\int_{\tau_{\mathrm{o}}}^{\tau}\frac{c_{\mathrm{p}}^{\mathrm{o}}}{\tau^2}\mathrm{d}\tau+\frac{1}{R}\int_{\tau_{\mathrm{o}}}^{\tau}\frac{c_{\mathrm{p}}^{\mathrm{o}}}{\tau}\mathrm{d}\tau, \tag{2.20}$$

where $\delta_{\mathrm{o}}=\rho_{\mathrm{o}}/\rho_{\mathrm{c}}$, $\tau_{\mathrm{o}}=T_{\mathrm{c}}/T_{\mathrm{o}}$, $h_{\mathrm{o}}^{\mathrm{o}}=h_{\mathrm{o}}(\rho_{\mathrm{o}},T_{\mathrm{o}})$ and $s_{\mathrm{o}}^{\mathrm{o}}=s_{\mathrm{o}}(\rho_{\mathrm{o}},T_{\mathrm{o}})$ are the reduced density and temperature; and the ideal gas enthalpy and entropy at arbitrary reference state (T_{o}, p_{o}, ρ_{o}). $c_{\mathrm{p}}^{\mathrm{o}}$ is the ideal gas heat capacity. The residual part of the Helmholtz energy is defined as

$$\alpha^{\mathrm{r}}(\delta,\tau)=\sum_{i=1}^{13}a_i\delta^{d_i}\tau^{t_i}+\exp\left(-\delta^2\right)\sum_{i=14}^{24}a_i\delta^{d_i}\tau^{t_i}+\exp\left(-\delta^4\right)\sum_{i=25}^{32}a_i\delta^{d_i}\tau^{t_i} \tag{2.21}$$

The exponential terms in the residual part of the Helmholtz energy, α^{r}, are necessary to represent the critical region accurately.

Jacobsen *et al.*[37] used the same expression for the Helmholtz energy, divided into an ideal part α^0 and a residual part α^{r}, with the same ideal gas term. They proposed a different formulation for the residual contribution:

$$\alpha^{\mathrm{r}}(\delta,\tau)=\sum_{k=1}^{N}a_k\delta^{i_k}\tau^{j_k}\exp\left(-\gamma\delta^{l_k}\right), \tag{2.22}$$

where N is the number of terms in the equation, i_k are positive integers, j_k are real numbers, $\gamma=0$ for $l_k=0$, and $\gamma=1$ for $l_k\neq 0$. This formulation allowed for accurate description of a complete thermodynamic surface for nitrogen and ethylene.[38,39]

There exist various formulations of the equation explicit in Helmholtz energy. The modern form of the equation is a multi-fluid approximation that intends to describe the thermodynamic properties of non-ideal mixtures accurately. It takes advantage of both of the mentioned formulations for the residual contributions.[36,38] It is similar to Eq. (2.19), but its definition includes a departure function with the Gaussian-bell shaped terms, thanks to which the critical region description becomes more accurate. This equation of state is described in detail in Chapter 3 before discussing the optimization methods for its development.

3 Developing the multi-parameter equations of state for mixtures

This chapter presents the equation of state used to describe the thermodynamic properties of mixtures of helium-neon, helium-argon, neon-argon, and helium-nitrogen. The steps that led to the development of the multiparameter, empirical equations of state are presented. After a rigorous selection of the measurement points collected from the literature, the established equation is fitted to the data. Weights are applied to the measurements, and constraints are used to limit the behavior of the fitter in the regions of limited data availability. The fitting process is described in detail and followed by a discussion on the performance of these newly developed equations and a discussion on the applicability limits. A new metric is introduced to evaluate the equation performance at the phase envelope and is later attempted to be used for equation development.

A large part of the work presented in this chapter has been published in the Journal of Physical and Chemical Reference Data under the title: *Equations of state for the thermodynamic properties of binary mixtures for helium–4, neon, and argon*.[40]

3.1 Modern form of the Helmholtz energy equation of state

Following the functional forms of the previously used equations of state, presented in Chapter 2, the modern form of the equation, explicit in Helmholtz energy, is discussed. The *Helmholtz energy of mixtures* is defined as a sum of the ideal and residual contributions:

$$\alpha(\delta,\tau,\overline{x}) = \frac{a(\rho,T,\overline{x})}{RT} = \alpha^{\mathrm{o}}(\rho,T,\overline{x}) + \alpha^{\mathrm{r}}(\delta,\tau,\overline{x}), \tag{3.1}$$

where $\overline{x}$ is the mole fraction vector, and R is the mole fraction-weighted average of the pure component values of the gas constant used for the development of the equations.

Table 3.1. Reducing temperature and density parameters

Y_r	$Y_{c,i}$	$\beta_{Y,ij}$	Y_{ij}
T_r	$T_{c,i}$	$\beta_{T,ij}$	$\beta_{T,ij}\gamma_{T,ij}\left(T_{c,i}T_{c,j}\right)^{0.5}$
v_r	$\dfrac{1}{\rho_{c,i}}$	$\beta_{v,ij}$	$\beta_{v,ij}\gamma_{v,ij}\dfrac{1}{8}\left(\dfrac{1}{\rho_{c,i}^{1/3}}+\dfrac{1}{\rho_{c,j}^{1/3}}\right)^3$

The Helmholtz energy is used in its reduced form, and it is a function of non-dimensional quantities – *reduced density* and *temperature*

$$\delta = \frac{\rho}{\rho_r} \quad \text{and} \quad \tau = \frac{T_r}{T}, \tag{3.2}$$

where $\rho_r = \rho_r(x)$ and $T_r = T_r(x)$ are the composition dependent *reducing density* and *temperature* respectively. The most recent formulation[41,42] allows for the use of a common form for both mixture reducing parameters, T_r and $v_r = \rho_r^{-1}$,

$$Y_r(\overline{x}) = \sum_{i=1}^{N} x_i^2 Y_{c,i} + \sum_{i=1}^{N}\sum_{j=i+1}^{N} 2x_i x_j \frac{x_i + x_j}{\beta_{Y,ij}^2 x_i + x_j} Y_{ij}, \tag{3.3}$$

where N is the number of components in the mixture, Y is the parameter of interest: the temperature T or the molar specific volume v, given in Table 3.1. $T_{c,i}$, $\rho_{c,i}$ are the critical temperature and density of the pure constituents. $\beta_{T,ij}$, $\gamma_{T,ij}$, $\beta_{v,ij}$, and $\gamma_{v,ij}$ are the fitted parameters with both β parameters being asymmetric, that is $\beta_{T,ij} = \beta_{T,ji}^{-1}$, and $\beta_{v,ij} = \beta_{v,ji}^{-1}$.

The statistical thermodynamics is capable of predicting the behavior of a fluid in the ideal-gas state. However, there exist no physically founded equation, which accurately describes the real thermodynamic behavior of a fluid in complete fluid region.[43] For this purpose the *residual contribution* to Helmholtz energy is determined in an empirical way. The ideal and residual contribution in Eq. (3.1) represent the Helmholtz energy for a mixture. Both are functions of the pure fluid Helmholtz energies

$$\alpha^o(\rho, T, \overline{x}) = \sum_{i=1}^{N} x_i \left(\alpha_{oi}^o(\rho, T) + \ln x_i\right), \tag{3.4}$$

$$\alpha^r(\delta, \tau, \overline{x}) = \sum_{i=1}^{N} x_i \alpha_{oi}^r(\delta, \tau) + \sum_{i=1}^{N-1}\sum_{j=i+1}^{N} x_i x_j F_{ij} \alpha_{ij}^r(\delta, \tau), \tag{3.5}$$

where x_i is the molar fraction of component i, α_{oi}^o is the pure fluid ideal Helmholtz energy, and α_{oi}^r is the pure fluid residual Helmholtz energy, both defined within the pure

fluid EOS. $\alpha^{\mathrm{r}}_{ij}(\delta,\tau)$ is a pairwise departure function, dependent only on the reduced variables δ and τ. *A departure function* is defined as the difference between the extended corresponding states model and the real fluid behavior. In the above case, the departure function is a concept introduced to further improve the thermodynamic surface description. F_{ij} is the scaling parameter applied to the departure function, and is set to unity when the departure function is fitted. The definitions of the pure fluid ideal and residual Helmholtz energies can vary depending on the formulation used by the author of the pure fluid equation. For helium–4,[44] they are defined as follows

$$\alpha^{\mathrm{o}}_{oi}(\delta,\tau)=\frac{h^{\mathrm{o}}_{\mathrm{o}}\tau}{RT_{\mathrm{c}}}-\frac{s^{\mathrm{o}}_{\mathrm{o}}}{R}-1+\ln\left(\frac{\delta\tau_{\mathrm{o}}}{\delta_{\mathrm{o}}\tau}\right)-\frac{\tau c^{\mathrm{o}}_{\mathrm{p}}}{R}\left(\frac{1}{\tau}-\frac{1}{\tau_{\mathrm{o}}}\right)+\frac{c^{\mathrm{o}}_{\mathrm{p}}}{R}\ln\left(\frac{\tau}{\tau_{\mathrm{o}}}\right), \tag{3.6}$$

$$\begin{aligned}\alpha^{\mathrm{r}}_{\mathrm{o}i}(\delta,\tau)=&\sum_{k=1}^{K_{\mathrm{p},i}} n_{\mathrm{o}i,k}\delta^{d_{\mathrm{o}i,k}}\tau^{t_{\mathrm{o}i,k}}+\sum_{k=K_{\mathrm{p},i}+1}^{K_{\mathrm{p},i}+K_{\mathrm{e},i}} n_{\mathrm{o}i,k}\delta^{d_{\mathrm{o}i,k}}\tau^{t_{\mathrm{o}i,k}}\exp\left(-\delta^{l_{\mathrm{o}i,k}}\right)\\&+\sum_{K_{\mathrm{p},i}+K_{\mathrm{e},i}+1}^{K_{\mathrm{p},i}+K_{\mathrm{e},i}+K_{\mathrm{c},i}} n_{\mathrm{o}i,k}\delta^{d_{\mathrm{o}i,k}}\tau^{t_{\mathrm{o}i,k}}\exp\left(-\eta_{\mathrm{o}i,k}\left(\delta-\epsilon_{\mathrm{o}i,k}\right)^2-\beta_{\mathrm{o}i,k}\left(\tau-\gamma_{\mathrm{o}i,k}\right)^2\right),\end{aligned} \tag{3.7}$$

where $K_{\mathrm{p},i}$, $K_{\mathrm{e},i}$, and $K_{\mathrm{c},i}$ represent the number of polynomial, exponential, and critical terms of the pure fluid i respectively. $n_{\mathrm{o}i,k}$, $d_{\mathrm{o}i,k}$, $t_{\mathrm{o}i,k}$, $l_{\mathrm{o}i,k}$, $\beta_{\mathrm{o}i,k}$, $\gamma_{\mathrm{o}i,k}$, $\epsilon_{\mathrm{o}i,k}$, and $\eta_{\mathrm{o}i,k}$ are the fitted parameters. The pure fluid equations of state, which use only the polynomial and exponential terms, can accurately reproduce the fluid behavior except for the critical region. The exponential terms improve the equation behavior in the critical region compared to the purely polynomial formulation. However, the *Gaussian-bell shaped terms* allow for even more accurate reproduction of this behavior close to the critical point. At the same time, they disappear when moving away from the critical point itself.

The last, previously undefined term from Eq. (3.5) is the departure function, $\alpha^{\mathrm{r}}_{ij}(\delta,\tau)$. Unlike in the GERG-2008 definition,[42] the exponential term in the departure function used in this work is temperature dependent:

$$\alpha^{\mathrm{r}}_{ij}(\delta,\tau)=\sum_{k=1}^{K} n_{ij,k}\delta^{d_{ij,k}}\tau^{t_{ij,k}}\exp\left(-\eta_{ij,k}\left(\delta-\epsilon_{ij,k}\right)^2-\beta_{ij,k}\left(\tau-\gamma_{ij,k}\right)^2\right), \tag{3.8}$$

where $d_{ij,k}$, $n_{ij,k}$, $t_{ij,k}$, $\beta_{ij,k}$, $\gamma_{ij,k}$, $\epsilon_{ij,k}$, and $\eta_{ij,k}$ are the fitted parameters. Although they are empirical and arbitrary, constraints on their values were used during the fitting process in order to obtain physically correct EOS behavior. The summation comprises the polynomial terms when $\beta_{ij,k}=\gamma_{ij,k}=\epsilon_{ij,k}=\eta_{ij,k}=0$, and the Gaussian bell-shaped

terms when all fitted parameters are non-zero. This functional term allows to accurately describe the thermal and caloric mixture properties within the uncertainty of measured data and ensures reasonable behavior of the model in regions with poor data coverage.[43]

Calculating thermodynamic properties from Helmholtz energy

The thermodynamic properties are functions of the Helmholtz energy and its derivatives. The modern formulation presented in the previous section allows calculating the derivatives and the properties analytically. A complete discussion on derivatives necessary to calculate the thermodynamic properties is presented in several publications and is not repeated here.[42–44] The notation, essential for understanding the calculations, is introduced in two examples of derivatives of the ideal gas part and the residual part of Helmholtz energies for mixtures:

$$\alpha^{\mathrm{o}}_{\tau} = \left(\frac{\partial \alpha^{\mathrm{o}}}{\partial \tau}\right)_{\delta,\overline{x}} = \sum_{i=1}^{N} x_i \frac{T_{\mathrm{c},i}}{T_{\mathrm{r}}} \left(\frac{\partial \alpha^{\mathrm{o}}_{\mathrm{o}i}}{\partial \left(T_{\mathrm{c},i}/T\right)}\right)_{\rho}, \tag{3.9}$$

$$\alpha^{\mathrm{r}}_{\delta} = \left(\frac{\partial \alpha^{\mathrm{r}}}{\partial \delta}\right)_{\tau,\overline{x}} = \sum_{i=1}^{N} x_i \left(\frac{\partial \alpha^{r}_{\mathrm{o}i}}{\partial \delta}\right)_{\tau} + \sum_{i=1}^{N-1} \sum_{j=i+1}^{N} x_i x_j F_{ij} \left(\frac{\partial \alpha^{\mathrm{r}}_{ij}}{\partial \delta}\right)_{\tau}. \tag{3.10}$$

Analogically, the second mixed derivative of residual Helmholtz energy and the second derivative with respect to density is denoted as

$$\alpha^{\mathrm{r}}_{\delta\tau} = \left(\frac{\partial^2 \alpha^{\mathrm{r}}}{\partial \delta \partial \tau}\right)_{\overline{x}} \quad \text{and} \quad \alpha^{\mathrm{r}}_{\delta\delta} = \left(\frac{\partial^2 \alpha^{\mathrm{r}}}{\partial \delta^2}\right)_{\tau,\overline{x}}. \tag{3.11}$$

The experimental data for four mixtures considered in this work is presented in Appendix A and is available for phase-equilibria, ρpT, speed of sound, and the second virial coefficient. The single-phase properties can be defined as a function of the Helmholtz energy:

$$p\left(\rho, T, \overline{x}\right) = \rho R T \left(1 + \delta \alpha^{\mathrm{r}}_{\delta}\right), \tag{3.12}$$

$$w\left(\rho, T, \overline{x}\right) = \sqrt{\frac{RT}{M}\left(1 + 2\delta\alpha^{\mathrm{r}}_{\delta} + \delta^2 \alpha^{\mathrm{r}}_{\delta\delta} - \frac{\left(1 + \delta\alpha^{\mathrm{r}}_{\delta} - \delta\tau\alpha^{\mathrm{r}}_{\delta\tau}\right)^2}{\tau^2\left(\alpha^{\mathrm{o}}_{\tau\tau} + \alpha^{\mathrm{r}}_{\tau\tau}\right)}\right)}, \tag{3.13}$$

$$\mu_{\mathrm{JT}}\left(\rho, T, \overline{x}\right) = \frac{1}{R\rho} \frac{-\left(\delta\alpha^{\mathrm{r}}_{\delta} + \delta^2\alpha^{\mathrm{r}}_{\delta\delta} + \delta\tau\alpha^{\mathrm{r}}_{\delta\tau}\right)}{\left(1 + \delta\alpha^{\mathrm{r}}_{\delta} - \delta\tau\alpha^{\mathrm{r}}_{\delta\tau}\right)^2 - \tau^2\left(\alpha^{\mathrm{o}}_{\tau\tau} + \alpha^{\mathrm{r}}_{\tau\tau}\right)\left(1 + 2\delta\alpha^{\mathrm{r}}_{\delta} + \delta^2\alpha^{\mathrm{r}}_{\delta\delta}\right)}, \tag{3.14}$$

$$B(T,\overline{x}) = \frac{1}{\rho_{\mathrm{r}}} \lim_{\delta \to 0} \alpha^{\mathrm{r}}_{\delta}. \tag{3.15}$$

Other, often used thermodynamic properties are presented in Table B.1 in a similar form. Apart from the single-phase properties, the criteria for phase equilibria in mixtures can be derived based on the Helmholtz energy formulation:

$$\begin{cases} T' = T'' \\ p' = p'' \\ \mu'_i = \mu''_i \quad i = 1, \ldots, N \end{cases}, \tag{3.16}$$

where $'$ and $''$ denote the liquid and vapor phases, respectively. μ_i is the chemical potential of fluid i, defined as

$$\mu_i = \left(\frac{\partial A}{\partial n_i}\right)_{T,V,n_{j\neq i}} = RT\left(\left(\frac{\partial n\alpha^{\mathrm{o}}}{\partial n_i}\right)_{T,V,n_{j\neq i}} + \left(\frac{\partial n\alpha^{\mathrm{r}}}{\partial n_i}\right)_{T,V,n_{j\neq i}}\right), \tag{3.17}$$

where $A = nRT\alpha$ and $n = \sum_i^N n_i$. The following work uses an existing *tracing algorithm* written for this purpose[45] – an algorithm for calculating and plotting the phase envelopes.

Scaling the properties of helium–4 and neon with any physical theory can be challenging because of the quantum phenomena influencing fluid behavior. Classical or quantum effects will dominate depending on the length scale of interactions versus the *thermal de Broglie wavelength*,

$$\lambda_{\mathrm{th}} = \sqrt{\frac{h^2}{2\pi m k_{\mathrm{B}} T}}, \tag{3.18}$$

where T is the temperature at which λ_{th} is calculated, h is the Planck constant, $m = M/N_{\mathrm{A}}$ is the particle mass with molar mass M; N_{A} is the Avogadro constant, and k_{B} is the Boltzmann constant, all given in Chapter Physical constants. Quantum effects are important in determining the thermodynamics of helium, and to a lesser extent, neon. Argon and nitrogen can be considered classical for most practical purposes. Despite dealing with the fluids that show high and moderate quantum effects, the discussion on quantum physics is secondary since the presented equations are empirical, and the question about the origins of the intermolecular forces is irrelevant.

It is expected that the equation of state described above, and used throughout this work, can successfully describe the properties of quantum fluids. However, the ratio of critical temperatures of neon and helium–4 reaches 8.6. Similarly high values can be found in

mixtures of methane with long-chain hydrocarbons and for hydrogen mixed with, e.g., carbon dioxide.[46] Describing the properties of mixtures, characterized by high critical temperature ratio, places high load on the departure function, necessary to accurately represent the state properties.

3.2 Optimization algorithm

3.2.1 Methodology

The optimization method used for the equation of state development is based on non-linear regression analysis and the *Lavenberg-Marquardt algorithm* (LMA),[47,48] also known as the damped least-squares. The LMA method is used to solve the non-linear least-square problems and the curve fitting in particular. It is similar to the Gauss-Newton algorithm but is characterized by higher robustness and lower speed.[49] The non-linear fitting is presently the most effective method used to develop the equations of state and compared to the previously used linear least-squares regression, it does not require linearizing data with the use of preliminary equations of state. Like many fitting algorithms, the LMA finds only a local minimum, not necessarily the global minimum. In order to find the global minimum or approach it sufficiently, so the EOS reproduces the experimental data within a satisfactory error, additional constants, randomized coefficients, and weights are applied to the *sum of squares* (SSQ) during the optimization procedure. Their impact on the SSQ minimization is described later in this chapter. The expression for the residual sum of squares is given by

$$\mathrm{SSQ} = \sum_{i=1}^{N_\rho} W_{\rho,i} F_{\rho,i}^2 + \sum_{i=1}^{N_w} W_{w,i} F_{w,i}^2 + \sum_{i=1}^{N_{c_p}} W_{c_p,i} F_{c_p,i}^2 + \ldots, \tag{3.19}$$

where $W_{y,i}$ is a weight applied to each data point of the thermodynamic property y. $F_{y,i}$ is the function used to minimize the relative deviation between the value calculated with the equation of state $y_{\mathrm{EOS},i}\left(\overline{x},\overline{\beta}\right)$ for a given vector of fitted parameters $\overline{\beta}$ and the data point $y_{\mathrm{DATA},i}$ measured at $\overline{x}$.[50] The function $F_{y,i}$ for a single experimental point i is evaluated as

$$F_{y,i} = \frac{y_{\mathrm{DATA},i} - y_{\mathrm{EOS},i}\left(\overline{x},\overline{\beta}\right)}{y_{\mathrm{DATA},i}}. \tag{3.20}$$

The algorithm minimizes the $\mathrm{SSQ} = \mathrm{SSQ}\left(\overline{x},\overline{\beta}\right)$ by changing $\overline{\beta}$ in an iterative procedure, starting from a guess value. In each iteration step, the parameter vector $\overline{\beta}$ is replaced

with a new guess value $\overline{\beta} + \delta$, and the function $y_{\mathrm{EOS},i}\left(\overline{x}, \overline{\beta} + \delta\right)$ is approximated as

$$y_{\mathrm{EOS},i}\left(\overline{x}, \overline{\beta} + \delta\right) = y_{\mathrm{EOS},i}\left(\overline{x}, \overline{\beta}\right) + J_i \delta, \tag{3.21}$$

where

$$J_i = \frac{\partial y_{\mathrm{EOS},i}\left(\overline{x}, \overline{\beta}\right)}{\partial \overline{\beta}}, \tag{3.22}$$

is the gradient of $y_{\mathrm{EOS},i}$ with respect to $\overline{\beta}$.

The initial guess value in the optimization process is often a recently developed equation of state for a similar fluid or mixture of fluids. Since this starting point is, most probably, far away from the global minimum in the multi-dimensional parameter space $\overline{\beta}$, the fitting process is a supervised optimization that requires regular adjustments of the coefficients for the sum of squares to decrease.

The variable quantities restricting the fitter behavior are:

- upper and lower bounds for the four parameters of the reducing function: $\beta_{T,ij}$, $\gamma_{T,ij}$, $\beta_{v,ij}$, $\gamma_{v,ij}$;
- upper and lower bounds for $n_{ij,k}$ coefficients of the departure function;
- upper and lower bounds for the temperature exponents $t_{ij,k}$ of the departure function;
- upper and lower bounds for each of the Gaussian-bell shaped term within the departure function;
- factors for randomized splitting the temperature exponents $t_{ij,k}$ within imposed bounds;
- factors for randomized splitting the Gaussian-bell shaped terms within bounds;
- penalty coefficients for exceeding the limits imposed by bounds.

The limits are applied to the parameter space, so the minimization process is constrained. This frequent optimization practice prevents the algorithm from failing for huge parameter values and allows the minimization process to advance quicker.

Fitting the single-phase properties to a fluid mixture data, with well-established equations for its pure constituents, is relatively simple and requires only an acceptable starting point and minor adjustments of the fitter coefficients. Fitting the phase envelope is a more complex procedure and is much more time-consuming. Because of this complexity, the first optimization goal is to model the phase envelope accurately. It requires a sensible choice of the experimental data to pin the dew and bubble lines and multiple

iterations to approach the global minimum, passing through the local minima with a use of random coefficients and variable penalties. When the phase envelope is fitted to a satisfactory level defined through a visual inspection, the single-phase properties are added to the sum of squares. The first solution often shows a trade-off between the accurate fit of the phase-envelope and the single-phase properties. Additional iterations and adjustments to the coefficients and penalties allow minimizing the total SSQ.

3.2.2 Fitter

The fitter is a program written in Fortran, specifically developed for the application to the equations of state. It is a constantly evolving project, developed for the last two decades, led by Eric W. Lemmon. Its core part was first written by Robert D. McCarty and Vincent D. Arp, and it was first used to develop the equation of state for helium–4.[51] The fitter has evolved tremendously since then, and thanks to its present state, it allows for fitting the equations to data for complex mixtures.

The fitter uses the functional form of the Helmholtz energy EOS from Eq. (3.1), an algebraic form of a relationship between a dependent variable and the explanatory variables. The fitter comprises the Helmholtz energy derivatives calculations, the thermodynamic properties, and the algorithm for tracing the phase equilibria.

The important starting point for the fluid mixture property description are the equations of state for pure fluids. The properties of helium–4,[44] neon,[13] argon,[52] and nitrogen[53] are well established and available in the form of the Helmholtz energy-explicit equations.

The variable parameters of the equation are the parameters of the departure function, described in Eq. (3.3) and Table 3.1, and the parameters within the departure function from Eq. (3.8). Depending on the number of Gaussian terms used in the equations, the total number of parameters varies from 42 to 49 in this work.

3.2.3 Constraining the fitter behavior

An important advantage of the non-linear regression methods is the possibility of applying unequal comparative operators (greater than or less than) in constraints for controlling the behavior of calculated properties. It is beneficial for properties extrapolated outside the experimental data availability regions. The slope and curvature of a thermodynamic surface can be adjusted in a region where no data is available, not impacting the EOS behavior in another region, where experimental data pin the surface.

Fortunately, the equation of state for a mixture takes advantage of the equations of state for pure fluids composing the mixture. As a result, the constraining process for the mixture EOS development can be much more straightforward than the necessary constraints applied to a pure fluid equation.

In order to construct a constraint, three parameters are necessary: the constraint property, a variable to hold constant, and the attribute of constraint property – a line, a slope, the third, or the fourth derivative. For all the equations optimized in this work, only a few constraints are necessary. An example of one of them, applied to the $^4\mathrm{He} - \mathrm{Ne}$ equation, is a positive curvature of the 40 K isotherm in the speed of sound calculations for pressures between 8 and 22 MPa.

3.2.4 Weighting the data

Weights are attributed to the data points or data sets during the EOS optimization procedure to impose direction for gradient calculations in the next minimization steps. A single measurement point with a high weight influences the SSQ more than a point with a small weight. For a known measurement uncertainty, U_i, the relative residual of an experimental point i, measured as a function of temperature and pressure, is calculated. An example for calculating the relative residual in density is given:

$$\zeta_i = \frac{\rho_{\mathrm{EOS},i}\left(p_{\mathrm{DATA},i}, T_{\mathrm{DATA},i}, x_{\mathrm{DATA},i}, \overline{\beta}\right) - \rho_{\mathrm{DATA},i}\left(p_{\mathrm{DATA},i}, T_{\mathrm{DATA},i}, x_{\mathrm{DATA},i}\right)}{U_i(\rho)}. \tag{3.23}$$

The absolute value of the relative residual equal to or lower than unity means that the property prediction from the EOS is within the limit of experimental uncertainty. The goal of assigning the weights to data is to drive the SSQ, so the relative residuals for most of the points decrease below unity.

A good starting point for weight w_i assigned to data point i is

$$W_i = \frac{1}{U_i^2}. \tag{3.24}$$

It favors the accurate measurements over the less accurate by increasing their weights and importance in the SSQ calculations. If a data set is provided without the uncertainty value or the specified uncertainty is questionable, the weighting process is subject to expertise and introduced corrections to further the optimization procedure.

3.3 Experimental data available for the equations development

Reviewing the literature to search the experimental data can be tedious. It includes searching for scientific publications, converting results between different unit systems, and translating languages. Fortunately, the work on the literature review for the thermodynamic properties was performed at NIST and is partly available within the ThermoLit library.[54] The scientific publications listed in ThermoLit are completed by additional literature review resulting in the data sets, presented in Tables A.1–A.4. A summary of the experimental data from these tables is available in Table 3.2, the $p-T$ space coverage of available experimental data for density measurements is plotted in Fig. 3.1.

In contrast to pure fluids, the region of existing state points is always broader for mixtures since it is also composition-dependent. The experimental data sets available for fluid mixtures are often smaller in size and more deficient in the thermodynamic properties coverage, e.g., the recent equation of state for helium–4 benefits from 145 data sets covering 15 different properties.[44] In contrast, the equation of state for $^4\mathrm{He}-\mathrm{Ne}$ is developed based on 8 data sets covering three properties. Therefore, it is more challenging to cover a comparable number of states for mixtures. Additionally, the pure fluids benefit from historically longer interest among the experimental scientists.

Because of the relatively small number of data sets, data inconsistency is visible mainly in the outliers. The outliers problem is easily solved by visualizing the complete data sets in their measurement space and removing the large SSQ points based on the deviation plots. Minor inconsistencies are encountered between different data sets since they rarely overlap. Some issues are visible at the phase envelopes. Fortunately, a visual inspection based on the continuity of thermodynamic properties – pressure and temperature, is sufficient to solve the inconsistency problems in this work. Another previously described problem is the unknown phase envelope behavior at higher pressures. It is visible for helium-neon and neon-argon and is subject to interpretation.

Table 3.2. Summary of the experimental data available for the equations development

fluid	no. of properties	no. of data sets	no. of data points
$^4\mathrm{He}-\mathrm{Ne}$	3	8	424
$^4\mathrm{He}-\mathrm{Ar}$	3	20	1974
$\mathrm{Ne}-\mathrm{Ar}$	3	11	497
$^4\mathrm{He}-\mathrm{N_2}$	3	28	3788

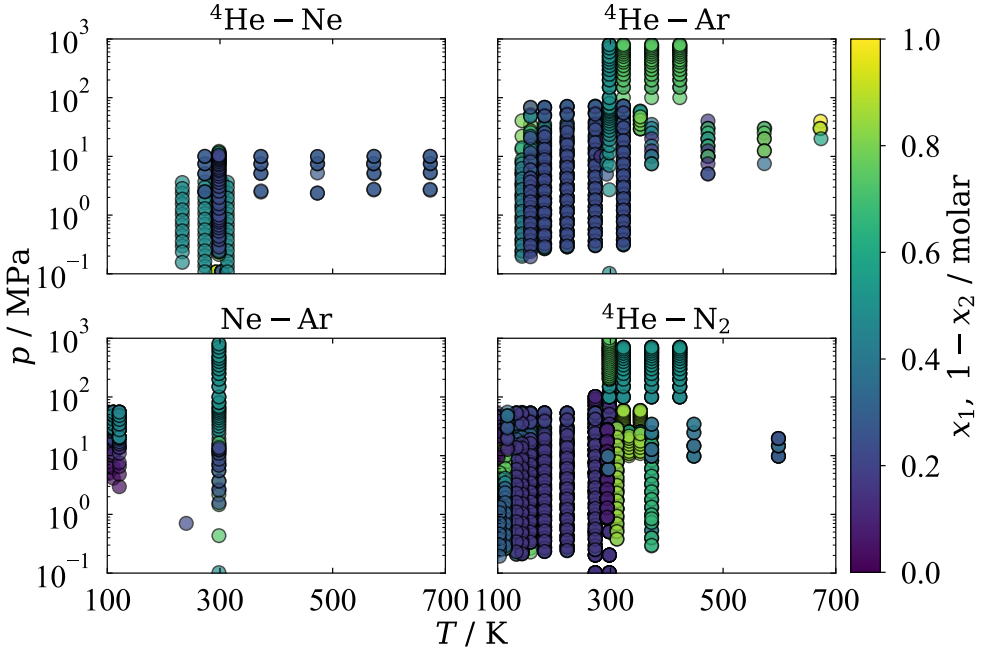

Fig. 3.1. $p-T$ coverage of available ρpT data with composition dependent color scale. x_1 is the molar concentration of a lighter component

The equilibrium data available for the mixture of helium-neon are limited in pressure up to 20 MPa. Even though the shape of the phase envelope at higher pressures is unknown, this data availability limit is higher than most engineering applications need. The model from this work shows satisfactory accuracy at lower pressures, with the extrapolation behavior being acceptable. The equilibrium data and ρpT data for other mixtures reach higher pressures, up to 1 GPa for helium-argon and helium-nitrogen, and 100 MPa for neon-argon. The data sets are categorized based on fluid mixture and measured property. In this form they are presented in Tables A.1–A.4. Whenever the authors provide a satisfactory uncertainty discussion, the uncertainty values are included in the table. Additionally, the last column in the table describes the *Average Absolute Deviation* (AAD) of the data set, compared to the equations of state developed in this work. The presented AAD values are calculated as follows:

$$\mathrm{AAD} = \frac{100}{N}\sum_{i}^{N}\left|\frac{y_{\mathrm{DATA},i}-y_{\mathrm{EOS},i}}{y_{\mathrm{DATA},i}}\right|, \tag{3.25}$$

where y is the thermodynamic property of choice and N is the size of the data set.

As shown in Appendix A, the only data that remain entirely unfitted in the EOS development are the cross-virial coefficients, B. Physics dictates that it should only be a function of temperature. However, the mixing rule also produces dependence on composition in the multi-fluid model and, therefore, yields incoherent results. A combination rule,

which allows accurately representing the cross-virial coefficients using one adjustable parameter, has been recently proposed[55] but is not implemented in this work. For computing the AAD corresponding to the data sets from Tables A.1–A.4, an effective B_{12} was calculated from the EOS at an equimolar composition.

3.4 Results of the equations of state development

The results are discussed for each mixture separately except for the binary specific parameters for all fluids presented in Table 3.3. The scaling parameter applied to departure function, F_{ij} is set to unity for all mixtures since the departure function is fitted in this work. Following the GERG monograph,[43] a larger number of significant digits is given for the N_k coefficients, compared to the other departure function parameters.

Depending on the mixture, the phase envelopes vary in shape, as discussed in Sec. 2.1.2; they are either closed or open, and they can either have the gas-gas equilibrium (GGE) locus or just the vapor-liquid equilibrium (VLE) dome. It is probable that all mixtures considered in this work behave similarly,[15,56] but this question is not investigated due to the lack of high-pressure data for ^{4}He − Ne and Ne − Ar.

The quality of the equations of state in single-phase is determined by comparing the calculated deviations of data points and predictions obtained with these equations. Deviations in density are plotted as a function of pressure and in speed of sound – as a function of temperature. The phase envelopes for VLE and GGE calculations are constructed with the tracing algorithm for equilibria calculations of binary mixtures.[45] The algorithm solves the differential equations, which become infinitely stiff in the close vicinity of the critical line. This property should be interpreted as the critical line prediction, and it is visible in all 3D and 2D figures as a white gap between the dew and bubble lines. The right plot in each equilibria figure is the projection of the phase envelope from the left figure on the two-dimensional $\log(p) - x$ plane.

Table 3.3. Binary specific parameters

$i - j$	$\beta_{T,ij}$	$\gamma_{T,ij}$	$\beta_{v,ij}$	$\gamma_{v,ij}$
^{4}He − Ne	0.793	0.728	1.142	0.750
^{4}He − Ar	1.031	1.113	1.048	0.862
Ne − Ar	1.033	0.967	0.919	1.035
^{4}He − N_2	1.028	1.229	1.036	0.935

3.4.1 Helium-neon

In addition to four reducing parameters from Table 3.3, the model optimization includes deriving the departure function from Eq. (3.8). The temperature and density-dependent parts of the departure function for the mixture of helium–4 and neon are presented in Table 3.4. This set of coefficients forms a valid equation of state.

The phase behavior of the helium-neon mixture is shown in Fig. 3.2. The phase envelope projection on $p-x$ plane with plotted isotherms allows evaluating the equation performance visually. Fig. 3.3 presents the relative deviations of the EOS with respect to the experimental data used for its development. The density deviations are small and do not exceed 0.5% except for the lower accuracy data at 30–40 K, as shown in Fig. 3.3a. The speed of sound deviations reach 6%, as presented in Fig. 3.3b. As shown in Fig. 3.1, the pressure range of available data for this binary pair is narrower for ρpT, compared to other mixtures discussed in this work. A $T-s$ diagram is shown in Fig. 3.4, as an exemplary plot of a thermodynamic property, calculated with the EOS. More plots for thermodynamic properties are available in Appendix B.

Table 3.4. Departure function coefficients for the helium-neon mixture

k	N_k	t_k	d_k	η_k	β_k	γ_k	ϵ_k
1	-4.346 849	1.195	1	0	0	0	0
2	-0.884 378	1.587	2	0	0	0	0
3	0.258 416	1.434	3	0	0	0	0
4	3.502 188	1.341	1	0.157	0.173	1.310	1.032
5	0.831 330	1.189	2	0.931	1.070	1.356	1.978
6	2.740 495	1.169	3	0.882	0.695	1.596	1.966
7	-1.582 230	0.944	4	0.868	0.862	1.632	1.709
8	-0.304 897	1.874	4	0.543	0.971	0.766	0.583

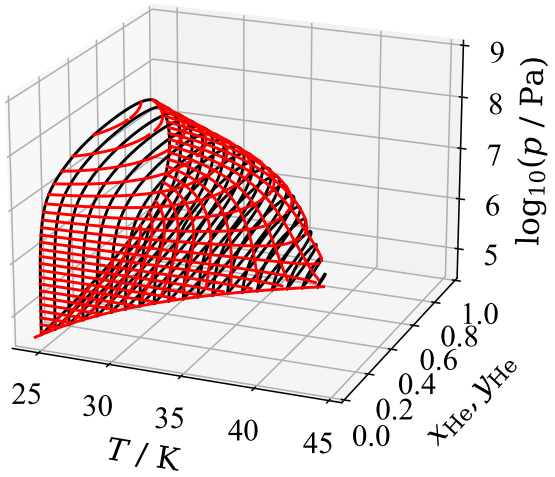

(a) Closed phase envelope shown in 3D space of $p-T-x$ with isobars in red and isotherms in black

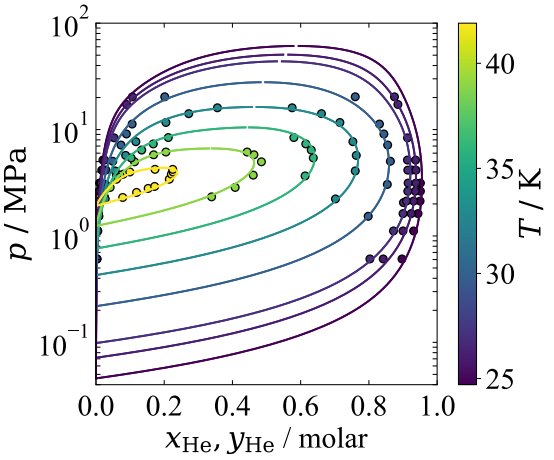

(b) Projection of the VLE isotherms on the $p-x$ plane plotted with experimental data[57,58] in temperature-dependent color scale

Fig. 3.2. Vapor-liquid equilibrium (VLE) of helium-neon

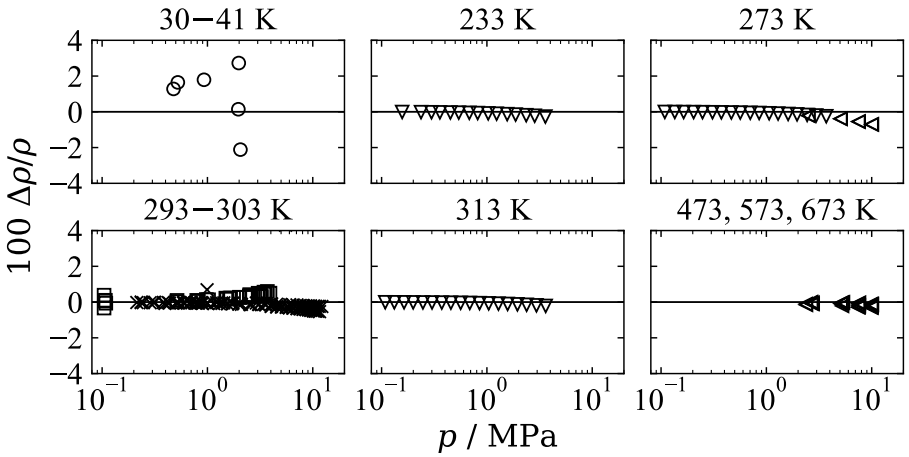

(a) Deviations from density data[59–63] as a function of pressure

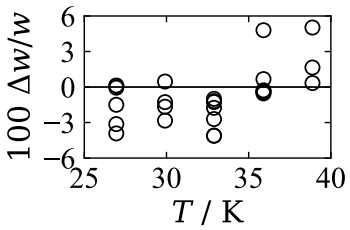

(b) Deviations in speed of sound for data from Pashkov *et al.* (1985)[64]

Fig. 3.3. Relative deviations of the ^{4}He − Ne equation from the single-phase data

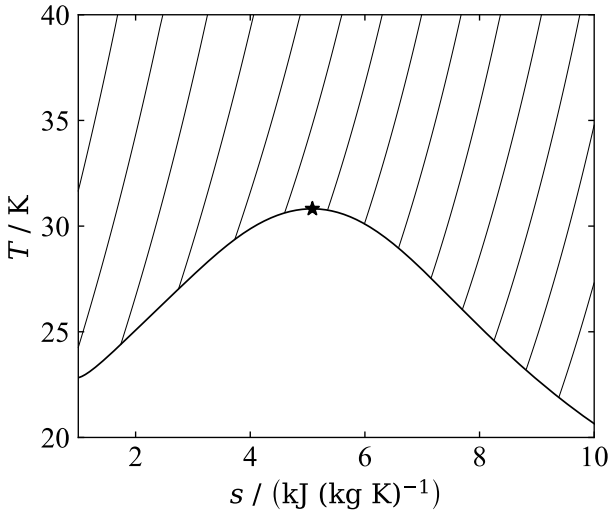

Fig. 3.4. Temperature-entropy diagram of the ^{4}He — Ne mixture at equimolar (0.5/0.5) composition with isobars, saturation line, and the critical point marked with a star. More plots are available in Fig. B.1.

3.4.2 Helium-argon

In analogy to the helium-neon mixture, the reducing parameters from Table 3.3 are completed with the departure function for helium-argon, given in Table 3.5. This EOS is capable of describing the fluid behavior in the vapor-liquid and gas-gas equilibria regions. The phase envelope for ^{4}He — Ar is of class III[15] and is shown in Fig. 3.5 in the three-dimensional, $p - T - x$ space, together with its projection on the $p - x$ plane.

Table 3.5. Departure function coefficients for the helium-argon mixture

k	N_k	t_k	d_k	η_k	β_k	γ_k	ϵ_k
1	-2.643 654	1.030	1	0	0	0	0
2	-0.347 501	0.288	2	0	0	0	0
3	0.201 207	0.572	3	0	0	0	0
4	1.171 326	1.425	1	0.371	0.320	1.409	0.378
5	0.216 379	1.987	1	0.081	1.247	1.709	0.741
6	0.561 370	0.024	2	0.375	1.152	0.705	0.322
7	0.182 570	1.434	3	0.978	0.245	1.162	1.427
8	0.017 879	0.270	4	0.971	1.030	0.869	2.088

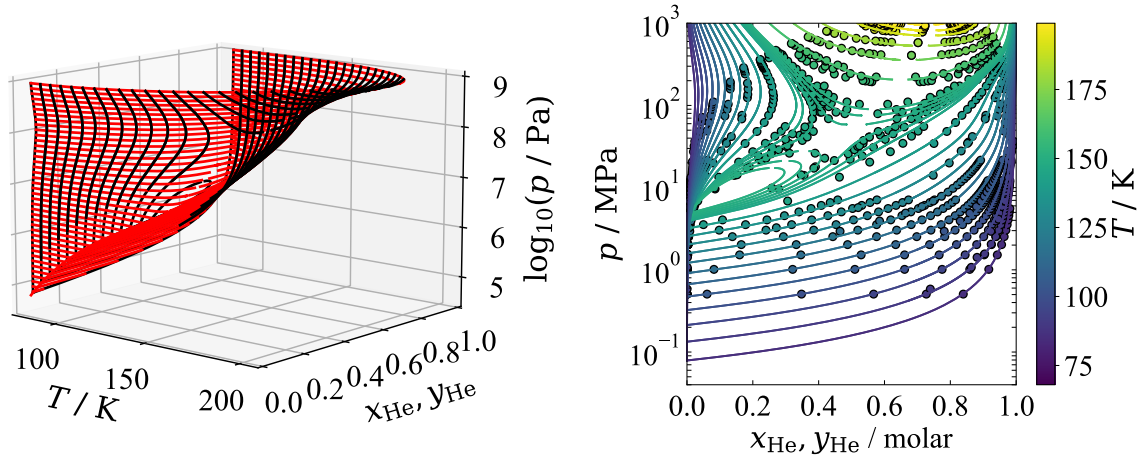

(a) Open phase envelope of class III shown in 3D space of $p-T-x$ with isobars in red and isotherms in black

(b) Projection of the VLE+GGE isotherms on the $p-x$ plane plotted with experimental data[65–72] in temperature-dependent color scale

Fig. 3.5. Vapor-liquid (VLE) and gas-gas equilibria (GGE) of helium-argon

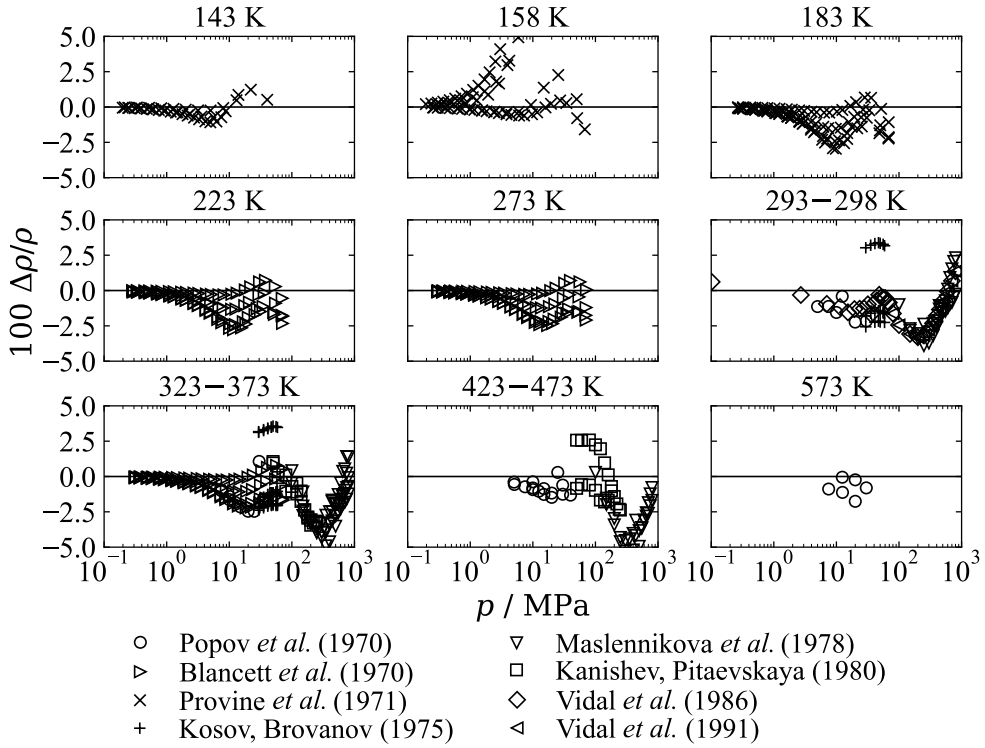

(a) Deviations from density data[73–80] as a function of pressure

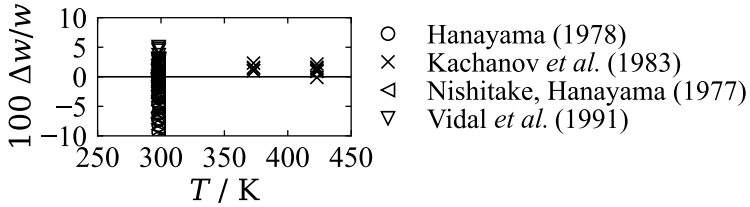

(b) Deviations from speed of sound from data[80–83] as a function of temperature

Fig. 3.6. Relative deviations of the ^{4}He − Ar equation from the single-phase data

The measurements for ^{4}He — Ar at equilibrium and in single-phase cover a broader range of temperature and pressure compared to helium-neon. Not only are there more data sets, but a broader range of pressure is covered by the experimental data, reaching 1 GPa for ρpT and the phase equilibria measurements. At low pressures (0-–10 MPa), the equation deviates by 0.5%—2.5% for 95% of density data points used for its development, as presented in Fig. 3.6a. The deviations in density at lower pressures are comparable with the measurement uncertainties, presented in Table A.2. However, for pressures above 100 MPa, the equation deviates from data by 5% in density, more than reported experimental uncertainties. The deviations of EOS to the speed of sound data are shown in Fig. 3.6b and reach 10% in the worst case.

3.4.3 Neon-argon

Similar to the helium–4 mixtures, the gas-gas equilibrium may exist at high pressures in the binary pair of neon and argon. However, no measurements are available in the literature on the gas-gas equilibrium. Therefore, the GGE shape is not anticipated, as the mathematical description is cut at 100 MPa – the highest available pressure for the equilibria measurements. Compared to the helium-neon mixture, the equilibria measurements for Ne — Ar provide a fuller description of the upper part of the phase envelope for the vapor-liquid equilibrium.

Following the two previous equations, the EOS for Ne — Ar is formed with the reducing parameters from Table 3.3 and the departure function from Table 3.6.

Fig. 3.7 presents the constructed phase envelope for the mixture and the projected isotherms. Figures 3.8a and 3.8b show deviations of the single-phase data used for the EOS development, ρpT and the speed of sound measurements respectively. The density measurements reach 55 MPa in cryogenic conditions and 1 GPa at ambient tem-

Table 3.6. Departure function coefficients for the neon-argon mixture

k	N_k	t_k	d_k	η_k	β_k	γ_k	ϵ_k
1	-1.039 686	0.723	1	0	0	0	0
2	0.593 776	1.689	2	0	0	0	0
3	-0.186 531	1.365	3	0	0	0	0
4	-0.223 315	0.201	1	1.018	0.360	1.119	2.490
5	0.160 847	0.164	2	0.556	0.373	1.395	1.202
6	0.405 228	0.939	2	0.221	0.582	1.010	2.468
7	-0.264 563	1.690	3	0.862	0.319	1.227	0.837
8	-0.033 569	1.545	4	0.809	0.560	1.321	2.144

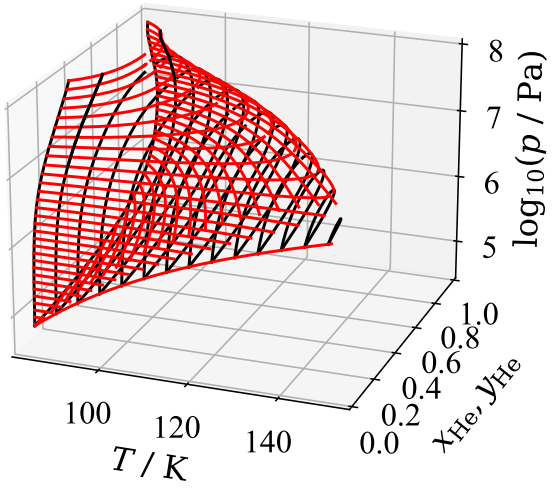

(a) Phase envelope with visible opening to GGE shown in 3D space of $p-T-x$ with isobars in red and isotherms in black

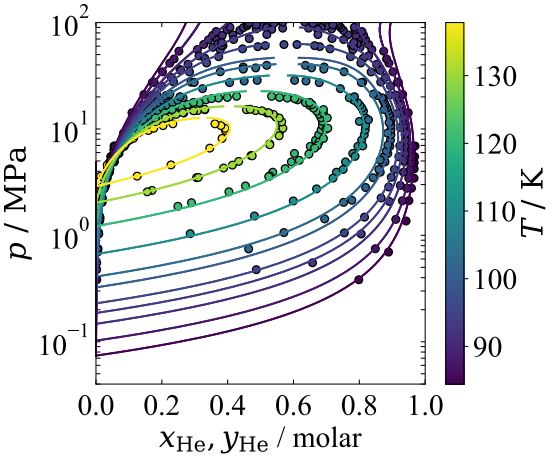

(b) Projection of the VLE isotherms on the $p-x$ plane plotted with experimental data[69,84–87] in temperature-dependent color scale

Fig. 3.7. Vapor-liquid equilibrium (VLE) of neon-argon

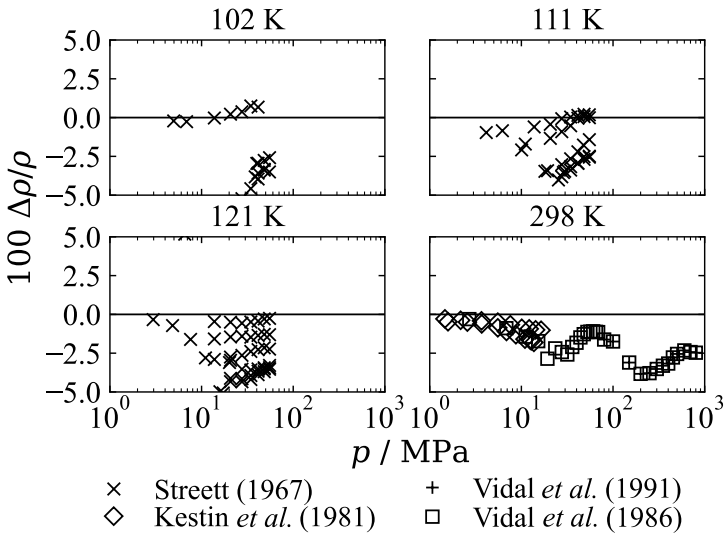

(a) Deviations from density data[60,79,80,85] as a function of pressure

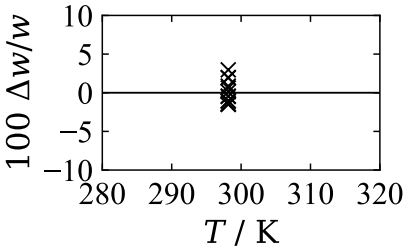

(b) Deviations in speed of sound for data from Konovodchenko *et al.* (1981)[88]

Fig. 3.8. Relative deviations of the Ne − Ar equation from the single-phase data

perature. The equation has maximal errors of 5% for the density data, but for 90% of data, the error stays below 3%. Data sets are available for only four temperature values and accurate experimental data are missing for temperatures from 120 to 298 K.

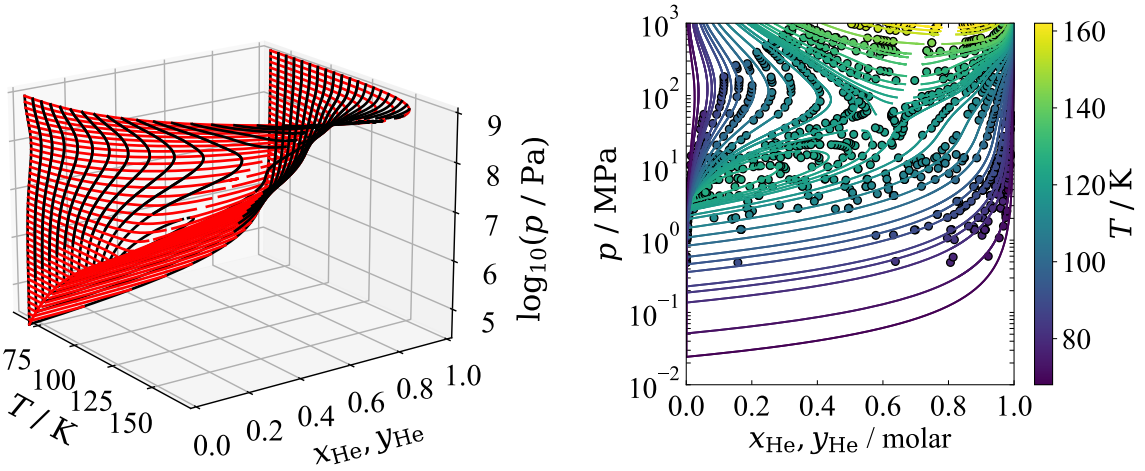

(a) Open phase envelope of class III shown in 3D space of $p-T-x$ with isobars in red and isotherms in black

(b) Projection of the VLE+GGE isotherms on the $p-x$ plane plotted with experimental data[69,72,89–99] in temperature-dependent color scale

Fig. 3.9. Vapor-liquid (VLE) and gas-gas equilibria (GGE) of helium-nitrogen

3.4.4 Helium-nitrogen

In contrary to the three mixtures described above, the equation of state for $^4\mathrm{He}-\mathrm{N}_2$ has not been published. It was developed during a time-constrained collaboration with the industry and needs further refinement to reach a satisfactory performance at the phase envelope and in single-phase. The primary goal of its development was the low-pressure (up to 5 MPa) phase-equilibria description, and in this region, the equation performs well. The coefficients from Tables 3.3 and 3.7 form the equation of state for the helium-nitrogen mixture.

Table 3.7. Departure function coefficients for the helium-nitrogen mixture

k	N_k	t_k	d_k	η_k	β_k	γ_k	ϵ_k
1	-3.122 496	0.786	1	0	0	0	0
2	-0.245 826	0.232	2	0	0	0	0
3	0.172 129	0.502	3	0	0	0	0
4	1.455 886	0.304	1	0.736	0.590	1.048	0.387
5	0.681 733	0.483	2	0.782	0.348	0.957	1.133
6	0.228 133	1.419	3	0.846	0.576	1.539	1.357
7	0.053 118	0.261	4	0.660	0.454	0.778	1.773

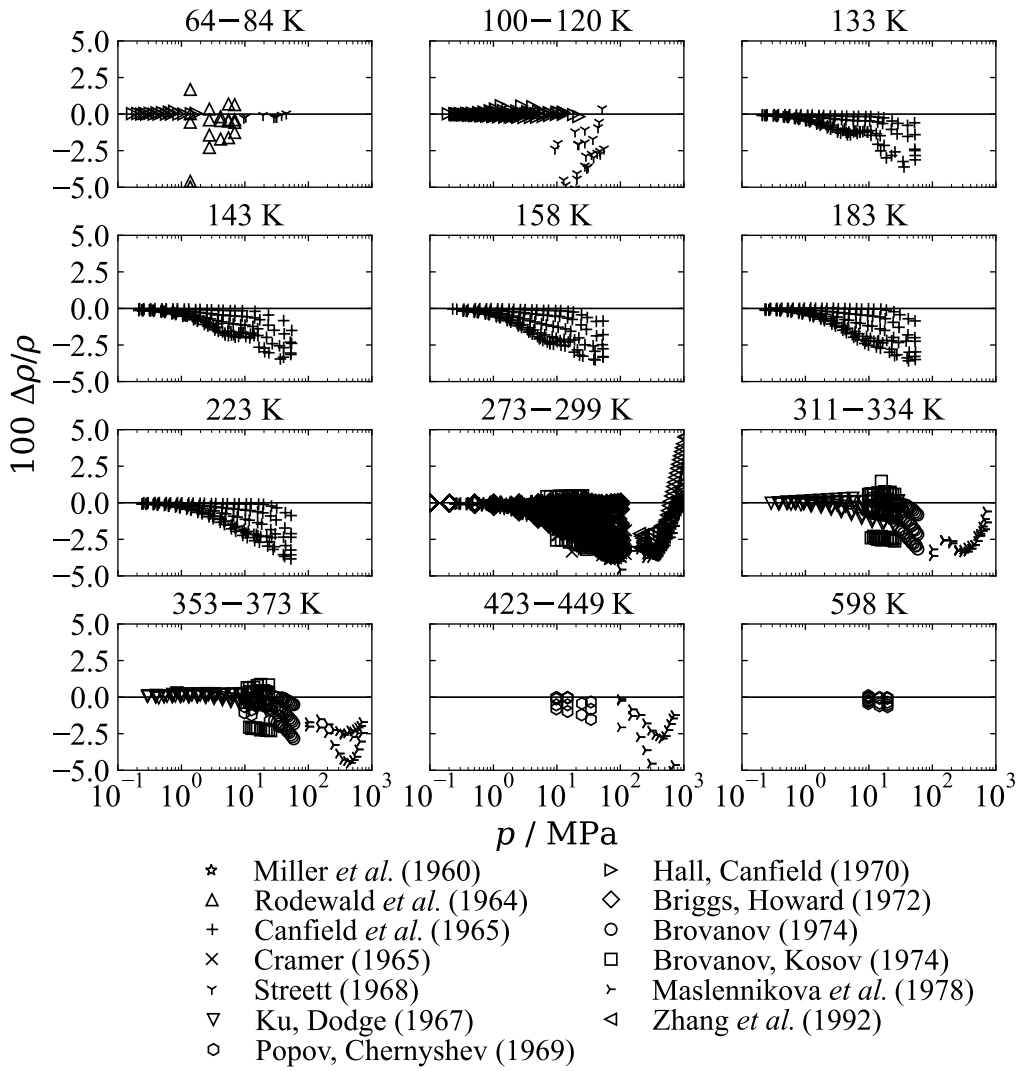

(a) Deviations from density data[96,100–113] as a function of pressure

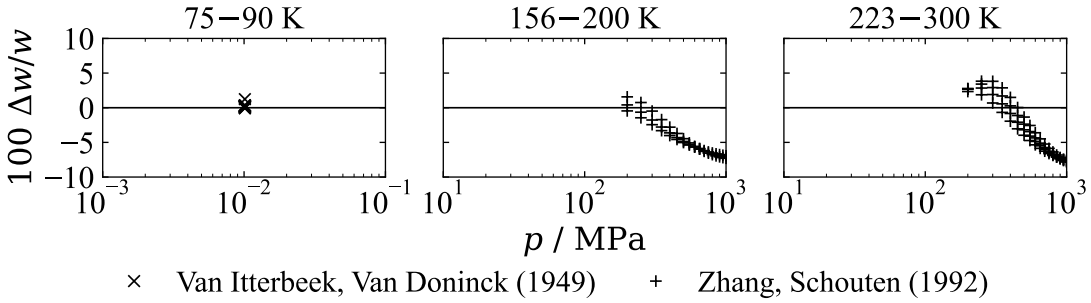

(b) Deviations from speed of sound data[114,115] as a function of pressure

Fig. 3.10. Relative deviations of the $^4He-N_2$ equation from the single-phase data

Fig. 3.9 shows the phase envelope for the mixture. Deviations in density are presented in Fig. 3.10a and deviations in speed of sound – in Fig. 3.10b. The $^4He-N_2$ equation provides similarly accurate predictions for density as, e.g., the ^4He-Ar equation. However, it fails more often in single-phase properties calculations. At pressure values higher

than 10 MPa, the equation deviates from density data for more than 2.5%. Additionally, the phase equilibria calculations are less accurate, particularly in the separation region. The equation should probably be refitted with a larger number of the departure function terms, so its accuracy improves.

3.5 Uncertainty discussion at phase boundary

When applying the isothermal error calculations based on the comparison of the bubble or dew pressures for a given mixture composition, large calculated deviations can be obtained when an isotherm in the $\log(p) - x$ plane is vertical or very steep. However, the data point may still be very close to the phase envelope, which is a degeneracy in the means of error quantification.

In order to evaluate errors at phase equilibria, the orthogonal length scale for data versus EOS is defined. The dimensionless, *orthogonal error* is calculated by finding the smallest distance between the experimental data point $((x_{\text{data}}, \hat{p}_{\text{data}}), T_{\text{data}})$ and the respective isotherm evaluated with the EOS $\left(\left(x_{\text{calc}}^{\text{min}}, \hat{p}_{\text{calc}}^{\text{min}}\right), T_{\text{calc}}\right)$, where $T_{\text{data}} = T_{\text{calc}}$ and $\hat{p}$ is the *reduced pressure*, defined as:

$$\hat{p} = \frac{p}{p_{\text{r}}}. \tag{3.26}$$

After comparing the impact of the reducing scales, p_{r}, on the error value, the logarithmic reducing scale has been selected among the linear and density-temperature reducing scale ($p_{\text{r}} = p(\rho_{\text{r}}, T_{\text{r}})$),

$$\begin{cases} p_{\text{r},x} = \exp\left(x_1 \ln\left(p_{\text{c},1}\right) + x_2 \ln\left(p_{\text{c},2}\right)\right) \\ p_{\text{r},y} = \exp\left(y_1 \ln\left(p_{\text{c},1}\right) + y_2 \ln\left(p_{\text{c},2}\right)\right) \end{cases}, \tag{3.27}$$

where $p_{\text{c},i}$ is the critical pressure of component i. $p_{\text{r,x}}$ reduces the pressure for the bubble points, and $p_{\text{r,y}}$ reduces the pressure for the dew points. The error itself is defined as a sum of distances between the data point x_{data} and the closest point from the respective isotherm in the earlier defined $\hat{p} - x$ plane

$$\begin{cases} \text{err}_x^{\text{vle}} = \pm\sqrt{\left(x_{\text{data}} - x_{\text{calc}}^{\text{min}}\right)^2 + \left(\ln\left(\hat{p}_{\text{data}}\right) - \ln\left(\hat{p}_{\text{calc},x}^{\text{min}}\right)\right)^2} \\ \text{err}_y^{\text{vle}} = \pm\sqrt{\left(y_{\text{data}} - y_{\text{calc}}^{\text{min}}\right)^2 + \left(\ln\left(\hat{p}_{\text{data}}\right) - \ln\left(\hat{p}_{\text{calc},y}^{\text{min}}\right)\right)^2} \end{cases}, \tag{3.28}$$

where x_{data} and $\hat{p}_{\text{data}}$ are the molar composition and reduced pressure for the experimental data point. $x_{\text{calc}}^{\text{min}}$ and $\hat{p}_{\text{calc,x}}^{\text{min}}$ are the molar composition and the reduced pressure evaluated with the EOS at the same temperature as the data point. This error definition

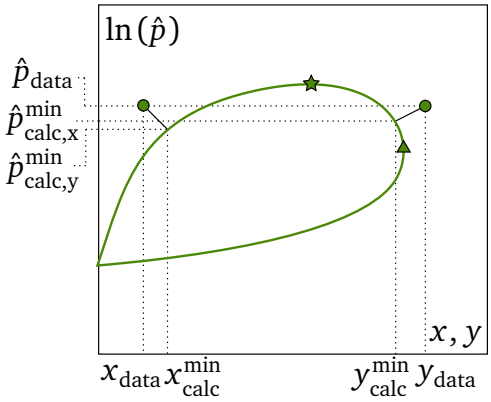

Fig. 3.11. Schematic representation of the orthogonal error calculations for the phase envelopes. Circles are the VLE experimental data, star is the critical point, and triangle is the maxcondentherm. Green line is an isotherm evaluated with the EOS plotted in the two-dimensional space of reduced pressure $\hat{p} = p/p_r$ versus mole fraction in liquid phase x and vapor phase y.

is represented schematically in Fig. 3.11, where the error value can be interpreted as the length of the solid black line. Numerically, the error is evaluated by calculating the distances between an experimental point and all points forming the respective isotherm. The error is the smallest value among them. The sign convention is chosen, so the positive error represents the EOS calculating too large a pressure compared to data and negative when calculating too small a pressure. Two experimental compositions for liquid and vapor from one measurement are marked with circles (the same pressure and temperature). It is essential to highlight that the compositions at the minimum point and experimental point can be different. The advantage of the orthogonal metric over the pressure-based metric is visible for the prediction giving too small a composition compared to the actual experimental point placed above the calculated maxcondentherm. For this case, the pressure-based metric does not provide the error value.

Fig. 3.12 presents results for the described error calculations. The orthogonal error is plotted for four mixtures with a color-coded absolute value of error in equilibria calculations. The same values are plotted as a function of pressure in Fig. 3.13. The histograms show the distribution of error values in the pressure range (x-axis) and the orthogonal error range (y-axis).

While the composition for the phase equilibrium calculations is always in the range of $[0, 1]$, the logarithm of reduced pressure $\ln(\hat{p})$ can reach values up to 7 for the absolute pressure of 1 GPa and the defined pressure metric. Therefore, the error definition from Eq. (3.28) and the chosen pressure metric emphasize the pressure error more than the composition error.

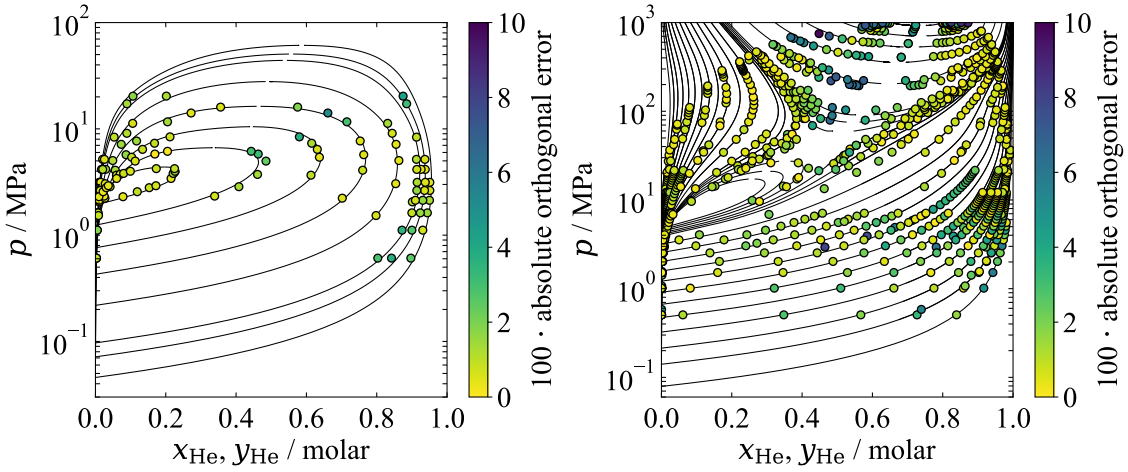

(a) ^{4}He – Ne phase envelope with maximal error of 0.038

(b) ^{4}He – Ar phase envelope with maximal error of 0.0979

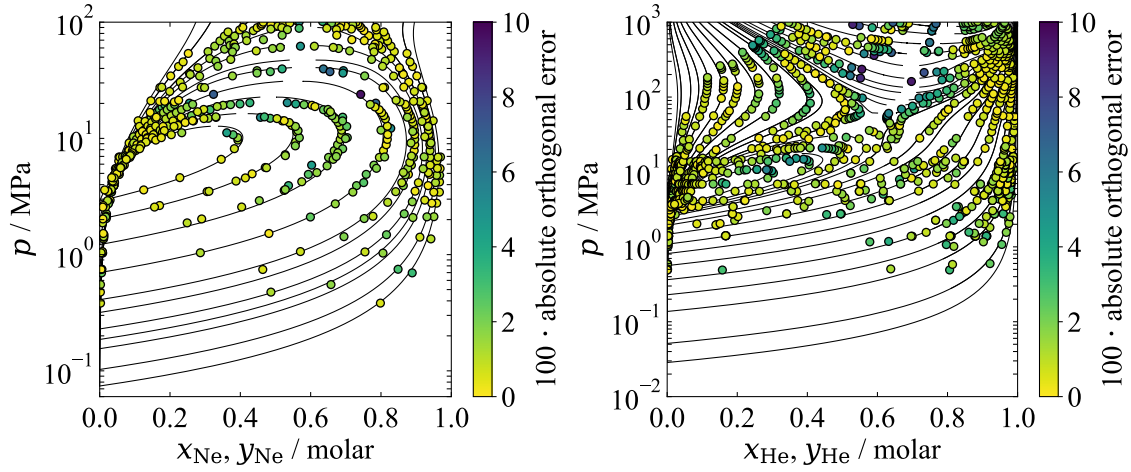

(c) Ne – Ar phase envelope with maximal error of 0.0957

(d) ^{4}He – N_2 phase envelope with maximal error of 0.0938

Fig. 3.12. Absolute orthogonal error for the vapor-liquid and gas-gas equilibria

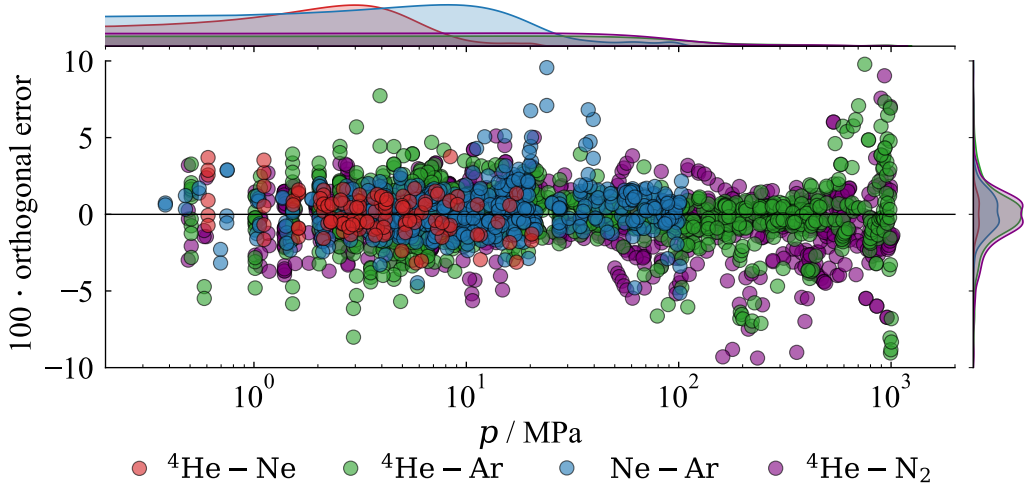

Fig. 3.13. Distribution of the orthogonal error values plotted with marginal histograms

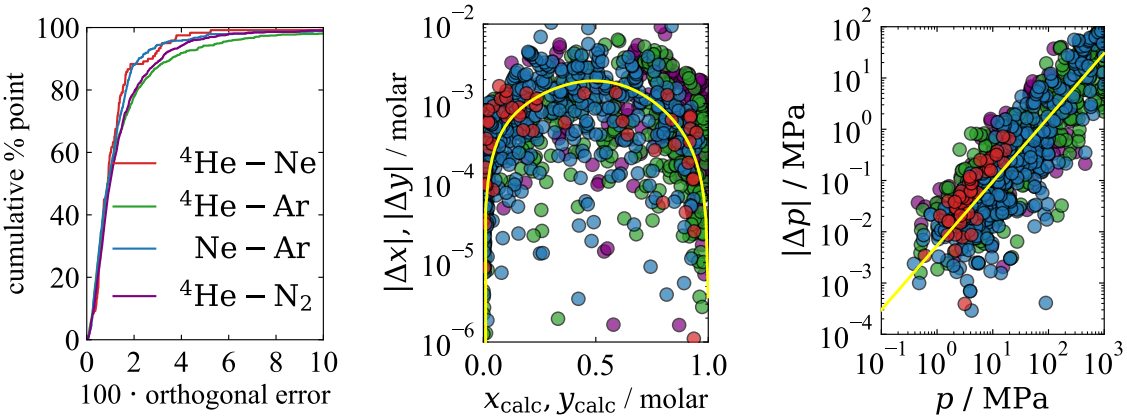

(a) Cumulative percentage of points with error less than the specified value of the equilibria orthogonal error for each EOS

(b) Orthogonal error unfolded to absolute error in composition plotted with yellow trend line

(c) Orthogonal error unfolded to absolute error in pressure plotted with yellow trend line

Fig. 3.14. Orthogonal error and resulting absolute errors plotted for four mixtures. Colors in subfigures (b) and (c) follow the colors imposed in subfigure (a).

Fig. 3.14a shows that 90% of all equilibria points have orthogonal error below 0.02 for ^{4}He — Ne and Ne — Ar; and 78% of ^{4}He — Ar points have orthogonal error in this range.

The orthogonal metric is less intuitive than the pressure-based error description. However, it can be unfolded to the absolute units. Fig. 3.14b shows the molar composition error in equilibria calculations, obtained with orthogonal metrics and recalculated to absolute values. The absolute error in composition increases symmetrically and reaches a maximum at equimolar composition. The error is expected to decrease to negative infinity for both endpoints, where the mixture equation becomes the pure fluid equation with no composition dependence. The pressure-dependent performance validation, visible in Fig. 3.14c shows a similar trend for all four equations. Compared to Fig. 3.13, where the error seems to be pressure-independent, its representation in absolute units reveals a clear pressure-dependence. This shortcoming of the orthogonal error definition can be explained by analyzing its definition from Eq. (3.28). While the composition error, $(x_{\text{data}} - x_{\text{calc}}^{\text{min}})$, takes uniform values over the composition range, the pressure error, calculated as an absolute difference of logarithms of reduced pressure, $(\ln(\hat{p}_{\text{data}}) - \ln(\hat{p}_{\text{calc},x}))$, underemphasizes the errors at higher pressure.

Fig. 3.12 may suggest that the phase equilibria description is more accurate for ^{4}He — Ne than for, e.g., ^{4}He — Ar. Fig. 3.14c shows that lower error values of the helium-neon phase envelope description are driven by a narrower pressure range of available experimental data, and complete error analysis can be made only after unfolding the orthogonal error to absolute units.

Compared to the conventional error evaluation, defined as a relative difference in pressure, the orthogonal metric is advantageous because it provides an error value for every data point independent of the slope of an isotherm. The pressure-based metric provides error values for 53.3% of points used for ^{4}He − Ar (the least out of four EOS) and 96.4% of points for Ne − Ar (the most out of four EOS).

3.6 EOS performance comparison

The previously defined empirical equations of state, used in REFPROP 10.0,[116] for mixtures of ^{4}He − Ne, ^{4}He − Ar, Ne − Ar, and ^{4}He − N_2 were developed by fitting the reducing parameters: β_T, γ_T, β_V, γ_V, together with the scaling parameter, F_{ij}. The departure functions were not binary-specific, and the equations did not accurately represent the phase envelopes but were sufficiently precise in single-phase. The equation of state for helium-neon used the departure function for the nitrogen-ethane mixture.[117] The helium-argon and helium-nitrogen EOS used the generic departure function for hydrocarbon mixtures.[43] The model for neon-argon used the reducing function only and did not fit the F_{ij} to any existing departure function.[118] As a result, the tracing routines for the phase equilibria failed for ^{4}He − Ne and ^{4}He − N_2, and did not provide any satisfactory description for the supercritical and high-pressure phase equilibria of ^{4}He − Ar. The routines only provided an approximate phase equilibria description for Ne − Ar, resulting in a maximal error in composition equal to 12 mol-%.

The most considerable advantage of fitting the reducing parameters, together with the binary-specific departure functions, is the accurate description of phase-envelope properties for all the mixtures. This advantage cannot be underestimated since it provides essential insights for engineering applications that consider liquefaction or working conditions in the vicinity of the two-phase region. The single-phase properties are also well represented in the equations developed in this work.

A comparison of the equations developed within this work to the previously used equations shows that 70% of density points for all mixtures are represented more accurately with new equations. However, only 41% of the speed of sound data is represented more accurately. 82% of the Joule-Thomson coefficients, discussed in Chapters 4 and 5, are represented more accurately with new equations. The inferior quality of the speed of sound representation is caused by fitting the new equations to the phase equilibria data. Since the new equations can model the behavior at phase envelopes, including the high-pressure gas-gas equilibrium, the lower precision for the single-phase property representation can be looked at as a cost.

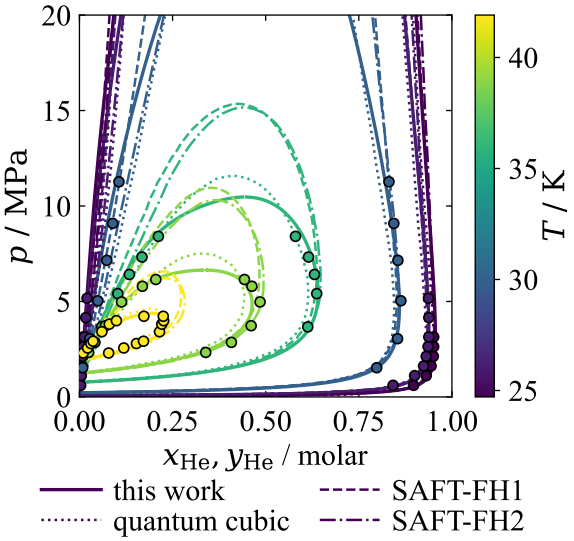

Fig. 3.15. VLE isenthalps of ^{4}He − Ne calculated with empirical equations of state from this work,[40] quantum-corrected cubic equation,[22] and quantum-corrected SAFT equations.[32] Circles mark the experimental data.

Fig. 3.15 shows a comparison of isotherms at phase envelope of ^{4}He − Ne, calculated with the empirical Helmholtz energy equation developed in this work and three other, recently published equations. The empirical equation gives by far the most accurate predictions in the phase equilibria calculations. It is the only one that is capable of providing the full description of the VLE and GGE phases for ^{4}He − Ar and ^{4}He − N_2.

3.7 Validation data

When implementing new equations of state in software, such as REFPROP,[116] CoolProp,[2] or Trend,[119] the EOS should be validated against the data points provided to verify if the implementation was successful. If the software uses the same pure fluid equations as given in this work (helium-4,[44] neon,[13] argon,[52] and nitrogen[53]), the implementation of mixture equations with CoolProp (version 6.4.2dev) should return the same results in pressure calculations up to the last significant digit. A script in the Python language is

Table 3.8. Data points at equimolar (0.5/0.5) composition for EOS validation

$i-j$	T/K	$\rho/\left(\text{mol dm}^{-3}\right)$	p/Pa
^{4}He − Ne	200.0	10.0	18 430 775.292 600 896
^{4}He − Ar	200.0	10.0	17 128 034.388 362 616
Ne − Ar	200.0	10.0	15 905 875.375 781 253
^{4}He − N_2	200.0	10.0	17 996 716.424 240 347

provided Appendix C in which calculations with CoolProp reproduce exactly the values in Table 3.8. The fluid files are also provided in text form and loaded at runtime. The calculated values in REFPROP 10.0 deviate by 10^{-3} Pa due to truncation of the reducing density for argon after converting from kg m^{-3} to mol dm^{-3}.

3.8 Conclusions from the EOS development

All of the presented equations of state show satisfactory performance in single-phase and at the phase envelope for pressures up to $10-20$ MPa, which covers most of the engineering applications. For higher pressures, if the experimental data is available, the performance of the equations decreases. However, the error remains within 5% margin for the ρpT data and within 10% margin for the speed of sound data. Since the experimental data is only available for these two single-phase properties, the conclusions on accuracy of the equations cannot be easily extended to calculations of, e.g., the isobaric specific heat or the enthalpy change. In order to perform a complete cryogenic process cycle design with known uncertainty of the equation of state, additional measurements of, e.g., the isobaric heat capacity are necessary.

The results obtained in this work, as well as the recent work performed by A. Aasen *et al.* show that the simple mixing rule, such as the Lorentz-Berthelot mixing rule,[120,121] can be successfully applied to quantum fluids. The quantum-corrected cubic equation[22] and the Feynman-Hibbs-corrected equation for Mie fluids[32] may be faster to develop as the optimization process requires only a few parameters to be fitted. The multiparameter empirical equation of state from this work seems to provide the most accurate description at the phase envelope. The single-phase properties are not compared as the publications on cubic and SAFT equations do not discuss their performance in single-phase.

The orthogonal error is helpful for the performance validation in the phase envelope calculations since it provides the error values for all the equilibria data points, unlike the standard pressure-composition error metric. The orthogonal metric can also be considered a criterion for a single-objective optimization. It may contribute to finding a global minimum of the multiparameter space and obtaining the desired performance of an equation in the phase equilibria calculations. Two weights, w_{xy} and w_p, are applied to the metric, defined in Eq. (3.28), forming the dew- and bubble-line contributions to the objective function:

$$\begin{cases} \mathrm{err}_x^{\mathrm{vle}} = \sqrt{w_{xy}\left(x_{\mathrm{d}} - x_{\mathrm{c}}^{\mathrm{min}}\right)^2 + w_p\left(\ln\left(\hat{p}_{\mathrm{d}}\right) - \ln\left(\hat{p}_{\mathrm{c,x}}^{\mathrm{min}}\right)\right)^2} \\ \mathrm{err}_y^{\mathrm{vle}} = \sqrt{w_{xy}\left(y_{\mathrm{d}} - y_{\mathrm{c}}^{\mathrm{min}}\right)^2 + w_p\left(\ln\left(\hat{p}_{\mathrm{d}}\right) - \ln\left(\hat{p}_{\mathrm{c,y}}^{\mathrm{min}}\right)\right)^2} \end{cases}. \tag{3.29}$$

The weights, w_{xy} and w_p, allow to compensate for unequal influence of composition errors compared to the reduced pressure errors in the sum of squares calculations:

$$\mathrm{SSQ}^{\mathrm{vle}} = \sum_{i=1}^{N} \mathrm{err}_{x,i}^{\mathrm{vle}} + \sum_{i=1}^{N} \mathrm{err}_{y,i}^{\mathrm{vle}}, \tag{3.30}$$

where vle marks all possible equilibria calculations: vapor-liquid, gas-gas, liquid-liquid, or any other. Additionally to the sum of squares defined above, the weighted single-phase errors are calculated conventionally, as defined in Eq. (3.19). The total sum of squares is the sum of the two:

$$\mathrm{SSQ} = \sum_{i=1}^{N_{\mathrm{vle}}} \mathrm{err}_{x,i}^{\mathrm{vle}} + \sum_{i=1}^{N_{\mathrm{vle}}} \mathrm{err}_{y,i}^{\mathrm{vle}} + \sum_{i=1}^{N_\rho} W_{\rho,i} F_{\rho,i}^2 + \sum_{i=1}^{N_w} W_{w,i} F_{w,i}^2 + \sum_{i=1}^{N_{\mu_{\mathrm{JT}}}} W_{\mu_{\mathrm{JT}},i} F_{\mu_{\mathrm{JT}},i}^2. \tag{3.31}$$

The single-phase experimental data available for the fluid mixtures considered in this work is limited to density, speed of sound, and the Joule-Thomson coefficients. Therefore, the sum of squares defined above is a function of these three properties. However, any other thermodynamic property can be analogously used to fit the equation to data.

Various stochastic and deterministic algorithms can be used, among which the Nelder-Mead method and differential evolution are tested and explored in more detail.[122–124]

Deterministic methods require a guess value to start minimization. The parameters from an existing EOS used as the starting values allow to successfully decrease the single-objective SSQ function and minimize deviations between the EOS and experimental data. Unfortunately, as discussed in Sec. 3.2.3, constraints are necessary to ensure the correct slope and curvature of the isolines. Since they are not implemented, the SSQ decreases over the iterations but the curvature of the isolines becomes incorrect.

Undoubtedly, the orthogonal metric has potential in EOS development. However, its correct implementation requires valid constraints applied on the slope and curvature of the isolines, which for the moment are missing in Eq. (3.31). Additional difficulty with the stochastic minimization is the sensitivity of the equilibria tracing algorithm to the departure function parameters. Initializing the stochastic algorithm, e.g., differential evolution with a random guess for both the reducing and departure functions, leads to repetitive failures in tracing the phase equilibria. Over the generations, many solutions are failures, which prevents the algorithm from calculating the orthogonal error and converging reliably.

Further work on the algorithm, and constraints, in particular, is necessary, but the discussed logic is a promising approach on the way to automatic EOS development.

4 Isenthalpic Joule-Thomson coefficient measurements

A limited number of experimental data is found in the literature for the mixture of ^{4}He − Ne at cryogenic temperatures. Fig. 3.3 and Table A.1 show no data available in the single-phase region for 50 – 230 K temperature range. This region overlays with the equation applicability for designing the precooling cycles of the next-generation scientific instruments, e.g., fusion reactors and particle accelerators.[3] Therefore, the equation performance should be confirmed experimentally, so the complete thermodynamic surface is validated and the equation becomes a well-grounded source of properties in broad $p-T-x$ space.

In this work, the measurements of the Joule-Thomson coefficient are discussed for temperature between 50 and 100 K and pressure up to 10 MPa. This $p-T$ region is chosen based on the interest of the process cycle engineering.

Compared to other thermodynamic properties, the isenthalpic Joule-Thomson coefficient, μ_{JT} has historically shown lower measurement accuracy. However, the experimental setup necessary for its acquisition can be simple and accessible.

This chapter describes the thermodynamics behind the Joule-Thomson (JT) coefficient and its meaning for the equations of state development. It reviews the literature on past measurements of the Joule-Thomson coefficient. Two measurement methods are presented, their advantages and shortcomings are discussed. One is chosen and adapted to the needs of this work.

4.1 Thermodynamic determination of the Joule-Thomson coefficient

The *Joule-Thomson effect* describes the temperature change of a real gas or liquid when throttled through a porous plug, a valve, or a capillary at constant enthalpy. The effect

is characterized by the *Joule-Thomson coefficient*, which is the thermodynamic quantity that measures a differential temperature change of a fluid with a differential pressure change at constant enthalpy and composition

$$\mu_{\mathrm{JT}} = \left.\frac{\partial T}{\partial p}\right|_{h,\bar{x}}, \tag{4.1}$$

where T is the temperature in K, p is the pressure in Pa, h is the specific enthalpy in J kg^{-1}, and $\bar{x}$ is the molar composition vector. In order to measure the JT coefficient, the fluid is maintained at constant temperature and pressure and throttled under steady-flow conditions into a lower-pressure region. The JT coefficient can be positive, which corresponds to a fluid temperature decrease in the throttling process, or negative, which corresponds to its temperature increase.

In the Joule-Thomson transformation, the enthalpy,

$$H = U + pV, \tag{4.2}$$

remains constant. In the equation above, U is the internal energy of a fluid, p is the pressure, and V is the volume.

The Joule-Thomson coefficient can be derived from the fundamental equation of thermodynamics, $\mathrm{d}H = T\mathrm{d}S + V\mathrm{d}p$ and it can be expressed as

$$\mu_{\mathrm{JT}} = \frac{1}{c_{\mathrm{p}}}\left(T\left.\frac{\partial v}{\partial T}\right|_{p} - v\right), \tag{4.3}$$

where c_{p} is the specific heat in J (kg K)$^{-1}$ and v is the specific volume in m^3 kg^{-1}.

Since $v = RT/p$ for ideal gas, the derivative $(\partial v/\partial T)_p$ simplifies to $v/T = R/p$. Therefore, the above, substituted into Eq. (4.3) results in $\mu_{\mathrm{JT}} = 0$ for ideal gas. There is no Joule-Thomson effect in ideal gas because there are no interactions – no attraction and no repulsion. In this perspective, the Joule-Thomson coefficient is an image of the interactions. However, compared to the compressibility factor or the virial coefficients this image is somewhat distorted. At the limit of zero density, a real gas is characterized by $Z = 1$ and $B = C = 0$ but $\mu_{\mathrm{JT}} \neq 0$.

The Joule-Thomson coefficient for a gas obeying the van der Waals equation of state can be derived from the virial equation approximation for the van der Waals gas[125]

$$\mu_{\mathrm{JT}} = \frac{\frac{2a}{RT} - b}{c_{\mathrm{p}}} + \ldots, \tag{4.4}$$

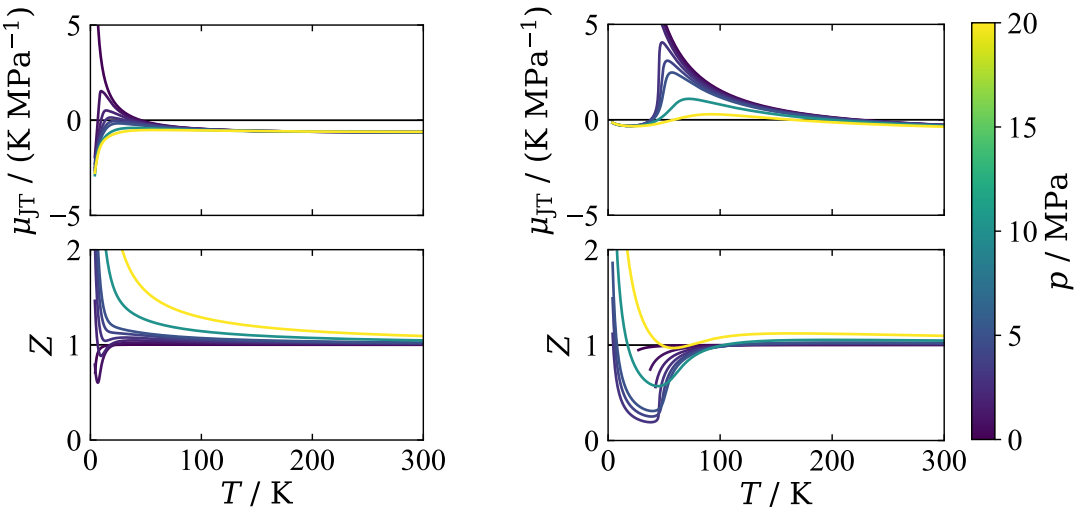

(a) helium–4 (b) neon

Fig. 4.1. Joule-Thomson coefficient and compressibility factor for pure helium–4 and pure neon, calculated with CoolProp.[2]

where a is the measure of the average attraction between particles and b is the co-volume or the repulsive term, as described in Sec. 2.2.3.

For low temperatures, when $T \to 0$, the Joule-Thomson coefficient can be, therefore, approximated with $2a/\left(c_p RT\right) + \ldots$. In contrast, for very high temperatures, it can be approximated with $-b/c_p + \ldots$ With these relations, it can be concluded that at low temperatures, the inter-molecular attraction is the most significant interaction. Whereas, at high temperatures, the repulsive force dominates. It has to be emphasized that the analysis above serves only to understand the Joule-Thomson phenomenon. In reality, a very cold gas also observes a negative Joule-Thomson coefficient as later shown with the inversion curves – lines in $p-T$ space at which μ_{JT} changes signs. When a real gas expands at low temperatures inside its inversion curve, the average distance between molecules increases. Since the molecules attract each other, this process requires energy. In the adiabatic transformation, i.e., the Joule-Thomson transformation, the only source of energy is the internal energy of the gas itself. Therefore, the temperature has to decrease in a real gas.

The compressibility factor, Z, is the ratio of pV of a real gas to pV of ideal gas at the same temperature. At low temperature, Z and pV increase as the gas expands, resulting in a positive μ_{JT}. At high temperatures, Z and pV decrease as the gas expands. If they decrease enough, the Joule–Thomson coefficient is negative. Both thermodynamic properties, μ_{JT} and Z, measure deviations of a real gas behavior compared to ideal gas.

Fig. 4.1 shows the Joule-Thomson coefficient and the compressibility factor for pure

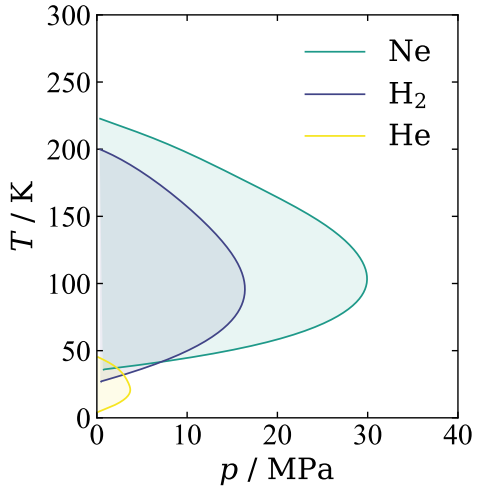

Fig. 4.2. Inversion curves for the only fluids with negative Joule-Thomson coefficients at ambient conditions. μ_{JT} is positive in colored regions.

helium and neon. It is visible that the lower the pressure and the higher the temperature, $\mu_{JT} \to 0$ and $Z \to 1$. That is where both helium and neon can be treated as ideal gas. At low temperature and high pressure, the ideal gas approximation is no more valid. It is important to emphasize that even in normal conditions, $\mu_{JT} \neq 0$ for neither of the fluids.

Both helium–4 and neon have the particularity of increasing their temperature when throttled from ambient temperature in the JT process. This phenomenon is visible for both gases in Fig. 4.1, where $\mu_{JT} < 0$ at 300 K independent on the pressure. Fig. 4.2 also shows this particularity with the use of inversion curves plotted in $p - T$ space. These curves are the lines on which μ_{JT} changes sign from positive – inside to negative – outside. For neither of the fluids, the positive μ_{JT} region reaches 300 K. The only other fluid experiencing similar behavior is hydrogen.[126] Those three fluids can, of course, experience cooling in the JT isenthalpic transformation but only when expanding from inside their Joule-Thomson *inversion temperatures*. This specific temperature depends on the expansion starting pressure, the nature of the fluid and occurs when the isenthalpic line is flat in the $p - T$ space – when $\mu_{JT} = 0$. Geometrically, this change of a real gas behavior indicates a change of slope of the isenthalpic lines from positive, when $\mu_{JT} = (\partial T/\partial p)_{h,\bar{x}} > 0$ to negative, when $(\partial T/\partial p)_{h,\bar{x}} < 0$.

The Joule-Thomson coefficients calculated from the virial, Eq. (2.13) or the Benedict-Webb-Rubin equation of state, Eq. (2.17) deviate from the experimental measurements by an inexplicably high value.[127] Modern equations of state, such as the empirical equation explicit in Helmholtz energy, Eq. (3.1) do not show this behavior. They can yield results coherent with measured Joule-Thomson coefficients, as discussed in Sec. 4.2.

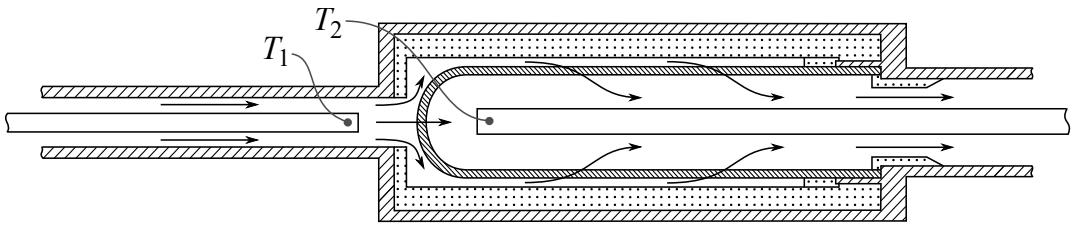

Fig. 4.3. One of the versions of the radial flow apparatus used by Roebuck *et al.*[128–133]

Therefore, if measured accurately, the JT coefficient can be a useful property for the equations of state validation. Moreover, its definition from Eq. (3.14) shows that it comprises almost all the residual Helmholtz energy first and second derivatives, except for $\alpha^{\mathrm{r}}_{\tau}(\delta,\tau,\overline{x}) = (\partial\alpha^{\mathrm{r}}/\partial\tau)_{\delta,\overline{x}}$. This definition makes the Joule-Thomson coefficient, next to the speed of sound, a good property to verify the equation behavior.

4.2 Literature review for the JT coefficient

Most of the research on the Joule-Thomson coefficient measurements in fluids was performed fifty to one hundred years ago. Extensive work on this topic was done by the team of J. R. Roebuck at the University of Wisconsin.[128–133] In the course of their studies, they developed the radial flow apparatus shown in Fig. 4.3, where a cylindrical-shaped porous material imposed a small pressure drop. Two thermometers were placed directly in the fluid before and after the porous plug, not impacting the temperature measurements by additional thermal conductivity. They measured the Joule-Thomson coefficients at ambient temperatures for air; and at low temperatures for helium, argon, nitrogen, and carbon dioxide. Limited uncertainty discussion concludes that the results for nitrogen differ from μ_{JT} data, calculated from compressibility factors[134] by 0.5% to 2.5%. However, the very accurate equation of state for pure nitrogen shows deviations in the order of 10% from measurements.[53] Roebuck *et al.* are the only authors to measure the Joule-Thomson coefficient at cryogenic temperatures. However, as shown later, the consistency and accuracy of their measurements decrease significantly when moving away from the ambient temperature.

R. C. King, J. H. Potter, and M. J. Levy[135,136] used an experimental setup similar to the Roebuck's and measured the JT coefficient in nitrogen with low Δp imposed by the axial-flow porous plug. The authors measured the JT coefficient only at above-ambient temperatures and pressures not exceeding 1 MPa.

More extensive work on the Joule-Thomson coefficient measurements for propane and n-butane was performed at the California Institute of Technology and is described in the

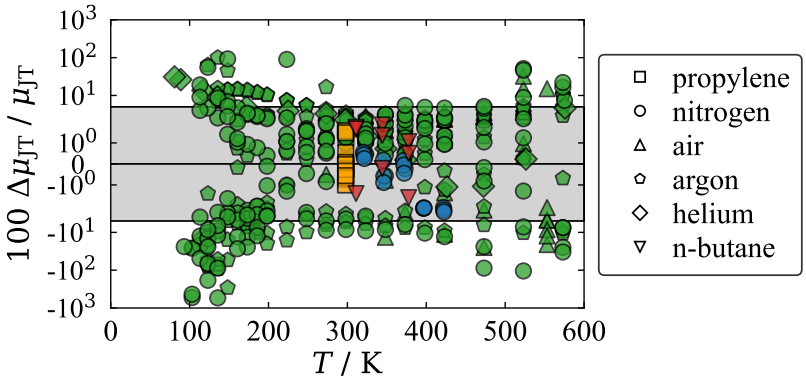

Fig. 4.4. Relative deviation of existing experimental data from EOS. Grey rectangle is the ±5% band. Colors vary for authors: green - Roebuck *et al.*, red - Smith, blue - Potter *et al.*, orange - Bier *et al.* A single outlier for nitrogen from Roebuck and Osterberg with deviation above 10^4% is not shown. A complete reference list for measurements and EOS for each fluid is available in Table 4.1.

Ph.D. thesis of R. L. Smith.[137] The author measured the JT coefficients in an axial-flow setup, similar to the Roebuck's for pressures up to 0.5 MPa and above ambient temperatures. The reported maximal relative error is equal to 1.5% and accurately corresponds to deviations calculated with the pure fluid Helmholtz EOS, shown in Table 4.1.

K. Bier, G. Ernst, and G. Maurer measured the Joule-Thomson coefficient values for propylene with a throttling valve.[138] These measurements at ambient temperature were somewhat subsidiary to the measurements of the isobaric specific heat. The authors reported 1.5% measurement uncertainty for μ_{JT}, which remains in agreement with deviations calculated from the pure fluid EOS.

The comparison of the μ_{JT} data found in literature with existing and accurate EOS explicit in Helmholtz energy is presented in Fig. 4.4 and Table 4.1. The Average Absolute Deviation for the experimental data set of measured property y is calculated as

$$\mathrm{AAD} = \frac{100}{N}\sum_{i}^{N}\left|\frac{y_{\mathrm{EOS},i} - y_{\mathrm{d},i}}{y_{\mathrm{EOS},i}}\right|. \tag{4.5}$$

In contrary to the analysis performed with Eq. (3.25), this time, the equations of state are treated as the reference values, and the measurement deviations are estimated against those accurate EOS for pure fluids. The gray area in Fig. 4.4 shows ±5% deviations of data compared to equations. 83.1% of all points are within ±5% of values calculated with EOS and 88.4% within ±10%. The 5% deviation obtained for most points shows that the Joule-Thomson coefficient can be measured with similar precision as the c_p or c_v, the caloric properties necessary to constrain the EOS behavior in single-phase. However, it cannot approach the precision of the speed of sound or density measurements (0.02%

Table 4.1. Deviations of existing experimental data for μ_{JT} from Helmholtz energy EOS

measurements	fluid (EOS)	$\max\left(\frac{\Delta\mu_{JT}}{\mu_{JT}}\right)$/%	AAD[a]/%	$n\left(\frac{\Delta\mu_{JT}}{\mu_{JT}} \geq 5\%\right)$[b]
Bier *et al.*[138]	propylene[142]	1.58	0.62	0/12
Potter *et al.*[135,136]	nitrogen[53]	2.87	1.20	0/15
Roebuck[128]	air[143]	32.29	4.28	9/63
Roebuck, Osterberg[129]	helium[44]	30.99	6.91	4/15
Roebuck, Osterberg[130]	argon[52]	290.10	12.29	57/134
Roebuck, Osterberg[131]	nitrogen[53]	539.24	19.61[c]	56/163
Smith[137]	n-butane[144]	1.85	1.27	0/9

[a] Average absolute deviation (AAD) of data set from EOS, calculated with Eq. (4.5).
[b] Number of measurement points with absolute deviation from EOS above 5%.
[c] Single outlier with deviation above 10^4% not taken into account.

error at easily accessible pressure and temperature[139–141]). When comparing the JT measurements against the equations at temperatures below 200 K, only 34.3% of data are within ±5% and 48.2% within ±10%. However, considering the advancements in cryogenic measurement techniques, the Joule-Thomson coefficient can be measured with uncertainties comparable with the specific heat.

Even if the temperature and pressure are measured with higher relative uncertainties, compared to, e.g., time which is used to calculate the speed of sound in fluids,[140,141] the experimental setup necessary to obtain the Joule-Thomson coefficients is simpler.

Part of the measurement sets, presented in Table 4.1, show coherent deviations from accurate EOS compared to the uncertainty values claimed by the authors. On the one hand, these measurements are characterized with AAD below 1.5%. On the other hand, they were performed at ambient – and above ambient temperatures. Deviations of the existing Joule-Thomson coefficient values, measured at cryogenic temperatures, are more significant when compared to EOS and, in the worst case, reach 50-70%, excluding the outliers.

4.3 Measurement methods

According to Smith,[137] the total derivative of temperature with respect to pressure can be described as

$$\left.\frac{\mathrm{d}T}{\mathrm{d}p}\right|_{\text{path}} = \left.\frac{\partial T}{\partial p}\right|_{h} + \left.\frac{\partial T}{\partial h}\right|_{p} \left.\frac{\mathrm{d}h}{\mathrm{d}p}\right|_{\text{path}} . \tag{4.6}$$

From a definition of the specific heat capacity, the equation above becomes:

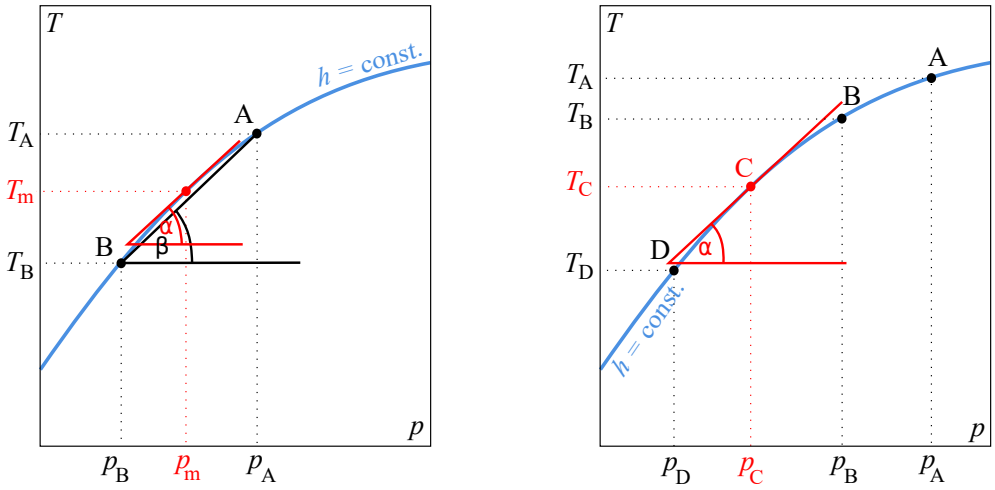

(a) Small $\Delta p_{(a)} = p_A - p_B$ measurements (b) Large $\Delta p_{(b)} = p_A - p_D$ measurements

Fig. 4.5. Schematic representation of two methodologies for the JT coefficient measurement with $\Delta p_{(a)} << \Delta p_{(b)}$, black dots representing the measurement points, and red dot representing the point at which the coefficient is to be defined.

$$\left.\frac{\mathrm{d}T}{\mathrm{d}p}\right|_{\text{path}} = \left.\frac{\partial T}{\partial p}\right|_{h} + \frac{1}{c_\text{p}} \left.\frac{\mathrm{d}h}{\mathrm{d}p}\right|_{\text{path}}. \tag{4.7}$$

If the energy is conserved in the system, the potential energy change is negligible, and no work is done on or by the system, the law of conservation of energy simplifies to:

$$\frac{\dot{Q}}{\dot{m}} = \mathrm{d}h + \mathrm{d}e_\text{k}. \tag{4.8}$$

Substituting Eq. (4.8) into Eq. (4.7) as the enthalpy change, the Joule-Thomson coefficient can be represented as the measured path-coefficient with two correction factors:

$$\mu_\text{JT} = \left.\frac{\partial T}{\partial p}\right|_{h,\overline{x}} = \left.\frac{\Delta T}{\Delta p}\right|_{\text{path}} - \frac{\dot{Q}}{\dot{m} c_\text{p} \Delta p} + \frac{\Delta e_\text{k}}{c_\text{p} \Delta p}, \tag{4.9}$$

where $\overline{x}$ is the mixture mole fraction vector, $\dot{Q}$ is the heat exchanged by the fluid in W, c_p is the average isobaric heat capacity in J (kg K)$^{-1}$, and Δe_k is the specific kinetic energy change in the throttling process in J kg^{-1}.

The Joule-Thomson coefficient can be determined directly from incrementally small pressure drop and respective temperature change, as done by Roebuck *et al.*,[128–133] Smith,[137] and Potter *et al.*[135,136] in the past. It can also be measured indirectly, as an integrated coefficient when the pressure drop is significant. Both methods have their advantages and limitations.

The first measurement method, well explored in the past, relies on small pressure changes

from which the isenthalpic Joule-Thomson coefficient can be directly derived. The smaller the pressure change, the more the measured angle β approaches the actual angle of the isenthalpic line α, as presented in Fig. 4.5a. Small pressure changes are imposed by small flow rates, which increase the thermal loss influence by decreasing the $\dot{m}$ and Δp in the denominator of the first correction term in Eq. (4.9). On the one hand, the method does not take advantage of the instrument accuracy, and the instrument errors significantly impact results. On the other hand, the kinetic energy change in the transformation can be neglected.

With a large pressure drop, the influence of the instrument inaccuracy decreases. Unfortunately, large Δp imposes large ΔT and increased thermal transfer, $\dot{Q}$. Large Δp also imposes large kinetic energy change Δe_{k}, as presented in Eq. (4.9), and therefore non-isenthalpic conditions. Additionally, the measured $p - T$ pairs are the Joule-Thomson integral values, and the differential values must be calculated posterior to the measurements. A schematic representation of this approach is presented in Fig. 4.5b, where multiple experimental points, marked in black, are measured. A blue isenthalpic line represents the integrated values of measured JT coefficient, from which, a local coefficient in $(p_{\mathrm{C}},\ T_{\mathrm{C}})$ point is calculated as $\tan\alpha$.

One of the critical problems, reported in the past, was the inability to keep the inlet conditions, especially the temperature, stable. With limitations of both methods and advancement in the measurement hardware and techniques, the large pressure drop measurements have been chosen in this work because of the simplicity of the test setup implementation and the potential of decreasing the measurement uncertainty with the accuracy of today's equipment. Additionally, despite its potential and usefulness, few results are obtained with this measurement method, which increases its attractiveness if successful.

4.4 Experimental setup design

Taking advantage of the existing equation of state for the helium-neon mixture, the experiment is planned by choosing regions of the highest expected accuracy within the regions of unavailable other experimental data. It is essential to notice, however, that the equations of state described in Chapter 3 do not discuss the correlations allowing for the transport properties calculations. Without the auxiliary equations, neither the viscosity nor the thermal conductivity is accurately calculated, hence the mole fraction-weighted transport properties are used. The apparatus is designed, and the equipment is chosen based on the results obtained with the thermophysical properties of fluids from

(a) Closed cycle with warm compressor (b) Open cycle with high-pressure storage

Fig. 4.6. Schematically represented cycles for the Joule-Thomson coefficient measurements with flow restriction, two pressure sensors, and two temperature sensors.

CoolProp[2] and REFPROP,[116] and the cryogenic properties of solids from CryoComp.[145]

Different approaches in choosing the flow rate and the pressure drop values should be taken according to the experiment structure. The fluid cycle can be either closed, constructed around a warm, high Δp compressor (Fig. 4.6a), or open, using fluid provided from large volume bottles (Fig. 4.6b). The closed cycle provides repeatability and a long measurement time with a limited amount of fluid used. However, the system complications introduced to minimize gas pollution are critical. To limit the complexity of the measurements, the open cycle is chosen as a base solution for the present work.

4.4.1 Equipment design and choice according to flow and thermal considerations

Imposing the pressure drop

The fluid has to experience a pressure drop in order to observe its temperature change. It can be provided by an orifice plate, a porous material, or a capillary tube. All solutions can result in the isenthalpic transformation of the fluid, but some show benefits over others.

The flow conditions in an orifice restriction and the necessary calculation procedure are described in the ISO norm 5167-2:2003.[146] The norm describes the pressure drop and the respective temperature change, which is schematically represented in Fig. 4.7. It is visible that the regions of well-established pressure and temperature downstream of the orifice are far from the restriction. More importantly, the actual Δp introduced by an orifice cannot be defined with the pressure reading in the close vicinity of the plate. Turbulent conditions introduce additional irreversibilities, impacting the fluid properties. Despite the orifice plate being a good industrial standard for the mass flow rate measurements, it is decided that it does not fulfill the requirements for the accurate $\Delta p - \Delta T$ measurements.

Another possibility to impose the pressure drop in the flow is a porous plug. Since it has

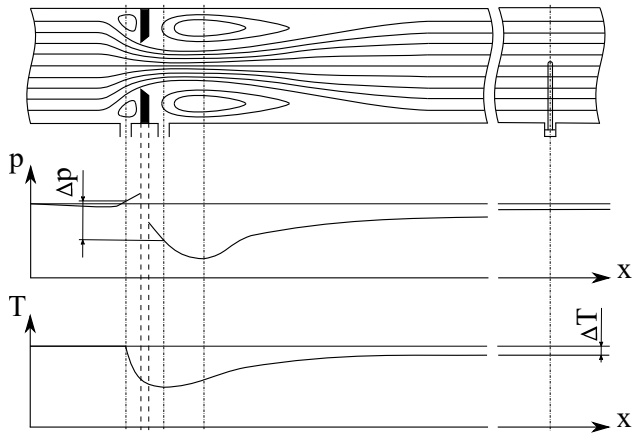

Fig. 4.7. Schematic fluid flow in the proximity of an orifice restriction.

already been used by Roebuck *et al.*,[128–133] Smith,[137] and others, it could be considered as an obvious solution. However, all the authors measured the local Joule-Thomson coefficients with similar cryostat designs and small Δp across the porous plug. Despite the advantages of the technique, such as the homogeneous temperature distribution and the inflow temperature measurements, it is difficult to guarantee the leak-tightness between the two sides of the plug with imposed large pressure drop values. Additionally, the industrial companies in charge of the porous material casting have no commercial off-the-shelf solution for the plug with porosity low enough to provide high Δp for the studied flow rates and sufficient material strength to withstand significant pressure drop values. An attempt was made in this work to design the porous plug assembly with industrially available cylindrical disks. However, the leak-tightness issue was not solved; the design was, therefore, abandoned.

In this work, a large pressure drop is provided to the fluid by a small diameter capillary. The pressure and temperature values are measured at the capillary inlet and outlet. Compared to the orifice plate and the porous plug, the leak-tightness and the pressure drop measurements are not expected to cause any complications. A broad range of capillary diameters and its freely chosen length allow for flexibility in the JT test bench design. A small enough capillary diameter can be chosen, so little gas is consumed per unit time. Choosing a small external diameter is also advantageous for the material strength at high pressures. As a result, the heat loss between the two ends of the capillary decreases with decreasing material cross-section area.

Calculations for the Joule-Thomson transformation in a capillary

The process allowing for the choice of the capillary size is iterative in its length. The pressure drop is defined by the Darcy-Weisbach equation[147]

$$\frac{\Delta p}{l} = f \, \frac{\rho}{2} \, \frac{\overline{u}^2}{D_\mathrm{h}}, \tag{4.10}$$

where ρ is the fluid density in kg m^{-3} averaged over the unitary length l, $\overline{u}$ is the mean flow velocity in m s^{-1}, f is the Darcy friction factor, D_h is the pipe hydraulic diameter in m. For a circular pipe $D_\mathrm{h} = D$, the Darcy friction factor is defined by the Colebrook-White equation[148]

$$\frac{1}{\sqrt{f}} = -2 \log \left(\frac{\epsilon}{3.7 D_\mathrm{h}} + \frac{2.51}{\mathrm{Re}\sqrt{f}} \right), \tag{4.11}$$

where ϵ / D_h is the relative pipe roughness and Re is the Reynolds number. Since the Colebrook-White equation defines the friction factor implicitly, it has to be solved iteratively. A fast and well suited algorithm for this type of continuous problem is the fixed-point iteration $x_{n+1} = f(x_n),\ n = 0, 1, 2, \ldots$.[149]

If the flow in a pipe is laminar, the friction factor is proportional to the reciprocal Reynolds number $f = 64\ \mathrm{Re}^{-1}$ and the Eq. (4.10) simplifies to

$$\frac{\Delta p}{l} = \frac{128}{\pi} \, \frac{\mu \dot{V}}{D^2}, \tag{4.12}$$

where μ is the dynamic viscosity of the fluid in Pa s and $\dot{V}$ is the volumetric flow rate in m^3 s^{-1}.

The capillary imposing the pressure drop is helical in the selected setup due to its length and the cryostat geometrical constraints. The Dean number, an additional factor increasing the Δp in a curved capillary, is defined.[150] It shows that the additional pressure drop is insignificant for the chosen geometry, and the curving radius being three orders of magnitude larger than the internal capillary diameter.

With Equations (4.10) and (4.11) the pressure p_out at the outlet of the unitary length is calculated. The temperature of a fluid expanding in the isenthalpic transformation is a function of inlet enthalpy and outlet pressure

$$T^h_\mathrm{out} = T\left(p_\mathrm{out}, h\left(p_\mathrm{in}, T_\mathrm{in}\right)\right). \tag{4.13}$$

However, the actual outlet temperature can be influenced by a transformation of the kinetic energy of translation to the kinetic energy of vibration, changing the temperature of the fluid. If a fluid undergoes a transformation, no heat is exchanged to or from the surroundings, no work is done on or by the surroundings, and the potential energy change is negligible ($dE_\mathrm{p} = 0$), the first law of thermodynamics simplifies to

$$\Delta E_{\mathrm{k}} \equiv \frac{m\Delta u^2}{2} = m\Delta h, \tag{4.14}$$

where ΔE_{k} is the kinetic energy change of the fluid in J. If the mass is conserved, the Eq. (4.14) can be reformulated:

$$h_{\mathrm{in}} + \frac{u_{\mathrm{in}}^2}{2} = h_{\mathrm{out}} + \frac{u_{\mathrm{out}}^2}{2}, \tag{4.15}$$

where h_{in}, u_{in} and h_{out}, u_{out} are the fluid specific enthalpy in J kg^{-1} and velocity values in m s^{-1} before and after the transformation respectively. The above equation states that the throttling process is truly isenthalpic only when no heat is exchanged with the surroundings and the kinetic energy of translation is not converted into the kinetic energy of vibration. The latter is only true when the fluid velocity change is negligible. According to the enthalpy definition:

$$h = c_{\mathrm{p}} T + \frac{p}{\rho}(1 - \beta T), \tag{4.16}$$

where $\beta = 1/v\,(\mathrm{d}v/\mathrm{d}T)_p$ is the isobaric expansion coefficient. In the first approximation, assuming $\beta = 1/T$, the enthalpy simplifies to $h = c_{\mathrm{p}} T$ and the corrected temperature in an isenthalpic transformation can be calculated as:

$$T_{\mathrm{out}} = T_{\mathrm{out}}^h - \frac{u_{\mathrm{out}}^2 - u_{\mathrm{in}}^2}{2c_{\mathrm{p,out}}}. \tag{4.17}$$

For the highest achievable pressure drop, the kinetic energy of translation is expected to convert into the kinetic energy of vibrations of molecules and results in the temperature change of fluid. If the error introduced by performing the measurements in non-isenthalpic conditions is to be kept below, e.g., 0.5%, the reduced pressure drop $\Delta p/\Delta p_{\mathrm{max}}$ should be kept below 0.9. As a result, if a fluid expands from, e.g., 10 MPa, the expansion is isenthalpic with 0.5% margin in T_{out}, only when performed down to 1.1 MPa.

With the outlet temperature calculated from Eq. (4.17), the capillary made from 304L stainless steel is assumed to conduct heat from the warm end of its unitary length l to the cold end. The tube is placed in a vacuum on a glass fiber support, which limits the convective and conductive thermal transfer with the environment. The radiation is minimized by a shield, thermally connected with the cold head, and wrapped in multilayer insulation. The capillary is expected to exchange only with the fluid, changing its temperature at the outlet of unitary length from T_{out}^h to T_{out}. The equations for the isenthalpic transformation with conductive heat transfer in the pipe wall are solved

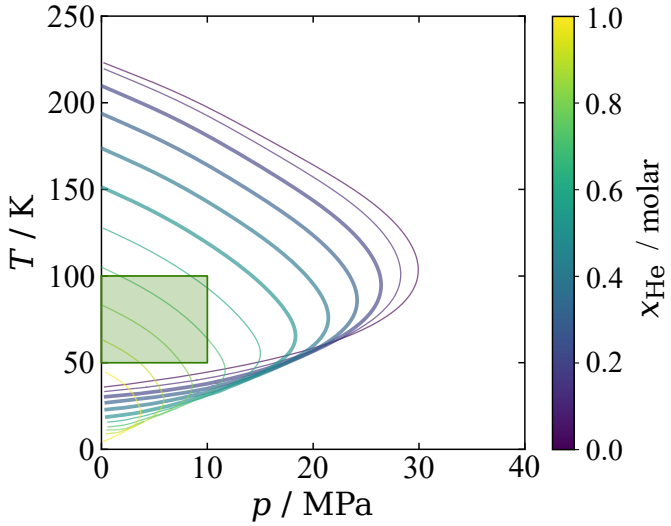

Fig. 4.8. Inversion curves for the ^{4}He − Ne mixture with helium mole fraction, x_{He} as a parameter. The green rectangle marks the target pressure and temperature ranges for the μ_{JT} measurements. Thick inversion curves mark the helium concentration range, $x_{\mathrm{He}} = \langle 0.2, 0.5 \rangle$, for which the Joule-Thomson coefficient is measured in this work.

numerically for T_{out} using standard `scipy.optimize.fsolve` algorithm.[122] The total heat transferred from the inlet to the outlet of the capillary is calculated with the one-dimensional Fourier's law

$$q_{\mathrm{L}} = -k(T)\frac{\mathrm{d}T}{\mathrm{d}L}, \tag{4.18}$$

where $k(T)$ is the 304L stainless steel thermal conductivity in W (m K)$^{-1}$, integrated over the capillary length with variable temperature, and $\mathrm{d}T/\mathrm{d}L$ is the temperature gradient in K m^{-1} with unitary length $\mathrm{d}L = l$.

The equations discussed above allow for determining the region of low measurement error according to the pressure drop, as discussed before. This region of low error is the region of experimental interest for the following work and is shown in the $p - T$ space in Fig. 4.8. It comprises the pressure from 0.1 to 10 MPa, the temperature from 40 to 100 K, and the helium–4 concentration from 20 to 50 mol − %. Following the analysis described above, a case study is performed for various capillary diameters and lengths as a function of inlet conditions ($p_{\mathrm{in}}, T_{\mathrm{in}}$), as presented in Fig. 4.9.

The pressure drop of a mixture in a capillary tube is also composition-dependent. To obtain the same pressure drop, e.g., $p_{\mathrm{in}} - p_{\mathrm{out}} = 10$ MPa − 1.1 MPa at $T_{\mathrm{in}} = 65$ K in ^{4}He − Ne

$$\frac{\dot{m}(x_{\mathrm{He}} = 0.2)}{\dot{m}(x_{\mathrm{He}} = 0.5)} \approx 1.34, \tag{4.19}$$

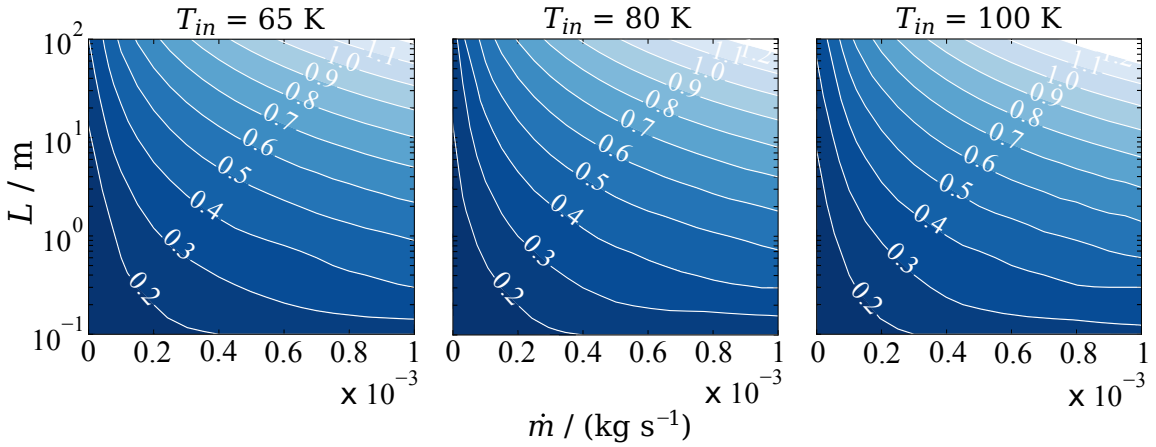

Fig. 4.9. Capillary length calculated for $p_{\text{in}} = 10$ MPa, $p_{\text{out}} = 1.1$ MPa, equimolar composition of ^{4}He — Ne, and internal diameter in mm as a parameter.

that is, 1.34 times higher mass flow rate of the mixture with low helium concentration is necessary to achieve a similar pressure drop in both mixtures.

With an appropriately chosen downstream valve, a single capillary length should allow performing all the measurements.

The smaller the diameter of the capillary, the less gas is consumed in a single measurement. At the same time, the smaller the diameter, the more susceptible to clogging the capillary is. With this constraint in mind, the 0.4 mm internal diameter capillary is chosen as the key component. The external diameter is selected, based on the available capillaries and the requirements coming from material strength for high-pressure use. In order to obtain the large enough pressure drop, the capillary should be at least 6 m long. This length should provide flexible measurement conditions with a flow rate ranging from near-zero to 0.2 g s^{-1}, assuring a long experimental time with an open cycle and few gas bottles used.

$$\begin{cases} D_{\text{int}} = 0.4 \text{ mm} \\ D_{\text{out}} = 1.0 \text{ mm} \\ L \in \langle 6, 10 \rangle \text{ m} \end{cases} \tag{4.20}$$

Choice of the thermodynamic conditions for the experiment

With the mixture inversion curves, presented earlier in Fig. 4.8, and the 1D pressure drop analysis concluded in Fig. 4.10, the thermodynamic conditions for the Joule-Thomson coefficient measurements are chosen.

First, the inversion curves allow to anticipate the gas behavior in the Joule-Thomson

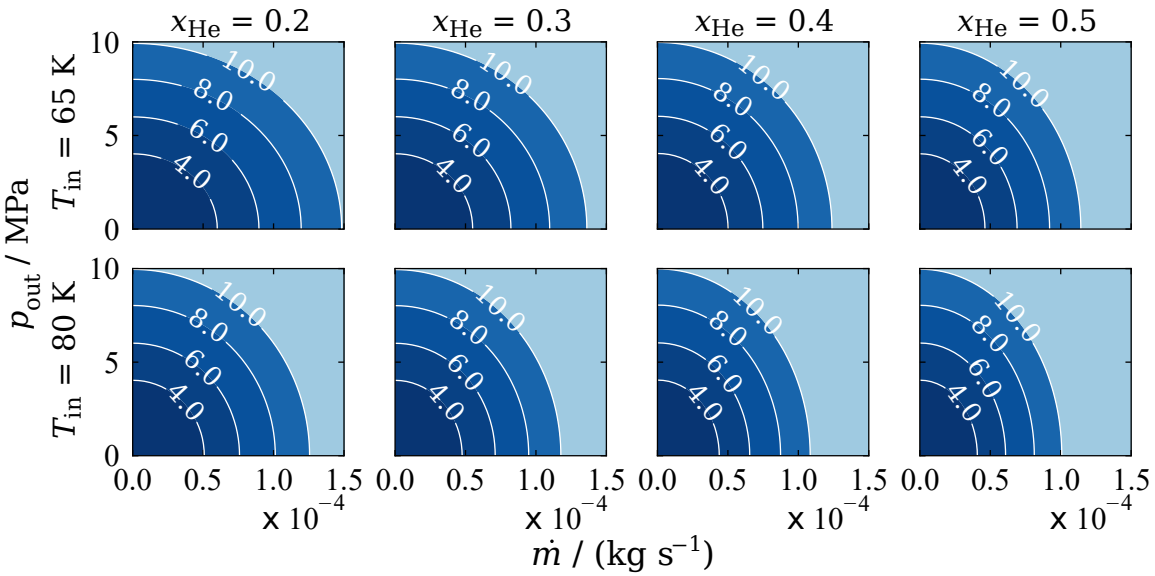

Fig. 4.10. Downstream pressure, p_{out} for 0.4 × 1 mm, 6 m long capillary calculated as a function of the mass flow rate, parametrized with inlet pressures ranging from 4 MPa to 10 MPa, plotted for four mixture compositions x_{He} (columns) and two inlet temperatures T_{in} (rows).

expansions process and choose the $p - T - x$ conditions for measurements with the largest ΔT. In the interest of increasing the experimental accuracy, the measurement points should be distant from the inversion curves, since in their proximity $\Delta T \to 0$, and the uncertainty increases. Thus, the method itself does not allow for precise qualification of the inversion temperatures. However, it allows to confirm or improve the overall equation performance and, as a result, confirm the fluid behavior in the vicinity of the inversion curves. When mixture is helium-rich, the inversion curves pass through the region of experimental interest for $T \in \langle 50, 100 \rangle$ K and $p \leq 10$ MPa, shown in Fig. 4.8. If a large ΔT is to be measured in the expansion process, no measurements are foreseen to be taken for the helium-rich mixture. Therefore, the limit of $x_{He} \leq 0.5$ is set on the helium concentration.

Second, the chosen capillary dimensions from Eq. (4.20) impose the pressure drop and the temperature change. The results for the expected downstream pressure values as a function of the molar composition and the inlet conditions are shown in Fig. 4.10. Those calculations provide insight into the expected mass flow rate necessary to obtain the required pressure drop and allow choosing the auxiliary equipment, such as the valves. Despite the full pressure drop available, there is little interest in performing measurements with full available Δp, as discussed in Sec. 4.4.1. The temperature change for the isenthalpic transformation can be calculated as a function of the absolute pressure. These calculations are performed for already chosen inlet temperature and molar

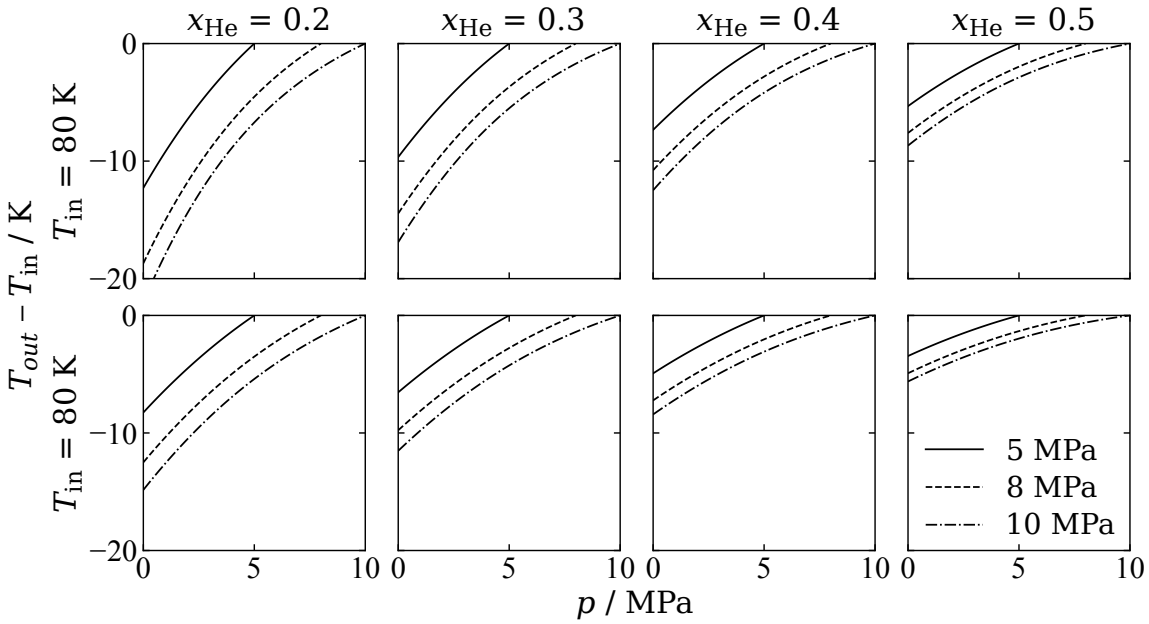

Fig. 4.11. Temperature change as a function of pressure, calculated for two inlet temperature values and four molar compositions with inlet pressure as a parameter.

composition values. From results presented in Fig. 4.11 the simple conclusions can be drawn:

1. The lower the inlet temperature, the higher the temperature drop in the expansion process;
2. The higher the inlet pressure, the lower the pressure drop obtained with the same mass flow rate;
3. Measurements at lower helium concentrations should be more precise since the expected temperature change is larger.

4.4.2 Test bench design

The Process Flow Diagram (PFD) is presented in Fig. 4.12, whereas the full Piping and Instrumentation Diagram (P&ID) is shown in Fig. D.1. The main fluid path consists of a 50 liters volume, where a mixture is stored at high pressure. It is connected to the pressure-reducing valve RV004A and, later, to the 1 U.S. gallon (3.596 liters) buffer volume. The buffer volume is necessary for two reasons. First, it compensates for the pressure instabilities of the reducing valve manual adjustments. Second, the p_{in} at the capillary inlet is dependent on the pressure in the mixture bottle, which decreases with time. This time variation causes a permanent, undesired pressure change at the capillary inlet. Without the buffer volume, the pressure conditions are unstable and must be

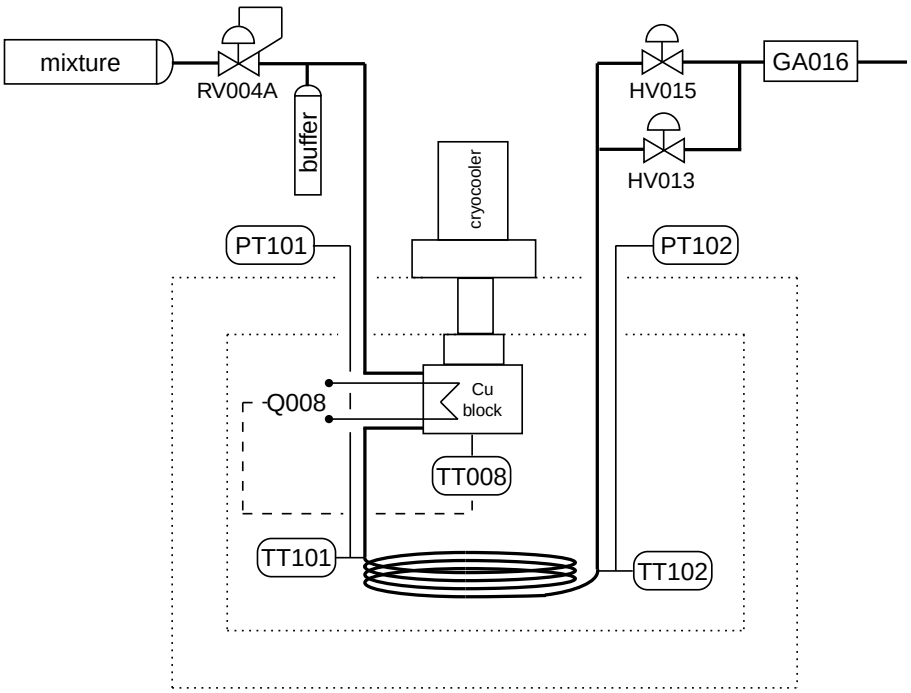

Fig. 4.12. Process flow diagram (PFD) of the Joule-Thomson measurement setup. For P&ID see Fig. D.1.

manually corrected every few seconds, resulting in permanent pressure fluctuations. The buffer smooths out the manual pressure corrections and decreases their frequency from seconds to minutes.

Inside the cryostat, marked with a dashed line, a copper block with a brazed heat exchanger is mounted on the cold head of the Cryomech AL300 cryocooler. It has sufficient capacity to cool down the flow from 300 K to around 40 K and can be regulated with a variable frequency ranging from 40 to 70 Hz. The minimal temperature of the cold head for the zero-load is 20 K. The pressure-reducing capillary is presented in a helical form, and two calibrated Lake Shore Cernox temperature sensors are placed upstream (TT101 measuring T_{in}) and downstream (TT102 measuring T_{out}) of the capillary. The temperature sensors wiring is thermalized at the cold head. PT101 and PT102 are the high accuracy CPT 6100 pressure transducers supplied by Mensor. They measure the capillary upstream p_{in} and downstream p_{out} pressure values.

Two fine-control needle valves HV013 and HV015, are installed in parallel in order to provide a broader range for regulating the downstream pressure p_{out}. A gas analyzer GA016 is placed at the outlet of the system, so its pressure-dependent measurements are always performed at the atmospheric pressure. A complete list of equipment used in the experiment, divided into functional categories, is presented in Table D.1.

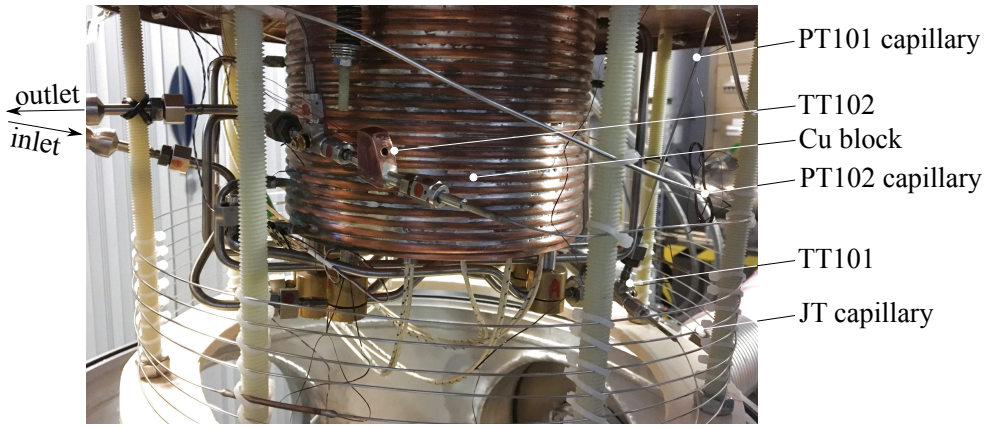

Fig. 4.13. Joule-Thomson expansion capillary and the surrounding hardware. More photos are available in Appendix D.

Temperature measurements

Two thermometers, essential for the Joule-Thomson coefficient measurements: TT101 and TT102 are shown in Fig. 4.13 and are schematically represented in Fig. 4.12. They are calibrated for temperatures ranging from 20 to 325 K (TT101) and 1.4 to 325 K (TT102). These Lake Shore Cernox sensors are chosen based on the expected measurement range to minimize the measurement uncertainty. The uncertainty varies from 11 to 14 mK for measurements from 50 to 100 K. Assuming minimal temperature to be measured equal to 50 K, the respective thermometer uncertainty is equal to ±12 mK. For the highest expected temperature of the ^4He-Ne mixture equal to 100 K, the uncertainty is ±17 mK. When measuring expansion in pure fluids or the $^4He-N_2$ mixture at temperature up to 200 K, a ±32 mK uncertainty is expected.

The above uncertainty values are given without considering the electronic measurement chain. The thermometers are interfaced with CABTR (*Centrale d'Acquisition Basses Températures Rapide*) – a temperature acquisition module, made by CEA/DSBT. All the uncertainty components of the measurement chain are later presented in Table 5.1 and discussed in Sec. 5.2.1.

The inlet thermometer is placed outside the capillary. The outlet thermometer is placed in a copper block in direct contact with the fluid. From the point of view of heat transfer, the most advantageous measurement setup would be to use two in-flow thermometers. However, the technical limitations of the high-pressure measurements with low capillary diameter drives the placement of the thermometers causing a difficult to qualify, systematic error from indirect measurements.

Pressure measurements

A particular effort was put into evaluating the impact of the pressure measurements on final results, however, there is a risk that the systematic error from the pressure taps impacts the measurements. Both the temperature and the pressure uncertainties are discussed in details, together with the results analysis in Sec. 5.2.1 and 5.2.2. In order to achieve the acceptably low measurement errors in μ_{JT}, compared to other thermophysical properties used for the EOS development, the pressure transducers with the highest achievable accuracy are used: $U(p) = 0.01\%$ of full scale with $p_{\max} = 13.7$ MPa.

Gas analyzer for composition measurements

The process gas analyzer BGA244HP manufactured by Stanford Research Systems is a binary gas analyzer that determines gas purity and mixture composition by measuring the temperature and the speed of sound in the gas. The measurements are based on the principle of corresponding states, with scaled fluid properties depending on the intermolecular forces. The analyzer determines the fluid composition with known mixture constituents with an accuracy of 0.1 mol − % by measuring the speed of sound in fluid and calculating the speed of sound in ideal gas:

$$w_0 = \sqrt{\frac{\kappa R T}{M}}, \tag{4.21}$$

where R is the ideal gas constant in J (mol K)$^{-1}$, T is the temperature in K, M is the molar mass in kg mol^{-1}, and $\kappa = c_{\mathrm{p}}/c_{\mathrm{v}} = c_{\mathrm{p}}/(c_{\mathrm{p}} - R)$ is the ratio of heat capacities, calculated from fitted correlations. The speed of sound of ideal gas, w_0, is corrected with empirical factors for viscosity, μ, thermal conductivity, k, second and third virial coefficients, B and C, known for each constituent. These empirical corrections allow to calculate the speed of sound of a real gas:

$$w = w_0 + f(\mu) + f(k) + f(B) + f(C). \tag{4.22}$$

A root-finding algorithm is employed on the calculated value of composition-dependent-corrected speed of sound and the measured value to find the molar composition ranging from 0 to 1. Unfortunately, it is unclear how each empirical correction impacts the calculated speed of sound since the user manual is incomplete, and the company is not willing to share any additional correlation nor fitted coefficients outside of the manual.[151]

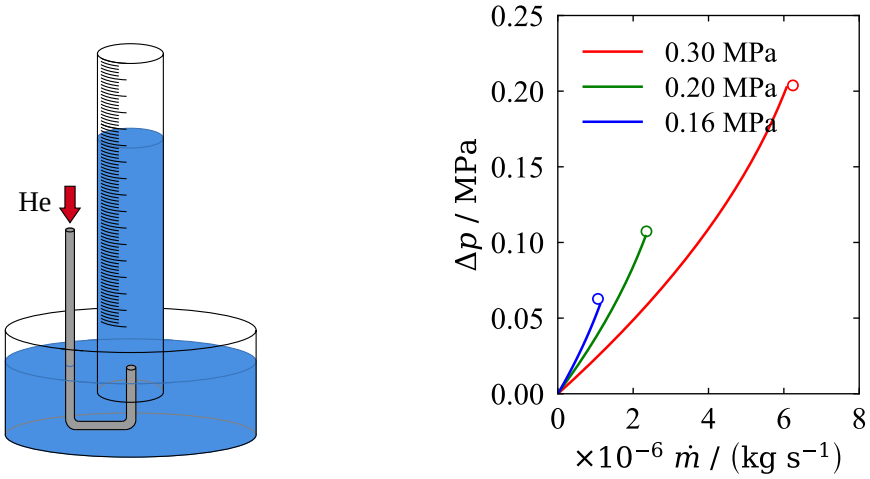

(a) Simple volumetric flow meter for capillary diameter validation.

(b) Mass flow rate calculations for 0.365 mm diameter overlaid with measurements at ambient pressure.

Fig. 4.14. Diameter verification flow meter scheme and measurement results for 2 m long capillary.

Capillary

Le Guellec SAS, the capillary manufacturer, specified the internal capillary diameter to be 0.4 ± 0.05 mm. However, the previous experiences in the laboratory showed that the diameter variation could be more considerable. A 10 m capillary is first assembled from 2 m pieces, brazed together using a 1.4 mm internal diameter capillary. The possible play in the capillary connections can introduce additional local, challenging to quantify pressure drop values. The capillary is tested to qualify the global pressure drop, compared with the design flow rate and the fine control valves accepted range. The tests are performed in a simple test setup at ambient temperature for a single 2 m piece and a complete 10 m long capillary. The only additional element with respect to the nominal test setup necessary for the capillary validation is the in-house made volumetric flow meter mounted at the outlet of the system. It is schematically shown in Fig. 4.14a. The flow measurements are performed with helium–4 and water by measuring the time for gas to fill the closed volume of the graduated cylinder. The helium-water pair is chosen since no single gas has a lower solubility in water than does helium. At 20°C and 1 bar, only 1.5 mg of helium dissolves in 1 kg of water, 13 times less than nitrogen in water and 130 times less than nitrogen in pure ethanol. The error introduced by helium dissolving in water can reach 1.7 mm in the meniscus position, which corresponds to the 2 ml readout error in the given geometry of the graduated cylinder.

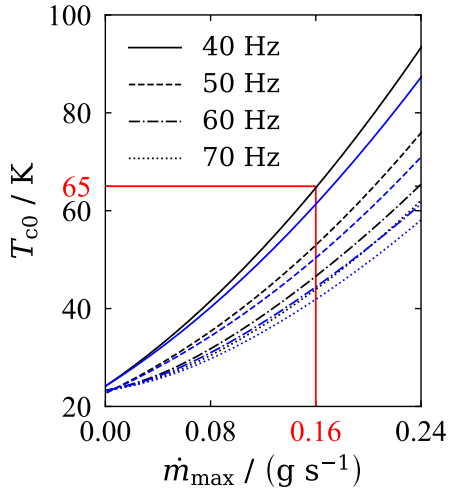

Fig. 4.15. Minimal achievable temperature of AL300 cold head for mass flow rate at 10 MPa cooled from 300 K to 65 K (black) and 80 K (blue).

The volumetric flow is measured for three inlet pressure values. Despite the method being very simple, the volumetric flow measurement error reaches 4% in the worst case. The 2 m long capillary provides the same pressure drop to the fluid as if it was a perfect, 0.365 mm diameter tube, as presented in Fig. 4.14b. Each of the three experimental points is averaged from 8 measurements, and all the measured values are coherent with calculations. It is, therefore, reasonable to use 0.365 mm as the internal capillary diameter in further calculations.

Validation of the 10 m long capillary shows unexpectedly large Δp, corresponding to an equivalent, calculated diameter of 0.24 mm. Therefore, the capillary is cut into two parts (6 and 4 m), and the pressure drop is measured for each of them. It appears that the 4 m piece provides a much more significant pressure drop with a probable singularity existing in the flow. In contrast, the 6 m piece provided the pressure drop expected for 0.365 mm internal diameter. It is decided to only use the 6 m long capillary in the measurements instead of the 10 m one. For this reason, the calculations presented in Fig. 4.10 and later in this work are performed for the length of 6 m.

Cold head

The cryocooler used in the system is the AL300 Gifford-McMahon cold head manufactured by Cryomech. Assuming the maximal pressure drop in the capillary in the order of 10 MPa, the maximal expected mass flow rate can reach 0.16 g s^{-1}, as presented in Fig. 4.10 for $T_{in} = 65$ K and $x_{He} = 0.2$. The cold head should be qualified for these conditions. According to the heat transfer computations and Fig. 4.15, the maximal flow rate can be cooled to the desired temperature of 65 K with cryocooler working at its

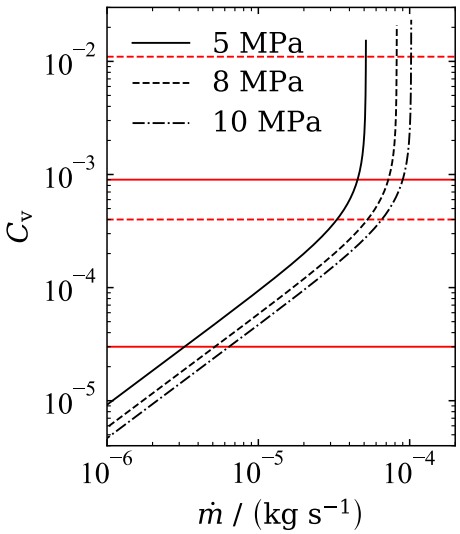

Fig. 4.16. Flow coefficient calculations for downstream valves HV013 and HV015. The horizontal red lines represent the minimal and maximal C_v values for two chosen valves.

minimal, 40 Hz frequency, leaving plenty of margin for higher refrigeration needs. The calculations are based on the cold head qualification performed in DSBT.

Measurement chain

Data from all the sensors in the system is acquired with 1 s time interval through Panorama E2 SCADA software. CABTR, for temperature measurements, is connected through the Modbus GateWay. The pressure sensors and the gas analyzer are directly connected through RS-232 to the Modbus GateWays. The Panorama software incorporates the proportional–integral–derivative controller and a safety thermal switch for the TT008 temperature regulation heaters.

Auxiliary equipment

Additional design choices are necessary to complete the choice of equipment installed on the test bench. The micrometric valves HV013 and HV015 are chosen based on the expected minimal and maximal mass flow rates presented in Fig. 4.10. The flow coefficient is calculated and shown in Fig. 4.16. The flow regions of both valves overlay but do not cover the full spectrum of necessary flow rates making the measurements with minimal pressure drop in the capillary impossible. However, no valve with smaller C_v is found on the market, and the smallest Δp measurements are expected to be less accurate as further discussed.

Additional safety precautions for valves and welds are taken. All components, except the pressure sensors, are tested at 14 MPa, whereas the safety valve SV005 sets the maximal operational pressure to 11 MPa.

4.5 Experimental procedure

Measurements of the Joule-Thomson coefficient in pure fluids and mixtures follow the same experimental procedure. The calculated deviations for pure fluids (nitrogen, argon, and helium) use the EOS as a reference because of high deviations of experimental values reported in the literature.[53,152]

4.5.1 Step-by-step measurement description

The fluid in the experimental setup undergoes the isenthalpic transformation when the inlet enthalpy $h_{\mathrm{in}} = h\,(p_{\mathrm{in}}, T_{\mathrm{in}})$ is constant. By varying the outlet pressure p_{out}, its outlet temperature $T_{\mathrm{out}} = T\,(p_{\mathrm{out}}, h_{\mathrm{in}})$ changes. The following steps are taken in the course of the measurements of a single isenthalpic line:

1. T_{in} value is set at TT101. p_{out} varies in the course of the isenthalpic line measurements what influences the flow rate and, therefore, singular and small adjustments to the T_{in} controller setting are necessary when the p_{out} is set to a new value.
2. p_{in} value is set at PT101 with pressure reducer RV004A. Regular manual adjustments are made every few minutes to compensate for pressure variations in the mixture supply bottle.
3. p_{out} is set at PT102 with either HV013 or HV015 valves, depending on the required pressure drop.
4. T_{out} stabilizes in the course of 15 to 20 minutes after keeping the other three measurement values constant.
5. After the T_{out} stability is reached and all four measurements (p_{in}, p_{out}, T_{in}, and T_{out}) are quasi-constant in the period of 1 minute, the timestamp is noted down for later data extraction. The 1 minute time is evaluated to be long enough since the p_{out} change results in changing T_{out} within few seconds ($t < 10$ s).
6. new p_{out} is set at PT102 by changing the setting at HV013 or HV015 valve.
7. Small adjustment in TT008 setting is necessary to keep the T_{in} reading from TT101 constant, as explained in the first step.

The presented analysis is performed with the helium-nitrogen mixture as a part of the setup validation process before the measurements of the Joule-Thomson coefficient in

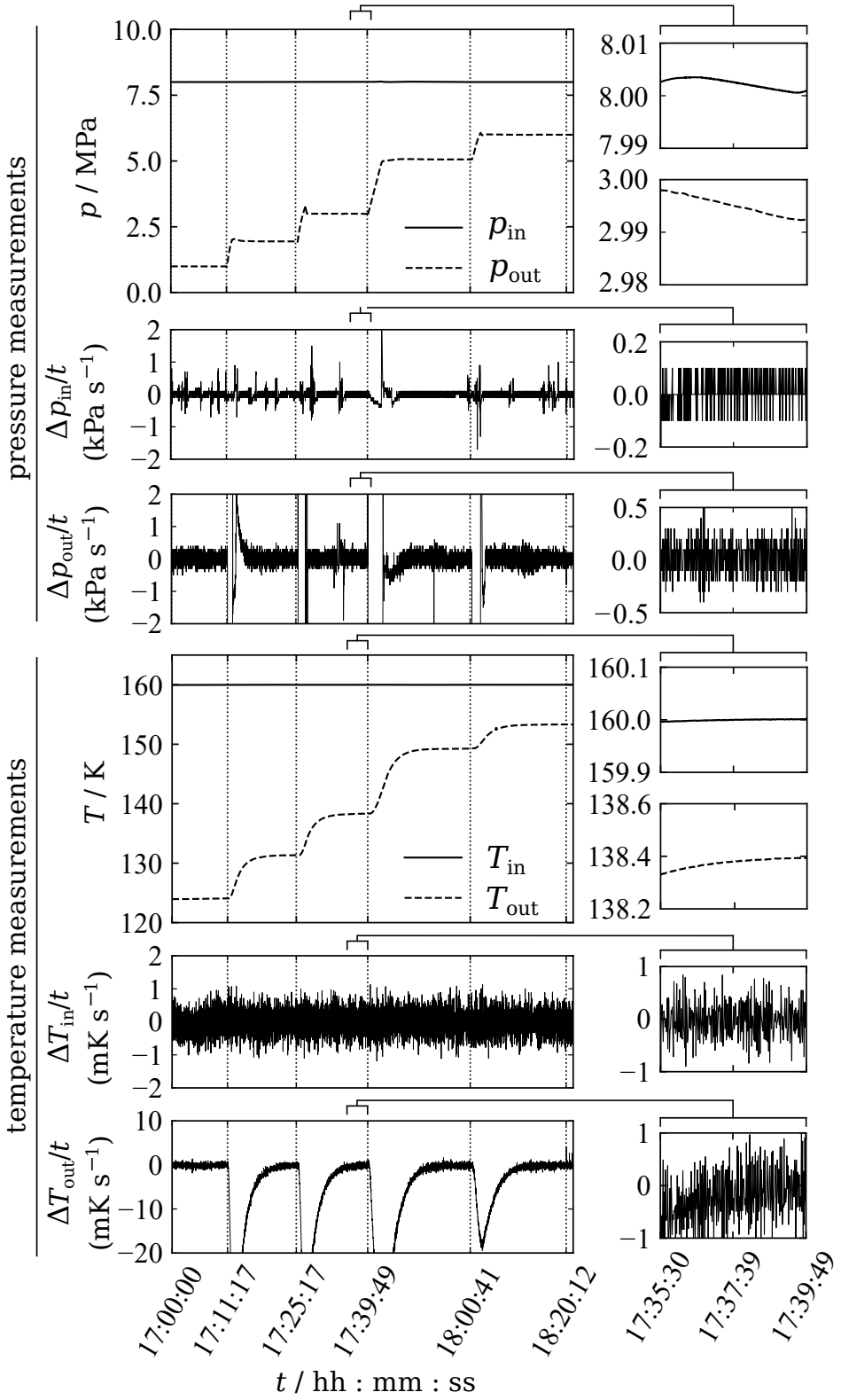

Fig. 4.17. Pressure and temperature evolution during a single isenthalpic line measurements of $He - N_2$.

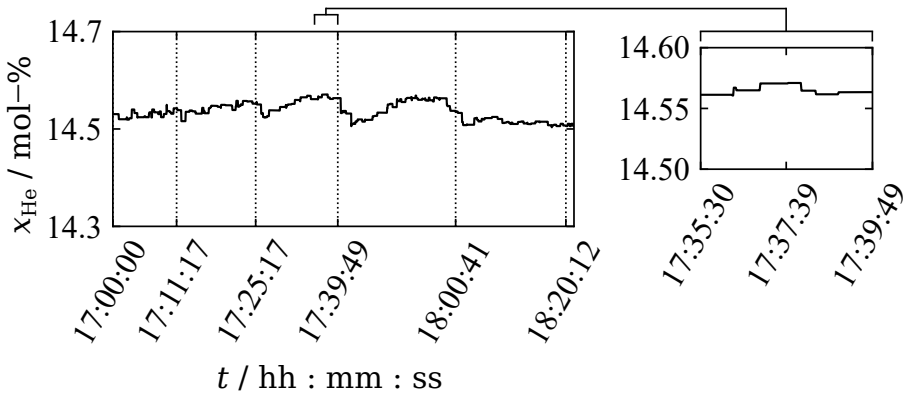

Fig. 4.18. Composition stability during a single isenthalpic line measurements of $He-N_2$.

helium-neon. Pressure variation during the single isenthalpic line measurements is shown in the three top figures of Fig. 4.17, whereas the temperature evolution for the same measurement is visualized in the three bottom figures. The vertical dashed lines in all six figures represent the timestamps of actual measurement points, where all four values are considered stable for 5 seconds. Over the stability period, five values of p_{in}, p_{out}, T_{in}, and T_{out} are acquired and their mean values are calculated. These mean values are used for further Joule-Thomson coefficient calculations in the post-processing analysis. The right column in Fig. 4.17 is the magnification of the measured values. The top graph for each property represents raw data extracted from the data acquisition software. In contrast, the other four figures represent the derivative in time of measured values, that is – their rate of change. They show the measurement stability and fluctuation more precisely.

The time-dependent mole fraction measurement shown in Fig. 4.18 is the data acquired in the same run as the pressure and temperature in Fig. 4.17. The composition variation in this particular measurement reaches 0.067 mol−% and is lower than the gas analyzer specified uncertainty.

Thermal hysteresis verification

In order to fully validate the measurement methodology, a single isenthalpic line is measured twice, following the line in both directions. First, starting from low p_{out} and decreasing the pressure drop $\Delta p = p_{in} - p_{out}$ in the course of the measurements. Second, starting from high p_{out} and increasing the pressure drop. A comparison of both measurement sets, performed with nitrogen, is presented in Fig. 4.19. The left sub-figure with blue and red points shows decreasing and increasing pressure drop measurements, respectively. Both measurements overlay and are indistinguishable in the $p-T$ space.

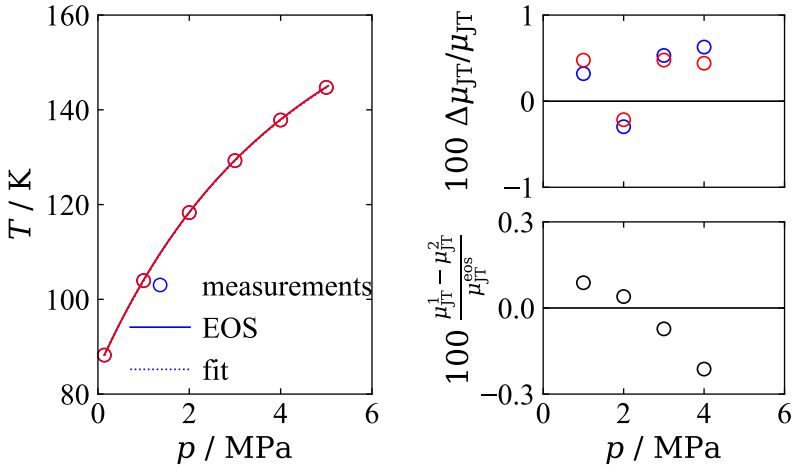

Fig. 4.19. Measurements for 'hysteresis' verification. The isenthalpic line in plotted in the left figure. The upper-right figure shows deviations of measured μ_{JT} with increasing (blue) and decreasing (red) pressure drop in the course of measurements. The lower-right figure shows a relative difference between the two values.

The difference is visible in the two right figures. In the top one – as a deviation from the calculated Joule-Thomson coefficients. In the bottom one – as a relative difference between both measurements, reaching 0.25% in the worst case. No systematic dependence is visible in T_{out} for increasing versus decreasing Δp measurements. Therefore, the measurements can follow an isenthalpic line with either increasing or decreasing Δp presenting no impact on the results.

4.5.2 Measured isenthalpic curves for pure fluids

To complete the experimental setup validation, the isenthalpic lines from the tabulated results in Table E.1 are shown in Fig. 4.20. Three sub-figures show the experimental points in the pressure-temperature space and the respective isenthalpic lines calculated from the pure fluid equations of state for nitrogen, helium–4, and argon.

The slope on an isenthalpic line is not monotonous if it reaches the saturation temperature. The above may happen if the pressure at the capillary outlet decreases below the saturation pressure – if the expansion, shown with the blue line for argon and the pink and yellow lines for nitrogen, continues to lower pressure values. Even though some measurements in nitrogen and argon approach the saturation line, marked in black in Fig. 4.20, the conditions at the capillary outlet always remain gaseous. Therefore, no liquefaction and no enthalpy change are observed. Whenever a gas liquefies, its transformation is no more isenthalpic, which is visible in the $T-p$ diagrams as the $h = \mathrm{const.}$ line slope change. The saturation line is avoided by setting a minimal value on the p_{out}

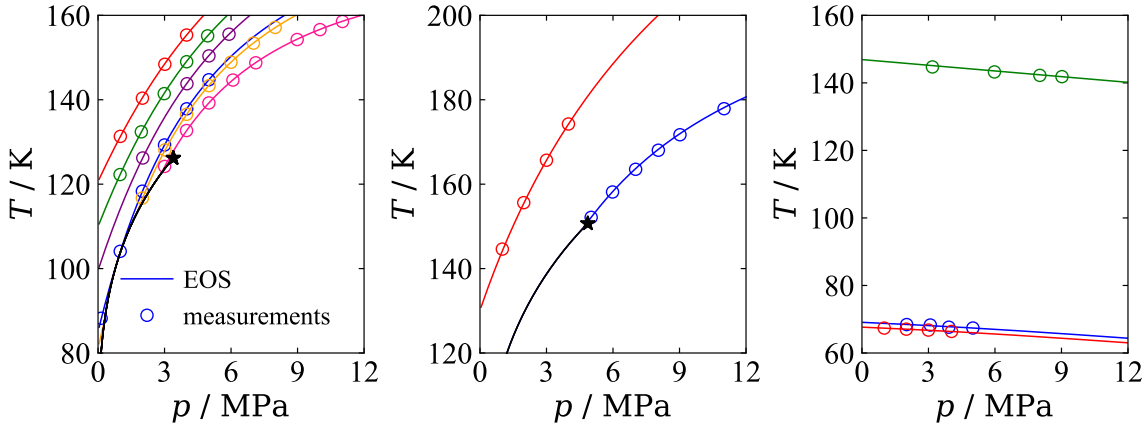

(a) nitrogen (b) argon (c) helium–4

Fig. 4.20. Results of the $p-T$ pairs measurements for pure fluids. Solid lines are the constant enthalpy lines calculated with EOS.[44,52,53] Black lines are the saturation lines, and black stars are the critical points. The color-coded numerical values of $p-T$ measurements are available in Table E.1 and are represented with circles.

for each p_{in}. Another reason for the measurements not being taken through the saturation line is the necessity of fitting a polynomial to the $p-T$ pairs in post-processing calculations. An accurate fit of a simple polynomial requires the isenthalpic line to be monotonous.

The measurements are qualitatively validated against their respective isenthalpic lines, calculated with the EOS. All measured points closely follow the lines. A quantitative validation with calculated Joule-Thomson coefficients is presented in the next chapter.

5 Measurements analysis and results comparison against EOS

In Chapter 4, the method for measuring the pressure-temperature pairs in fluid at constant enthalpy is discussed. The Joule-Thomson coefficient values can be interpreted as the derivatives of an isenthalpic line in the $p-T$ space w.r.t. pressure. In this chapter, the actual isenthalpic Joule-Thomson coefficients, μ_{JT} are calculated and compared against the existing equations of state. First, the post-processing calculations are performed for the pure fluids, so the measurements are qualified against the known equations of state. Later, the measurements for mixtures are compared against the equations developed in this work. Since the Joule-Thomson coefficient in a mixture is not directly dependent on mixture molar composition, the uncertainty discussion is completed with the Monte Carlo analysis quantifying the influence of the molar composition uncertainty on the final results.

5.1 Determining the Joule-Thomson coefficient

The results of performed measurements are the pressure-temperature pairs for pure fluids and the pressure-temperature pairs at constant molar composition for mixtures. The $p-T$ pairs measured at a single isenthalpic line for constant (p_{in}, T_{in}) form a measurement set, s. The Joule-Thomson coefficient can be geometrically represented as the slope of an isenthalpic line in the two-dimensional space of pressure and temperature. A line is fitted to measured $p-T$ pairs so the coefficients can be determined. With a sensibly chosen equation of the fit, its first derivative is calculated for each measured pressure. This derivative is the isenthalpic Joule-Thomson coefficient, μ_{JT}.

5.1.1 Fitting a polynomial and choosing its degree

Each measurement set s of size len(s) for both the pure fluids and mixtures is presented in Tables E.1 and E.2. In order to fit an isenthalpic line to set s, the equation for this line has to be chosen. The `numpy.polynomial` package,[153] used for fitting the equations and calculating their derivatives offers multiple polynomials forms:

1. power series;
2. Chebyshev polynomial;
3. Legendre polynomial;
4. Laguerre polynomial;
5. Hermite polynomial.

The equations of these polynomials are known and are described in detail in the `numpy` package documentation. The Chebyshev polynomial is selected for fitting the measurement data and calculating the Joule-Thomson coefficients. The influence of the polynomial choice on measured μ_{JT} is later compared and is presented in Sec. 5.2.3.

The *Chebyshev polynomial* of the first kind at $p = p_0$ is given by

$$T(p_0) = \sum_{k=1}^{n} a_k C_k(p_0),\ n < \mathrm{len}(s). \tag{5.1}$$

where T is the temperature in K, p is the pressure in Pa, a_k are the fit coefficients in K $\mathrm{Pa}^{-\mathrm{k}}$, and n is the order of the fit. The order n always has to be lower than the number of data points. The coefficients C_k can be obtained from the recurrence relation

$$\begin{cases} C_0(p_0) = 1 \\ C_1(p_0) = p_0 \\ C_{k+1}(p_0) = 2pC_k(p_0) - C_{k-1}(p_0) \end{cases}. \tag{5.2}$$

The Joule-Thomson coefficient is given by

$$\mu_{\mathrm{JT}}(p_0) = \sum_{k=1}^{n} a_k Q_k(p_0),\ n < \mathrm{len}(s), \tag{5.3}$$

where the coefficients Q_k are defined recurrently

$$\begin{cases} Q_0(p_0) = 0 \\ Q_1(p_0) = 1 \\ Q_{k+1}(p_0) = 2C_k(p_0) + 2p_0 Q_k(p_0) - Q_{k-1}(p_0) \end{cases}. \tag{5.4}$$

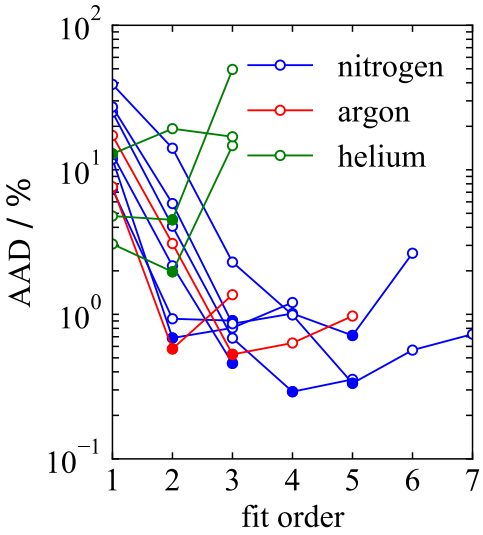

Fig. 5.1. AAD calculated for the Joule-Thomson coefficient of pure fluids as a function of the fit order. The filled points are the minima of the measurements deviations from the EOS.

Apart from choosing the equation of the fitted function, the order of this equation has to be selected. A simple analysis shows that not choosing the maximal possible order of the function ($n = \text{len}(s) - 1$) often allows minimizing the Average Absolute Deviation Eq. (3.25) of equation and data, as shown in Fig. 5.1. The reason for the AAD to decrease with a lower order of the fit is that some of the measurement errors are 'fitted out' for those lower-order polynomials, and the slope of this fit – the Joule-Thomson coefficient is somewhat corrected.

5.1.2 Fit behavior at extremities

The necessity of fitting a polynomial to data brings an issue of diverging results at data set extremities. It is visualized for an arbitrary function $f(x)$ in Fig. 5.2. In the analogy to thermodynamics, the solid curve in the top figure represents an exemplary isenthalpic line; the points are the perfect measurements of the $p - T$ pairs, exactly overlaying the $h = \text{const.}$ line, whereas the dashed line represents a polynomial fit to those points. The calculated Joule-Thomson coefficients measure the slope of the dashed line, not the solid line. As shown in the top figure, the dashed fit line deviates when extrapolating the solid line behavior. It is significant to the analysis since the slope of the fit is different at two extremities compared to the slope of the solid line $f(x)$. The bottom graph in Fig. 5.2 shows the relative deviations of values calculated with the fit versus the exact values from the polynomial $\mathrm{d}f \,/\, \mathrm{d}x$. This pessimistic case of a strongly curved line with little measurement points shows that even the ideal measurements with zero errors in x and

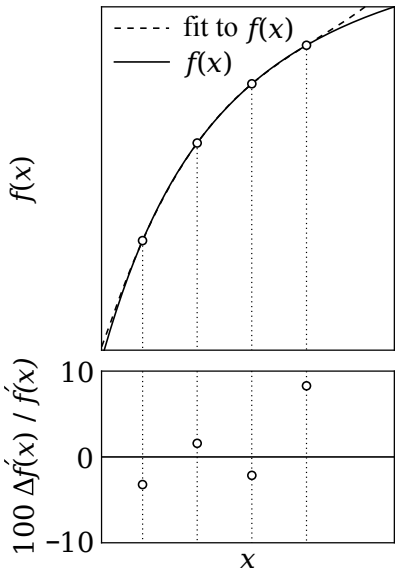

Fig. 5.2. Deviations of a fit (dashed line) from the polynomial (solid line).

y can cause the final results to deviate only because the fit-to-line does not accurately represent the line. In this particular case, the order of the fit function is chosen, so the sum of errors is minimal; therefore, it does not influence the analysis. The derivatives of the fitted polynomial show maximal relative deviation of one of the extrema equal to 8.3%, whereas the maximum deviation of one of the intermediate points is equal to 2.2%. A complete analysis of the influence of fitted polynomial is later discussed in Sec. 5.2.2. It is, however, decided that the extremities of measured isenthalpic lines are fitted but are not included in the μ_{JT} calculations to limit their impact on derivation.

5.1.3 Removing inlet measurements from the analysis

Since the Joule-Thomson transformation is isenthalpic, it is expected that all the output pairs $(p_{\mathrm{out}}, T_{\mathrm{out}})$ follow the same isenthalpic line as the input pair $(p_{\mathrm{in}}, T_{\mathrm{in}})$. Unfortunately, the unfavorable placement of the inlet thermometer (outside of a stainless steel T-piece) most probably causes a permanent offset of measured T_{in} value. The inlet pressure-temperature values in each measurement set are, therefore, removed from the analysis and fitting. They are only used throughout the measurements to keep the inlet conditions stable, but they are not used for the μ_{JT} calculations in the post-processing analysis.

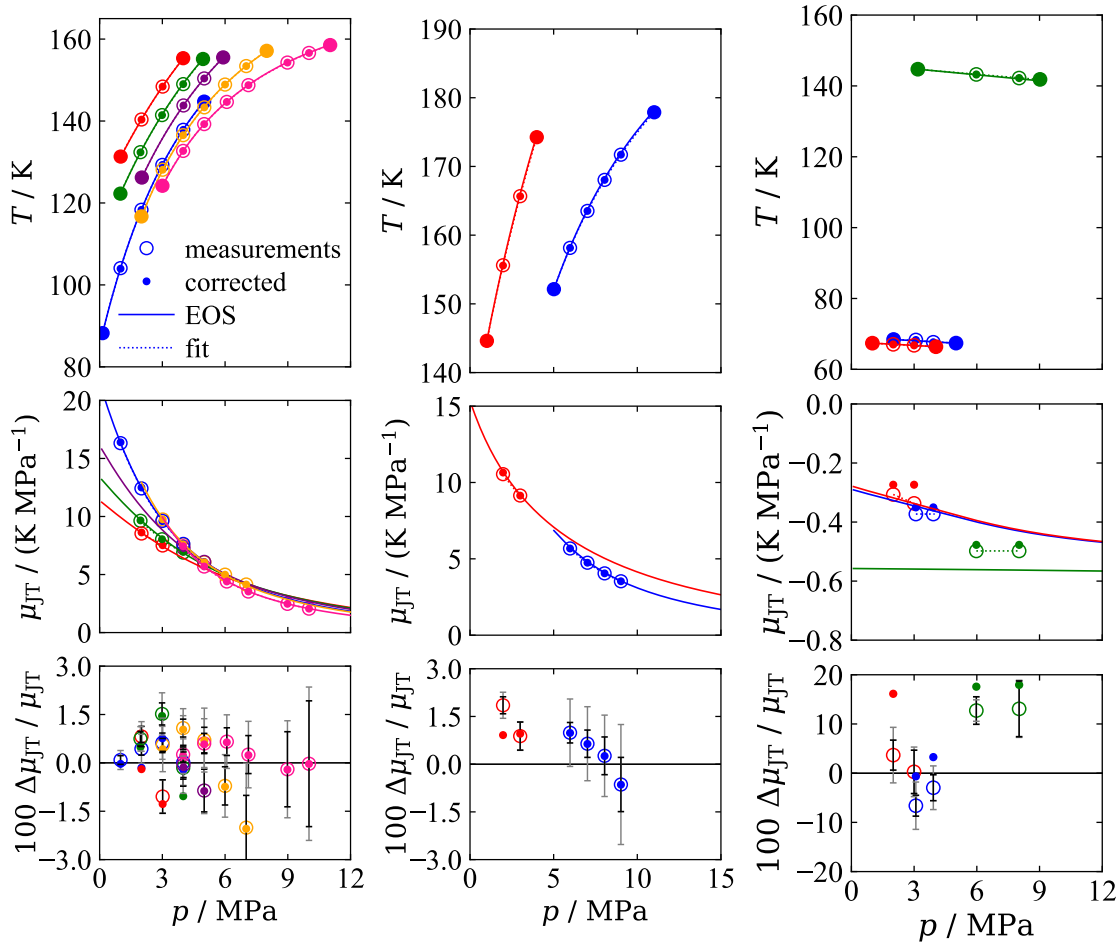

(a) nitrogen (b) argon (c) helium–4

Fig. 5.3. Measured $p-T$ pairs (top figures), resulting Joule-Thomson coefficients (middle figures), and measurement deviation relative to EOS (bottom figures) plotted with uncertainty bars from conventional analysis in black and the Monte Carlo analysis in grey. The color-coded numerical values of $p-T$ measurements at $h = \text{const.}$ are available in Table E.1, the calculated Joule-Thomson coefficients – in Table E.3.

5.2 Results analysis for pure fluids

The measurement results for pure fluids are tabulated in Table E.3. Fig. 5.3 discusses these results for three pure fluids: nitrogen, argon, and helium–4 (in columns). The top row shows the Chebyshev polynomial from Eq. (5.2) fitted to the measured $p-T$ pairs for each isenthalpic line separately. The fits are plotted with dotted lines and the isenthalpic lines, calculated with the EOS – with solid lines. The two lines are indistinguishable because they overlay perfectly. Filled large points at extremities are not used for μ_{JT} calculations. Rings represent the raw measurements, and small filled circles are the measurements corrected with the kinetic energy change from Eq. (4.17). The coeffi-

cients of the fit are used to calculate the Joule-Thomson coefficients with Eq. (5.3). The middle row shows the Joule-Thomson coefficient values, calculated with the EOS (solid lines) and calculated from the fit to measurements (points). The bottom row shows deviations of measured μ_{JT} coefficients, compared to accurate pure fluid EOS. The uncertainty bars from the conventional analysis are illustrated in black. The uncertainty bars from the Monte Carlo analysis are shown in gray.

Even though the polynomial fit and the isenthalpic line, calculated with the EOS, are indistinguishable in the $p-T$ plane, the errors of derived Joule-Thomson coefficients from measured data are significant for helium–4. The conventional uncertainty propagation from Sec. 5.2.1 does not fully explain the encountered errors. An attempt to discuss the uncertainty of integrated measurements is made in Sec. 5.2.2.

The correction introduced to the outlet temperature through Eq. (4.17) does not bring complete consistency to the results. The deviations from the EOS partially decrease except for helium–4 and single points in nitrogen. The change in the Joule-Thomson coefficient values, calculated with the kinetic energy correction, is often minor for nitrogen and argon. It is so because the precautions to the measurements are taken, and no $p-T$ pairs are measured for $p_{out} = 0.1$ MPa, where the expected influence on T_{out} from the kinetic energy conversion is significant.

5.2.1 Conventional uncertainty analysis

Since the measurement error is temperature-, pressure-, and molar composition-dependent, the uncertainty analysis performed prior to the experiment is used to choose the measurement regions characterized with low uncertainty values. The measurement uncertainty can be calculated with a general formula for *error propagation* of quantities with independent uncertainties.[154,155]

If $x,\ldots,w$ are measured with independent uncertainties $U(x),\ldots,U(w)$, and are used to compute quantity $q = x+\ldots+z-(u+\ldots+w)$, the uncertainty in q is the sum

$$U(q) = \sqrt{(U(x))^2+\ldots+(U(z))^2+(U(u))^2+\ldots+(U(w))^2}. \tag{5.5}$$

If the same quantities are measured and used to compute $q = \dfrac{(x\times\ldots\times z)}{(u\times\ldots\times w)}$, the relative uncertainty in q is the quadratic sum

$$\frac{U(q)}{|q|} = \sqrt{\left(\frac{U(x)}{x}\right)^2+\ldots+\left(\frac{U(z)}{z}\right)^2+\left(\frac{U(u)}{u}\right)^2+\ldots+\left(\frac{U(w)}{w}\right)^2}, \quad q\neq 0. \tag{5.6}$$

The logic above, applied to the Joule-Thomson coefficient, defined in Eq. (4.1), results in the following correlation for the uncertainty of differential temperature and pressure measurements

$$U(\Delta T) = \sqrt{U^2(\Delta T)} = \sqrt{U^2(T_{\text{in}}) + U^2(T_{\text{out}})}, \tag{5.7}$$

$$U(\Delta p) = \sqrt{U^2(\Delta p)} = \sqrt{U^2(p_{\text{in}}) + U^2(p_{\text{out}})}, \tag{5.8}$$

where $U(T)$ is the uncertainty of the complete chain of temperature measurements – the sum of the thermometer uncertainty, uncertainty of fitting the temperature to resistance specified for each thermometer, and the temperature acquisition module uncertainty. As described before, the measured (p_{in}, T_{in}) pair is only used to drive the conditions at the capillary inlet and to keep them stable. Since it does not directly contribute to the measurements, it could be replaced with measured instability values for p_{in} and T_{in}. However, the inlet temperature and pressure are more stable throughout the measurements than their respective uncertainties. Therefore, the larger out of two values – the uncertainty is used as an input to the *expanded relative standard uncertainty* calculations, equal to

$$\frac{U_{\text{r}}(\mu_{\text{JT}})}{|\mu_{\text{JT}}|} = k\sqrt{\frac{U^2(T_{\text{in}}) + U^2(T_{\text{out}})}{(T_{\text{in}} - T_{\text{out}})^2} + \frac{U^2(p_{\text{in}}) + U^2(p_{\text{out}})}{(p_{\text{in}} - p_{\text{out}})^2}}, \tag{5.9}$$

where k is the *coverage factor* for expanding the uncertainty. If $k = 1$ and the probability distribution characterized by the measurements of the Joule-Thomson coefficient μ_{JT} is approximately normal, $U(\mu_{\text{JT}})$ is an estimate of the standard deviation of μ_{JT}. The interval $\mu_{\text{JT}} \pm U(\mu_{\text{JT}})$ embraces the value of μ_{JT} with a *level of confidence* of 68% that μ_{JT}

Table 5.1. Uncertainties of the key components

Component	Measurement range	Uncertainty
Temperature sensors: TT101 and TT102	$20-325$ K	$\pm 9-18.7$ mK[a]
$T(R)$ polynomial fit for TT101 and TT102	$20-325$ K	$\pm 3.6-13.5$ mK[a]
Temperature acquisition module[b]	$1-300$ K	$\pm 1.3-7.1$ mK[a]
Pressure sensors: PT101 and PT102	$0.1-13.7$ MPa	$\pm 0.01\%$ FS
Binary gas analyzer: GA016	$0-100$ mol$-\%$	± 0.1 mol$-\%$ ($k=2$)[c]

[a] For a single measurement in $20-100$ K temperature range.
[b] CABTR
[c] Coverage factor for 95.45% confidence interval.

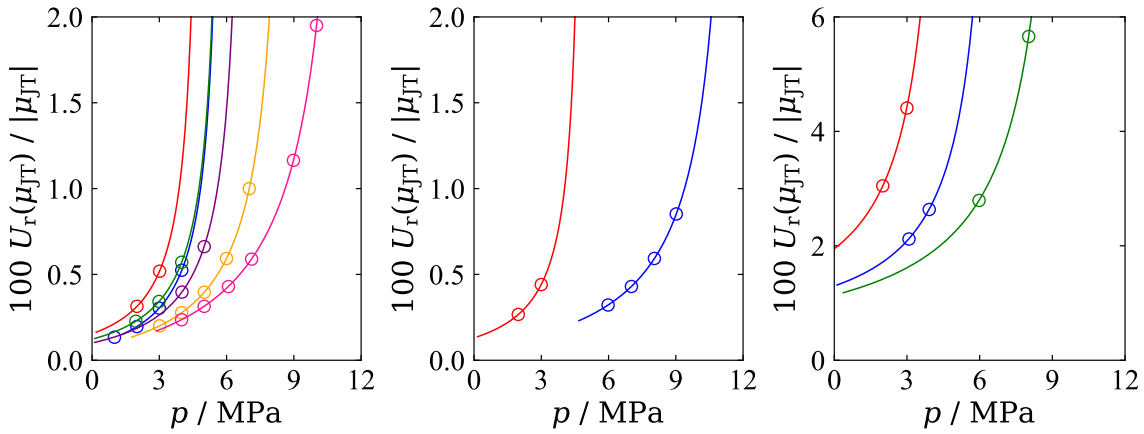

(a) nitrogen (b) argon (c) helium–4

Fig. 5.4. Relative expanded uncertainties for measured isenthalpic lines, calculated with Eq. (5.10). Circles mark values of measured $p-T$ pairs from Fig. 5.3 and Table E.1.

is within the range of measured $\mu_{JT} \pm U(\mu_{JT})$ from the mean value of μ_{JT}. Increasing the coverage factor from 1 to 2 or 3 increases the level of confidence of measurements to 95.45% or 99.73%. The uncertainty of pressure, temperature, and composition measurements of the hardware used in the experiment is given for $k = 2$ with the confidence interval of 95.45%.

The same formulation for the expanded relative standard uncertainty of the Joule-Thomson coefficient can also be obtained with differential analysis for uncertainty propagation:

$$\begin{aligned}
\frac{U_r(\mu_{JT})}{|\mu_{JT}|} &= \frac{k}{|\mu_{JT}|}\sqrt{\left(\frac{\partial \mu_{JT}}{\partial(\Delta T)}\right)^2 U^2(\Delta T) + \left(\frac{\partial \mu_{JT}}{\partial(\Delta p)}\right)^2 U^2(\Delta p)} \\
&= k\left|\frac{\Delta p}{\Delta T}\right|\sqrt{\left(\frac{1}{\Delta p}\right)^2 U^2(\Delta T) + \left(-\frac{\Delta T}{\Delta p^2}\right)^2 U^2(\Delta p)} \\
&= k\sqrt{\frac{\cancel{\Delta p^2}^{\,1}}{\Delta T^2}\frac{1}{\cancel{\Delta p^2}^{\,1}}U^2(\Delta T) + \frac{\cancel{\Delta p^2}^{\,1}}{\cancel{\Delta T^2}^{\,1}}\frac{\cancel{\Delta T^2}^{\,1}}{\cancel{\Delta p^4}^{\,\Delta p^2}}U^2(\Delta p)} \\
&= k\sqrt{\frac{U^2(T_{in}) + U^2(T_{out})}{(T_{in} - T_{out})^2} + \frac{U^2(p_{in}) + U^2(p_{out})}{(p_{in} - p_{out})^2}}.
\end{aligned} \tag{5.10}$$

The analysis above, together with the hardware uncertainty, specified in Table 5.1, were used to choose the regions of low measurement uncertainty. Fig. 5.4 shows the results of calculated uncertainty values for actual measurements, marked with circles.

The first major shortcoming of the analysis above is that it does not discuss the composition measurement uncertainty for the measurements with fluid mixtures. Since the composition is constant in the Joule-Thomson coefficient formulation and is constant during the measurements, it is not included in the relative standard uncertainty calculations. The second deficiency is that it does not consider the necessity for deriving the measured values to obtain the isenthalpic Joule-Thomson coefficient. These two issues are addressed in the Monte Carlo analysis.

5.2.2 Monte Carlo simulation for uncertainty propagation

The derived Joule-Thomson coefficient value $\mu_{\mathrm{JT}} = \mu_{\mathrm{JT}}(p,\ T)$ depends on a complete set of measurements, the number of points $n = \mathrm{len}(s)$ – measured on a single isenthalpic line – and the polynomial fitted to data. The number of measurement points n also has a non-negligible and variable impact on the final results. An attempt to quantify all these factors is presented below.

A single isenthalpic line for a given $(p,\ T)$ conditions is calculated with existing EOS. A number of n points overlay the isenthalpic line and represent the perfect measurements. For each point i, $i \in \langle 1,\ n \rangle$, a randomly distributed error, within the uncertainty range from Table 5.1, is added to temperature and pressure. Next, a polynomial is fitted to points with added random errors, and its derivative is calculated in all points n. The derivative values are the Joule-Thomson coefficients – they are compared against values obtained with the EOS. The calculations are repeated $300 \times n$ times, so the distribution of errors is obtained for all points n. Finally, the standard deviation of $\Delta\mu_{\mathrm{JT}} \ / \ \mu_{\mathrm{JT}}^{\mathrm{EOS}}$ is computed, and the uncertainty is reported for each point separately for 95.45% confidence interval.

A schematic representation for the error calculations is illustrated in Fig. 5.5. The solid line is the isenthalpic line, calculated with an equation of state. Three points are the points mimicking the measurements distributed over the isenthalpic line. A pressure-dependent uncertainty in pressure $U(p)$ and a temperature-dependent uncertainty in temperature $U(T)$ embrace all possible solutions for a $p - T$ pair forming the elliptical region of statistical uncertainty. The selected measurement-like points are shown with a ring. The fit-line passes through all the points and allows for calculating its derivative – the Joule-Thomson coefficient. In the end, the calculated value is reported as a mean relative uncertainty expanded to 95.45% confidence interval.

The results of the analysis are shown in Fig. 5.6a and 5.6b. Each point in the figures represents the expanded mean relative uncertainty of all the points placed on a single

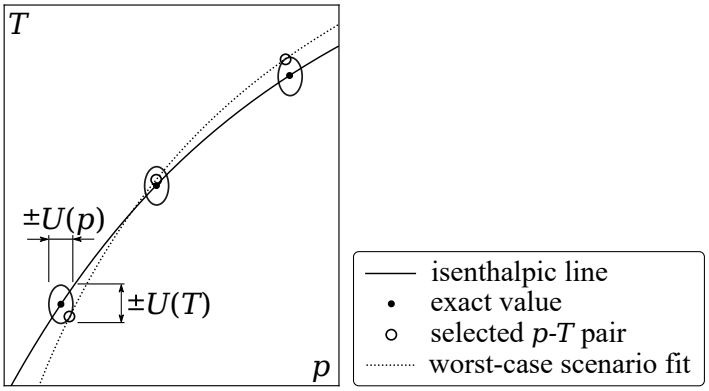

Fig. 5.5. Visual representation of an isenthalpic line measurement error. Black points are the perfect measurements, ellipses are their statistically calculated uncertainties, and rings are the randomly selected measurements within the uncertainty bounds.

isenthalpic line. Since these are the mean values, the information about the uncertainty distribution on a single isenthalpic line is lost. The exact values are given for actual measurements. Each of the six sub-figures presents the results for a different number of points $n \in \langle 3, 8 \rangle$ distributed over a single line. The $|\Delta T| \ / \ \Delta p_{\mathrm{max}}$ on the x-axes is the temperature change in the isenthalpic transformation, relative to the pressure change $\Delta p_{\mathrm{max}} = p_{\mathrm{in}} - p_{\mathrm{atm}}$. It is geometrically equivalent to the isenthalpic line steepness in the $p - T$ plane and thermodynamically equivalent to the temperature change in the Joule-Thomson process from p_{in} to p_{atm}. The absolute value of ΔT is used since it is insignificant to the analysis whether the temperature change is positive or negative.

Colors show the degree of the $h = \mathrm{const.}$ line, that is – its curvature. For $\mathrm{deg} = 1$ and dark blue points, the isenthalpic line is linear in the $p-T$ plane, whereas for $\mathrm{deg} = 6$ and yellow points it is strongly curved, and in the complete $\Delta p = p_{\mathrm{in}} - p_{\mathrm{atm}}$ space it can only be accurately fitted with a polynomial of degree 6 (for the coefficient of determination $R^2 > 0.999$).

Fig. 5.6a shows the average measurement error calculated with all n points, including the two points at the extremities. These extremities bring the highest error to the measurements, as discussed in Sec. 5.1.2 and Fig. 5.2. Fig. 5.6b calculates the average error excluding the extrema. The extremities are necessary to fit a polynomial accurately but the slope of the fit at these points can diverge significantly from the slope of the isenthalpic line. For this reason, dropping the extremities decreases the expected error of all μ_{JT} measured on a single isenthalpic line.

Decreasing the number of measurement points always results in increasing error. However, even for many points, the mean error calculated for helium–4 does not decrease. Even though the isenthalpic lines of helium can often be linearly approximated, the ΔT

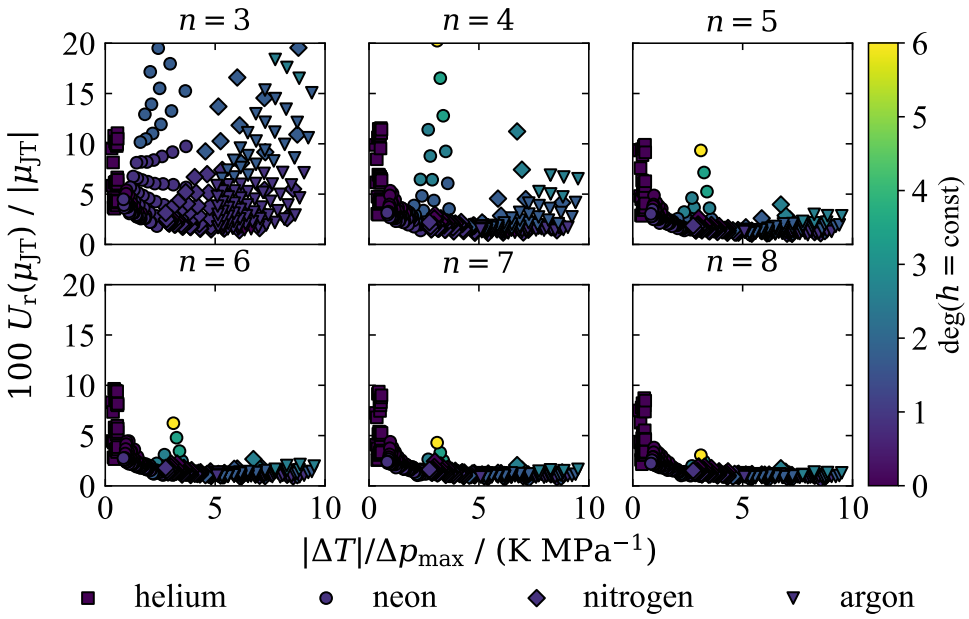

(a) Mean uncertainty including points at extremities.

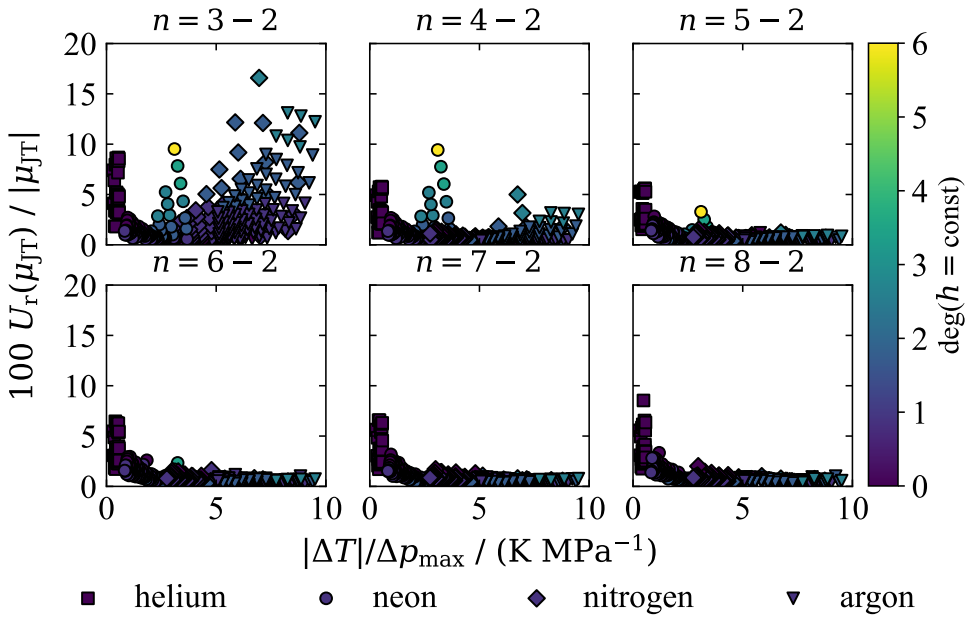

(b) Mean uncertainty excluding points at extremities.

Fig. 5.6. Mean relative expanded uncertainty for the measurements of the integrated Joule-Thomson coefficient in pure fluids, calculated with Monte Carlo uncertainty propagation.

of the Joule-Thomson process is near-zero, which directly translates to high measurement error.

It can be concluded from Fig. 5.6b that a single isenthalpic line measured for neon, nitrogen, or argon with at least $n = 5-2$ measurement points should yield errors lower

than 2% for most cases except a few strongly curved isenthalpic lines of neon. A more significant number of points measured at a single isenthalpic line for helium–4 is not expected to decrease the errors. If the extremities were to be kept in analysis, at least $n = 7$ points should be measured at a single line to decrease the mean error to the level of $n = 5 - 2$ points at the same line without the extremities.

In analogy to conventional uncertainty analysis and the black error bars in Fig. 5.3, the gray bars represent the error values calculated with the Monte Carlo simulations, including the fitted polynomial derivation process. In contrast to the conventional analysis, it can be concluded that most of the measurements are taken with errors within the uncertainty range compared to the values calculated from the EOS. Another important conclusion, not available from the conventional uncertainty analysis, is that the order of a polynomial, its fitting, and derivation significantly influence final results and the uncertainties.

5.2.3 Polynomial selection to fit the data

The analysis from the previous Section and Fig. 5.6 is repeated using different polynomials available within the `numpy.polynomial` to fit the measurements and calculate the derivatives. The errors are averaged for each fluid, independent from the $|\Delta T|$ / $p_{\max}$ value and the results are presented in Fig. 5.7. Each set of lines represents the averaged differences between the calculated Joule-Thomson coefficient and the coefficients obtained with an EOS for four different fluids. Every line in each set of lines calculates the same results using a different polynomial. The left subfigure presents the average values from Fig. 5.6a, the right one – from Fig. 5.6b. It is remarkable to the analysis that the polynomial type has no impact on the calculated derivative values, that is, the Joule-Thomson coefficients. All five lines of each color in both figures overlay for neon, nitrogen, and argon. Little differences are visible for helium–4, but the impact is also considered negligible since there is no obvious tendency.

The average error values presented in Fig. 5.7 are used only to compare the polynomials against each other. It is essential to notice that some of the errors brought by the differentiation encountered in the pure fluid measurements are much larger than the presented mean values.

Since no influence of the polynomial type on the calculated Joule-Thomson coefficients exists, each one, out of five compared polynomials, can be used for analysis. In this work, the Chebyshev series is applied to the measurements to calculate the isenthalpic Joule-Thomson coefficients.

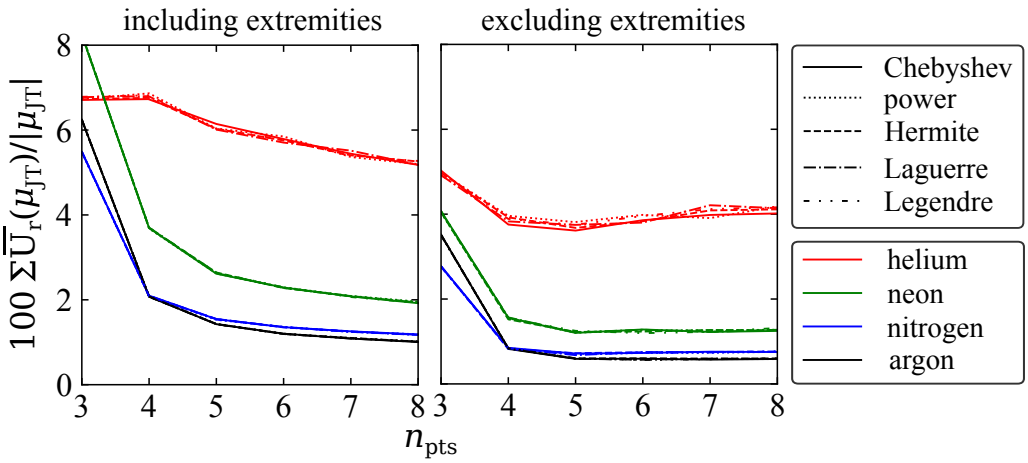

Fig. 5.7. Influence of the type of polynomial used for fitting the measurements on the Joule-Thomson coefficient results.

5.3 Results analysis for mixtures

The measurements of the isenthalpic Joule-Thomson coefficient in mixtures are performed at constant molar composition. Compared to the pure fluid measurements, preparing the gas mixture in a 50 liters volume is necessary before the measurements. Precisely measured molar composition is fundamental to obtain the results with acceptably low uncertainty. The composition cannot be accurately calculated from the pressure measurements in the mixing process. Its precision does not decrease below ±2 mol − % according to the gas vendor. As shown in Table 5.1, the gas analyzer measures the molar composition of a binary mixture with known constituents with ±0.1 mol − % uncertainty.

Apart from the differences described above, the measurements for mixtures are performed by following the procedure detailed in Sec. 4.5. Numerical results from the Joule-Thomson coefficient measurements for helium-neon and helium-nitrogen are presented in Table E.2.

In analogy to the pure fluids, the Chebyshev polynomial from Eq. (5.1) is fitted to each isenthalpic line separately, and the Joule-Thomson coefficients are calculated from Eq. (5.3). The values, resulting from these calculations, are presented in Table E.4 and for the helium-neon mixture are visualized in Fig. 5.8. Columns show measurements performed at four different mixture molar concentrations. Solid lines in the top figure are the isenthalpic lines calculated with the equations of state, developed in Chapter 3. Dotted lines represent the Chebyshev polynomials fitted to the experimental $p-T$ points. The subfigures in the middle row show the calculated and measured Joule-Thomson coefficients. The bottom row shows relative deviations between the measurements and

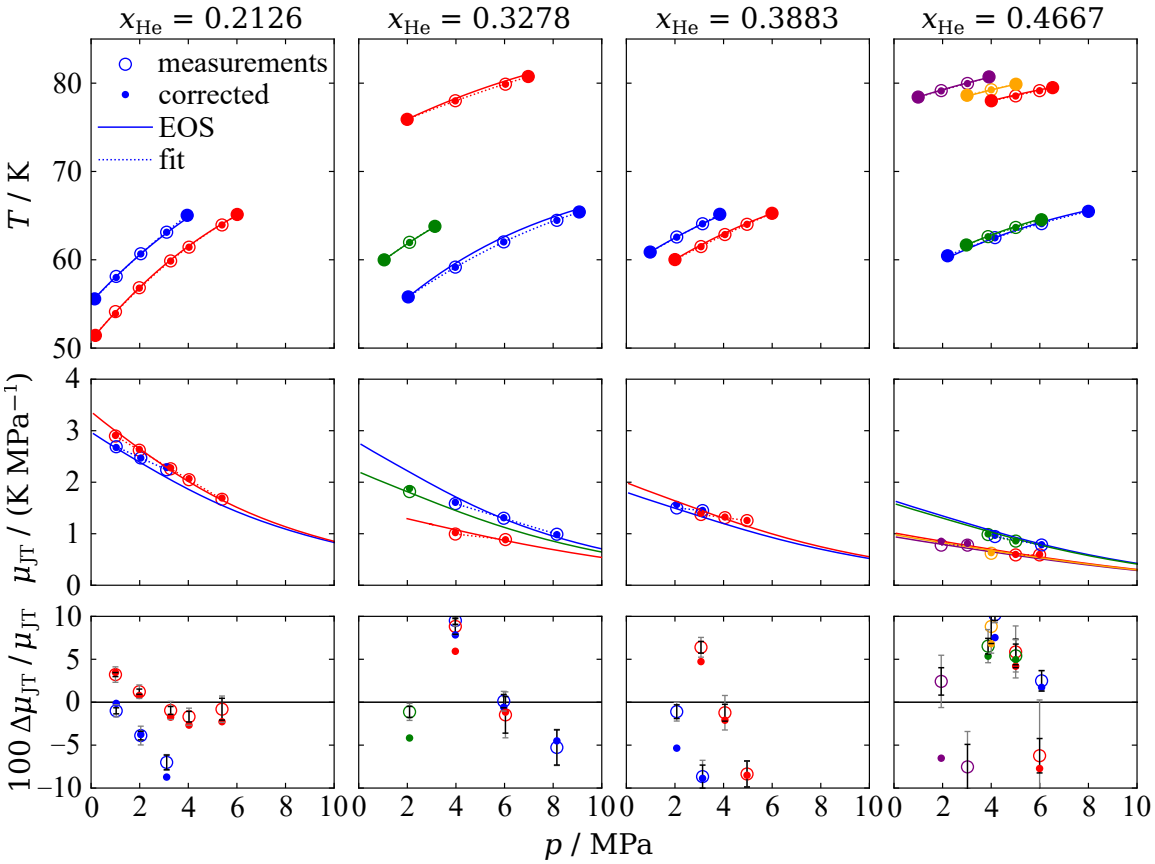

Fig. 5.8. Measured $p-T$ pairs for ^{4}He – Ne mixture with variable molar composition (top row). Resulting Joule-Thomson coefficients (middle row) and the relative deviation from the EOS (bottom row) presented with black uncertainty bars from Eq. (5.10) and gray bars from the Monte Carlo analysis. The color-coded numerical values of $p-T$ measurements are available in Table E.2. The calculated Joule-Thomson coefficients are given in Table E.4.

the EOS. Black error bars are calculated with Eq. (5.9), gray – with the Monte Carlo simulations. Similarly, the Joule-Thomson coefficient measurements for pure fluids, rings in all figures are the raw measurements, and dots are the measurements with applied kinetic energy correction. By analogy, the measurements for helium-nitrogen, at two different molar concentrations, are plotted in Fig. 5.9.

As described before, the derivation process necessary to calculate μ_{JT} is expected to bring additional errors to the analysis. However, the Joule-Thomson coefficients for both mixtures are measured at helium–4 concentrations below 50 mol–%. As a consequence, the resulting temperature change often approaches the one observed for pure nitrogen and argon. Besides, the curvature of most of the isenthalpic lines, measured for mixtures in this work, is not excessive. These two conditions should result in limited error caused by the derivation of a fit. However, it is visible in Figures 5.8 and 5.9 that the deviations between the measurements and the EOS are more significant compared to the pure

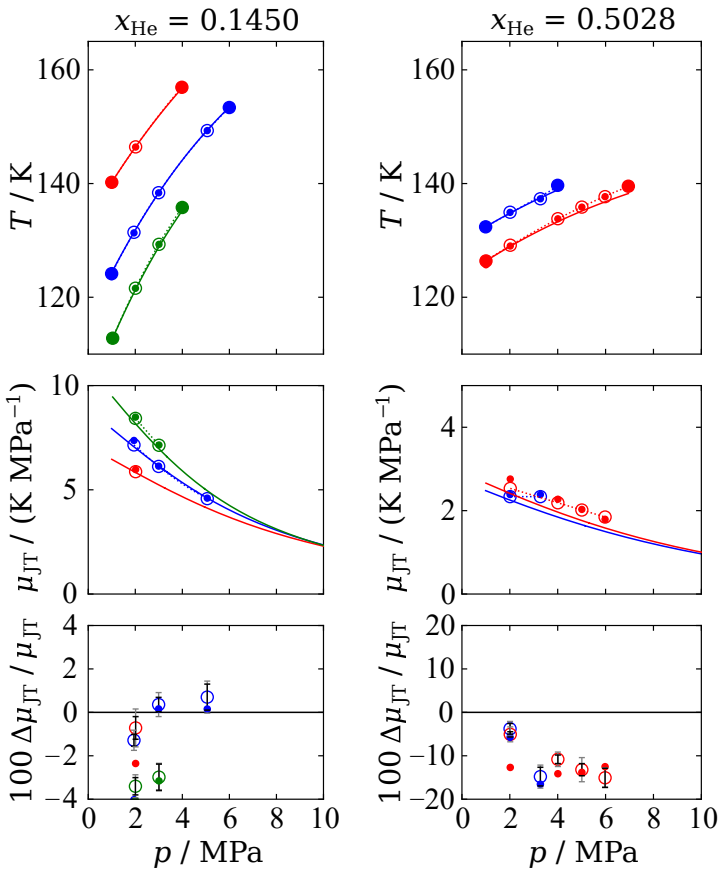

Fig. 5.9. Measured $p-T$ pairs and μ_{JT} values for $^4He-N_2$ mixture and two molar composition values. The color-coded numerical values of $p-T$ measurements are available in Table E.2. The calculated Joule-Thomson coefficients are given in Table E.4.

fluids. The reason for those higher deviations can lay either in incorrect measurements, incorrect coefficients of developed equations of state, or possibly – limited capabilities of the modern functional form of the equation of state in the Joule-Thomson coefficient representation for mixtures with high critical temperature ratio.

As discussed in Sec. 3.4.4, the equation of state for the mixture of helium–4 and nitrogen is primarily developed to describe the phase equilibria at lower pressures. The single-phase properties are fitted with low weights, compared to the other equations from this work, therefore, further refinement should be possible. However, the equation of state for helium–4 and neon should not result in too high a deviation, considering the advancement of its development. The influence of the composition measurement uncertainty on the Joule-Thomson coefficient is evaluated before the conclusions from the measurements are drawn.

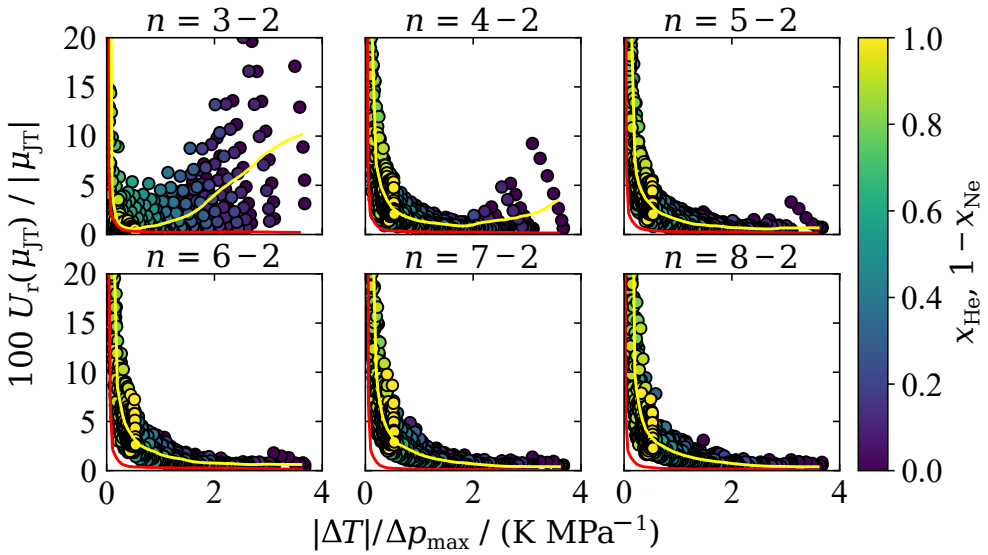

Fig. 5.10. Measurement error of differentiated isenthalpic Joule-Thomson coefficient for ^{4}He − Ne, plotted for a variable number of points on a single h = const. line, excluding the extremities, averaged over a number of points on the isenthalpic line. Figures show results of the Monte-Carlo analysis for mixture measurement uncertainty. The yellow lines are the moving average for plotted points – including all uncertainty components. The red lines are the moving average estimating the composition uncertainty influence on μ_{JT} measurements.

5.3.1 Influence of the composition uncertainty

The influence of the measurement conditions and the hardware uncertainties on the Joule-Thomson coefficients, measured for ^{4}He − Ne, is evaluated. The analysis corresponds to the one presented for the pure fluids in Fig. 5.6. In addition to the methodology discussed for the pure fluids, points on the isenthalpic line of a mixture are influenced by the composition error. The specified uncertainty of the gas analyzer is independent of the composition and is equal to ±0.1 mol − % for $k = 2$. In the Monte Carlo analysis, the error in composition is applied to each point randomly, similarly to pressure and temperature.

The mean error of the Joule-Thomson coefficient in Fig. 5.10 is calculated as a function of the isenthalpic line steepness, its curvature, number of the $p-T$ points measured on a single line, and the mixture molar composition. The x-axes represents the temperature change in the isenthalpic transformation, relative to the pressure change $\Delta p_{max} = p_{in} - p_{atm}$. It characterizes the isenthalpic line steepness on the $p-T$ plane. The points show the mean error of a single Joule-Thomson coefficient for a variable number of points n measured on a single isenthalpic line. The color of a point represents the mixture molar concentration ranging from pure helium in yellow to pure neon in blue. The

yellow lines are the moving averages calculated with all uncertainty components from Table 5.1. The red trend lines are the moving averages calculated only for the influence of the composition uncertainty, determined as the differences of the yellow lines and the values obtained with all uncertainty components except the composition uncertainly.

High measurement error is visible for pure helium, where little temperature change is observed, and for pure neon with few experimental points taken, where the isenthalpic line curvature is the most pronounced. It is visible that at least $n = 5-2 = 3$ points are necessary to approach the minimal measurement error, with better results obtained for $n = 6-2 = 4$ points on a single line. Above this number, the derivation process does not influence the results in given conditions.

The impact of the composition measurement uncertainty on the Joule-Thomson coefficient is illustrated with the red lines and is independent of the number of points. This influence on the total error is marginal except for very low helium concentration values, where a minor change in the slope of a flat isenthalpic line results in a significant relative error. The helium concentration for measurements taken with ^4He-Ne ranges from 20 to 50 mol$-$%, the mean error brought by the composition measurement uncertainty within these limits is equal to 0.3% in μ_{JT}, the maximal error is equal to 1.5%.

Most of the isenthalpic lines in Fig. 5.8 are constructed using four to six measurement points. The mean, relative errors in the Joule-Thomson coefficient for the mixture with 20 to 50 mol$-$% of helium, calculated with the Monte Carlo simulations, are smaller than 5%. Therefore, neither the Eq. (5.9) nor the presented analysis explain the encountered differences between the EOS and the measurements.

5.3.2 Corrections for heat losses and kinetic energy

Too little information is available to calculate the thermal losses to the capillary assembly and thermometers in particular. An attempt to estimate the heat losses is made based on the minimization of μ_{JT} deviations. Fig. 5.11 presents the measurements deviations from the EOS, plotted with circles. Filled points show deviations of the corrected measurements assuming that a constant heat loss $\dot{Q} = 27$ mW is applied to the temperature sensor at the capillary outlet. The calculations impact only the outlet temperature, T_{out}. The presented value is similar to the heat loss estimated in the experiment design process.

The 27 mW heat in-leak is obtained by minimizing the sum of deviations of all the Joule-Thomson coefficients, measured for nitrogen, helium, argon, and helium-neon. It is not used to correct the values of measured Joule-Thomson coefficients since it does

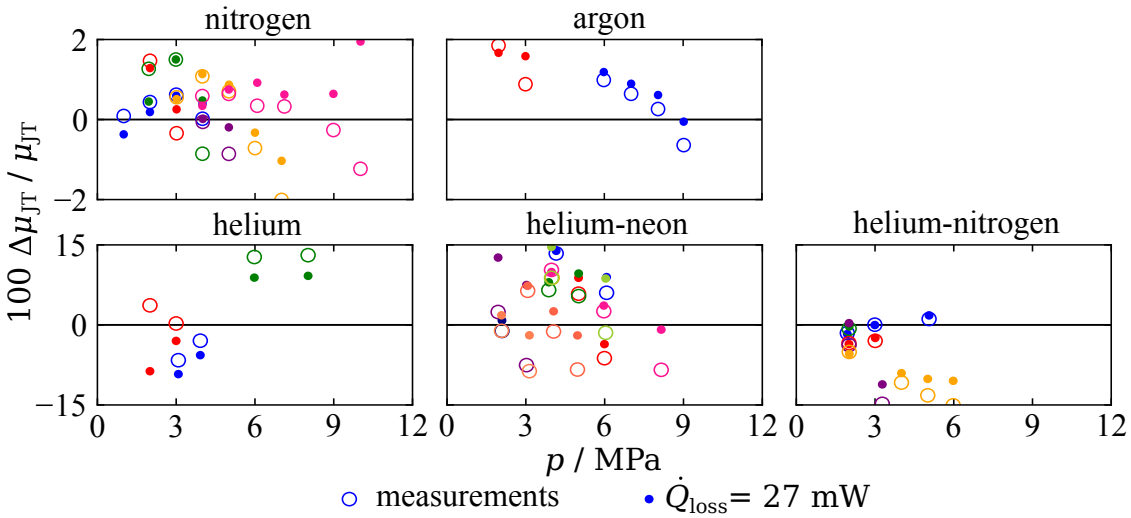

Fig. 5.11. Estimated heat loss impact on deviations of measurements and EOS. Colors in the figures match the colors given in Tables E.3 and E.4.

not provide coherent results for all measurements, yielding higher deviations for part of corrected results.

The correction factors from Eq. (4.9) are quantified for the experimental conditions from this work and are presented in Table 5.2. The estimations are based on the calculated mass flow rate (verified with the volumetric flow meter) and the calculated heat loss, impacting the T_{out} measurement. The relative values for nitrogen and argon are lower since the isenthalpic lines in the $p-T$ measurement space for these two fluids are steeper, yielding larger absolute values of the Joule-Thomson coefficients. The correction for kinetic energy may have been large for the large Δp measurement method. However, successfully applied precautions limit Δe_{k} for all the measured $p-T$ values, as discussed in Sec. 4.4.1.

On the one hand, the analysis shows that the heat losses and the kinetic energy change have a non-negligible impact on final results. On the other hand, the applied corrections do not consistently decrease the observed deviations.

Table 5.2. Mean absolute and relative corrections to $\left.\frac{\Delta T}{\Delta p}\right|_{\mathrm{path}}$ from Eq. (4.9)

correction	N_2	Ar	^{4}He	^{4}He − Ne
$-\frac{\dot{Q}}{\dot{m} c_{\mathrm{p}} \Delta p}$	0.012 K MPa^{-1} (0.19%)	0.070 K MPa^{-1} (0.79%)	0.011 K MPa^{-1} (2.93%)	0.049 K MPa^{-1} (2.13%)
$\frac{\Delta e_{\mathrm{k}}}{c_{\mathrm{p}} \Delta p}$	0.006 K MPa^{-1} (0.06%)	0.009 K MPa^{-1} (0.09%)	0.010 K MPa^{-1} (2.77%)	0.009 K MPa^{-1} (0.76%)

5.4 Conclusions from the measurements

The isenthalpic Joule-Thomson coefficient measurements in pure fluids (nitrogen and argon) are within the expected uncertainty from the accurate equations of state. The obtained precision allows for validating the experimental setup. The measurements characterized by small temperature change (pure helium–4) are burdened with high uncertainties, as shown with the Monte Carlo simulations. For helium, the encountered deviations from the EOS are even higher than expected as the thermal losses may strongly influence the isenthalpic process characterized by very low-temperature change.

The μ_{JT} measurements for mixtures are characterized by higher deviations from the EOS compared to the pure fluids, excluding helium–4. An attempt was made to use the obtained experimental data and refit the equation of state for the mixture of helium–4 and neon. The minimization algorithm was not able to decrease the deviations between the EOS and the μ_{JT} data, keeping the equation constrained by the phase envelope. Even after releasing the phase envelope and fitting only the measured Joule-Thomson coefficients, the optimization did not result in significantly lower deviations than already presented. This minimization attempt is considered a valid answer to whether it is possible to further optimize the equation coefficients with given values of the Joule-Thomson coefficients. It is not – the deviations between the EOS for $^4\mathrm{He} - \mathrm{Ne}$ and μ_{JT} reach 9%.

The analysis proposed by Smith[137] does not provide significant insights into encountered deviations between the measurements and EOS. As shortly discussed in Sec. 5.3.2, Smith's corrections only sometimes minimize the deviations of results with respect to EOS. As the analysis is assessed to be qualitatively correct, it yields incoherent corrections for the complete set of pure fluid and mixture measurements.

Neither of the uncertainty discussions thoroughly explains the deviations between the measurements and the equations of state. An additional source of errors can be the inlet thermometer placement, which regulates the isenthalpic conditions. Despite removing the $(p_{in},\ T_{in})$ pair from the measurement analysis, the inlet thermometer reading is used to keep the inlet temperature constant. Assuming a constant heat in-leak to the capillary assembly, the heat transfer from the fluid to the inlet thermometer varies with the mass flow rate. Therefore, the heat losses impacting the temperature measurements may cause the supposedly constant inlet temperature to change throughout a single isenthalpic line measurement, becoming another source of error.

Compared to the previously measured Joule-Thomson coefficients, the errors encountered in this work are lower, especially when studying other measurements in cryogenic

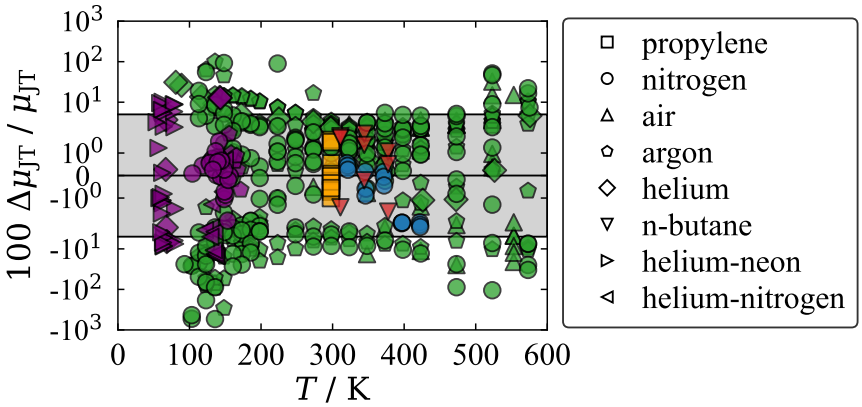

Fig. 5.12. Relative deviation of existing experimental data from Fig. 4.4, extended with data from this work, compared to the EOS. Grey rectangle is the ±5% band. Colors vary for authors: green - Roebuck and Osterberg, red - Smith, blue - King and Potter, orange - Bier *et al.*, purple - this work. A complete reference list for measurements and EOS for each fluid is available in Table 4.1.

conditions. Fig. 5.12 presents the results obtained in this work, compared with the measurements from the literature. Even though not all the measurements from this work fit within 5% relative error, the results are satisfying and show that the Joule-Thomson coefficient can approach the precision of the specific heat measurements.

6 CONCLUSIONS

The presented work has been motivated by the development of new cryogenic facilities and improved cooling production efficiency at intermediate temperatures. The demand for accurate equations of state for mixtures has been identified. As a result, this work evolved from thermodynamic cycle-oriented to thermophysical property-oriented.

The state-of-the-art empirical formulation for the Helmholtz energy has been used to develop the equations of state for the binary mixtures of cryogenic fluids: helium-neon, helium-argon, neon-argon, and helium-nitrogen. For each equation, the errors in single-phase are evaluated, and the phase envelopes are constructed in the $p-T-x$ space.

The equation of state for helium-nitrogen allows to accurately predict the fluid behavior at low-pressures of the phase envelope – its primary region of interest. However, the equation should be refined, so its reliability and accuracy improve. It fails more often to provide a single-phase property prediction compared to, e.g., the equation for helium-neon.

Extensive analysis of the errors at phase envelopes of the developed equations is concluded with a new metric implementation. In contrast to the traditional pressure-based metric, the new orthogonal metric defines the deviations at phase envelopes for the entire data set. The orthogonal distance definition has been presented and is a valuable metric for validating an equation of state at phase envelopes.

An attempt was made to employ the defined metric to develop the equation of state for the $^4He-H_2$ mixture. The stochastic minimization algorithms may minimize the sum of orthogonal distances between the isotherms and the experimental points, but no guess value used by these algorithms negatively influences the convergence. All attempts showed that it is difficult for the algorithm to converge when the reducing parameters are fitted together with all the departure function parameters. More precisely, the stochastic minimization is not successful due to the sensitivity of the phase equilibria tracing algorithm to the random guess values of the departure function parameters. The algorithm minimizing the sum of orthogonal distances was demonstrated to work with a deterministic approach and good starting values for all the parameters. However,

its successful operation requires the constraints on the thermodynamic properties to be implemented. The automatic optimization and successful convergence shall be the goal of future studies for which the orthogonal distance indicates the path.

The Joule-Thomson coefficient measurement setup has been designed, constructed, and used to measure the coefficients for pure fluids and mixtures. The results obtained with the indirect measurement method, where the integral of the Joule-Thomson coefficient has been measured, resulted in challenging post-processing analysis. The measurements with pure nitrogen, argon, and helium validated the experiment and the methodology. The Joule-Thomson coefficients for helium-neon and helium-nitrogen were acquired for few different composition values in the regions of little or no experimental data. The measurements have been concluded with extensive uncertainty discussion and Monte Carlo analysis. The measured coefficients have been compared with the equations of state for mixtures developed within this work and are in good agreement with them.

The Joule-Thomson coefficient definition in terms of the Helmholtz energy contains almost all the first and second derivatives of the residual contribution, except for the first derivative w.r.t. reduced temperature, $\alpha^{\mathrm{r}}_{\tau}$. Therefore, μ_{JT} is an attractive property for the equation of state validation. The measurements reach relative errors in the order of $\Delta\mu_{\mathrm{JT}} \,/\, \mu_{\mathrm{JT}} \leq 2\%$ for pure fluids in advantageous conditions (nitrogen and argon for significant temperature difference in the isenthalpic process). Even with higher relative errors observed for mixtures (9%), a comparison with other existing cryogenic measurements shows that the results presented in this work are competitive and often more accurate. Performed measurements of the isenthalpic Joule-Thomson coefficient confirm the performance of the equations of state at cryogenic temperatures. The measurements should be repeated for other mixtures in different conditions, so the pure fluid errors demonstrated in this work are observed for mixtures. Additional important question should be raised on whether the modern functional form of the equation of state is capable of accurately describing all the state points for a mixture characterized by a high critical temperature ratio.

The accuracy of predictions for enthalpy, entropy, isobaric, and isochoric specific heat remains unknown for all presented mixtures as no measurements for these properties exist. Additionally, the question about the high-pressure phase envelope behavior of helium-neon is unanswered as the only two sources of measurements for the equilibria properties show some inconsistencies and are incomplete. Similarly, the potentially existing gas-gas equilibrium for neon-argon is not modeled because of lacking data. With very few measurements reported for the density of neon-argon, further studies are needed to check whether the EOS provides accurate predictions. The presented set of

equations available for the binary mixtures allows forming a model for a ternary mixture from the binary constituents. The additional measurements for any thermodynamic property of a given ternary mixture, e.g., helium-neon-nitrogen, would allow validating the so far unknown predictions for ternary mixtures.

The presented work on the equations of state has already found industrial and academic use. Air Liquide Advanced Technologies have applied the equations of state for helium-neon and helium-nitrogen to the cryogenic Brayton cycle calculations with mixed refrigerants. The ^4He-Ne equation has also been used for the cryogenic cycle calculations of the precooling stage for the Future Circular Collider, performed at Dresden University of Technology.[156] Developed equations show significant application potential with the helium-neon mixture being used for hydrogen liquefaction. The attractiveness of published equations for ^4He-Ne, ^4He-Ar, and $Ne-Ar$ has been recently emphasized by following publications on other equations of state for the thermodynamic properties of quantum mixtures.[22,32] The work on the equations and the parallel work on their application continues in Linde, SINTEF, and the University of Stuttgart. The developed equations of state fit in the industrial trend on applying fluid mixtures and open doors to the design of next-generation large-scale scientific infrastructures, such as the FCC or DEMO. The presented equations of state answer the industrial and scientific needs and can be easily integrated into the fluid property databases, such as REFPROP,[116] CoolProp,[2] or TREND.[119]

BIBLIOGRAPHY

[1] E. Tiesinga, P. J. Mohr, D. B. Newell, and B. N. Taylor. The 2018 CODATA recommended values of the fundamental physical constants. Database developed by J. Baker, M. Douma, and S. Kotochigova, National Institute of Standards and Technology, Gaithersburg, MD 20899, 2019. http://physics.nist.gov/constants. (Cited on page xxvii)

[2] I. H. Bell, J. Wronski, S. Quoilin, and V. Lemort. Pure and pseudo-pure fluid thermophysical property evaluation and the open-source thermophysical property library CoolProp. *Industrial & Engineering Chemistry Research*, 53(6):2498–2508, 2014. (Cited on pages xxviii, 40, 45, 52, 93, and 125)

[3] A. Abada *et al.* FCC-hh: The hadron collider. *The European Physical Journal Special Topics*, 228(4):755–1107, 2019. (Cited on pages 2 and 43)

[4] H. Quack, C. Haberstroh, I. Seemann, and M. Klaus. Nelium, a refrigerant with high potential for the temperature range between 27 and 70 K. *Physics Procedia*, 67:176–182, 2015. (Cited on page 2)

[5] S. Savelyeva *et al.* Natural neon-helium mixture as working fluid for 40-80 K cryogenic refrigerators. In *Proceedings of the 15th Cryogenics 2019 IIR International Conference*. International Institute of Refrigeration (IIR), 2019. (Cited on page 2)

[6] F. Millet *et al.* Preliminary conceptual design of FCC-hh cryoplants: Linde evaluation. *IOP Conference Series: Materials Science and Engineering*, 502:012131, 2019. (Cited on page 2)

[7] L. Tavian *et al.* Preliminary conceptual design of FCC-hh cryo-refrigerators: Air Liquide study. *IOP Conference Series: Materials Science and Engineering*, 755(1):012085, 2020. (Cited on page 2)

[8] B. Felder *et al.* Development of a cryogenic helium-neon gas mixture cooling system for use in a Gd-bulk HTS synchronous motor. *IEEE Transactions on Applied Superconductivity*, 21(3):2213–2216, 2011. (Cited on page 2)

[9] H.-M. Chang *et al.* Thermodynamic design of 10 kW Brayton cryocooler for HTS cable. In *Advances in Cryogenic Engineering*, volume 1434, pages 1664–1671. AIP, 2012. (Cited on page 2)

[10] J. Tanchon *et al.* A 40 K turbo-Brayton cryocooler for Earth observation applications. In S. D. Miller, Jr. R. G. Ross, and J. R. Raab, editors, *Cryocoolers 20, International Cryocooler Conference*, 2018. https://cryocooler.org/resources/Documents/C20/337.pdf. (Cited on page 2)

[11] H. K. Onnes and J. D. A. Boks. Further experiments with liquid helium. U. (Isotherms of monoatomic substances and their binary mixtures XXIV). Isotherms of helium at

4.2 degrees K. And lower. V. The variation of density of liquid helium below the boiling point. In *Proceedings of the Fourth International Congress of Refrigeration*, volume 170, pages 13–23. Communications from the Laboratory of Physics at the University of Leiden, 1924. (Cited on page 3)

[12] R. Gilgen, R. Kleinrahm, and W. Wagner. Measurement and correlation of the (pressure, density, temperature) relation of argon II. Saturated-liquid and saturated-vapour densities and vapour pressures along the entire coexistence curve. *The Journal of Chemical Thermodynamics*, 26(4):399–413, 1994. (Cited on page 3)

[13] M. Thol *et al.* Thermodynamic properties for neon for temperatures from the triple-point to 700 K at pressures to 700 MPa. Unpublished, 2018. (Cited on pages 3, 22, and 40)

[14] J. W. Gibbs. On the equilibrium of heterogeneous substances. *Transactions of the Connecticut Academy of Arts and Sciences*, 3:108–248, 1876. (Cited on page 4)

[15] U. K. Deiters and T. Kraska. *High-pressure fluid phase equilibria: phenomenology and computation*, volume 2. Elsevier, Amsterdam, 2012. https://www.elsevier.com/books/high-pressure-fluid-phase-equilibria/deiters/978-0-444-56347-7. (Cited on pages 5, 26, and 29)

[16] J. H. Vera and J. M. Prausnitz. Generalized van der Waals theory for dense fluids. *The Chemical Engineering Journal*, 3:1–13, 1972. (Cited on page 7)

[17] J. L. Lebowitz. Exact derivation of the van der Waals equation. *Physica*, 73(1):48–60, 1974. (Cited on page 7)

[18] T. Y. Kwak and G. A. Mansoori. Van der Waals mixing rules for cubic equations of state. Applications for supercritical fluid extraction modelling. *Chemical Engineering Science*, 41(5):1303–1309, 1986. (Cited on page 7)

[19] J. S. Rowlinson and F. L. Swinton. *Liquids and liquid mixtures*. Elsevier, 1982. https://doi.org/10.1016/c2013-0-04175-8. (Cited on page 8)

[20] D. Y. Peng and D. B. Robinson. A new two-constant equation of state. *Industrial & Engineering Chemistry Fundamentals*, 15(1):59–64, 1976. (Cited on page 8)

[21] R. Stryjek and J. H. Vera. PRSV2: A cubic equation of state for accurate vapor-liquid equilibria calculations. *The Canadian Journal of Chemical Engineering*, 64(5):820–826, 1986. (Cited on page 8)

[22] A. Aasen *et al.* Accurate quantum-corrected cubic equations of state for helium, neon, hydrogen, deuterium and their mixtures. *Fluid Phase Equilibria*, 524:112790, 2020. (Cited on pages 9, 40, 41, and 93)

[23] H. Reiss, H. L. Frisch, and J. L. Lebowitz. Statistical mechanics of rigid spheres. *The Journal of Chemical Physics*, 31(2):369–380, 1959. (Cited on page 9)

[24] N. F. Carnahan and K. E. Starling. Equation of state for nonattracting rigid spheres. *The Journal of Chemical Physics*, 51(2):635–636, 1969. (Cited on page 9)

[25] E. A. Guggenheim. Variations on van der Waals' equation of state for high densities. *Molecular Physics*, 9(2):199–200, 1965. (Cited on page 9)

[26] A. Mulero, C. Galan, and F. Cuadros. Equations of state for hard spheres. A review of accuracy and applications. *Physical Chemistry Chemical Physics*, 3(22):4991–4999, 2001. (Cited on page 10)

[27] O. Redlich and J. N. S. Kwong. On the thermodynamics of solutions. V. An equation of state. Fugacities of gaseous solutions. *Chemical Reviews*, 44(1):233–244, 1949. (Cited on page 10)

[28] S. Beret and J. M. Prausnitz. Perturbed hard-chain theory: An equation of state for fluids containing small or large molecules. *AIChE Journal*, 21(6):1123–1132, 1975. (Cited on page 11)

[29] R. Privat, R. Gani, and J.-N. Jaubert. Are safe results obtained when the PC-SAFT equation of state is applied to ordinary pure chemicals? *Fluid Phase Equilibria*, 295(1):76–92, 2010. (Cited on page 11)

[30] W. G. Chapman, G. Jackson, and K. E. Gubbins. Phase equilibria of associating fluids. *Molecular Physics*, 65(5):1057–1079, 1988. (Cited on page 11)

[31] J. E. Lennard-Jones. On the forces between atoms and ions. *Proceedings of the Royal Society of London. Series A, Containing Papers of a Mathematical and Physical Character*, 109(752):584–597, 1925. (Cited on page 12)

[32] A. Aasen, M. Hammer, E. A. Müller, and Ø. Wilhelmsen. Equation of state and force fields for Feynman–Hibbs-corrected Mie fluids. II. Application to mixtures of helium, neon, hydrogen, and deuterium. *The Journal of Chemical Physics*, 152(7):074507, 2020. (Cited on pages 12, 40, 41, and 93)

[33] M. Benedict, G. B. Webb, and L. C. Rubin. An empirical equation for thermodynamic properties of light hydrocarbons and their mixtures I. Methane, ethane, propane and n-butane. *The Journal of Chemical Physics*, 8(4):334–345, 1940. (Cited on page 12)

[34] R. T. Jacobsen and R. B. Stewart. Thermodynamic properties of nitrogen including liquid and vapor phases from 63 K to 2000 K with pressures to 10,000 bar. *Journal of Physical and Chemical Reference Data*, 2(4):757–922, 1973. (Cited on page 13)

[35] B. A. Younglove and M. O. McLinden. An international standard equation of state for the thermodynamic properties of refrigerant 123 (2,2-Dichloro-1,1,1-Trifluoroethane). *Journal of Physical and Chemical Reference Data*, 23(5):731–779, 1994. (Cited on page 13)

[36] R. Schmidt and W. Wagner. A new form of the equation of state for pure substances and its application to oxygen. *Fluid Phase Equilibria*, 19(3):175–200, 1985. (Cited on pages 13 and 14)

[37] R. T. Jacobsen, R. B. Stewart, M. Jahangiri, and S. G. Penoncello. A new fundamental equation for thermodynamic property correlations. In *Advances in Cryogenic Engineering*, pages 1161–1168. Springer US, 1986. (Cited on page 14)

[38] R. T. Jacobsen, R. B. Stewart, and M. Jahangiri. A thermodynamic property formulation for nitrogen from the freezing line to 2000 K at pressures to 1000 MPa. *International Journal of Thermophysics*, 7(3):503–511, 1986. (Cited on page 14)

[39] M. Jahangiri, R. T. Jacobsen, R. B. Stewart, and R. D. McCarty. A thermodynamic property formulation for ethylene from the freezing line to 450 K at pressures to 260 MPa. *International Journal of Thermophysics*, 7(3):491–501, 1986. (Cited on page 14)

[40] J. Tkaczuk *et al.* Equations of state for the thermodynamic properties of binary mixtures for helium-4, neon, and argon. *Journal of Physical and Chemical Reference Data*, 49(2):023101, 2020. (Cited on pages 15 and 40)

[41] I. H. Bell and E. W. Lemmon. Automatic fitting of binary interaction parameters for multi-fluid Helmholtz-energy-explicit mixture models. *Journal of Chemical & Engineering Data*, 61(11):3752–3760, 2016. (Cited on page 16)

[42] O. Kunz and W. Wagner. The GERG-2008 wide-range equation of state for natural gases and other mixtures: an expansion of GERG-2004. *Journal of Chemical & Engineering Data*, 57(11):3032–3091, 2012. (Cited on pages 16, 17, and 18)

[43] O. Kunz, R. Klimeck, W. Wagner, and M. Jaeschke. The GERG-2004 wide-range equation of state for natural gases and other mixtures. In *GERG TM15*, volume 6. Fortschritt-Berichte VDI, 2007. http://www.gerg.eu/public/uploads/files/publications/technical_monographs/tm15_04.pdf. (Cited on pages 16, 18, 26, and 39)

[44] D. O. Ortiz Vega. *A new wide range equation of state for helium-4*. PhD thesis, Texas A&M University, 2013. http://oaktrust.library.tamu.edu/handle/1969.1/151301. (Cited on pages 17, 18, 22, 24, 40, 49, and 70)

[45] I. H. Bell and U. K. Deiters. On the construction of binary mixture p-x and T-x diagrams from isochoric thermodynamics. *AIChE Journal*, 64(7):2745–2757, 2018. (Cited on pages 19 and 26)

[46] R. Beckmüller *et al.* New equations of state for binary hydrogen mixtures containing methane, nitrogen, carbon monoxide, and carbon dioxide. *Journal of Physical and Chemical Reference Data*, 50(1):013102, 2021. (Cited on page 20)

[47] K. Levenberg. A method for the solution of certain non-linear problems in least squares. *Quarterly of Applied Mathematics*, 2(2):164–168, 1944. (Cited on page 20)

[48] D. W. Marquardt. An algorithm for least-squares estimation of nonlinear parameters. *Journal of the Society for Industrial and Applied Mathematics*, 11(2):431–441, 1963. (Cited on page 20)

[49] R. Mittelhammer. *Econometric foundations*. Cambridge University Press, New York, 2000. (Cited on page 20)

[50] J. W. Leachman, R. T. Jacobsen, E. W. Lemmon, and S. G. Penoncello. *Thermodynamic properties of cryogenic fluids*. Springer International Publishing, Cham, 2017. https://doi.org/10.1007/978-3-319-57835-4. (Cited on page 20)

[51] R. D. McCarty and V. D. Arp. A new wide range equation of state for helium. In *Advances in Cryogenic Engineering*, volume 35, pages 1465–1475. Springer US, 1990. (Cited on page 22)

[52] C. Tegeler, R. Span, and W. Wagner. A new equation of state for argon covering the fluid region for temperatures from the melting line to 700 K at pressures up to 1000 MPa. *Journal of Physical and Chemical Reference Data*, 28(3):779–850, 1999. (Cited on pages 22, 40, 49, and 70)

[53] R. Span *et al.* A reference equation of state for the thermodynamic properties of nitrogen for temperatures from 63.151 to 1000 K and pressures to 2200 MPa. *Journal of Physical and Chemical Reference Data*, 29(6):1361–1433, 2000. (Cited on pages 22, 40, 47, 49, 66, and 70)

[54] A. Kazakov *et al.* NIST/TRC SOURCE data archival system: The next-generation data model for storage of thermophysical properties. *International Journal of Ther-*

mophysics, 33(1):22–33, 2011. https://trc.nist.gov/thermolit/. (Cited on page 24)

[55] A. Jäger, C. Breitkopf, and M. Richter. The representation of cross second virial coefficients by multifluid mixture models and other equations of state. *Industrial & Engineering Chemistry Research*, 2021. (Cited on page 26)

[56] A. Deerenberg, J. A. Schouten, and N. J. Trappeniers. Vapour-liquid and gas-gas equilibria in simple systems. *Physica A: Statistical Mechanics and its Applications*, 101(2-3):459–476, 1980. (Cited on page 26)

[57] C. K. Heck and P. L. Barrick. Liquid-vapor equilibria of the neon-helium system. In *Advances in Cryogenic Engineering*, volume 12, pages 714–718. Springer US, 1967. (Cited on pages 28 and 109)

[58] M. Knorn. Vapour-liquid equilibria of the neon-helium system. *Cryogenics*, 7(1-4):177, 1967. (Cited on pages 28 and 109)

[59] L. Holborn and J. Otto. Uber die Isothermen einiger Gase bis 400° und ihre Bedeutung fur das Gasthermometer. *Zeitschrift für Physik (GER)*, 23(1):77–94, 1924. (Cited on pages 28 and 109)

[60] J. Kestin, Ö. Korfali, J. V. Sengers, and B. Kamgar-Parsi. Density dependence and composition dependence of the viscosity of neon-helium and neon-argon mixtures. *Physica A: Statistical Mechanics and its Applications*, 106(3):415–442, 1981. (Cited on pages 28, 32, 109, and 111)

[61] J. Kestin and A. Nagashima. Viscosity of neon-helium and neon-argon mixtures at 20° and 30°C. *The Journal of Chemical Physics*, 40(12):3648–3654, 1964. (Cited on pages 28 and 109)

[62] I. Richardson and J. W. Leachman - unpublished results, Washington State University. (Cited on pages 28 and 109)

[63] W. F. Vogl and K. R. Hall. Compressibility data and virial coefficients for helium, neon and one mixture. *Physica*, 59(3):529–535, 1972. (Cited on pages 28 and 109)

[64] V. V. Pashkov, E. V. Konovodchenko, and O. V. Evdokumova. Speed of sound in the solution of helium with cryogenic liquids. *Journal of Engineering Physics (USSR)*, 4(51):603–608, 1985. (Cited on pages 28 and 109)

[65] J. C. Mullins. *Phase equilibria in the argon-helium and argon-hydrogen systems*. PhD thesis, Georgia Institute of Technology, Atlanta, 1965. https://smartech.gatech.edu/handle/1853/32791. (Cited on pages 30 and 110)

[66] J. C. Mullins and W. T. Ziegler. The system helium-argon from 65° to 140°K up to pressures of 120 atm. Correlation of available phase equilibrium data. Technical report 3 (project A-764), pp. 9, Georgia Institute of Technology, Atlanta, Engineering Experiment Station, 1965. (Cited on pages 30 and 110)

[67] J. C. Mullins and W. T. Zeigler. Phase equilibria in the argon-helium and argon-hydrogen systems from 68° to 108°K and pressures to 120 atmoshperes. In *International Advances in Cryogenic Engineering*, volume 10, pages 171–181. Springer US, 1965. (Cited on pages 30 and 110)

[68] J. E. Sinor and F. Kurata. Solubility of helium in liquid argon, oxygen, and carbon monoxide. *Journal of Chemical & Engineering Data*, 11(4):537–539, 1966. (Cited on pages 30 and 110)

[69] V. G. Skripka and N. N. Lobanova. Phase and volume ratios at low temperatures and high pressures. Experimental study of solubility of helium and neon in liquid oxygen, nitrogen, and argon. *Collection of papers Cryogenmash*, 13:90–103, 1971. (Cited on pages 30, 32, 33, 110, 111, and 112)

[70] W. B. Streett. Gas-liquid and fluid-fluid phase separation in the system helium+argon at high pressures. *Transactions of the Faraday Society*, 65:696, 1969. (Cited on pages 30 and 110)

[71] W. B. Streett and J. L. E. Hill. Phase equilibria in fluid mixtures at high pressures: The helium-argon system. *Transactions of the Faraday Society*, 67:622, 1971. (Cited on pages 30 and 110)

[72] W. B. Streett and A. L. Erickson. Phase equilibria in gas mixtures at high pressures: Implications for planetary structures. *Physics of the Earth and Planetary Interiors*, 5:357–366, 1972. (Cited on pages 30, 33, 110, and 112)

[73] A. L. Blancett, K. R. Hall, and F. B. Canfield. Isotherms for the He-Ar system at 50°C, 0°C and -50°C up to 700 atm. *Physica*, 47(1):75–91, 1970. (Cited on pages 30, 110, and 111)

[74] B. E. Kanishev and L. L. Pitaevskaya. Speed of sound and density of binary mixtures of helium with argon. *Journal of Engineering Physics (USSR)*, 39:1090–1094, 1980. (Cited on pages 30 and 110)

[75] N. D. Kosov and I. S. Brovanov. Compressibility of binary mixtures of helium, nitrogen, and argon with carbon dioxide from $59 \cdot 10^5$ to $590 \cdot 10^5$ Pa. *Teploenergetika (USSR)*, pages 77–79, 1975. (Cited on pages 30 and 110)

[76] V. Y. Maslennikova, V. A. Abovskii, A. N. Egorov, and D. S. Tsiklis. Compressibility of homogeneous gaseous solutions under high pressures: helium-argon system. *Russian Journal of Physical Chemistry (USSR)*, 52(11):2968–2969, 1978. (Cited on pages 30 and 110)

[77] V. N. Popov, V. I. Chernyshev, and V. R. Petrov. P-V-T-x dependence of helium-argon mixtures. *Moscow Energy Institute (USSR)*, 75:69–74, 1970. (Cited on pages 30 and 110)

[78] J. A. Provine and F. B. Canfield. Isotherms for the He-Ar system at -130, -115, and -90°C up to 700 atm. *Physica*, 52(1):79–91, 1971. (Cited on pages 30 and 110)

[79] D. Vidal, L. Guengant, P. Malbrunot, and J. Vermesse. Densities of argon-helium and argon-neon dense mixtures uo to 8000 bar. *Physica A: Statistical Mechanics and its Applications*, 137(1-2):417–424, 1986. (Cited on pages 30, 32, 110, and 111)

[80] D. Vidal, P. Malbrunot, and J. Vermesse. Sound velocity of equimolar dense noble-gas mixtures. *International Journal of Thermophysics*, 12(5):943–948, 1991. (Cited on pages 30, 32, 110, and 111)

[81] Y. Hanayama. Measurements on adiabatic compressibility of mixed gases (He-Xe, He-Ar) under high pressure. *Ehime Daigaku Kiyo, Dai-3-bu (JAP)*, 9(1):23–31, 1978. (Cited on pages 30 and 110)

[82] Y. L. Kachanov, B. E. Kanishev, and L. L. Pitaevskaya. Speed of sound in argon and in mixtures helium+argon and nitrogen+carbon dioxide at high pressures. *Journal of Engineering Physics (USSR)*, 44:5–8, 1983. (Cited on pages 30 and 110)

[83] T. Nishitake and Y. Hanayama. Measurements on adiabatic compressibility of helium-argon mixed gas under high pressure. Technical Report 4, Ehime University, 1977. Section III, Volume 8, pp. 507-513. (Cited on pages 30 and 110)

[84] W. B. Streett. Liquid-vapor equilibrium in the system neon-argon. *The Journal of Chemical Physics*, 42(2):500–503, 1965. (Cited on pages 32 and 111)

[85] W. B. Streett. Liquid-vapor phase behavior and liquid phase density in the system neon-argon at high pressures. *The Journal of Chemical Physics*, 46(9):3282–3286, 1967. (Cited on pages 32 and 111)

[86] W. B. Streett and J. L. E. Hill. Phase equilibria in fluid mixtures at high pressures: The neon-argon system. *The Journal of Chemical Physics*, 54(12):5088–5094, 1971. (Cited on pages 32 and 111)

[87] N. J. Trappeniers and J. A. Schouten. Vapour-liquid and gas-gas equilibria in simple systems II. The system neon-argon. *Physica*, 73(3):539–545, 1974. (Cited on pages 32 and 111)

[88] E. V. Konovodchenko, V. V. Pashkov, and Y. I. Khokhlov. Volumetric thermodynamic properties of Ne-Ar solutions. *Ukrainian Journal of Physics (UKR)*, 26:1480–1485, 1981. (Cited on pages 32 and 111)

[89] R. J. Burch. Low temperature phase equilibria of the gas-liquid system helium-neon-nitrogen. *Journal of Chemical & Engineering Data*, 9(1):19–24, 1964. (Cited on pages 33 and 112)

[90] G. Buzyna, R. A. Macriss, and R. T. Ellington. Vapor-liquid equilibrium of the helium-nitrogen system. *Chemical Engineering Progress Symposium Series*, 59(44):101, 1963. (Cited on pages 33 and 112)

[91] J. A. Davis, N. Rodewald, and F. Kurata. An apparatus for phase studies between 20° K and 300° K. *Industrial & Engineering Chemistry*, 55(11):36–42, 1963. (Cited on pages 33 and 112)

[92] I. A. Davydov and S. S. Budnevich. Investigation of the equilibrium composition of a nitrogen-helium mixutre. *Journal of Engineering Physics (USSR)*, 20(6):776–779, 1971. (Cited on pages 33 and 112)

[93] W. E. DeVaney, B. Dalton, and J. C. Meeks Jr. Vapor-liquid equilibria of the helium-nitrogen system. *Journal of Chemical & Engineering Data*, 8(4):473–478, 1963. (Cited on pages 33 and 112)

[94] M. G. Gonikberg and V. G. Fastovskii. Solubility of gases in liquids at low temperatures and high pressures: II solubility of helium in liquid nitrogen at temperatures of 78-109 K and pressures up to 295 atm. *Russian Journal of Physical Chemistry (USSR)*, 14:257, 1940. (Cited on pages 33 and 112)

[95] F. F. Kharakhorin. Phase relations in systems of liquified gases the binary system nitrogen+helium. *Journal of Technical Physics (USSR)*, 10:1533–1540, 1940. (Cited on pages 33 and 112)

[96] N. C. Rodewald, J. A. Davis, and F. Kurata. The heterogeneous phase behavior of the helium-nitrogen system. *AIChE Journal*, 10(6):937–943, 1964. (Cited on pages 33, 34, 112, and 113)

[97] W. B. Streett and J. L. E. Hill. Phase equilibria in fluid mixtures at high pressures: The helium-nitrogen system. *The Journal of Chemical Physics*, 52(3):1402–1406, 1970. (Cited on pages 33 and 112)

[98] W. B. Streett. Gas-liquid and fluid-fluid phase separation in the system helium-nitrogen near the critical temperature of nitrogen. *Chemical Engineering Progress Symposium Series*, 63(81):37–42, 1967. (Cited on pages 33 and 112)

[99] P. C. Tully, W. E. DeVaney, and H. L. Rhodes. Phase equilibria of the helium-nitrogen system from 122 to 126°K. In *Advances in Cryogenic Engineering*, pages 88–95. Springer US, 1971. (Cited on pages 33 and 112)

[100] T. C. Briggs and A. R. Howard. *Compressibility data for helium, nitrogen, and helium-nitrogen mixtures at 0°, 25°, and 50°C and at pressured to 1000 atmospheres*, volume 7639 of *Report of Investigation*. U.S. Bureau of Mines, 1972. (Cited on pages 34 and 112)

[101] I. S. Brovanov. Compressibility of binary mixtures of helium with nitrogen and argon at pressures of 300-600 bar. *Diffuziya v Gazakh i Zhidkostyakh (USSR)*, pages 104–108, 1974. (Cited on pages 34 and 112)

[102] I. S. Brovanov and N. D. Kosov. Experimental investigation of the compressibility of binary mixtures of helium with nitrogen up to 300 bar in the temperature range of 273-373 K. *Prikladnaya i Teoreticheskaya Fizika (USSR)*, 6:124–129, 1974. (Cited on pages 34 and 112)

[103] F. B. Canfield, T. W. Leland, and R. Kobayashi. Compressibility factors for helium-nitrogen mixtures. *Journal of Chemical & Engineering Data*, 10(2):92–96, 1965. (Cited on pages 34 and 112)

[104] J. D. Cramer. *The compressibility of gaseous mixtures of helium-nitrogen and helium-deuterium at high pressures*. Los Alamos, N.M.: Los Alamos Scientific Laboratory of the University of California, 1965. https://catalog.hathitrust.org/Record/012213836. (Cited on pages 34 and 112)

[105] K. R. Hall and F. B. Canfield. Isotherms for the He-N_2 system at -190°C, -170°C and -160°C up to 700 ATM. *Physica*, 47(2):219–226, 1970. (Cited on pages 34 and 112)

[106] P. S. Ku and B. F. Dodge. Compressibility of the binary systems: helium-nitrogen and carbon dioxide-ethylene. *Journal of Chemical & Engineering Data*, 12(2):158–164, 1967. (Cited on pages 34 and 113)

[107] V. Y. Maslennikova, A. N. Egorov, and D. S. Tsiklis. The compressibility of homogeneous gaseous solutions at ultrahigh pressures. The helium-nitrogen system. *Russian Journal of Physical Chemistry (USSR)*, 51(11):1712–1713, 1977. (Cited on pages 34 and 113)

[108] V. Y. Maslennikova, A. N. Egorov, and D. S. Tsiklis. Compressibility of homogenious gases: helium-nitrogen at high pressures. *Proceedings of the USSR Academy of Sciences (USSR)*, pages 115–117, 1978. (Cited on pages 34 and 113)

[109] J. E. Miller, L. Stroud, and L. W. Brandt. Compressibility of helium-nitrogen mixtures. *Journal of Chemical & Engineering Data*, 5(1):6–9, 1960. (Cited on pages 34 and 113)

[110] J. E. Miller, L. W. Brandt, and L. Stroud. *Compressibility factors for helium and helium-nitrogen mixtures*, volume 5845 of *Report of Investigation*. U.S. Bureau of Mines, 1961. (Cited on pages 34 and 113)

[111] V. N. Popov and V. I. Chernyshev. Experimental determination of compressibility of the nitrogen-helium mixtures. *Teploenergetika (USSR)*, pages 82–84, 1969. (Cited on pages 34 and 113)

[112] W. B. Streett. Liquid phase density in the system helium-nitrogen. *Journal of Chemical & Engineering Data*, 13(2):210–212, 1968. (Cited on pages 34 and 113)

[113] W. Zhang, S. N. Biswas, and J. A. Schouten. Compressibility isotherms of helium-nitrogen mixtures at 298.15 K and up to 10 kbar. *Physica A: Statistical Mechanics and its Applications*, 182(3):353–364, 1992. (Cited on pages 34 and 113)

[114] A. Van Itterbeek and W. Van Doninck. Measurements on the velocity of sound in mixtures of hydrogen, helium, oxygen, nitrogen and carbon monoxide at low temperatures. *Proceedings of the Physical Society. Section B*, 62(1):62–69, 1949. (Cited on pages 34 and 113)

[115] W. Zhang and J. A. Schouten. The sound velocity of a mixture of He and N_2 up to 10 kbar and from 157 K to 298 K. *Fluid Phase Equilibria*, 79:211–220, 1992. (Cited on pages 34 and 113)

[116] E. W. Lemmon, I. H. Bell, M. L. Huber, and M. O. McLinden. NIST Standard Reference Database 23: Reference Fluid Thermodynamic and Transport Properties – REFPROP, Version 10.0, National Institute of Standards and Technology, 2018. https://www.nist.gov/srd/refprop. (Cited on pages 39, 40, 52, and 93)

[117] E. W. Lemmon. Preliminary equation of state for helium-neon mixture. Unpublished, 2016. (Cited on page 39)

[118] I. Cullimore and E. W. Lemmon. Preliminary equation of state for neon-argon mixture. Unpublished, 2010. (Cited on page 39)

[119] R. Span *et al.* TREND. Thermodynamic Reference and Engineering Data 4.0. Lehrstuhl für Thermodynamik. Ruhr-Universität Bochum: Bochum, Germany, 2019. http://www.thermo.ruhr-uni-bochum.de/. (Cited on pages 40 and 93)

[120] H. A. Lorentz. Ueber die Anwendung des Satzes vom Virial in der kinetischen Theorie der Gase. *Annalen der Physik (GER)*, 248(1):127–136, 1881. (Cited on page 41)

[121] D. Berthelot. Sur le mélange des gaz. *Comptes Rendus (FR)*, 126:1703–1706, 1898. (Cited on page 41)

[122] P. Virtanen *et al.* SciPy 1.0: fundamental algorithms for scientific computing in python. *Nature Methods*, 17:261–272, 2020. (Cited on pages 42 and 56)

[123] J. A. Nelder and R. Mead. A simplex method for function minimization. *The Computer Journal*, 7(4):308–313, 1965. (Cited on page 42)

[124] R. Storn and K. Price. Differential evolution – a simple and efficient heuristic for global optimization over continuous spaces. *Journal of Global Optimization*, 11(4):341–359, 1997. (Cited on page 42)

[125] P. P. J. Gans. Joule-Thomson expansion. Physical chemistry I, 1993. https://tccc.iesl.forth.gr/education/local/Labs-PC-II/articles/JT.pdf. (Cited on page 44)

[126] G. W. Castellan. *Physical chemistry*. Addison-Wesley Publishing Company, Inc., 1971. (Cited on page 46)

[127] F. S. Manning and L. N. Canjar. Joule-Thomson and second virial coefficients for hydrocarbons. *Journal of Chemical & Engineering Data*, 6(3):364–365, 1961. (Cited on page 46)

[128] J. R. Roebuck. The Joule-Thomson effect in air. *Proceedings of the National Academy of Sciences of the United States of America*, 12(1):55–58, 1926. (Cited on pages 47, 49, 50, and 53)

[129] J. R. Roebuck and H. Osterberg. The Joule-Thomson effect in helium. *Physical Review*, 43(1):60–69, 1933. (Cited on pages 47, 49, 50, and 53)

[130] J. R. Roebuck and H. Osterberg. The Joule-Thomson effect in argon. *Physical Review*, 46(9):785–790, 1934. (Cited on pages 47, 49, 50, and 53)

[131] J. R. Roebuck and H. Osterberg. The Joule-Thomson effect in nitrogen. *Physical Review*, 48(5):450–457, 1935. (Cited on pages 47, 49, 50, and 53)

[132] E. S. Burnett and J. R. Roebuck. On a radial flow porous plug and calorimeter. *Physical Review (Series I)*, 30(4):529–531, 1910. (Cited on pages 47, 50, and 53)

[133] E. S. Burnett. Experimental study of the Joule-Thomson effect in carbon dioxide. *Physical Review*, 22(6):590–616, 1923. (Cited on pages 47, 50, and 53)

[134] E. W. Deming and L. S. Deming. Some physical properties of compressed gases. V. The Joule-Thomson coefficient for nitrogen. *Physical Review*, 48:448–449, 1935. (Cited on page 47)

[135] R. C. King and J. H. Potter. An axial-flow porous plug apparatus. *Journal of Engineering for Industry*, 84(1):180, 1962. (Cited on pages 47, 49, and 50)

[136] J. H. Potter and M. J. Levy. An axial-flow porous plug apparatus II. In *Progress in International Research on Thermodynamic and Transport Properties*, pages 147–152. Elsevier, 1962. (Cited on pages 47, 49, and 50)

[137] R. L. Smith. *Joule-Thomson coefficients of propane and n-butane*. PhD thesis, California Institute of Technology, 1970. https://doi.org/10.7907/1TJD-R369. (Cited on pages 48, 49, 50, 53, and 89)

[138] K. Bier, G. Ernst, and G. Maurer. Flow apparatus for measuring the heat capacity and the Joule-Thomson coefficient of gases. *The Journal of Chemical Thermodynamics*, 6(11):1027–1037, 1974. (Cited on pages 48 and 49)

[139] T. Eisenbach *et al.* Speed-of-sound measurements and a fundamental equation of state for propylene glycol. *Journal of Physical and Chemical Reference Data*, 50(2):023105, 2021. (Cited on page 49)

[140] H. Gedanitz, M. J. Dávila, E. Baumhögger, and R. Span. An apparatus for the determination of speeds of sound in fluids. *The Journal of Chemical Thermodynamics*, 42(4):478–483, 2010. (Cited on page 49)

[141] L. F. S. Souza, S. Herrig, R. Span, and J. P. Martin Trusler. Experimental density and an improved Helmholtz-energy-explicit mixture model for (CO_2 + CO). *Applied Energy*, 251:113398, 2019. (Cited on page 49)

[142] E. W. Lemmon, M. O. McLinden, U. Overhoff, and W. Wagner. A reference equation of state for propylene for temperatures from the melting line to 575 K and pressures up to 1000 MPa. Unpublished, 2018. (Cited on page 49)

[143] E. W. Lemmon, R. T. Jacobsen, S. G. Penoncello, and D. G. Friend. Thermodynamic properties of air and mixtures of nitrogen, argon, and oxygen from 60 to 2000 K at pressures to 2000 MPa. *Journal of Physical and Chemical Reference Data*, 29(3):331–385, 2000. (Cited on page 49)

[144] D. Bücker and W. Wagner. Reference equations of state for the thermodynamic properties of fluid phase n-butane and isobutane. *Journal of Physical and Chemical Reference Data*, 35(2):929–1019, 2006. (Cited on page 49)

[145] P. Eckels and R. Stewart. CryoComp, Eckels Engineering Inc., version 5.0, 2009. http://www.eckelsengineering.com/. (Cited on page 52)

[146] ISO 5167-2:2003. Measurement of fluid flow by means of pressure differential devices inserted in circular cross-section conduits running full – Part 2: Orifice plates. Technical report, International Organization for Standardization, Geneva (CH), 2003. https://www.iso.org/standard/30190.html. (Cited on page 52)

[147] G. O. Brown. The Darcy-Weisbach equation. *Oklahoma State University–Stillwater*, 2000. (Cited on page 53)

[148] C. F. Colebrook. Turbulent flow in pipes, with particular reference to the transition region between the smooth and rough pipe laws. *Journal of the Institution of Civil Engineers*, 11(4):133–156, 1939. (Cited on page 54)

[149] R. L. Burden and J. D. Faires. *Numerical analysis (Third ed.)*. Prindle, Weber & Schmidt, Boston, MA, USA, 1985. (Cited on page 54)

[150] W. R. Dean. Note on the motion of fluid in a curved pipe. *The London, Edinburgh, and Dublin Philosophical Magazine and Journal of Science*, 4(20):208–223, 1927. (Cited on page 54)

[151] Stanford Research Systems. *BGA244 binary gas analyzer user manual*. https://www.thinksrs.com/downloads/pdfs/manuals/BGA244m.pdf. (Cited on page 62)

[152] R. Span and W. Wagner. A new equation of state for carbon dioxide covering the fluid region from the triple-point temperature to 1100 K at pressures up to 800 MPa. *Journal of Physical and Chemical Reference Data*, 25(6):1509–1596, 1996. (Cited on page 66)

[153] C. R. Harris *et al.* Array programming with NumPy. *Nature*, 585:357–362, 2020. (Cited on page 72)

[154] S. Bell. *A beginner's guide to uncertainty measurement no. 11*. Centre for Basic, Thermal and Length Metrology, National Physical Laboratory, 1999. https://www.dit.ie/media/physics/documents/GPG11.pdf. (Cited on page 76)

[155] M. Palmer. Experimental techniques in fluids. Propagation of uncertainty through mathematical operations. http://web.mit.edu/fluids-modules/www/exper_techniques/2.Propagation_of_Uncertaint.pdf. (Cited on page 76)

[156] S. Savelyeva, C. Haberstroh, S. Klöppel, and H. Quack. Specification for Nelium refrigeration system. Technical report, Dresden University of Technology for EASITrain, 2021. https://fcc.web.cern.ch/easitrain/Documents/WP4/Milestone%20and%20Deliverables/D4.2/EASITrain-WP4-D4.

2-SpecificationForNeliumRefrigerationSystem_V0100.pdf. (Cited on page 93)

[157] R. Berman, F. A. B. Chaves, D. M. Livesley, and C. D. Swartz. The solubility of solid H_2 and Ne in high-pressure ^{4}He. *Journal of Physics C*, 12(20):777–780, 1979. (Cited on page 109)

[158] J. Brewer and G. W. Vaughn. Measurement and correlation of some interaction second virial coefficients from -125° to 50°C. I. *The Journal of Chemical Physics*, 50(7):2960–2968, 1969. (Cited on pages 109, 111, and 113)

[159] M. B. Iomtev *et al.* Solubility of neon in gaseous helium. *Russian Journal of Physical Chemistry (USSR)*, 51:1373–1376, 1977. (Cited on page 109)

[160] C. M. Knobler, J. J. M. Beenakker, and H. F. P. Knaap. The second virial coefficient of gaseous mixtures at 90°K. *Physica*, 25(7-12):909–916, 1959. (Cited on pages 109, 111, and 113)

[161] N. K. Kalfoglou and J. G. Miller. Compressibility of gases. V. Mixtures of spherically symmetric molecules at higher temperatures. The helium-argon and helium-tetafluoromethane systems. *The Journal of Physical Chemistry*, 71(5):1256–1264, 1967. (Cited on page 111)

[162] M. L. Martin, R. D. Trengove, K. R. Harris, and P. J. Dunlop. Excess second virial coefficients for some dilute binary gas mixtures. *Australian Journal of Chemistry*, 35(8):1525, 1982. (Cited on page 111)

[163] C. C. Tanner and I. Masson. The pressures of gaseous mixtures. Part III. *Proceedings of the Royal Society A: Mathematical, Physical, and Engineering Sciences*, 126(801):268–288, 1930. (Cited on page 111)

[164] J. F. Mathews and D. C. D. Morey. Compressibilities of helium-nitrogen mixtures. *The Canadian Journal of Chemical Engineering*, 49(2):282–285, 1971. (Cited on page 113)

[165] A. E. Edwards and W. E. Roseveare. The second virial coefficients of gaseous mixtures. *Journal of the American Chemical Society*, 64(12):2816–2819, 1942. (Cited on page 113)

[166] W. C. Pfefferle, J. A. Goff, and J. G. Miller. Compressibility of gases. I. The Burnett method. An improved method of treatment of the data. Extension of the method to gas mixtures. *The Journal of Chemical Physics*, 23(3):509–513, 1955. (Cited on page 113)

[167] K. F. Liu. *Phase equilibria in the helium-carbon dioxide, -argon, -methane, -nitrogen, and -oxygen systems*. PhD thesis, Georgia Institute of Technology, Atlanta, 1969. http://hdl.handle.net/1853/11853. (Cited on page 113)

[168] G. M. Kramer and J. G. Miller. Compressibility of gases. III. The second and third virial coefficients of mixtures of helium and nitrogen at 30°. *The Journal of Physical Chemistry*, 61(6):785–788, 1957. (Cited on page 113)

[169] T. N. Bell and P. J. Dunlop. Excess and interaction second virial coefficients for seven binary gaseous systems. *Chemical Physics Letters*, 84(1):99–103, 1981. (Cited on page 113)

[170] F. B. Canfield, T. W. Leland, and R. Kobayashi. Volumetric behavior of gas mixtures at low temperatures by the Burnett method: The helium-nitrogen system, 0° to -140°C.

In *Advances in Cryogenic Engineering*, pages 146–157. Springer US, 1963. (Cited on page 113)

[171] R. J. Witonsky and J. G. Miller. Compressibility of gases. IV. The Burnett method applied to gas mixtures at higher temperatures. The second virial coefficients of the helium-nitrogen system from 175° to 475°. *Journal of the American Chemical Society*, 85(3):282–286, 1963. (Cited on page 113)

[172] W. Zhang, J. A. Schouten, H. M. Hinze, and M. Jaeschke. PVT-x behavior of helium-nitrogen mixtures from 270 to 353 K and up to 280 bar. *Journal of Chemical & Engineering Data*, 37(1):114–119, 1992. (Cited on page 113)

Appendix A - Experimental data for the EOS development

Table A.1. Experimental data for ^{4}He — Ne

Reference	Data points Available	Used	T/K	p/MPa	x_{He}	Uncertainty[a]	AAD[b]/%
				VLE data			
[57]	76	36	27 - 42	0.3 - 20	0.01 - 0.36	±3% in p	15.0
[58]	22	22	25 - 27	0.6 - 5.1	0.002 - 0.03	± 0.02 K in T ±0.02% in x ±0.1% in y	4.3
				ρpT data			
[59]	39	39	273 - 673	2.5 - 10	0.28	N/A[c]	0.26
[60]	97	97	298	0.2 - 12.2	0.23, 0.80	±0.1% in ρ	0.20
[61]	90	73	293 - 303	0.1 - 6.3	0.26 - 0.95	±0.1% in ρ	0.24
[62]	8	6	32 - 41	0.5 - 2.1	0.02 - 0.03	N/A[c]	2.0
[63]	51	51	233 - 313	0.1 - 3.6	0.49	±0.04% in Z	0.081
				Speed of sound (w)			
[64]	41	36	26 - 38	0.1 - 15	0.01 - 0.29	±0.1% in w	9.6
				Second virial coefficient (B)			
[157]	3	0	15 - 20			±5% in B	**55.3**[d]
[158]	8	0	148 - 323			±5% in B	**3.9**[d]
[59]	5	0	273 - 673			N/A[c]	**8.8**[d]
[159]	6	0	15 - 20			±6% in B	**57.6**[d]
[160]	1	0	90			±3% in B	**5.9**[d]
[63]	3	0	233 - 313			±4% in B	**3.6**[d]

[a] Author claimed uncertainty.
[b] Average absolute deviation (AAD) of data set from EOS, calculated with Eq. (3.25).
[c] Undefined or poor uncertainty analysis.
[d] EOS not fitted to this data set.

Table A.2. Experimental data for ^{4}He − Ar

Reference	Data points Available	Used	T/K	p/MPa	x_{He}	Uncertainty[a]	AAD[b]/%
				VLE / GGE data			
65	354	0	68 - 108	2.0 - 12	0.001 - 0.02	±0.03 K in T ±0.5% in p ±2% in x ±3% in y	**24.0**[d]
66	187	187	85 - 140	0.5 - 12	$6 \cdot 10^{-5}$ - 0.02	±0.03 K in T ±0.5% in p ±2% in x ±3% in y	3.4
67	50	0	86 - 108	2.0 - 12	0.002 - 0.02	±0.03 K in T ±0.5% in p ±1 − 2% in x	**3.6**[d]
68	29	0	93 - 148	1.7 - 14		±0.5% in p ±1.0% in x	**12.0**[d]
69	77	64	90 - 115	2.9 - 22	0.0005 - 0.002	±0.02 vol. % in x	3.5
70	56	48	91 - 148	1.4 - 69	0.002 - 0.44	±0.02 K in T ±2 mol % in x	15.0
71	202	176	91 - 160	0.6 - 422	0.02 - 0.60	±0.1% in p ±0.01 K in T ±0.1 mol % in x	15.0
72	81	74	150 - 199	386 - 1048	0.27 - 0.72	±0.01 K in T ±100 psi in p ±0.15 mol % in x	7.7
				***ρpT* data**			
73	288	288	223 - 323	0.3 - 73	0.21 - 0.80	±0.03 K in T ±0.06% in Z	0.72
74	41	41	373, 473	50 - 180	0.66, 0.95	N/A[c]	1.8
75	59	59	293 - 353	29 - 59	0.24 - 0.79	±0.05 K in T ±0.3% in ρ	2.2
76	116	116	293 - 423	180 - 800	0.31, 0.74	±0.5% in ρ	2.4
77	45	45	293 - 673	5.0 - 40	0.11 - 0.98	±0.05 K in T ±0.05% in p ±0.02% in x_{He}	1.3
78	212	212	143 - 183	0.2 - 68	0.22 - 0.80	N/A[c]	1.2
79	31	31	298	0.1 - 800	0.50	±0.2% in ρ	1.5
80	13	13	298	80 - 800	0.50	±0.2% in ρ	1.9
				Speed of sound (w)			
81	51	27	298	109 - 1972	0.50 - 0.90	±0.5% in w	5.1
82	22	20	298 - 422	100 - 700	0.21	±0.63% in w	1.3
83	47	47	298	201 - 1696	0.50 - 0.90	±0.5% in w	11.0
80	13	13	298	80 - 800	0.50	±0.2% in w	2.4

[a] Author claimed uncertainty.
Continued on next page
[b] Average absolute deviation (AAD) of data set from EOS, calculated with Eq. (3.25).
[c] Undefined or poor uncertainty analysis.
[d] EOS not fitted to this data set.

Table A.2. (*Continued.*)

Reference	Data points Available	Used	T/K	p/MPa	x_{He}	Uncertainty[a]	AAD[b]/%
			Second virial coefficient (B)				
73	15	0	223 - 323			±0.03 K in T ±0.3% in B	**21.0**[d]
158	8	0	148 - 323			±5% in B	**11.0**[d]
161	60	0	303 - 773			±1.31% in B	**16.9**[d]
160	1	0	90			± 2 - 3% in B	**6.1**[d]
162	3	0	290 - 320			greater than 1.2%	**5.9**[d]
163	14	0	298			N/A[c]	**18.9**[d]

[a] Author claimed uncertainty.
[b] Average absolute deviation (AAD) of data set from EOS, calculated with Eq. (3.25).
[c] Undefined or poor uncertainty analysis.
[d] EOS not fitted to this data set.

Table A.3. Experimental data for Ne — Ar

Reference	Data points Available	Used	T/K	p/MPa	x_{Ne}	Uncertainty[a]	AAD[b]/%
			VLE data				
69	84	54	91 - 120	2.9 - 20	0.03 - 0.31	±0.02 vol. % in x	8.0
84	54	53	84 - 130	0.4 - 7.3	0.05 - 0.73	±0.01 K in T ±0.01 MPa in p	11.0
85	37	36	95 - 130	7.5 - 62	0.09 - 0.57	N/A[c]	12.0
86	58	58	87 - 93	6.4 - 103	0.002 - 0.09	±0.02 K in T ±0.1% in p ±0.1 mol % in x	6.7
87	67	59	93 - 138	0.5 - 101	0.002 - 0.57	±0.1 mol % in x	13.0
			ρpT data				
60	21	21	298	0.4 - 13.7	0.23, 0.73	±0.1% in ρ	0.43
85	109	107	102 - 121	3.0 - 55.2	0.04 - 0.50	±1.0% in ρ	2.5
79	31	31	298	0.1 - 800	0.50	±0.2% in ρ	1.6
80	13	13	298	80 - 800	0.50	±0.2% in ρ	2.8
			Speed of sound (w)				
88	10	0	102, 121	1.3 - 15	0.22	N/A[c]	**60.0**[d]
80	13	13	298	80 - 800	0.50	±0.2% in w	1.2
			Second virial coefficient (B)				
158	9	0	123 - 323			±5% in B	**9.7**[d]
160	1	0	90			± 2-3% in B	**5.9**[d]

[a] Author claimed uncertainty.
[b] Average absolute deviation (AAD) of data set from EOS, calculated with Eq. (3.25).
[c] Undefined or poor uncertainty analysis.
[d] EOS not fitted to this data set.

Table A.4. Experimental data for $^4He - N_2$

Reference	Data points Available	Used	T/K	p/MPa	x_{He}	Uncertainty[a]	AAD[b]/%
				VLE / GGE data			
[89]	12	11	82, 113	0.5 - 5	0.002 - 0.04	±0.2 K in T ±0.1% in p ±0.15 mol % in x ±2 mol % in y	16.7
[90]	30	20	77 - 123	1.1 - 6.9	0.003 - 0.09	N/A[c]	26.7
[91]	18	7	77	3.6 - 6.8	0.008 - 0.015	±0.1 K in T ±2% in x	93.3
[92]	25	0	77 - 126	2 - 10	0.11 - 0.20	N/A[c]	54.5
[93]	280	131	76 - 120	0.5 - 13.8	0.001 - 0.14	±0.5 K in T ±0.2 mol % in x	45.0
[94]	29	13	78 - 109	2.7 - 28	0.009 - 0.18	N/A[c]	42.4
[95]	84	59	68 - 111	0.45 - 21.8	0.001 - 0.14	N/A[c]	43.1
[96]	19	0	65 - 77	0.04 - 2.2	0.55 - 0.61	±0.5 K in T ±10% in p	15.8
[69]	25	13	67 - 90	0.6 - 2.6	0.0007 - 0.009	±0.02 vol. % in x	45.5
[97]	151	108	77 - 137	13 - 410	0.04 - 0.64	±0.01 K in T ±100 psi in p ±0.15 mol % in x	12.1
[98]	86	63	77 - 121	6.8 - 83	0.06 - 0.56	N/A[c]	19.8
[72]	125	96	112 - 162	246 - 1020	0.24 - 0.77	±0.01 K in T ±100 psi in p ±0.15 mol % in x	17.6
[99]	77	46	122 - 126	3 - 21	0.006 - 0.34	±0.01 K in T ±2 psi(a) in p ±0.04% in x_{He}	20.0
				ρpT data			
[100]	462	396	273 - 298	0.1 - 101	0.1 - 0.9	±0.015 K in T ±0.01% in p ±1.0% in ρ	1.1
[101]	98	98	293 - 353	29 - 59	0.41 - 0.84	N/A[c]	1.5
[102]	185	185	273 - 373	6.9 - 29.4	0.21 - 0.84	N/A[c]	0.96
[103]	884	851	133 - 273	0.3 - 55	0.15 - 0.87	±0.15% in Z	0.84
[104]	43	43	298	10 - 122.5	0.13 - 0.92	±0.01 K in T ±0.3% in p ±1.0% in x	2.3
[105]	134	131	83 - 113	0.16 - 22	0.3 - 0.88	N/A[c]	0.08

[a] Author claimed uncertainty.

Continued on next page

[b] Average absolute deviation (AAD) of data set from EOS, calculated with Eq. (3.25).

[c] Undefined or poor uncertainty analysis.

[d] EOS not fitted to this data set.

Table A.4. (*Continued.*)

Reference	Data points Available	Used	T/K	p/MPa	x_{He}	Uncertainty[a]	AAD[b]/%
[106]	153	109	311, 373	0.3 - 29.9	0.16 - 0.67	±0.02 K in T ±0.02% in p ±0.015% in ρ ±0.2% in B	0.24
[107,108]	208	201	298 - 423	100 - 700	0.30, 0.54	±0.5% in ρ	2.8
[109,110]	306	306	294	0.9 - 10.0	0.06 - 0.99	±0.14% in Z	0.40
[111]	55	37	295 - 598	5.8 - 34	0.22 - 0.79	±0.05 K in T ±0.05% in p ±0.02% in x_{He}	0.48
[96]	30	30	69, 77	1.4 - 6.9	0.01 - 0.99	±0.5 K in T ±10% in p	21.0
[112]	34	34	77 - 117	9.6 - 55	0.016 - 0.35	±0.02 K in T ±0.5 atm in p ±1.0% in x	2.1
[113]	103	100	298	212 - 1018	0.25 - 0.75	±0.005 K in T ±0.05% in p ±0.1% in ρ	2.0
				Speed of sound (w)			
[114]	20	20	75 - 90	0.01	0.1 - 0.7	N/A[c]	0.25
[115]	112	98	156 - 298	200 - 1000	0.498	±0.002 K in T ±0.05% in p ±0.15% in w	4.5
				Second virial coefficient (B)			
[164]	30	0	310 - 449			±0.1 K in T ±0.1% in p ±1.25% in Z	**2.4**[d]
[111]	29	0	296 - 598			±0.05 K in T ±0.05% in p ±0.02% in x_{He}	**2.6**[d]
[165]	1	0	298			±5% in B	**24.9**[d]
[166]	4	0	303			±2% in B	**4.7**[d]
[167]	30	0	100 - 750			±3 - 5% in B	**8.0**[d]
[168]	21	0	303			N/A[c]	**3.0**[d]
[169]	10	0	292 - 321			±2% in B	**9.1**[d]
[170]	54	0	133 - 273			N/A[c]	**4.0**[d]
[158]	8	0	148 - 323			±5% in B	**9.6**[d]
[171]	58	0	298 - 748			±1.7% in B	**1.8**[d]
[160]	1	0	90			±2 - 3% in B	**2.9**[d]
[172]	31	0	270 - 253			±2 - 5% in B	**5.6**[d]

[a] Author claimed uncertainty.
[b] Average absolute deviation (AAD) of data set from EOS, calculated with Eq. (3.25).
[c] Undefined or poor uncertainty analysis.
[d] EOS not fitted to this data set.

Appendix B - Thermodynamic properties calculated with the EOS

Table B.1. Single-phase properties as a function of Helmholtz energy.

Property	Relation to Helmholtz energy
$p = -\left(\frac{\partial a}{\partial v}\right)_{T,\overline{x}}$	$\rho RT\left(1+\delta\alpha_\delta^{\mathrm{r}}\right)$
$Z = -\frac{1}{\rho RT}\left(\frac{\partial a}{\partial v}\right)_{T,\overline{x}}$	$1+\delta\alpha_\delta^{\mathrm{r}}$
$u = a + Ts$	$RT\left(\tau\left(\alpha_\tau^{\mathrm{o}}+\alpha_\tau^{\mathrm{r}}\right)\right)$
$h = u + pv$	$RT\left(1+\tau\left(\alpha_\tau^{\mathrm{o}}+\alpha_\tau^{\mathrm{r}}\right)+\delta\alpha_\delta^{\mathrm{r}}\right)$
$s = -\left(\frac{\partial a}{\partial T}\right)_{v,\overline{x}}$	$R\left(\tau\left(\alpha_\tau^{\mathrm{o}}+\alpha_\tau^{\mathrm{r}}\right)-\alpha^{\mathrm{o}}-\alpha^{\mathrm{r}}\right)$
$c_{\mathrm{v}} = \left(\frac{\partial u}{\partial T}\right)_{v,\overline{x}}$	$-R\tau^2\left(\alpha_{\tau\tau}^{\mathrm{o}}+\alpha_{\tau\tau}^{\mathrm{r}}\right)$
$c_{\mathrm{p}} = \left(\frac{\partial h}{\partial T}\right)_{p,\overline{x}}$	$R\left(-\tau^2\left(\alpha_{\tau\tau}^{\mathrm{o}}+\alpha_{\tau\tau}^{\mathrm{r}}\right)+\frac{\left(1+\delta\alpha_\delta^{\mathrm{r}}-\delta\tau\alpha_{\delta\tau}^{\mathrm{r}}\right)^2}{1+2\delta\alpha_\delta^{\mathrm{r}}+\delta^2\alpha_{\delta\delta}^{\mathrm{r}}}\right)$
$g = h - Ts$	$RT\left(1+\alpha^{\mathrm{o}}+\alpha^{\mathrm{r}}+\delta\alpha_\delta^{\mathrm{r}}\right)$
$w = \sqrt{\frac{1}{M}\left(\frac{\partial p}{\partial \rho}\right)_{s,\overline{x}}}$	$\sqrt{\frac{RT}{M}\left(1+2\delta\alpha_\delta^{\mathrm{r}}+\delta^2\alpha_{\delta\delta}^{\mathrm{r}}-\frac{\left(1+\delta\alpha_\delta^{\mathrm{r}}-\delta\tau\alpha_{\delta\tau}^{\mathrm{r}}\right)^2}{\tau^2\left(\alpha_{\tau\tau}^{\mathrm{o}}+\alpha_{\tau\tau}^{\mathrm{r}}\right)}\right)}$
$\mu_{\mathrm{JT}} = \left(\frac{\partial T}{\partial p}\right)_{h,\overline{x}}$	$\frac{1}{R\rho}\,\frac{-\left(\delta\alpha_\delta^{\mathrm{r}}+\delta^2\alpha_{\delta\delta}^{\mathrm{r}}+\delta\tau\alpha_{\delta\tau}^{\mathrm{r}}\right)}{\left(1+\delta\alpha_\delta^{\mathrm{r}}-\delta\tau\alpha_{\delta\tau}^{\mathrm{r}}\right)^2-\tau^2\left(\alpha_{\tau\tau}^{\mathrm{o}}+\alpha_{\tau\tau}^{\mathrm{r}}\right)\left(1+2\delta\alpha_\delta^{\mathrm{r}}+\delta^2\alpha_{\delta\delta}^{\mathrm{r}}\right)}$
$B = \lim_{\rho\to 0}\left(\frac{\partial Z}{\partial \rho}\right)_{T,\overline{x}}$	$\frac{1}{\rho_{\mathrm{r}}}\lim_{\delta\to 0}\alpha_\delta^{\mathrm{r}}$

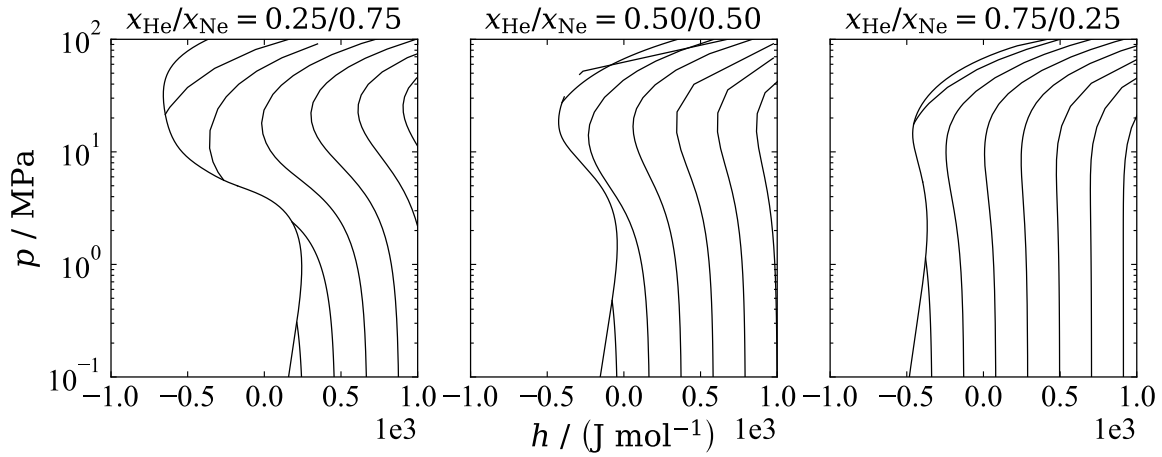

(a) Pressure-enthalpy diagrams with T = const. isolines

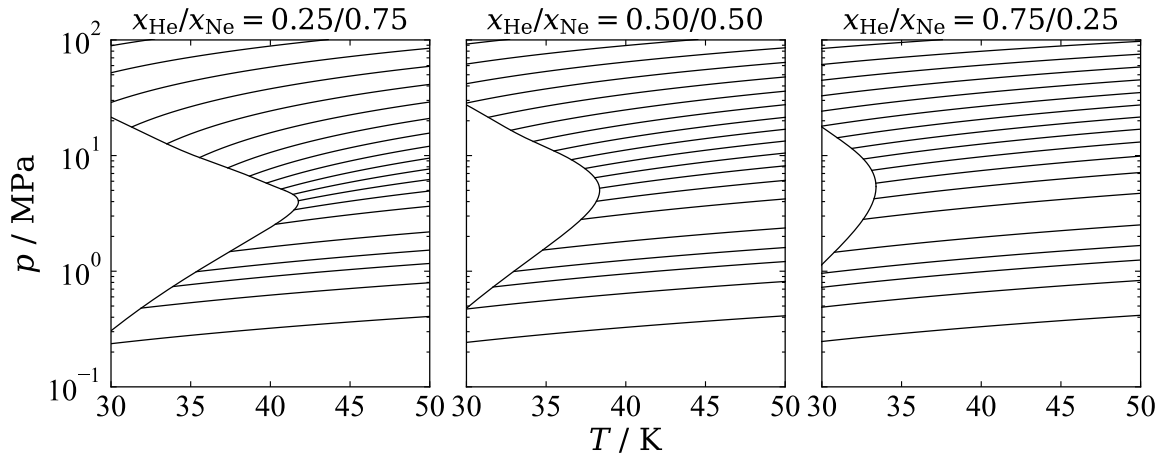

(b) Pressure-temperature diagrams with ρ = const. isolines

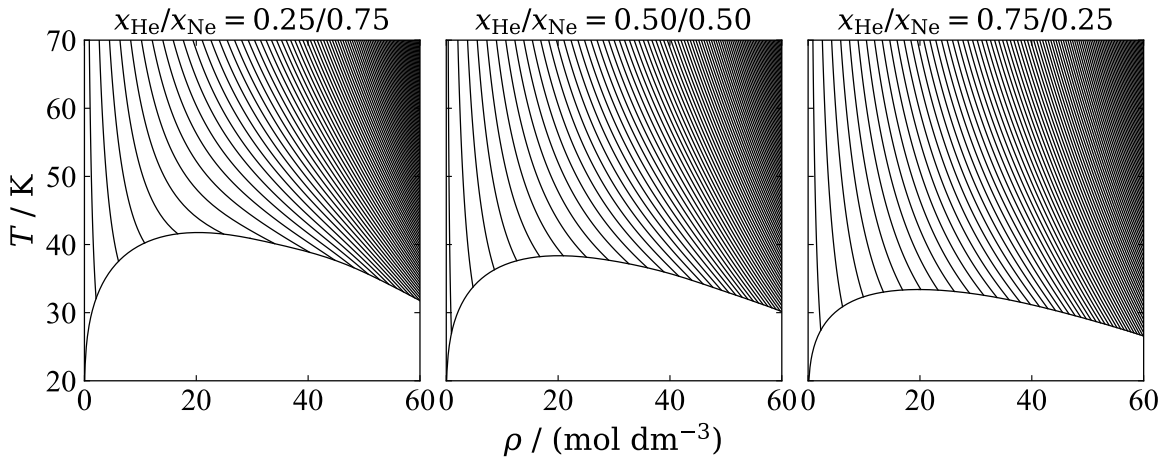

(c) Temperature-density diagrams with p = const. isolines

Fig. B.1. Characteristic plots for ^{4}He − Ne. *Continued on next page*

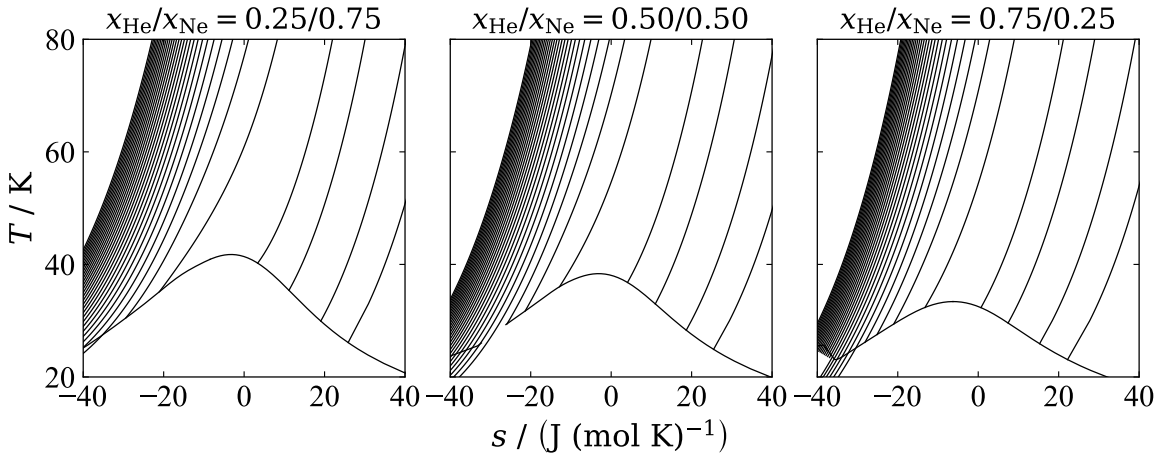

(d) Temperature-entropy diagrams with p = const. isolines

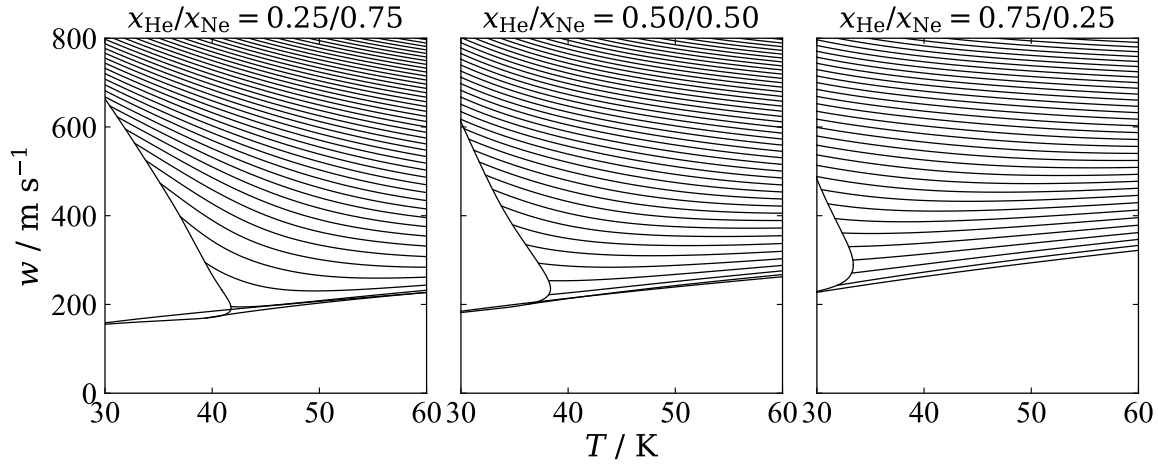

(e) Speed of sound-temperature diagrams with p = const. isolines

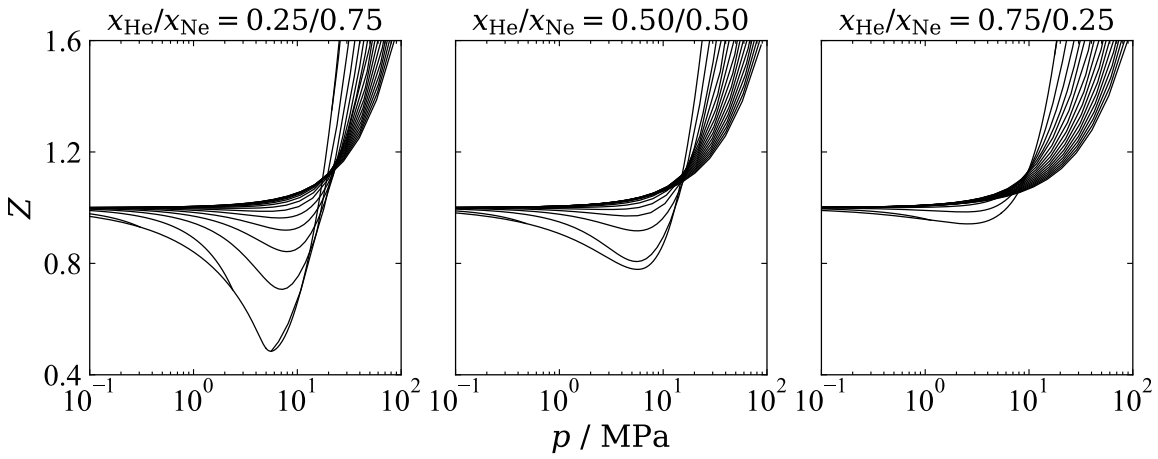

(f) Compressibility factor-pressure diagrams with T = const. isolines

Fig. B.1. Characteristic plots for ^{4}He − Ne.

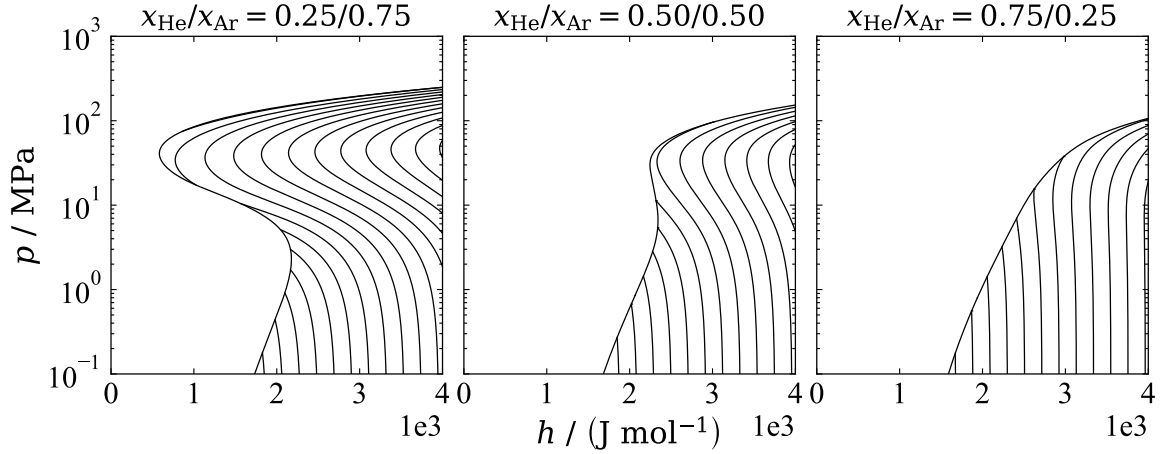

(a) Pressure-enthalpy diagrams with T = const. isolines

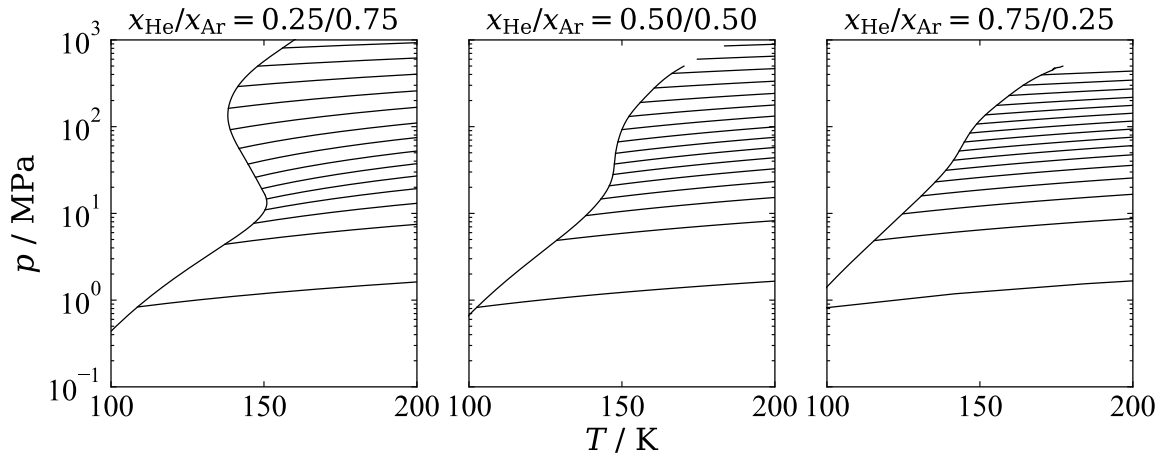

(b) Pressure-temperature diagrams with ρ = const. isolines

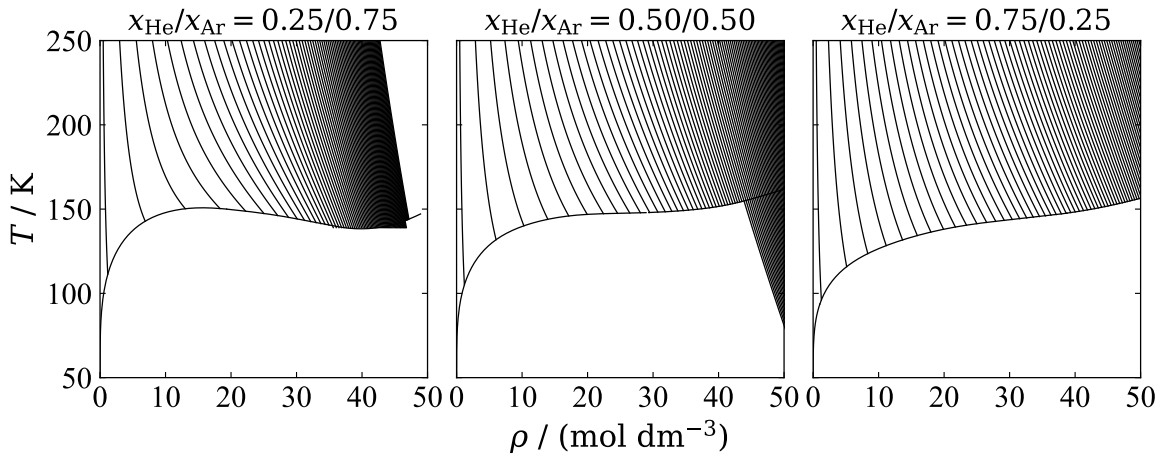

(c) Temperature-density diagrams with p = const. isolines

Fig. B.2. Characteristic plots for ^{4}He − Ar. *Continued on next page*

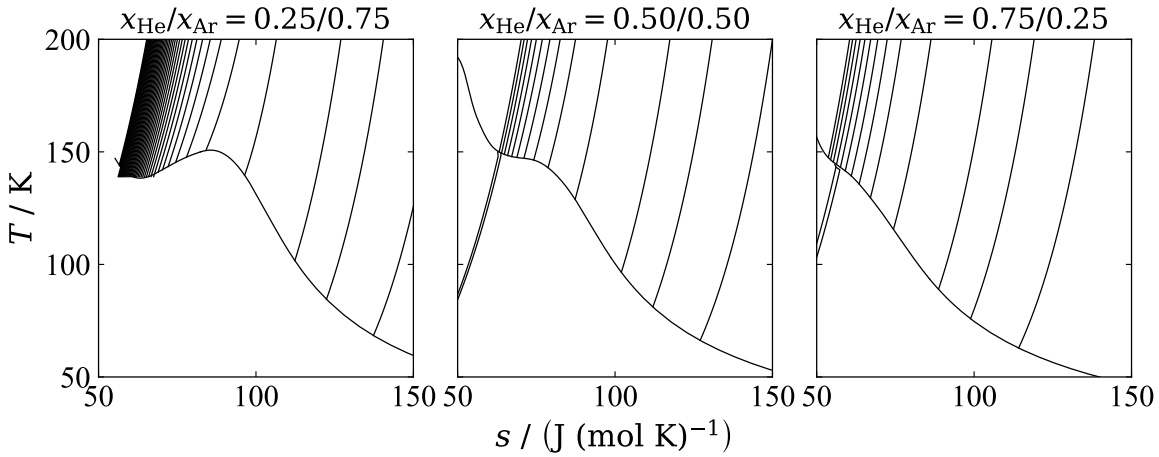

(d) Temperature-entropy diagrams with p = const. isolines

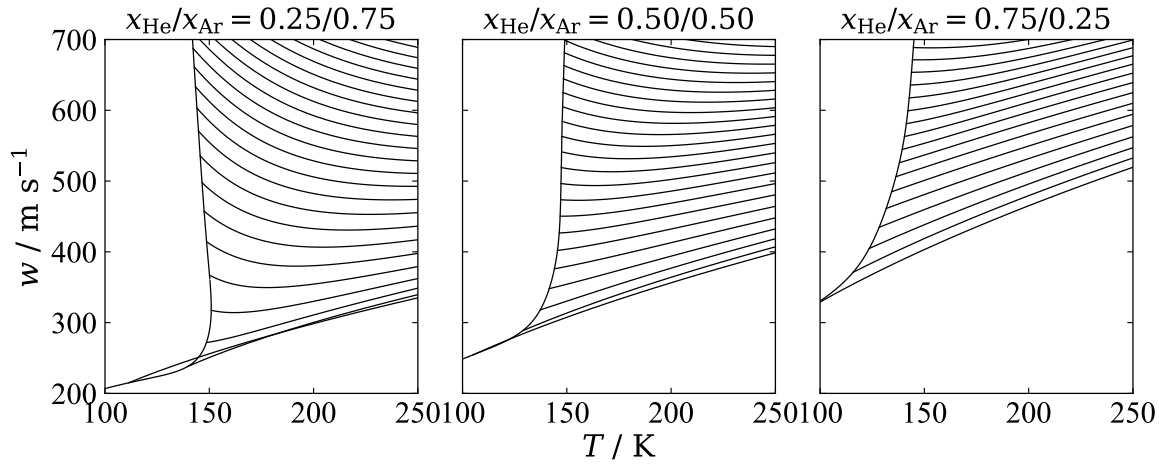

(e) Speed of sound-temperature diagrams with p = const. isolines

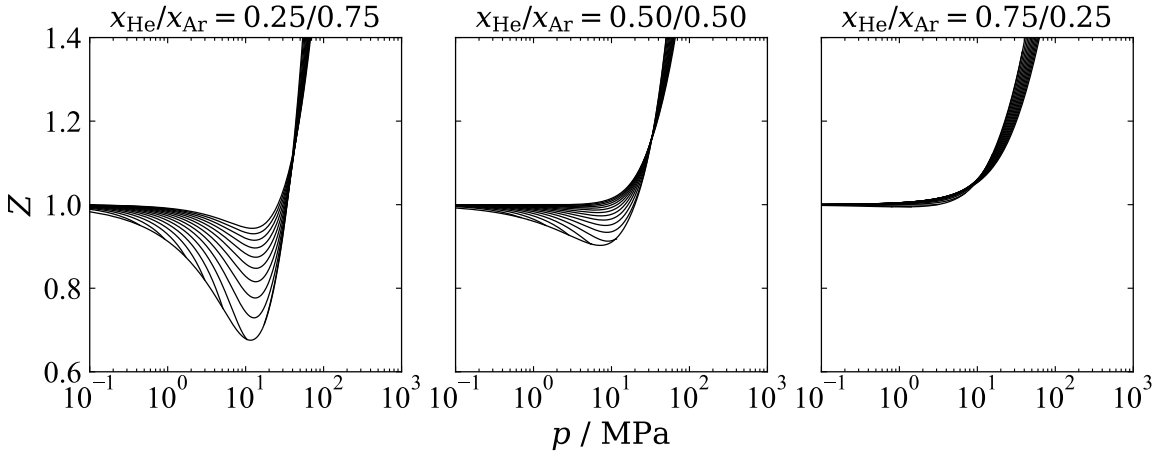

(f) Compressibility factor-pressure diagrams with T = const. isolines

Fig. B.2. Characteristic plots for ^{4}He − Ar.

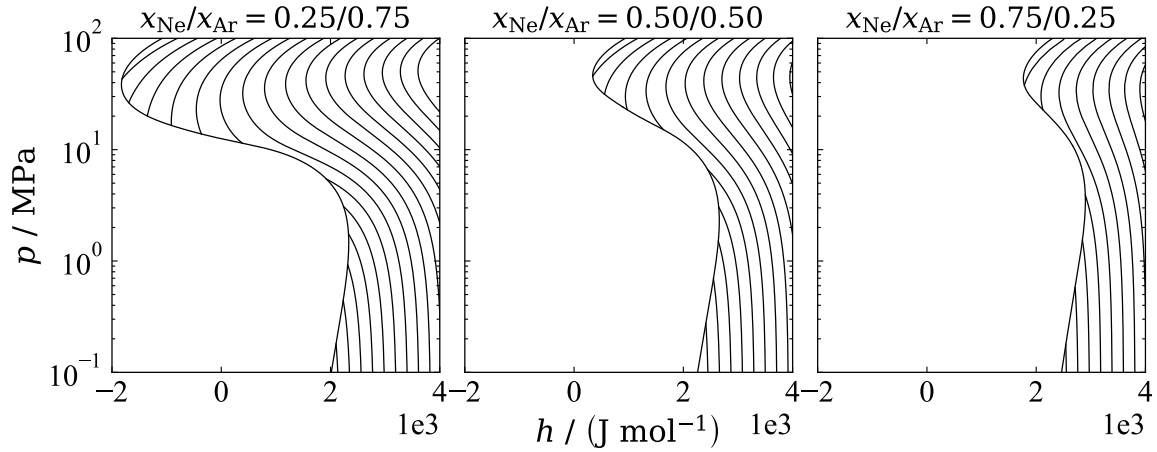

(a) Pressure-enthalpy diagrams with T = const. isolines

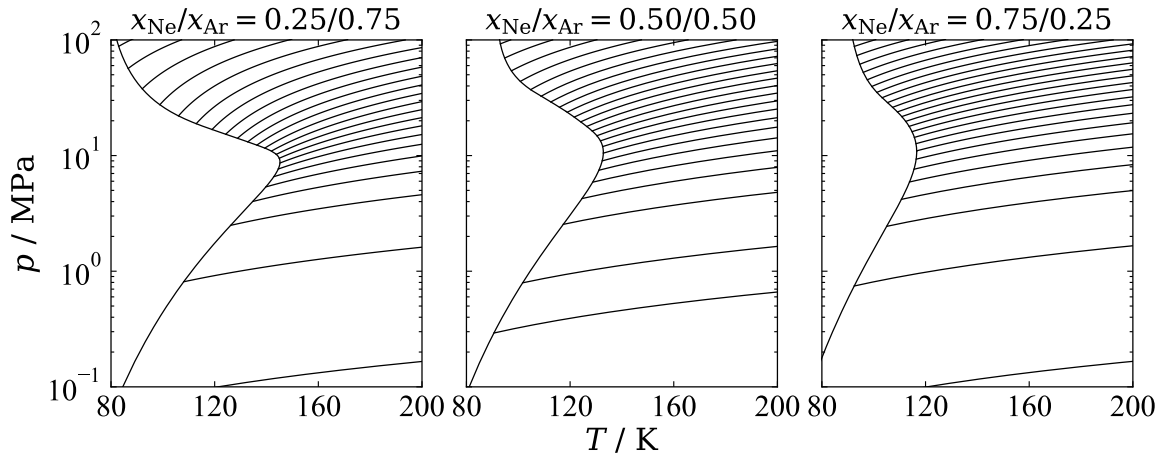

(b) Pressure-temperature diagrams with ρ = const. isolines

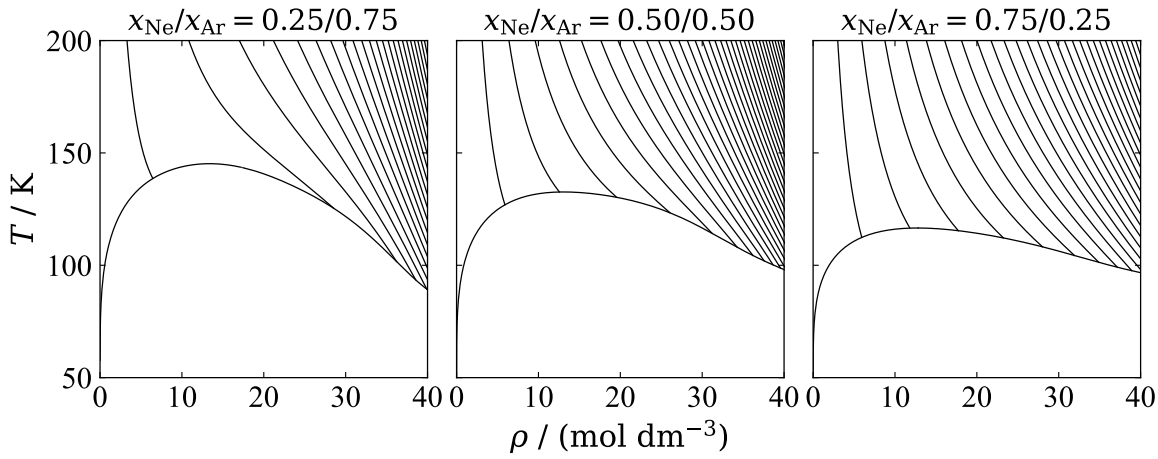

(c) Temperature-density diagrams with p = const. isolines

Fig. B.3. Characteristic plots for Ne — Ar. *Continued on next page*

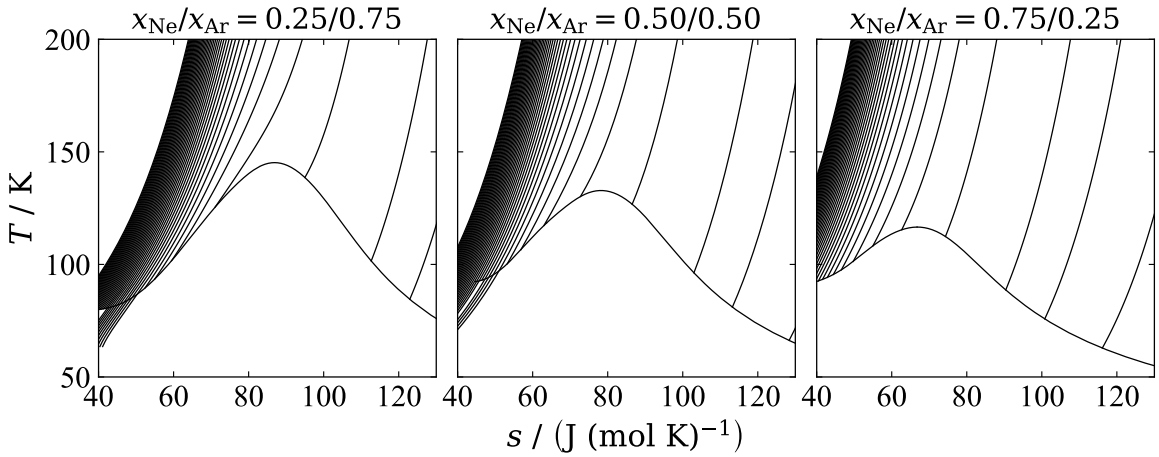

(d) Temperature-entropy diagrams with p = const. isolines

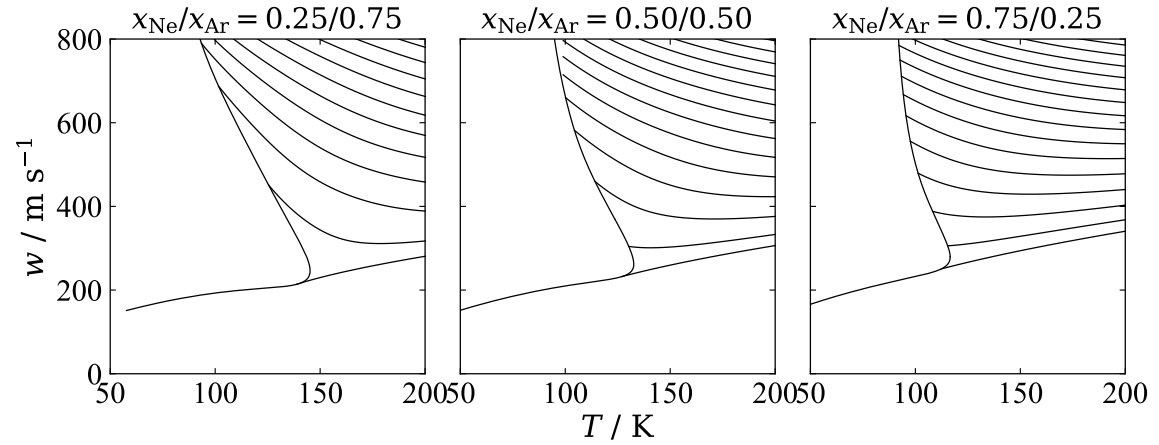

(e) Speed of sound-temperature diagrams with p = const. isolines

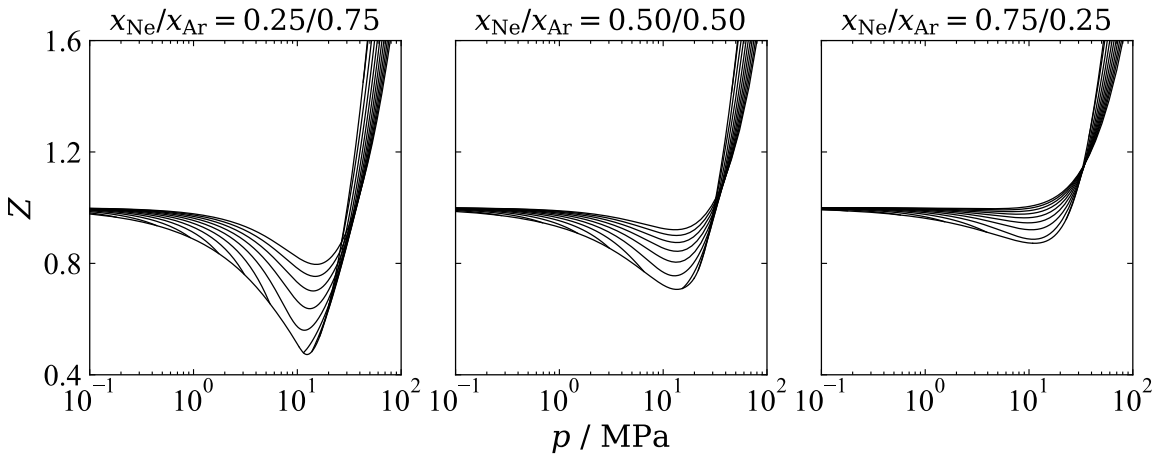

(f) Compressibility factor-pressure diagrams with T = const. isolines

Fig. B.3. Characteristic plots for Ne − Ar.

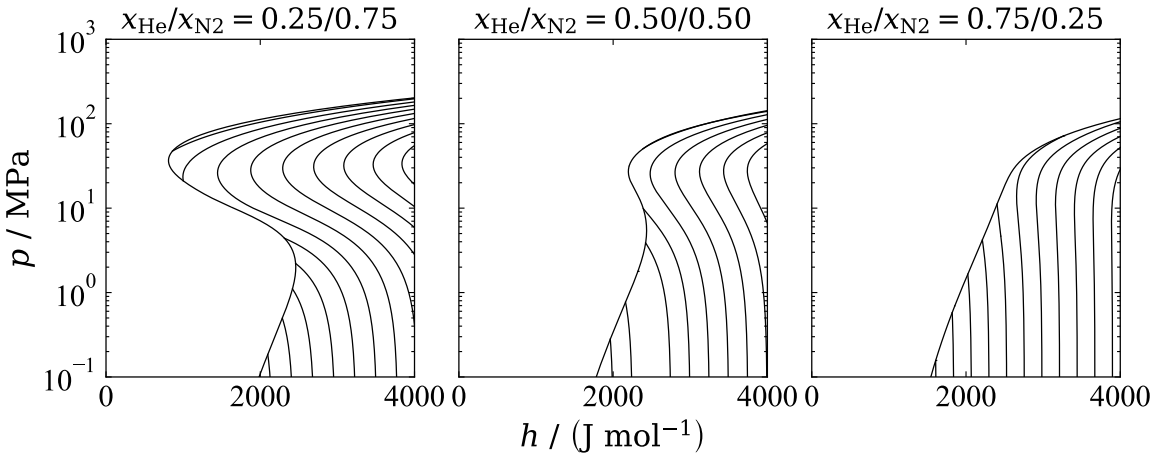

(a) Pressure-enthalpy diagrams with T = const. isolines

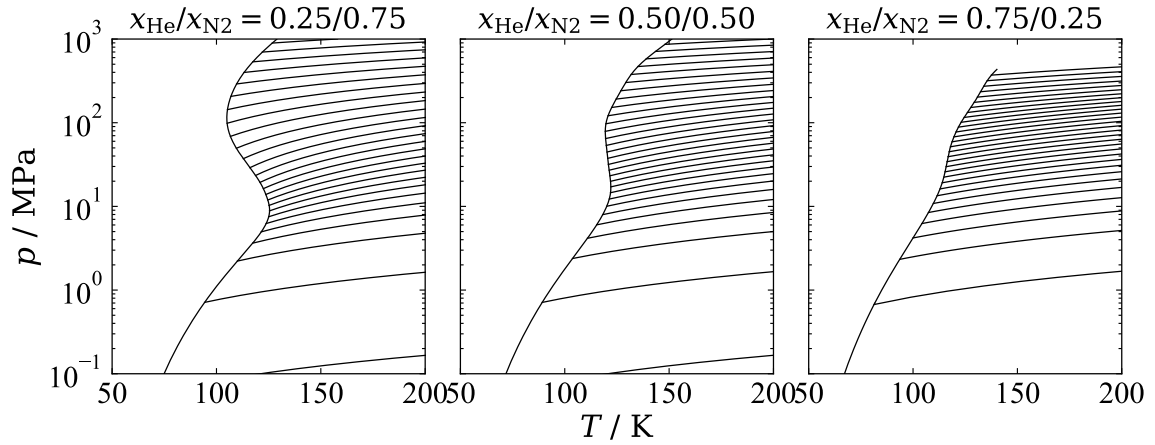

(b) Pressure-temperature diagrams with ρ = const. isolines

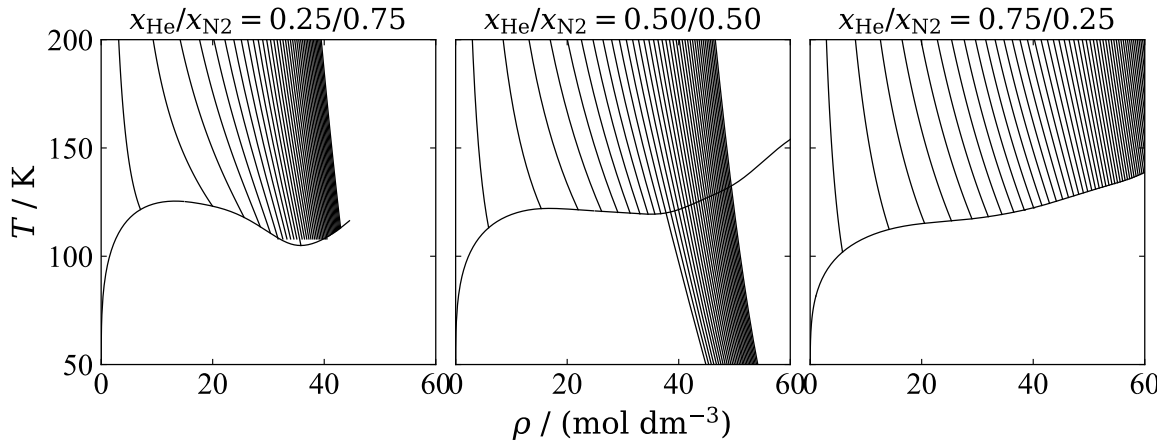

(c) Temperature-density diagrams with p = const. isolines

Fig. B.4. Characteristic plots for $^4He - N_2$. *Continued on next page*

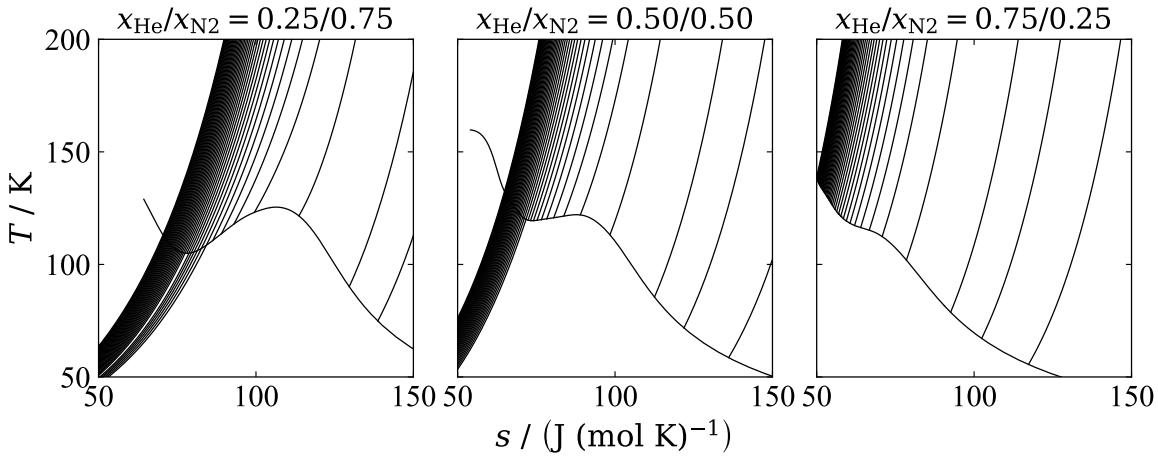

(d) Temperature-entropy diagrams with p = const. isolines

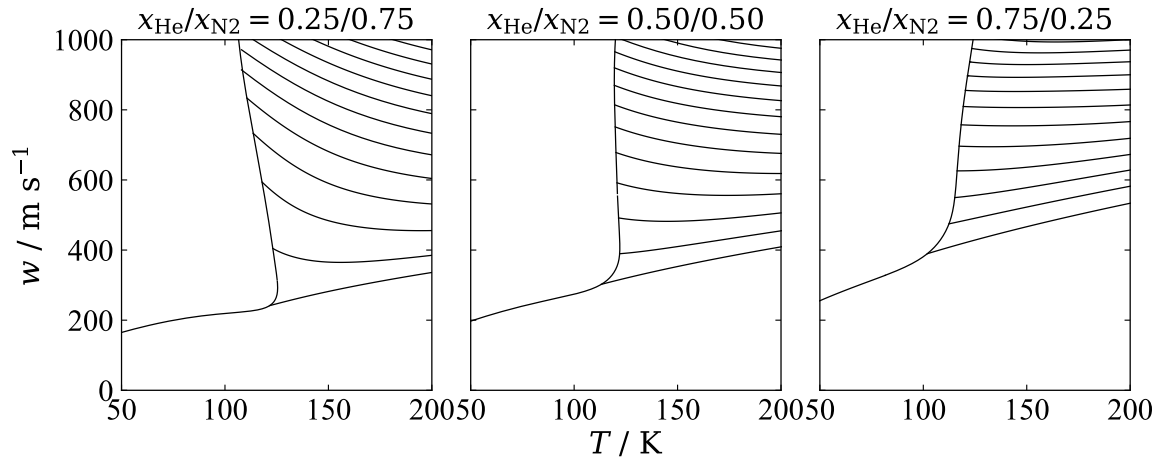

(e) Speed of sound-temperature diagrams with p = const. isolines

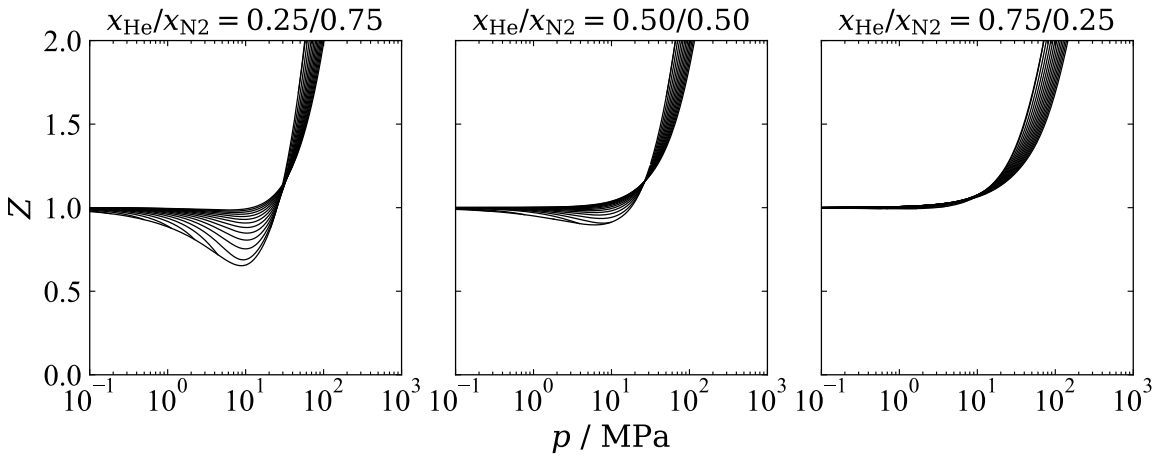

(f) Compressibility factor-pressure diagrams with T = const. isolines

Fig. B.4. Characteristic plots for $^4He - N_2$.

Appendix C - Python script for validating EOS implementation

CoolProp[2] is required to run the `test_data.py` python script. It can be installed from the following link: `CoolProp-automatic-installation`.

`Helium.json`, `Neon.json`, `Argon.json`, and `Nitrogen.json` files need to be placed in the same directory as `test_data.py`. These json files are copies of the CoolProp fluid files from `CoolProp/dev/fluids` directory.
`test_data.py` file:

```
import json
import itertools
from collections import namedtuple
import CoolProp
import CoolProp.CoolProp as CP
print('CoolProp version:', CoolProp.__version__)
print('CoolProp git revision:', CoolProp.__gitrevision__)

def setup_CoolProp(fluids):
  CP.set_config_bool(CP.OVERWRITE_FLUIDS,True)

  # Read in the fluid files
  for fluid in fluids:
    contents = json.load(open(fluid+'.json'))
    CP.add_fluids_as_JSON('HEOS',json.dumps([contents]))

  # departure functions for EOS developed in this work
  departure_JSON = [
  {
    "Name": "Helium-Neon",
    "aliases" : [],
    "type" : "Gaussian+Exponential",
    "BibTeX" : "Tkaczuk-2020",
    "Npower" : 3,
    "n": [-4.346849, -0.884378, 0.258416, 3.502188, 0.831330, 2.740495, -1.582230, -0.304897],
    "t": [1.195, 1.587, 1.434, 1.341, 1.189, 1.169, 0.944, 1.874],
    "d": [1, 2, 3, 1, 2, 3, 4, 4],
    "l": [0, 0, 0, 0, 0, 0, 0, 0],
    "eta": [0.000, 0.000, 0.000, 0.157, 0.931, 0.882, 0.868, 0.543],
    "beta": [0.000, 0.000, 0.000, 0.173, 1.070, 0.695, 0.862, 0.971],
    "gamma": [0.000, 0.000, 0.000, 1.310, 1.356, 1.596, 1.632, 0.766],
```

```
    "epsilon": [0.000, 0.000, 0.000, 1.032, 1.978, 1.966, 1.709, 0.583]
  },
  {
    "Name": "Helium-Argon",
    "aliases" : [],
    "type" : "Gaussian+Exponential",
    "BibTeX" : "Tkaczuk-2020",
    "Npower" : 3,
    "n": [-2.643654, -0.347501, 0.201207, 1.171326, 0.216379, 0.561370, 0.182570, 0.017879],
    "t": [1.030, 0.288, 0.572, 1.425, 1.987, 0.024, 1.434, 0.270],
    "d": [1, 2, 3, 1, 1, 2, 3, 4],
    "l": [0, 0, 0, 0, 0, 0, 0, 0],
    "eta": [0.000, 0.000, 0.000, 0.371, 0.081, 0.375, 0.978, 0.971],
    "beta": [0.000, 0.000, 0.000, 0.320, 1.247, 1.152, 0.245, 1.030],
    "gamma": [0.000, 0.000, 0.000, 1.409, 1.709, 0.705, 1.162, 0.869],
    "epsilon": [0.000, 0.000, 0.000, 0.378, 0.741, 0.322, 1.427, 2.088]
  },
  {
   "Name": "Neon-Argon",
   "aliases" : [],
   "type" : "Gaussian+Exponential",
   "BibTeX" : "Tkaczuk-2020",
   "Npower" : 3,
   "n": [-1.039686, 0.593776, -0.186531, -0.223315, 0.160847, 0.405228, -0.264563, -0.033569],
   "t": [0.723, 1.689, 1.365, 0.201, 0.164, 0.939, 1.690, 1.545],
   "d": [1, 2, 3, 1, 2, 2, 3, 4],
   "l": [0, 0, 0, 0, 0, 0, 0, 0],
   "eta": [0.000, 0.000, 0.000, 1.018, 0.556, 0.221, 0.862, 0.809],
   "beta": [0.000, 0.000, 0.000, 0.360, 0.373, 0.582, 0.319, 0.560],
   "gamma": [0.000, 0.000, 0.000, 1.119, 1.395, 1.010, 1.227, 1.321],
   "epsilon": [0.000, 0.000, 0.000, 2.490, 1.202, 2.468, 0.837, 2.144]
  },
  {
    "Name": "Helium-Nitrogen",
    "aliases" : [],
    "type" : "Gaussian+Exponential",
    "BibTeX" : "Tkaczuk-2021",
    "Npower" : 3,
    "n": [-3.122496,-0.245826, 0.172129, 1.455886, 0.681733, 0.228133, 0.053118],
    "t": [0.786, 0.232, 0.502, 0.304, 0.483, 1.419, 0.261],
    "d": [1, 2, 3, 1, 2, 3, 4],
    "l": [0, 0, 0, 0, 0, 0, 0],
    "eta": [0.000, 0.000, 0.000, 0.736, 0.782, 0.846, 0.660],
    "beta": [0.000, 0.000, 0.000, 0.590, 0.348, 0.576, 0.454],
    "gamma": [0.000, 0.000, 0.000, 1.048, 0.957, 1.539, 0.778],
    "epsilon": [0.000, 0.000, 0.000, 0.387, 1.133, 1.357, 1.773]
  }
  ]
  CP.set_config_bool(CP.NORMALIZE_GAS_CONSTANTS, False)
  CP.set_departure_functions(json.dumps(departure_JSON))
  for pair in itertools.combinations(fluids, 2):
    CP.apply_simple_mixing_rule(pair[0], pair[1], 'Lorentz-Berthelot')

BIPs = namedtuple('BIPS', ['betaT', 'gammaT', 'betaV', 'gammaV', 'Fij'])
def get_AS(fluids):
  BIP = {
```

```
    # reducing parameters from this work
    ("Helium","Neon"):     (0.793, 0.728, 1.142, 0.750, 1.0),
    ("Helium","Argon"):    (1.031, 1.113, 1.048, 0.862, 1.0),
    ("Neon","Argon"):      (1.033, 0.967, 0.919, 1.035, 1.0),
    ("Helium","Nitrogen"): (1.028, 1.229, 1.036, 0.935, 1.0),
  }
  AS = CP.AbstractState('HEOS', '&'.join(fluids))
  b = BIPs( BIP[fluids])
  for k in ['betaT', 'gammaT', 'betaV', 'gammaV', 'Fij']:
    AS.set_binary_interaction_double(0, 1, k, getattr(b, k))
  AS.set_binary_interaction_string(0, 1, 'function', '-'.join(fluids))
  return AS

def do_calc(z):
  setup_CoolProp(['Helium', 'Neon', 'Argon', 'Nitrogen'])
  print('mixture, pressure/Pa, alphar, rho_reducing/(mol m^{-3}), R/(J/mol K)')
  for pair, rhomolar in [
      (('Helium','Neon'), 1e4),
      (('Helium','Argon'), 1e4),
      (('Neon','Argon'), 1e4),
      (('Helium','Nitrogen'), 1e4)
      ]:
    AS = get_AS(pair)
    AS.specify_phase(CP.iphase_gas)
    AS.set_mole_fractions(z)
    AS.update(CP.DmolarT_INPUTS, rhomolar, 200)
    res = [AS.p(), AS.alphar(), AS.rhomolar_reducing(), AS.gas_constant()]
    print(pair[0] + ' - ' + pair[1] + ':', res)

if __name__ == '__main__':
  do_calc([0.5, 0.5])
```

APPENDIX D - EXPERIMENTAL SETUP FOR THE JOULE-THOMSON COEFFICIENT MEASUREMENTS

Table D.1. List of equipment used for measurements

	Control	
P&ID tag	Equipment type	Manufacturer and model
RV001	Pressure regulator	Alphagaz LTH 400
PI001	Pressure indicator	Alphagaz LTH 400
HV002	Diaphragm sealed valve	Nupro SS-DSV51
HV003	Diaphragm sealed valve	Nupro SS-DSV51
RV004A	Pressure regulator	Alphagaz LTH 400
PI004A	Pressure indicator	Alphagaz LTH 400
HV004B	Diaphragm sealed valve	Nupro SS-DSV51
SV005	Safety valve	Swagelok SS-6R3A-MM
HV006	Diaphragm sealed valve	Nupro SS-DSV51
TT007	Platinum temperature sensor	
TT008	Platinum temperature sensor	
Q008	Resistive heater in copper mass	
TT009	Platinum temperature sensor	
TT010	Platinum temperature sensor	
Q011	Resistive heater	
HV012	Diaphragm sealed valve	Swagelok SS-DLVC04
HV013	Needle valve	Hoke Mili-Mite 1335G4Y
HV014	Diaphragm sealed valve	Swagelok SS-DLVC04
HV015	Needle valve	Hoke Micromite 1654G4YA

Continued on next page

Table D.1. (*Continued.*)

HV016	Needle valve	Swagelok SS-4BMW-VCR
HV017	Diaphragm sealed valve	Swagelok SS-DLVC04
NV018	Check valve	Swagelok
cryocooler	Gifford-McMahon refrigerator	Cryomech AL300
	Measurements	
P&ID tag	Equipment type	Manufacturer and model
GA016	Gas analyzer	SRS BGA244HP
PT101	Absolute pressure transducer	Mensor CPT 6100
TT101	Cernox temperature sensor	Lake Shore CX-1080-CU-HT-20L
PT102	Gauge pressure transducer	Mensor CPT 6100
TT102	Cernox temperature sensor	Lake Shore CX-1050-SD-HT-1.4L
	Vacuum	
P&ID tag	Equipment type	Manufacturer and model
M301	Turbo-molecular pump	Alcatel
PT301	Vacuum pressure transmitter	Alcatel CF2P
M302	Roughing pump	Alcatel
HV303A	Diaphragm sealed valve	Nupro SS-DSV51
HV303B	Manual vacuum valve	
M303	Roughing pump	
PT303	Vacuum pressure transmitter	Adixen ACC2009-SP
HV304	Bellow sealed valve	Swagelok SS-4H-V71
PI304	Pressure indicator	Bourdon Haenni M1
M305	Turbo-molecular pump	
M306	Roughing pump	
PV306	Solenoid valve	
PT307	Vacuum pressure transmitter	Pfeiffer IKR 251

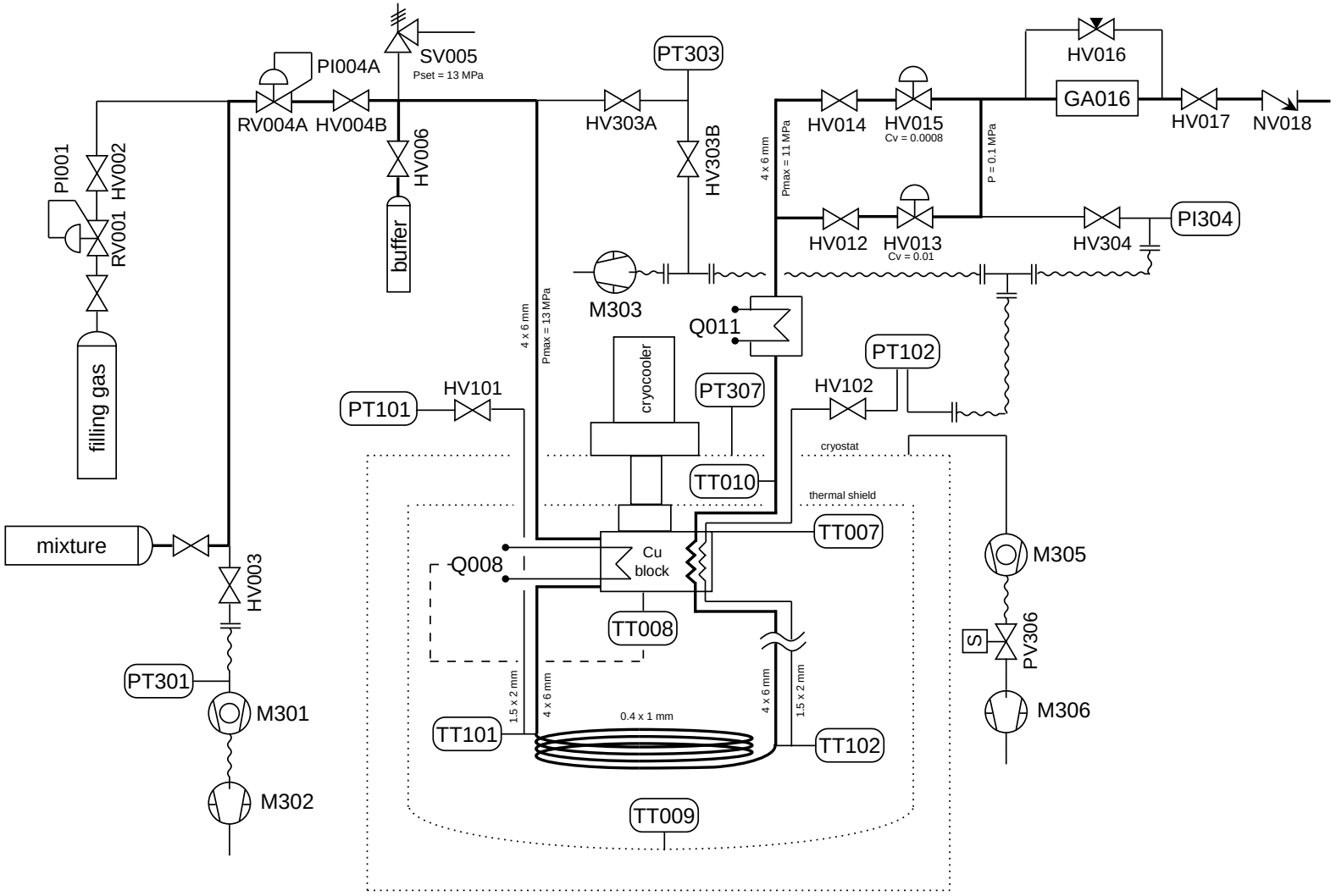

Fig. D.1. Piping and instrumentation diagram (P&ID) of the Joule-Thomson measurements setup. For PFD see Fig. 4.12.

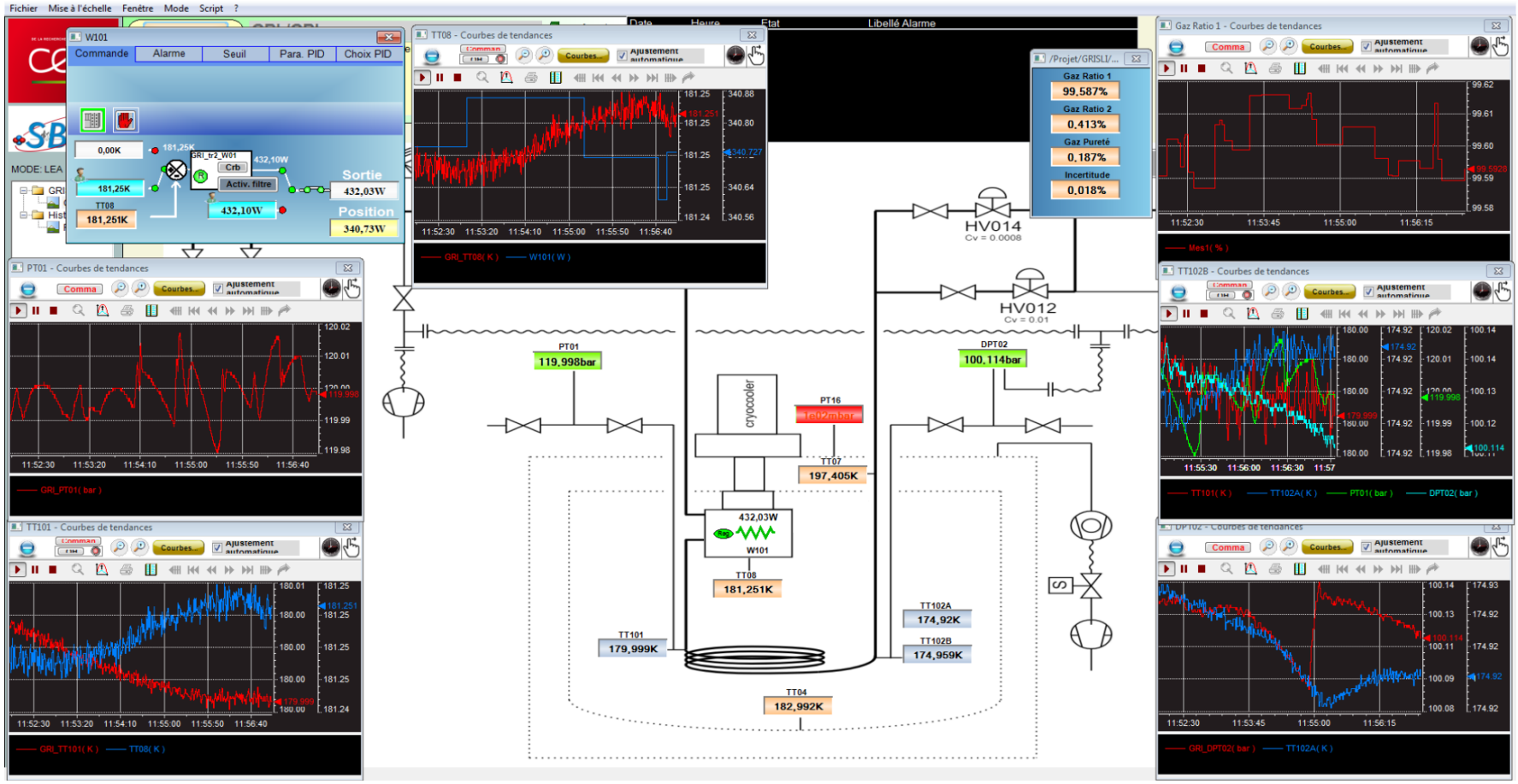

Fig. D.2. Print screen from Panorama E2 SCADA - software for data acquisition and hardware control. Image taken during test setup validation with pure argon.

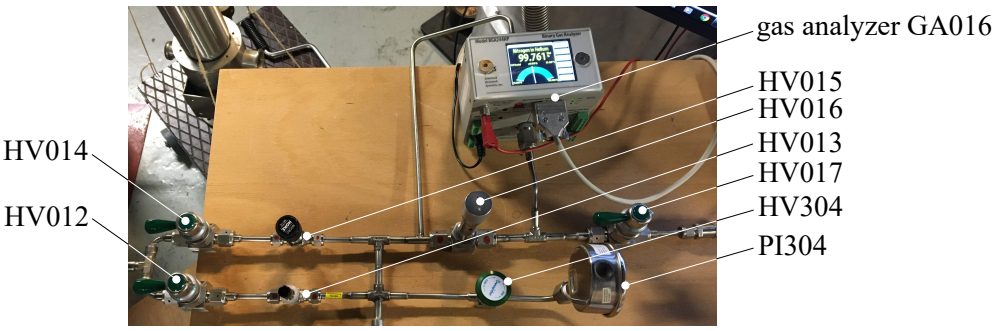

Fig. D.3. Gas manifold.

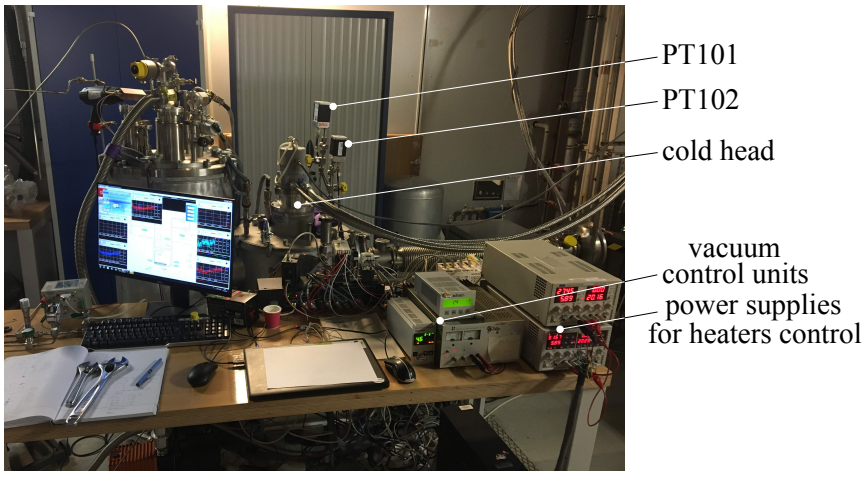

Fig. D.4. Complete experimental setup.

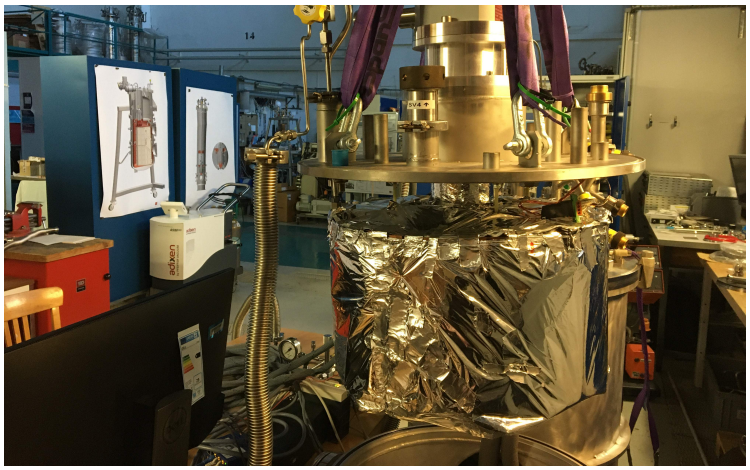
Fig. D.5. Multi-layer insulation on the thermal shield around the capillary.

Appendix E - Results from the Joule-Thomson coefficient measurements

Raw measurements of the $p-T$ pairs for pure fluids are given in Table E.1, for mixtures – in Table E.2. Uncertainty(x) characterizes the purity measurements for pure fluids and the composition measurements for mixtures. The measurements are reported separately for each fluid, each isenthalpic line, and each mixture composition. The color code in the first columns of Tables E.1 – E.4 represents points measured on different isenthalpic lines and matches the color codes in Figures 4.20, 5.3, 5.4, 5.8, 5.9, and 5.11. The calculated isenthalpic Joule-Thomson coefficients are reported in Table E.3 for pure fluids and in Table E.4 for mixtures.

Table E.1. $p-T$ measurements for the Joule-Thomson coefficient in pure fluids

Color	TT008/K	TT101/K	TT102/K	PT101/MPa	PT102/MPa	Impurity	Uncertainty(x)
				nitrogen			
Red	160.949	160.000	155.335	5.0000	3.9955	0.0096	0.0004
	161.068	160.000	148.407	5.0005	3.0135	0.0096	0.0004
	161.130	160.000	140.377	5.0005	2.0024	0.0096	0.0004
	161.170	160.001	131.322	5.0008	1.0065	0.0096	0.0004
Green	161.246	160.001	155.143	6.0000	4.9438	0.0014	0.0002
	161.309	160.001	149.009	6.0030	3.9984	0.0015	0.0002
	161.323	160.002	141.449	5.9998	2.9859	0.0014	0.0002
	161.341	160.003	132.400	5.9999	1.9534	0.0010	0.0002
	161.339	159.999	122.275	6.0000	0.9938	0.0013	0.0002

Table E.1. (*Continued.*)

Color	TT008/K	TT101/K	TT102/K	PT101/MPa	PT102/MPa	Impurity	Uncertainty(x)
Purple	161.315	160.002	155.529	7.0001	5.9090	0.0016	0.0002
	161.345	160.002	150.394	7.0002	5.0027	0.0016	0.0002
	161.351	160.001	143.799	7.0000	4.0111	0.0015	0.0002
	161.317	159.999	126.207	6.9999	2.0183	0.0014	0.0002
Blue	150.945	149.805	144.736	6.0004	5.0000	0.0013	0.0002
	150.946	149.803	137.855	6.0000	4.0007	0.0014	0.0002
	150.957	149.803	129.290	6.0000	3.0002	0.0013	0.0002
	150.965	149.805	118.338	6.0000	1.9998	0.0013	0.0002
	150.964	149.806	104.094	6.0000	1.0007	0.0012	0.0002
	150.970	149.804	88.229	6.0000	0.1410	0.0009	0.0002
Yellow	161.208	159.991	157.131	9.0004	7.9904	0.0017	0.0002
	161.186	159.990	153.414	9.0001	7.0112	0.0017	0.0002
	161.147	159.997	148.901	8.9999	5.9972	0.0018	0.0002
	161.157	159.994	143.339	8.9999	5.0070	0.0016	0.0002
	161.206	159.998	136.550	9.0000	3.9947	0.0013	0.0002
	161.187	160.002	128.117	9.0000	3.0169	0.0008	0.0002
	161.149	160.001	116.714	9.0000	2.0005	0.0004	0.0002
Pink	161.371	159.984	158.539	11.9900	11.0257	0.0021	0.0002
	161.362	160.000	156.617	12.0001	10.0132	0.0023	0.0002
	161.258	159.992	154.270	12.0010	8.9826	0.0017	0.0002
	161.256	160.000	148.758	12.0003	7.1160	0.0007	0.0002
	161.224	160.000	144.666	11.9994	6.0834	0.0010	0.0002
	161.219	160.000	139.251	12.0001	5.0011	0.0018	0.0002
	161.190	160.000	132.706	12.0000	3.9939	0.0021	0.0002
	161.174	160.000	124.200	11.9990	3.0037	0.0024	0.0002
argon							
Red	180.835	180.000	174.256	5.0000	3.9900	0.0008	0.0002
	180.944	180.003	165.672	4.9999	2.9990	0.0008	0.0002
	181.034	180.001	155.620	5.0000	1.9738	0.0007	0.0002
	181.062	180.000	144.619	5.0003	1.0080	0.0006	0.0002

Table E.1. (*Continued.*)

Color	TT008/K	TT101/K	TT102/K	PT101/MPa	PT102/MPa	Impurity	Uncertainty(x)
Blue	181.218	180.000	177.882	11.9999	11.0105	0.0014	0.0002
	181.254	180.002	171.711	11.9985	9.0211	0.0021	0.0002
	181.264	180.000	168.043	12.0000	8.0453	0.0022	0.0002
	181.265	180.000	163.525	11.9997	7.0206	0.0020	0.0002
	181.241	180.000	158.147	12.0000	5.9797	0.0020	0.0002
	181.234	180.000	152.137	12.0010	5.0147	0.0020	0.0002
helium-4							
Green	141.657	140.641	141.842	10.0000	9.0221	0.0015	0.0002
	141.628	140.643	142.220	10.0002	8.0238	0.0004	0.0002
	141.538	140.639	143.243	10.0056	5.9759	0.0009	0.0002
	141.464	140.641	144.719	10.0038	3.1790	0.0013	0.0002
Blue	64.920	65.000	67.403	7.0019	5.0047	0.0004	0.0002
	64.872	64.997	67.639	7.0000	3.9188	0.0005	0.0002
	64.857	65.008	68.288	7.0000	3.0835	0.0009	0.0002
	64.791	64.990	68.422	7.0000	2.0181	0.0007	0.0002
Red	64.996	64.992	66.387	5.0000	4.0426	0.0007	0.0002
	64.971	64.998	66.787	5.0001	2.9983	0.0006	0.0002
	64.951	64.998	67.059	5.0008	2.0013	0.0005	0.0002
	64.914	64.996	67.383	5.0002	1.0044	0.0005	0.0002

Table E.2. $p-T-x$ measurements for the Joule-Thomson coefficient in mixtures

Color	TT008/K	TT101/K	TT102/K	PT101/MPa	PT102/MPa	x_1	x_2	Uncertainty(x)
helium-4 – nitrogen								
Blue	161.161	160.009	153.377	7.9999	5.9964	0.1451	0.8549	0.0003
	161.161	159.999	149.319	8.0000	5.0593	0.1454	0.8546	0.0003
	161.150	160.001	138.391	8.0002	2.9918	0.1456	0.8544	0.0003
	161.136	159.996	131.425	8.0000	1.9437	0.1455	0.8545	0.0003
	161.125	160.006	124.148	8.0000	0.9940	0.1454	0.8546	0.0003
Green	140.920	140.000	135.793	5.0000	3.9977	0.1450	0.8550	0.0003
	140.990	140.000	129.309	5.0000	3.0062	0.1451	0.8549	0.0003
	140.999	140.000	121.591	4.9998	2.0059	0.1450	0.8550	0.0003
	141.012	140.000	112.796	5.0000	1.0390	0.1449	0.8551	0.0003

Table E.2. (*Continued.*)

Color	TT008/K	TT101/K	TT102/K	PT101/MPa	PT102/MPa	x_1	x_2	Uncertainty(x)
Red	160.868	160.001	156.934	5.0000	3.9806	0.1449	0.8551	0.0003
	161.031	160.001	146.451	5.0000	2.0139	0.1449	0.8551	0.0003
	161.010	160.001	140.220	4.9990	1.0004	0.1448	0.8552	0.0003
Blue	140.800	140.005	139.685	5.0000	3.9984	0.5025	0.4975	0.0002
	140.898	140.001	137.326	4.9990	3.2769	0.5026	0.4974	0.0002
	140.969	139.998	134.955	5.0000	2.0098	0.5027	0.4973	0.0002
	141.000	140.000	132.385	5.0000	0.9901	0.5027	0.4973	0.0002
Red	140.929	140.007	139.531	8.0000	6.9508	0.5026	0.4974	0.0002
	140.980	139.999	137.696	7.9999	5.9792	0.5027	0.4973	0.0002
	140.994	140.006	135.858	8.0000	5.0089	0.5027	0.4973	0.0002
	141.000	140.003	133.818	8.0000	4.0073	0.5028	0.4972	0.0002
	140.990	140.003	129.153	7.9997	2.0185	0.5030	0.4970	0.0002
	140.992	140.011	126.386	8.0000	1.0034	0.5028	0.4972	0.0002
helium-4 – neon								
Blue	65.094	65.053	65.035	5.0000	3.9540	0.2154	0.7846	0.0004
	65.125	65.053	63.124	5.0000	3.1092	0.2155	0.7845	0.0004
	65.134	65.053	60.685	5.0000	2.0442	0.2154	0.7846	0.0004
	65.133	65.053	58.115	5.0000	1.0334	0.2154	0.7846	0.0004
	65.140	65.053	55.572	5.0000	0.1467	0.2154	0.7846	0.0004
Red	65.119	65.047	65.132	7.0000	6.0111	0.2005	0.7995	0.0004
	65.126	65.043	63.945	7.0000	5.3862	0.2096	0.7904	0.0004
	65.115	65.046	61.429	7.0000	4.0289	0.2150	0.7850	0.0004
	65.106	65.043	59.869	7.0000	3.2727	0.2157	0.7843	0.0004
	65.103	65.045	56.836	6.9999	1.9843	0.2158	0.7842	0.0004
	65.101	65.044	54.131	7.0000	1.0031	0.2158	0.7842	0.0004
	65.105	65.046	51.438	7.0002	0.1758	0.2157	0.7843	0.0004
Blue	65.236	65.142	65.412	10.0001	9.0746	0.3138	0.6862	0.0003
	65.241	65.148	64.467	9.9999	8.1522	0.3145	0.6855	0.0003
	65.200	65.143	62.025	10.0000	5.9672	0.3068	0.6932	0.0003
	65.179	65.144	59.168	10.0006	3.9757	0.3029	0.6971	0.0003
	65.162	65.146	55.796	10.0002	2.0371	0.3157	0.6843	0.0003
Red	80.565	80.435	80.755	7.9999	6.9743	0.3263	0.6737	0.0003
	80.546	80.432	79.884	7.9999	6.0370	0.3277	0.6723	0.0003
	80.516	80.436	78.012	7.9997	3.9751	0.3275	0.6725	0.0003
	80.505	80.435	75.904	7.9998	1.9925	0.3280	0.6720	0.0003

Table E.2. (*Continued.*)

Color	TT008/K	TT101/K	TT102/K	PT101/MPa	PT102/MPa	x_1	x_2	Uncertainty(x)
Green	65.292	65.162	63.787	5.0006	3.1349	0.3279	0.6721	0.0003
	65.283	65.160	61.978	5.0092	2.0914	0.3278	0.6722	0.0003
	65.284	65.158	59.991	5.0000	1.0472	0.3278	0.6722	0.0003
Blue	65.069	65.014	65.150	5.0000	3.8435	0.3967	0.6033	0.0003
	65.100	65.016	64.081	5.0009	3.1354	0.3993	0.6007	0.0003
	65.099	65.014	62.581	5.0000	2.0727	0.3994	0.6006	0.0003
	65.110	65.015	60.875	4.9999	0.9803	0.3995	0.6005	0.0003
Red	65.028	64.995	65.263	7.0085	5.9934	0.3941	0.6059	0.0003
	65.068	64.996	64.018	7.0031	4.9649	0.3903	0.6097	0.0003
	65.079	64.997	62.858	6.9998	4.0554	0.3869	0.6131	0.0003
	65.051	64.995	61.497	6.9979	3.0707	0.3799	0.6201	0.0003
	65.065	64.998	60.024	7.0030	1.9997	0.3903	0.6097	0.0003
Blue	65.841	65.702	65.483	10.0000	7.9988	0.4623	0.5377	0.0003
	65.739	65.702	64.091	9.9999	6.0732	0.4554	0.5446	0.0003
	65.703	65.700	62.505	9.9998	4.1545	0.4625	0.5375	0.0003
	65.690	65.701	60.453	10.0011	2.2046	0.4640	0.5360	0.0003
Green	65.031	64.991	64.533	7.9997	6.0656	0.4673	0.5327	0.0003
	65.025	64.990	63.662	8.0000	5.0095	0.4665	0.5335	0.0003
	65.029	64.990	62.621	8.0001	3.8718	0.4668	0.5332	0.0003
	65.014	64.991	61.677	7.9999	2.9771	0.4671	0.5329	0.0003
Red	79.932	79.899	79.493	10.0002	6.5270	0.4666	0.5334	0.0003
	79.925	79.897	79.152	10.0001	5.9909	0.4669	0.5331	0.0003
	79.925	79.901	78.558	10.0010	5.0058	0.4672	0.5328	0.0003
	79.908	79.903	78.008	10.0003	4.0051	0.4672	0.5328	0.0003
Purple	80.045	80.005	80.711	5.0000	3.9098	0.4670	0.5330	0.0003
	80.072	80.004	79.964	5.0000	3.0241	0.4669	0.5331	0.0003
	80.068	80.005	79.158	5.0006	1.9438	0.4669	0.5331	0.0003
	80.060	80.005	78.427	5.0009	0.9947	0.4668	0.5332	0.0003
Yellow	80.090	79.994	79.880	7.0003	5.0184	0.4667	0.5333	0.0003
	80.074	79.997	79.257	7.0000	4.0014	0.4667	0.5333	0.0003
	80.076	79.999	78.631	7.0008	3.0050	0.4668	0.5332	0.0003

Table E.3. Calculated Joule-Thomson coefficient values for pure fluids

Color	p/MPa	T/K	Uncorrected		Corrected	
			μ_{JT}/(K MPa^{-1})	$100\Delta\mu_{JT}/\mu_{JT}$	μ_{JT}/(K MPa^{-1})	$100\Delta\mu_{JT}/\mu_{JT}$
nitrogen						
Red	3.0135	148.407	7.5026	-1.0448	7.5209	-1.2774
Red	2.0024	140.377	8.5331	0.8188	8.6234	-0.1955
Green	3.9984	149.009	6.8900	-0.1527	6.9516	-1.0353
Green	2.9859	141.449	8.0387	1.5179	8.0448	1.4558
Green	1.9534	132.400	9.6312	0.7467	9.6622	0.4894
Purple	5.0027	150.394	6.0872	-0.8579	6.0881	-0.8724
Purple	4.0111	143.799	7.2672	-0.0584	7.2732	-0.1359
Blue	4.0007	137.855	7.6352	0.0197	7.6532	-0.2152
Blue	3.0002	129.290	9.6162	0.6212	9.6034	0.7615
Blue	1.9998	118.338	12.4185	0.4365	12.4963	-0.1512
Blue	1.0007	104.094	16.3176	0.0892	16.3901	-0.0319
Yellow	7.0112	153.414	4.1402	-2.0086	4.1417	-2.0432
Yellow	5.9972	148.901	4.9880	-0.7138	4.9894	-0.7411
Yellow	5.0070	143.339	6.0531	0.7067	6.0537	0.6957
Yellow	3.9947	136.550	7.6008	1.0793	7.6043	1.0333
Yellow	3.0169	128.117	9.7416	0.5574	9.7556	0.4258
Pink	10.0132	156.617	2.0602	-0.0267	2.0604	-0.0336
Pink	8.9826	154.270	2.4743	-0.1982	2.4746	-0.2101
Pink	7.1160	148.758	3.5361	0.2572	3.5366	0.2386
Pink	6.0834	144.666	4.4002	0.6588	4.4009	0.6378
Pink	5.0011	139.251	5.6895	0.6007	5.6905	0.5743
Pink	3.9939	132.706	7.4314	0.2591	7.4332	0.2235
argon						
Red	2.9990	165.672	9.1458	0.8829	9.1401	0.9558
Red	1.9738	155.620	10.5451	1.8516	10.6486	0.9142
Blue	9.0211	171.711	3.5305	-0.6392	3.5307	-0.6446
Blue	8.0453	168.043	4.0474	0.2627	4.0476	0.2557
Blue	7.0206	163.525	4.7442	0.6431	4.7444	0.6353
Blue	5.9797	158.147	5.6777	0.9887	5.6777	0.9812
helium-4						
Blue	3.9188	67.639	-0.3729	-2.9601	-0.3504	3.2639
Blue	3.0835	68.288	-0.3729	-6.6128	-0.3504	-0.6474
Red	2.9983	66.787	-0.3368	0.2690	-0.2736	23.4193

Table E.3. (*Continued.*)

Color	p/MPa	T/K	Uncorrected		Corrected	
			μ_{JT}/(K MPa^{-1})	$100\Delta\mu_{JT}/\mu_{JT}$	μ_{JT}/(K MPa^{-1})	$100\Delta\mu_{JT}/\mu_{JT}$
Red	2.0013	67.059	-0.3067	3.6708	-0.2736	16.1308
Green	8.0238	142.220	-0.4978	13.0741	-0.4773	17.9450
Green	5.9759	143.243	-0.4978	12.7272	-0.4773	17.5797

Table E.4. Calculated Joule-Thomson coefficient values for mixtures

Color	p/MPa	T/K	x_1	x_2	Uncorrected μ_{JT}/(K MPa^{-1})	Corrected μ_{JT}/(K MPa^{-1})
helium-4 – nitrogen						
Blue	5.0593	149.319	0.1451	0.8549	4.5754	4.6006
Blue	2.9918	138.391	0.1451	0.8549	6.1213	6.1361
Blue	1.9437	131.425	0.1451	0.8549	7.1524	7.3672
Green	3.0062	129.309	0.1450	0.8550	7.1358	7.1490
Green	2.0059	121.591	0.1450	0.8550	8.4263	8.4867
Red	2.0139	146.451	0.1449	0.8551	5.8698	5.9704
Blue	3.2769	137.326	0.5025	0.4975	2.3361	2.3856
Blue	2.0098	134.955	0.5025	0.4975	2.3361	2.3856
Red	5.9792	137.696	0.5026	0.4974	1.8470	1.7931
Red	5.0089	135.858	0.5026	0.4974	2.0151	2.0296
Red	4.0073	133.818	0.5026	0.4974	2.1885	2.2738
Red	2.0185	129.153	0.5026	0.4974	2.5329	2.7586
helium-4 – neon						
Blue	3.1092	63.124	0.2154	0.7846	2.2417	2.2841
Blue	2.0441	60.685	0.2154	0.7846	2.4711	2.4695
Blue	1.0334	58.115	0.2154	0.7846	2.6888	2.6742
Red	5.3862	63.945	0.2005	0.7995	1.6688	1.6937
Red	4.0289	61.429	0.2005	0.7995	2.0490	2.0699
Red	3.2727	59.869	0.2005	0.7995	2.2608	2.2795
Red	1.9843	56.836	0.2005	0.7995	2.6217	2.6365
Red	1.0031	54.131	0.2005	0.7995	2.8965	2.9085
Blue	8.1522	64.467	0.3138	0.6862	0.9903	0.9824
Blue	5.9672	62.025	0.3138	0.6862	1.3009	1.3103
Blue	3.9757	59.168	0.3138	0.6862	1.5840	1.6091

Table E.4. (*Continued.*)

Color	p/MPa	T/K	x_1	x_2	Uncorrected μ_{JT}/(K MPa^{-1})	Corrected μ_{JT}/(K MPa^{-1})
Red	6.0370	79.884	0.3264	0.6736	0.8864	0.8836
Red	3.9751	78.012	0.3264	0.6736	0.9943	1.0219
Green	2.0913	61.978	0.3279	0.6721	1.8181	1.8769
Blue	3.1354	64.081	0.3967	0.6033	1.4491	1.4525
Blue	2.0727	62.581	0.3967	0.6033	1.5003	1.5686
Red	4.9649	64.018	0.3942	0.6058	1.2550	1.2570
Red	4.0554	62.858	0.3942	0.6058	1.3120	1.3238
Red	3.0707	61.497	0.3942	0.6058	1.3737	1.3962
Blue	6.0732	64.091	0.4623	0.5377	0.7811	0.7870
Blue	4.1545	62.505	0.4623	0.5377	0.9452	0.9690
Green	5.0096	63.662	0.4673	0.5327	0.8568	0.8605
Green	3.8718	62.621	0.4673	0.5327	0.9843	0.9955
Red	5.9909	79.152	0.4666	0.5334	0.5887	0.5983
Red	5.0058	78.558	0.4666	0.5334	0.5887	0.5983
Purple	3.0241	79.964	0.4670	0.5330	0.7786	0.8130
Purple	1.9438	79.159	0.4670	0.5330	0.7786	0.8539
Yellow	4.0014	79.257	0.4667	0.5333	0.6202	0.6321